5-1-1989

Report on a Periodic Extrinsic Infrared (PEIR) Photoconductor

P. E. Welsh
Purdue University

R. J. Schwartz
Purdue University

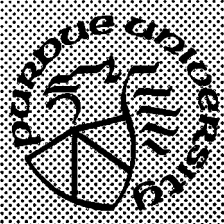

Report on a Periodic Extrinsic Infrared (PEIR) Photoconductor

P. E. Welsh
R. J. Schwartz

TR-EE 89-28
May, 1989

School of Electrical Engineering
Purdue University
West Lafayette, Indiana 47907

REPORT ON A PERIODIC EXTRINSIC INFRARED (PEIR) PHOTOCONDUCTOR

By
P.E. Welsh
R.J. Schwartz

School of Electrical Engineering
Purdue University
West Lafayette, IN 47907

TR-EE 89-28

May 1989

ACKNOWLEDGMENTS

We gratefully acknowledge the support of the NASA Lewis Research Center under grant NAG 3-433. Most of the previous work instrumental to the writing of this technical report was undertaken under grant NAG 3-433. One of the authors (PEW) would also like to thank the GTE Corporation for offering a fellowship during the last year and a half.

TABLE OF CONTENTS

Page

Page

APPENDICES

LIST OF TABLES

LIST OF FIGURES

LIST OF SYMBOLS

α .....absorption coefficient
a_H^o .....Bohr radius
a_H .....effective Bohr radius
A .....Richardson constant
A^* .....effective Richardson constant
A_C .....area of the contacts of the photoconductor
A_D .....area of the detector
b ..... $\frac{\mu_n}{\mu_p}$
B_I .....energy width of the impurity band
β_e .....electron ionization coefficient
β_h .....hole ionization coefficient
c .....speed of radiation
C .....capacitance
d .....average distance between ionized impurities
d_{BL} .....blocking layer width
d_{IL} .....impurity band layer width
d_x .....detector element width in the x-direction.
d_T .....one length of the detector area
d_y .....detector element width in the y-direction.
d_z .....detector element width in the z-direction.
d_{z2} .....distance between contacts in a PEIR photoconductor
D_i^- .....Cluster of i impurity atoms that contain an extra electron
D^* .....D-star
D_{RG}^* .....D-star in a conventional photoconductor when RG noise dominates
D_{BLIP}^* .....D-star for background limited infrared photodetector(BLIP)
$D_{B_I}(E)$ .....density of states of the impurity band ground state energy levels
ΔB .....bandwidth
ΔE_C .....total lowering of the ionization energy (n-type)
ΔE_{C1} .....lowering of the ionization energy (n-type)
due to the overlap of the ionized donor potentials
ΔE_{C2} .....total lowering of the ionization energy (n-type)
due to the tunneling of the bound electron

ΔE_{te} .....thermionic emission barrier height
Δf.....bandwidth
e .....electric charge
E_A .....Acceptor impurity atom ground state energy level
E_C .....conduction band energy
E_D .....Donor impurity atom ground state energy level
E_F.....Fermi energy
E_{Hy} .....ground state energy of a hydrogen atom
E_I .....ionization or activation energy
$E_{I_{th}}$ .....Theoretical ionization or activation energy - design parameter
E_{Ieff}.....ionization energy due to the effective mass theory
E_V .....valence band energy
E_λ.....photon energy
ϵ_A .....$E_A - E_V$
ϵ_o.....dielectric constant of air
ϵ_s .....static dielectric constant
ϵ_{sr} .....relative static dielectric constant
f(E).....Fermi distribution function
F(r).....hydrogenic wave function
g .....generation rate
G .....gain
h.....Planck's constant
$\hbar$ .....Planck's constant / (2π)
$\underline{i(t)}_{1/2}$.....current in a photoconductor
$\underline{(i_B^2)}_{1/2}$.....rms noise current source for background radiation
$\underline{(i_{RG}^2)}_{1/2}$ .....rms current source for RG noise
$\underline{(i_S^2)}_{1/2}$.....rms noise current source for signal radiation
$\underline{(i_{Th}^2)}_{1/2}$ .....rms current source for thermal noise
(I_n^2) .....total rms current source for noise
I_B.....background current
I_d .....dark current
I_{DC}.....dark current
$\overline{I_n^2}$.....mean square current of the noise terms
I_{op}.....optical current
I_s .....signal current
I_{te} .....thermionic emission current
$J_B(\lambda_a)$.....background current
$J_{op}(\lambda_a)$.....optical current density at wavelength λ_a
$J_s(\lambda_a)$.....signal current density at wavelength λ_a
J_{te}.....thermionic emission current density
J_{tun} .....tunnel current density
k.....Boltzmann constant

$\mathbf{k}$.....crystal momentum
κ.....imaginary part of the index of refraction
L.....distance between photoconductor contacts
λ.....wavelength of radiation
λ_d.....wavelength of radiation the detector is designed to detect
λ_D.....overall screening length
λ_{De}.....extrinsic Debye length
λ_{Di}.....intrinsic Debye length
λ_{min}.....minimum radiation wavelength that can be efficiently detected
λ_{max}.....maximum radiation wavelength that can be efficiently detected
m_e.....electron mass
m_e^*.....effective electron mass in the conduction band
m_r^*.....relative effective electron mass
m^*.....effective electron mass
μ.....mobility
μ_n.....electron mobility
n.....electron concentration
$\hat{n}(t)$.....number of electrons
$\hat{n}_o$.....steady state number of electrons
n_c.....complex index of refraction
n_r.....real part of the index of refraction
N_A.....compensation dopant concentration (n-type device)
$\hat{N}_A$.....number of compensation dopants (n-type device)
$N_{\bar{A}}$.....compensation dopant concentration (n-type device)
$N_\cap$.....number of recombination centers
N_D.....majority dopant concentration (n-type device)
$\hat{N}_D$.....number of majority dopants (n-type device)
N_D^+.....ionized majority dopant concentration (n-type device)
N_{DIL}^+.....ionized majority dopant concentration (n-type device) in the impurity band layer
N_D^o.....neutral majority dopant concentration (n-type device)
N_I.....majority dopant concentration
N_I^o.....neutral majority dopant concentration
p(E).....distribution of potential due to the ionized impurities
$\hat{p}(t)$.....number of holes
$\hat{p}_o$.....steady state number of holes
P.....power of incoming radiation
ϕ.....photon flux
ϕ_B.....background photon flux
ϕ_k.....wavefunction
ϕ_a.....orbital wavefunction
q.....electric charge

r_c .....contact resistivity
R .....resistance
R_1 .....contact resistance
R_2 .....resistance of the active region
R_3 .....transparent contact resistance
R_4 .....contact resistance
R_5 .....resistance of the metal
R_{2l} .....reflection coefficient for two layers (power)
R_{em} .....reflection coefficient (power)
$R_\square$ .....sheet resistance
ρ .....resistivity
ρ_{em} .....reflection coefficient (electric field)
S .....grid spacing
$S_i(f)$ .....spectral noise density
σ_{abs} .....absorption cross section
$\sigma_{abs_{th}}$ .....theoretical absorption cross section
$\sigma_{abs_{ex}}$ .....experimental absorption cross section
σ_{cap} .....Capture cross section
σ_{dos} .....Gaussian standard deviation for density of states
T .....temperature
T_{em} .....transmission coefficient (power)
T_B .....background blackbody temperature
τ .....lifetime
τ_d .....dielectric relaxation time
τ_{abs} .....inverse of the absorption rate
τ_{cap} .....carrier lifetime
τ_{em} .....transmission coefficient (electric field)
τ_{SR} .....Shockley-Read recombination lifetime
v_{av} .....average velocity of the carrier
v_c .....velocity of radiation in a medium
V .....voltage
V(r) .....impurity atom potential
ω .....frequency of radiation
ξ .....electric field
ξ_d .....electric field in a BIB detector at the impurity band layer-blocking layer interface
η .....efficiency
η_{metal} .....efficiency due to transmission through the metal grid
η_{TC} .....efficiency due to transmission through the transparent contact

ABSTRACT

An infrared photoconductor, designated as the Periodic Extrinsic InfraRed (PEIR) photoconductor, is proposed. A PEIR photoconductor will be useful for detecting wavelengths from 7 μm (1400 cm^{-1}) to longer than 100 μm (100 cm^{-1}). Through epitaxial growth, a PEIR photoconductor is made up of heavily doped layers separated by lightly doped layers. The heavily doped layers are doped such that an impurity band forms but are not doped high enough to cause the impurity band to merge with the conduction or valence band. The lightly doped layers are used to confine the carriers in the impurity bands and consequently, conduction can only occur due to carriers excited to the conduction (n-type device) or valence (p-type device) band. Radiation excites the carriers from the impurity band to the conduction or valence band. The impurity band layers are thin enough that even if the electric field in the impurity band layers is small, there is a high probability the excited carrier will scatter into the lightly doped layer and be swept away by the electric field in the lightly doped layer.

A PEIR photoconductor will have two major advantages. First, the absorption coefficient will be high because of the high impurity concentration in the impurity band layers. The absorption coefficient will be from $10^3 cm^{-1}$ to as high as $10^4 cm^{-1}$. Additionally, a method has been found to approximately determine the highest absorption coefficient attainable in specific host

semiconductor:impurity dopant materials systems. Consequently, one can determine the optimum host semiconductor:impurity dopant system to be used in a PEIR photoconductor designed to detect a certain wavelength. Second, some host semiconductors that are being considered are Si and GaAs, which are much easier to work with than HgCdTe (the material of choice for intrinsic photoconductors at wavelengths longer than 7 μm).

1. OPERATION OF A PERIODIC EXTRINSIC INFRARED (PEIR) PHOTOCONDUCTOR

1.1 Introduction

Three types of photodetectors are predominant today - pin photodiodes, avalanche photodiodes (APDs) and photoconductors (PCs) [Forrest 1986; Elliott 1981; Long 1977]. For wavelengths longer than 7 μm though, conventional photodetectors degrade in performance because of serious device materials problems (See sec. 1.2). The Periodic Extrinsic InfraRed (PEIR) photoconductor, described in sec. 1.3, is proposed as an alternative for the detection of wavelengths greater than 7 μm.

Section 1.2 describes the problems encountered by conventional detectors at long wavelengths. Section 1.3 describes how a PEIR photoconductor operates. Section 1.4 presents the important physical relationships in the PEIR photoconductor. Section 1.5 presents the advantages and disadvantages of the PEIR photoconductor as compared to conventional photodetectors. Section 1.6 describes the remaining chapters in the report.

1.2 Problems encountered by conventional photodetectors at long wavelengths

The pin photodiode, the APD and the intrinsic photoconductor operate through band to band absorption. When a photon is absorbed, an electron is excited to the conduction band, leaving a hole in the valence band. Two carriers (an electron and a hole) participate in this process. In the extrinsic photoconductor, on the other hand, the radiation excites the electron in an n-type PC (or hole in a p-type PC) from a donor (acceptor) site into the conduction (valence) band. This is a one carrier process.

The major problem for two carrier photodetectors at long wavelengths is finding a suitable semiconductor with a small band gap. For two carrier detectors, the band gap must be small enough for a long wavelength photon to cause a valence band to conduction band transition. For wavelengths longer than 7 μm, there are only three materials that are seriously considered for two carrier photodetectors - $Hg_{1-x}Cd_xTe$, $Pb_{1-x}Sn_xSe$, and $Pb_{1-x}Sn_xTe$ [Elliott 1981; Dennis 1986]. The lead salts, $Pb_{1-x}Sn_xSe$ and $Pb_{1-x}Sn_xTe$, have serious

high frequency limits [Elliott 1981; Dennis 1986] and are only considered because $Hg_{1-x}Cd_xTe$ has undesirable materials properties [Elliott 1981; Dennis 1986].

Due to these serious materials problems, the extrinsic photoconductor is the device most commonly used at wavelengths "beyond a few microns" [Sze 1981] or at this time, approximately 15 μm ([Walter & Dereniak 1986a; Walter & Dereniak 1986b; Stillman, Wolfe, & Dimmock 1977] - The exact value of this wavelength depends on the geometry of the device, whether the device is used by itself or in an array, and what is acceptable as a yield [Walter & Dereniak 1986a; Walter & Dereniak 1986b]). The one carrier characteristic of the extrinsic photoconductor means that the troublesome narrow gap semiconductor of the two carrier detector is replaced with a wider gap semiconductor with more desirable materials parameters. Unfortunately, the impurity dopant concentration in an extrinsic photoconductor must be less than the amount that will induce conduction in the impurity band [Bratt 1977]. Consequently, the absorption coefficient in extrinsic photoconductors is inevitably low (See sec. A.2).

The PEIR photoconductor, described in the next section, and the other novel photoconductors in sec. A.2 have been proposed as alternative photoconductors that attempt to avoid the narrow band gap problems of two carrier photodetectors and the low absorption coefficient problems of the extrinsic photoconductor.

1.3 Description of the Periodic Extrinsic InfraRed (PEIR) photoconductor

An infrared photoconductor, the Periodic Extrinsic InfraRed (PEIR) photoconductor is proposed which will have the capability of detecting infrared radiation in the wavelength range from 7 μm (1400 cm^{-1}) to longer than 100 μm (100 cm^{-1}). Below 7 μm, intrinsic photoconductors with good materials properties can be fabricated. The long wavelength limit is determined by the quality of the growth of the material used in a PEIR photoconductor. As the impurity band dopant concentration becomes more uniform throughout each impurity band layer, more uniform from impurity band layer to impurity band layer, and easier to calibrate, the long wavelength limit will increase.

A geometrical model of a PEIR photoconductor is shown in Fig. 1.1. It is made up of two contact layers with accompanying metalization and an active (or photoconductive) region. The active region which is the most important part of the device, is shown with ideal metal contacts in Fig. 1.2 (unbiased) and Fig. 1.3 (biased). A worst case configuration is shown in Fig. 1.4 and will be considered in more depth when discussing the possible accumulation of electrons

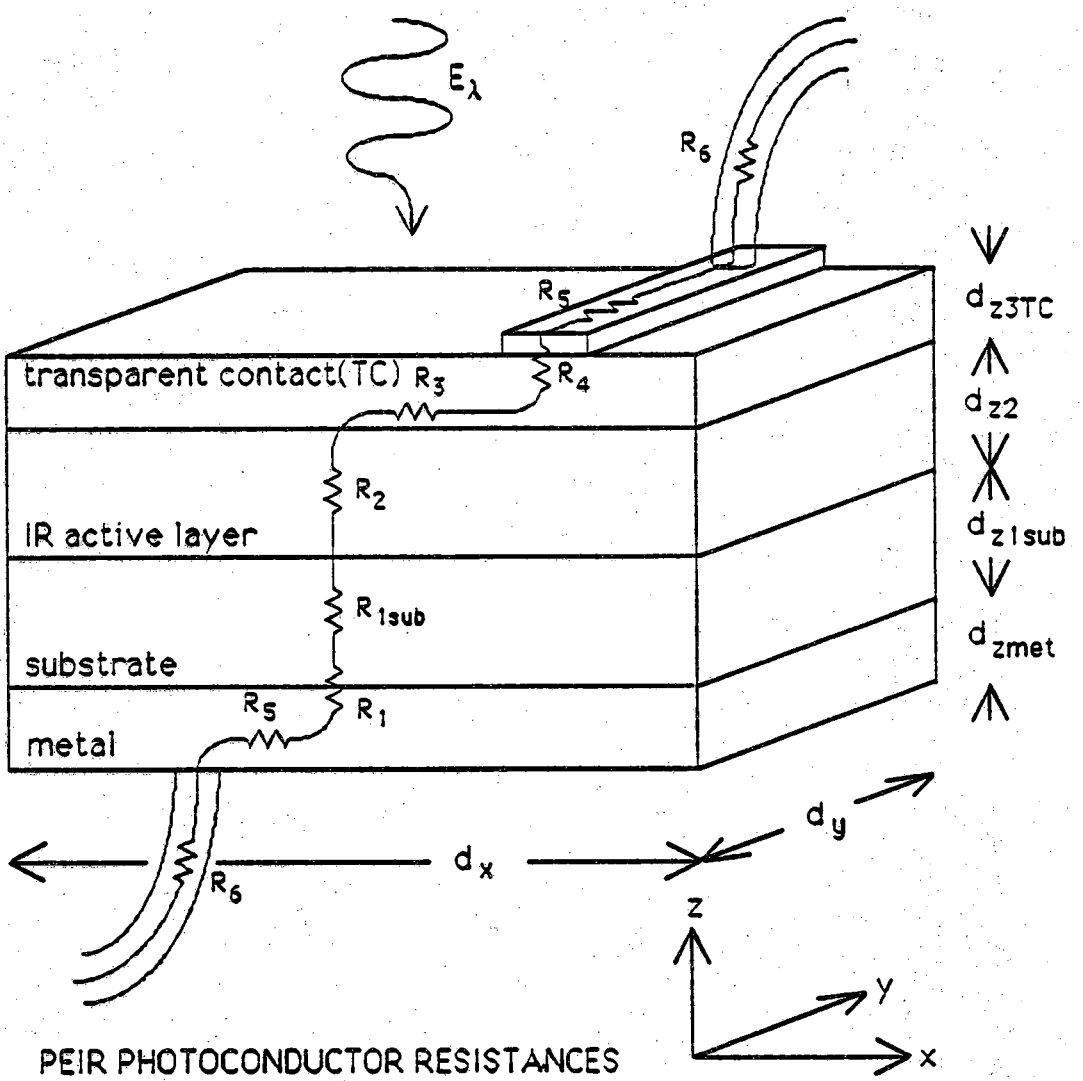

Figure 1.1 Geometrical model of a PEIR photoconductor

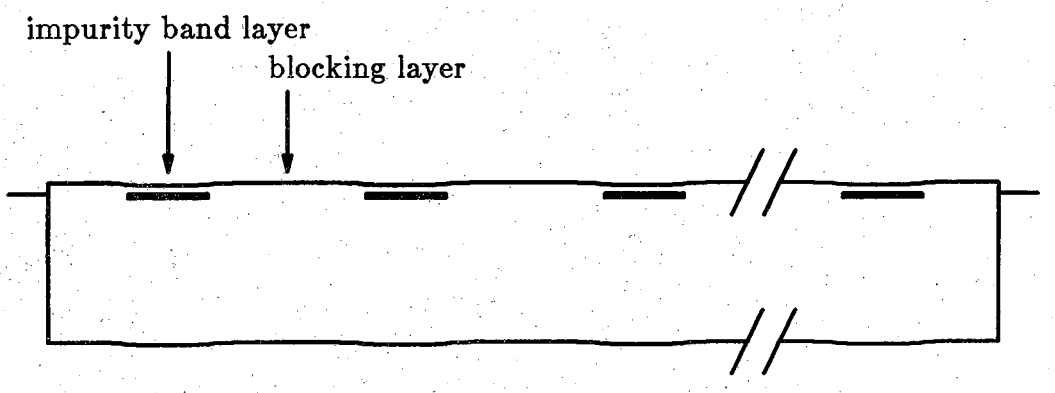

Figure 1.2 A PEIR photoconductor - unbiased

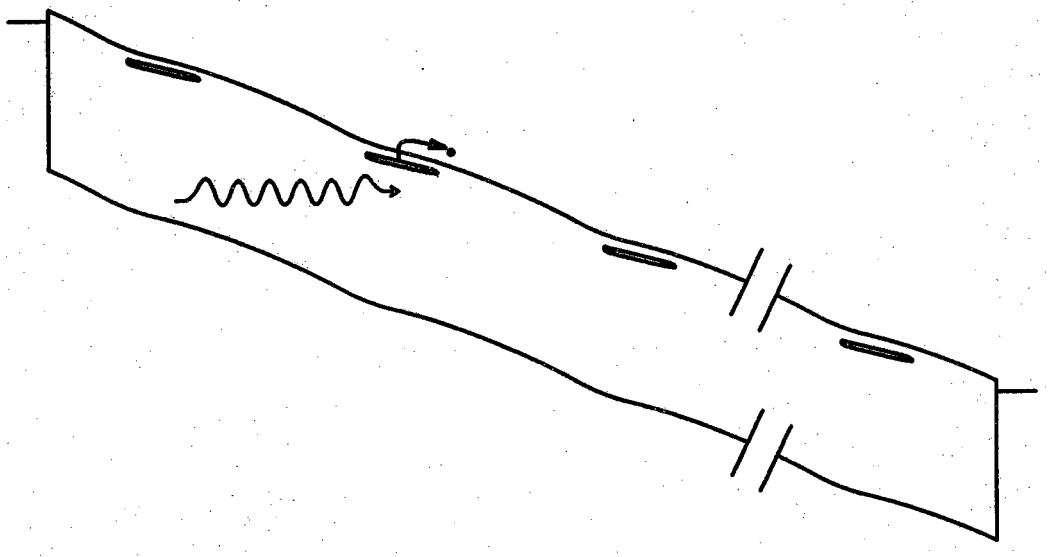

Figure 1.3 A PEIR photoconductor - biased

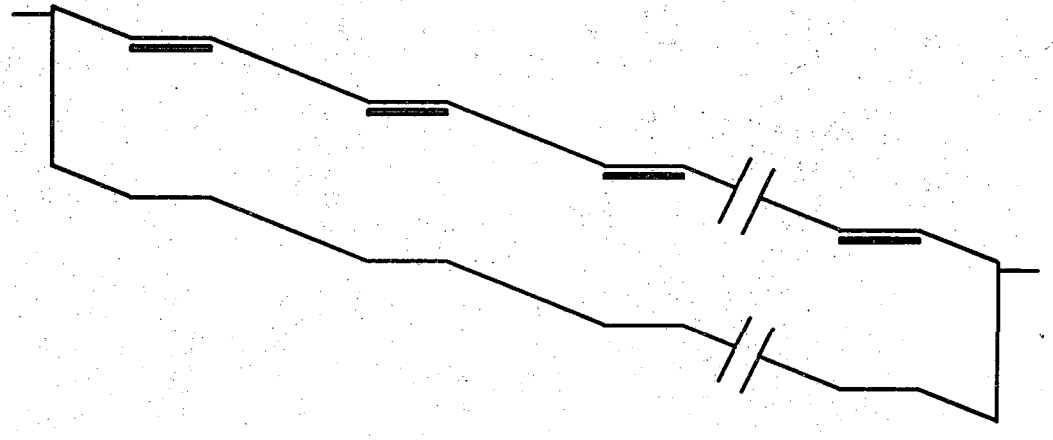

Figure 1.4 A PEIR photoconductor - worst case

at one end of the impurity band layers. A PEIR photoconductor is made up of heavily doped layers, labeled as impurity band layers, separated by lightly doped layers, labeled as blocking layers. The impurity band layers are doped enough to form an impurity band but not enough to cause the donor level energy states and conduction band energy states to overlap (for an n-type device). One impurity band layer with an impurity band energy width of B_I is shown in Fig. 1.5 where $(E_C - E_D)_{min}$ is the separation between the top of the donor level energy states and the conduction band energy states. E_I is the ionization energy of an isolated donor state. The blocking layers prevent impurity band conduction, leaving only conduction in the conduction band. The blocking layers are doped less than is needed to form an impurity band [Petroff & Stapelbroek 1986; Walter & Dereniak 1986a; Bratt 1977].

The radiation propagates perpendicular to the layers and excites electrons out of the impurity bands. The impurity band layers are thin enough (on the order of 100 Å) that even if the electric field is small in the impurity band layers (See Fig. 1.4), the electron can scatter into an adjacent blocking layer and be swept away by the electric field in the blocking layer. In the impurity band, the impurity band dopant atoms are spaced close enough together that electrons can flow from one impurity site to another [Bratt 1977]. In a donor impurity band, the empty sites can be labeled as impurity band "holes". These impurity band "holes" in the donor impurity band, which are actually ionized donors, flow to one end (the left side in Fig. 1.3) of the impurity band layers, decreasing the electric field in the impurity band layers. In the same way as in extrinsic photoconductors, electrons in the conduction band recombine with the impurity band "holes". This discussion describes the situation with n-type impurity band dopants, but an analogous argument can be used for p-type impurity band dopants with similar results.

The concentration of impurity dopants in impurity band layers can be 100 times larger than the concentration of impurity dopants allowed in an extrinsic photoconductor because the blocking layers prevent conduction in the impurity band. Consequently, a PEIR photoconductor will have a much higher absorption coefficient than a extrinsic photoconductor (See chap. 4). Due to this higher absorption coefficient, the temperature of operation in a PEIR photoconductor can be higher than in a extrinsic photoconductor (See app. B) and if one can adjust the carrier capture cross section (See app. C), the operating temperature can be higher than in a intrinsic photoconductor (See app. B). In addition, the radiation absorption process that excites the carriers from the dopant levels to the conduction band peaks at a certain energy (See chap. 4), which means that much of the background radiation can be filtered

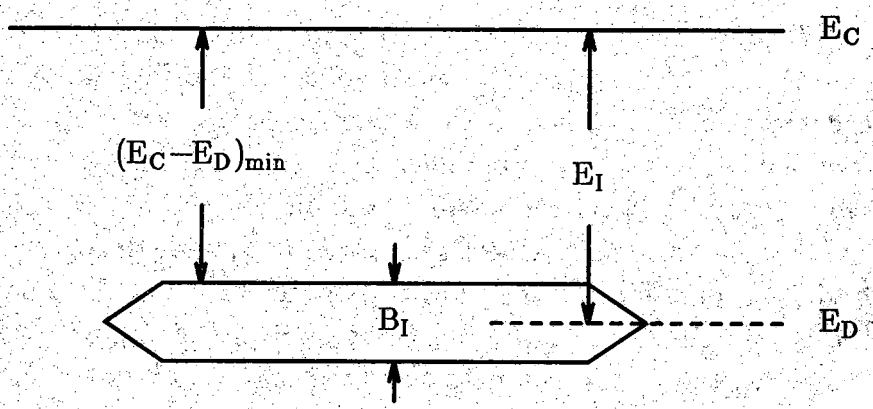

Figure 1.5 Heavy doping parameters in the impurity band layer

(See chap. 5). Consequently, a PEIR photoconductor can be more sensitive than a conventional photoconductor in background limited conditions (higher D^*_{BLIP}) (See chap. 5).

The ohmic contacts will most likely be a heavily doped substrate and a heavily doped transparent layer on top of the epitaxial layers (See Fig. 1.6a). This is the contact configuration used in the Blocked Impurity Band (BIB) detector (See sec. A.2.3). For a blocking contact configuration (See Fig. 1.6b), an insulator blocks the passage of the carriers. Although impact ionization must be avoided in the ohmic contact configuration [Bratt 1977], it can possibly be an advantage in the blocking contact configuration [Levine, Choi, Bethea, Walker, & Malik 1987a]. With the transparent contact, a PEIR photoconductor will be ideally suited for an array using either of these contact configurations [Wang, Richards, Beeman, Haegel, & Haller 1986].

A PEIR photoconductor can be fabricated with a variety of different host semiconductor:impurity atom combinations. There are two designs being actively pursued at this time. One possible design is to build a Si:P PEIR photoconductor. The absorption coefficient in this n-type PEIR photoconductor can approach $3x10^3 cm^{-1}$ for an impurity band dopant concentration of $2x10^{18} cm^{-3}$. The other design choice is a GaAs:Be photoconductor. The absorption coefficient in this p-type PEIR photoconductor can approach $1.5x10^3 cm^{-1}$ for an impurity band dopant concentration of $1x10^{18} cm^{-3}$. These absorption coefficients are two to four times larger than those obtained in some Si:As BIB detectors [Petroff & Stapelbroek 1984]. Moreover, even better host semiconductor:impurity atom alternatives exist. One better alternative can be Si:Bi (n-type) which can exceed $5x10^3 cm^{-1}$ for an impurity band dopant concentration of $7x10^{18} cm^{-3}$. The precise absorption coefficient is difficult to predict because it depends upon the width of the impurity band (B_I). A procedure to determine the best host semiconductor:impurity atom combinations to detect a predetermined wavelength is described in sec. 4.6 and sec. 4.7.

1.4 Important physical phenomena in a PEIR photoconductor

The operation of a PEIR, as described in sec. 1.3, is straightforward. The more difficult problem is to determine the capability of the device. There are several basic physical parameters that determine this capability. Most of these parameters and how they affect the operation of the device are presented in app. C.

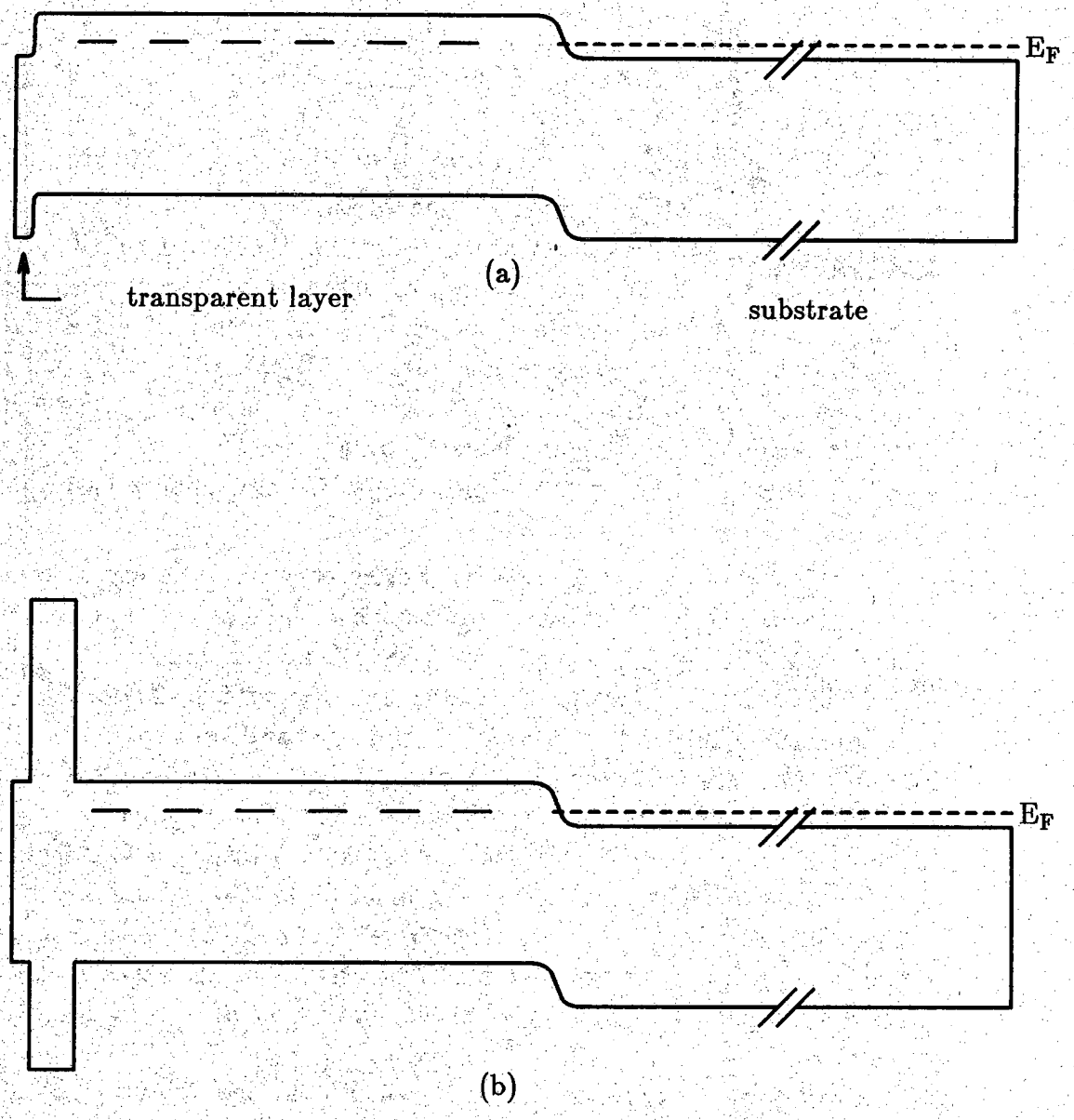

Figure 1.6 Contact configuration in equilibrium. (a) Ohmic contacts. (b) Blocking contacts.

There are five physical phenomena that greatly influence the operation of a PEIR photoconductor. These are 1) space charge formation (See chap. 2) , 2) heavy doping parameters - ΔE_C, σ_{dos}, B_I (See chap. 3), 3) infrared radiation absorption (See chap. 4), 4) generation and ionization processes (See app. B and app. D), and 5) carrier lifetime. Each of these phenomena is now described in more detail.

1.4.1 Space charge formation

Space charge formation determines the electric field distribution in the active region and the performance of a PEIR photoconductor depends directly upon this electric field distribution. Four space charge components cause the electric field, ξ, to vary with position in a PEIR photoconductor: 1) compensation dopants [Bratt 1977], 2) carriers in the conduction band, 3) excess carriers in the impurity band (negatively charged donor impurities), and 4) ionized impurities (positively charged donor impurities). The effect of these components on the electric field distribution is discussed in chap. 2.

As shown in chap. 2, the space charge formation determines the distribution of the electric field in a PEIR photoconductor. First, as the compensation dopant concentration and the carrier concentration in the conduction band increases, the electric field in the impurity band layers decreases slightly (See Fig. 1.3). Second, if electrons can accumulate at one end of the impurity band layers, the electric field in the impurity band layers decreases significantly. At first, this electron accumulation may appear to be a serious problem because the electrons excited into the conduction band may immediately recombine into the impurity band but since the layers are so thin (on the order of 100 Å), the electrons excited into the conduction band could very likely escape from the impurity band layer into an adjacent blocking layer and be swept away by the electric field.

1.4.2 Heavy doping parameters - ΔE_C, σ_{dos}, B_I

The heavy doping parameters are defined as [Lee & McGill 1975]: ΔE_C is the reduction of the energy difference between the donor level ground states and the bottom of the conduction band produced by the average distribution of ionized majority impurities [Lee & McGill 1975]. σ_{dos} is the standard deviation of the Gaussian potential distribution where the Gaussian potential distribution is produced by the random distribution of ionized impurities. B_I is the energy width of the impurity band produced by the distribution of majority impurities.

The heavy doping parameter effects on a PEIR photoconductor are described in more depth in chap. 3. The conclusion in chapter 3 is that ΔE_C and σ_{dos} are small enough to be negligible because the compensation doping is small and the carrier concentration (produced by the background photon flux or thermal generation) is small. B_I is not negligible because N_D (the majority dopant concentration) is necessarily large to obtain a high absorption coefficient.

1.4.3 Infrared radiation absorption

This section is divided into two parts. The first part describes the problems of theoretically calculating an absorption coefficient as the impurity band widens. The second part shows the requirements needed for the semiconductor and the dopant impurity that will be incorporated into a PEIR photoconductor.

For an infrared signal to be detected in a PEIR photoconductor, the infrared radiation must excite an electron from the impurity band to the conduction band (n-type device). In an extrinsic photoconductor, the absorption coefficient equals the number of neutral impurities times the absorption cross section. This absorption cross section is a function of energy [Bratt 1977] and is assumed to be the same for all the impurities in an extrinsic photoconductor. This assumption is reasonable because the ground state energy level is at the same energy for all the impurities. As an impurity band forms in a PEIR photoconductor, the ground state energy levels begin to take on a range of values and the absorption cross section as a function of energy (defined herein as the absorption spectrum) may begin to depend upon the energy of ground state energy level of an impurity. Consequently, the precise absorption coefficient is difficult to predict because it depends upon the width of the impurity band. The major concern is that the peak absorption coefficient may not be as large as predicted. There are three arguments that alleviate this concern. 1) The absorption coefficient needs to be only $2x10^3 cm^{-1}$ to get reasonable operation of a PEIR photoconductor and for this case, B_I can be reasonably small. 2) The absorption spectrum has a half energy width about equal to the ionization energy. 3) The peak absorption coefficient may be smaller, but will not lower drastically because the absorption spectrum also broadens. If the impurity band width is less than the ionization energy, the peak absorption coefficient may still be close to the peak values shown in chap. 4.

There are two major requirements for any host semiconductor:impurity atom system used in a PEIR photoconductor. 1) The absorption coefficient needs to be high. 2) The impurity band must be separated from the conduction band (in an n-type device) which places a limit on the absorption coefficient.

This separation equals $(E_C-E_D)_{min}$ (See Fig. 1.5).

As shown in chap. 3, the impurity band is formed by the impurity ground state energy levels, not the impurity excited state energy levels. Two assumptions are made herein when analyzing a PEIR photoconductor. 1) The impurity band remains centered about E_I as the impurity dopant concentration is increased. When considering that the value of ΔE_C defined in the previous section is very small in a PEIR photoconductor (See chap. 3), this assumption should be acceptable. 2) The impurity band is symmetric about E_I. This assumption is not necessarily correct but $(E_C-E_D)_{min}$ is more important than the symmetry. Using those assumptions,

$$(E_C-E_D)_{min} = E_I-(B_I/2) \ .$$

Four special host semiconductor:impurity atom combinations are described in sec. 4.6 where the absorption coefficient is necessarily large while simultaneously having $(E_C-E_D)_{min}$ greater than zero meV.

For example, Si:P with a impurity dopant concentration of $2x10^{18}cm^{-3}$ will have $\alpha \simeq 3.x10^{3}cm^{-1}$ (See chap. 4) and $B_I \simeq 50meV$ (See chap. 3). Considering $E_I = 45meV$, $(E_C-E_D)_{min} \simeq 20meV$. Hence, the absorption coefficient can be large while retaining an effective gap.

1.4.4 Generation and ionization processes

In a PEIR photoconductor, the carriers in the conduction band are produced by several generation or ionization effects that cause the carriers to be excited out of the impurity band into the conduction band. These are:
1) thermal generation, 2) generation due to the background or signal radiation, 3) thermal-field emission ionization (the Poole-Frenkel effect - See app. C), 4) tunneling-field emission ionization (this is analogous to Zener tunneling - See app. C), and 5) impact ionization. The relative importance of these generation or ionization effects on the carrier concentration and their dependence upon the electric field are now discussed.

The two most important effects are thermal generation and radiation generation. If a PEIR photoconductor is operated in the background limited condition, only the radiation generation process (process 2) in sec. 1.4.4 is important. Thermal generation will become more important as the temperature of operation is increased or the background radiation is lowered (See app. B).

Thermal-field emission ionization, tunneling-field emission ionization, and impact ionization (See sec. 1.4.4) can be neglected because if they exist at a certain electric field, the electric field throughout a PEIR photoconductor (with ohmic contacts) will decrease until these ionization processes are negligible. Of course, thermal-field emission ionization, tunneling-field emission ionization, and impact ionization can degrade the device because the detector might have to be biased to a less desirable operating point [Bratt 1977]. On the other hand, impact ionization can be used as an advantage if the contacts are blocking instead of ohmic.

The background photon flux is very important because when the noise is due mainly to the background radiation (BLIP operation), the photon flux determines the number of carriers in the photoconductor. The number of carriers helps determine 1) the value of the heavy doping parameters and 2) the resistance in the active area of a PEIR photoconductor.

In the testing procedure that will be used to test the device, this assumption that the carriers are predominantly produced by the background radiation is a reasonable assumption (In a low background condition, the carriers will be generated thermally or by the signal and noise sources other than background noise become important). The condition when some other noise becomes important is not considered an ideal condition and will not be considered except to show the limits on ideal operation (See chap. 5).

It appears that the heavy doping parameters are not greatly influenced by the photon flux (See chap. 3). The value of the resistance of the active area is very important though because there are parasitic resistances that can hinder the operation of the device (See app. D). As the background flux decreases, these parasitic resistances become less important (See app. D).

1.4.5 Carrier lifetime

Carrier lifetime (τ_{cap}) in a PEIR photoconductor has not been extensively considered. Considering [Rose 1963]

$$\tau_{cap} = 1/(\sigma_{cap} N_{cap} v_{av}) \ ,$$

the carrier lifetime depends upon the carrier capture cross section, σ_{cap}, the number of recombination centers, N_{cap}, and the average velocity of the carrier, v_{av}. In an extrinsic photoconductor, N_{cap} usually equals the compensation dopant concentration.

Two assumptions are made at this time about the value of the carrier lifetime. First, it is assumed that the carrier capture cross section in the impurity band is not much different from a carrier capture cross section in a conventional extrinsic photoconductor. The actual value may change because as the impurity bands begin to form, the excited state energy levels broaden into a band. The carrier capture cross section depends upon these excited state energy levels [Lax 1960], and it is unknown at this time whether this broadening will increase or decrease the carrier capture cross section. Second, it is assumed that the number of recombination centers remains the same. This assumption will be correct as long as electrons cannot accumulate at one end of the impurity band layer (See sec. 1.4.1). If electrons can accumulate, the number of recombination centers can increase (See sec. 2.2). This increase in recombination centers will most likely be negligible unless electrons can accumulate in the impurity bands with a concentration higher than the compensation dopant concentration (See sec. 2.2).

1.5 Advantages and disadvantages of a PEIR photoconductor

A PEIR photoconductor will have several advantages over conventional infrared photodetectors.

1) The device has a simple design and uses materials with desirable, well known materials properties. There are many semiconductor - impurity dopant systems from which to choose. The semiconductors most likely to be used are Si, Ge and $Al_xGa_{1-x}As$. There are a wide variety of dopants with different ionization energies that cover most wavelengths of interest. Additionally, as the composition of Al is varied in $Al_xGa_{1-x}As$, the ionization energy changes. As the ionization energy changes, the wavelength response will change.

2) The absorption coefficient can be as high as $1.x10^4 cm^{-1}$ in a PEIR photoconductor. Most likely, the absorption coefficient will be around $2.x10^3 cm^{-1}$ which will be high enough if the active region is around 10 μm thick.

3) The front to back contact configuration is much more advantageous than the side to side contact configuration when the elements are placed in an array.

4) Since the contacts are only separated by a few microns, the gain-bandwidth product can be larger than those available in conventional photoconductors

5) Due to the absorption process, D^*_{BLIP} of a PEIR photoconductor can exceed that of a conventional extrinsic photoconductor (See chap. 5).

6) By choosing the proper host semiconductor, the impurity atom, and the dopant concentration, a PEIR photoconductor can be built to detect any

wavelength from 7 μm to more than 100 μm.

7) The temperature of operation will be higher in a PEIR photoconductor than in an extrinsic photoconductor designed to detect the same wavelength.

8) If one assumes that the carrier capture cross sections in a PEIR photoconductor are about the same as in a extrinsic photoconductor, the response time of a PEIR photoconductor will be as fast as the response time of a extrinsic photoconductor.

9) It may be possible that an electric field can be applied across a PEIR photoconductor that exceeds the field needed to induce impact ionization. Impact ionization can be an asset in an array of PEIR photoconductors because most arrays use a charge collection process (charge-coupled devices (CCD), charge injection devices(CID), direct voltage readout (DVR) [Sibille 1986]) where the elements have blocking contacts. Impact ionization will amplify the radiation signal, which is subsequently collected at the blocking contact. Additionally, there is a possibility that the excess noise due to impact ionization in a PEIR photoconductor may be as small as a photomultiplier [Teich, Matsuo, and Saleh 1986]. On the other hand, to prevent saturation of charge at the blocking contact, the background radiation generation and thermal generation are smaller in photoconductors with blocking contacts (PEIR or conventional) incorporating impact ionization than in photoconductors with ohmic contacts.

10) Phonon absorption can filter out some of the background noise. In Si and Ge [Moss 1959], the phonon absorption is too small to seriously filter out any radiation, but the phonon absorption in $Al_xGa_{1-x}As$ exceeds $10^4 cm^{-1}$ and will filter out the radiation around the phonon energy (known as the reststrahlen range [Blakemore 1982]). Additionally, this phonon energy varies as the Al composition varies and consequently, one can tailor the $Al_xGa_{1-x}As$ to filter out a specific energy.

11) One big advantage of a PEIR photoconductor over compositional superlattice photoconductors [Levine, Choi, Bethea, Walker, & Malik 1987a; Levine, Choi, Bethea, Walker, & Malik 1987b; Smith, Chiu, Margalit, Yariv, & Cho 1983] is the avoidance of a discontinuous conduction (n-type device) or valence (p-type device) band at the heterojunction. Since the semiconductor in the heavily doped layer and the blocking layer is the same, there will be no barrier hindering the escape of the electron. Hence, the gain and efficiency will be larger in a PEIR photoconductor than in a superlattice detector.

There are several disadvantages for a PEIR photoconductor.

1) The device is a photoconductor, which is more noisy than a photodiode. This is not a serious problem because the narrow gap materials needed for photodiodes have undesirable materials properties.

2) The low field limited by impact ionization may be a problem. This problem also exists in conventional extrinsic photoconductors. If used in an array with blocking contacts, this impact ionization might be advantageous.

3) A PEIR photoconductor may be difficult to fabricate but will be less difficult than an IS-PC or a tunneling IS-PC (See sec. A.2), which incorporate active regions with heterojunctions having band gap discontinuities.

4) Phonon absorption can be larger than radiation absorption. This will only be true for certain wavelengths and can be avoided by using a different composition of Al in $Al_xGa_{1-x}As$. In Si and Ge, the phonon absorption can be considered negligible.

5) Parasitic resistances may be a problem but there are ways to minimize their effect (See app. D and app. E).

6) It becomes more difficult to make a transparent contact as the wavelength to be detected increases.

7) For this type of device, an accumulation mode charge-coupled device (CCD) [Nelson 1987] will have to be used instead of a depletion mode CCD. There is some criticism of the accumulation-mode CCD [Nelson 1987]. One major problem is the low temperature of operation, but the operating temperature in a PEIR photoconductor is necessarily low due to thermal ionization and the long wavelengths detected. In any case, it has been stated that GaAs will not have the temperature problems that occur in Si [Nelson 1987]. Another problem is relatively low transfer efficiencies [Nelson 1987; Milton 1977] - CIDs can be used if this problem cannot be surmounted [Milton 1977].

1.6 Description of the remaining chapters

Chapter 2 discusses the effect of the space charge components on the performance of a PEIR photoconductor. Chapter 3 describes the heavy doping parameters that will exist in the impurity band layers, the excited state energy levels of the impurity band, and the dependence of the PEIR photoconductor performance on these impurity band effects. Chapter 4 discusses the absorption of radiation that will excite the electrons from the impurity band to the conduction band (n-type device) and presents one method to determine the potential absorption coefficients that can exist in some host semiconductor:impurity atom systems. Chapter 5 describes the noise and D^* in a PEIR photoconductor. Chapter 6 presents the design considerations for the device. Chapter 7 presents the conclusions of the work and recommendations for future work.

2. SPACE CHARGE FORMATION

2.1 Introduction

The electric field, ξ, varies with position in a PEIR photoconductor. Four space charge components cause this spatial dependence of the electric field. Section 2.2 describes these four components and how they are formed. Section 2.3 describes the electric field distribution due to these space charge components.

2.2 Space charge components

The four space charge components are (See Fig. 2.1): 1) compensation dopants [Bratt 1977], 2) carriers in the conduction band, 3) excess carriers in the impurity band (negatively charged donor impurities), and 4) ionized impurities (positively charged donor impurities).

2.2.1. Compensation dopants

Compensation dopants are defined herein as the impurity dopant of the opposite type of the impurity band dopant. In an n-type (p-type) device, the compensation dopants are acceptors (donors). Usually, these compensation dopants are unavoidable and degrade the performance of the device.

Due to the low operating temperature, the compensation dopants are always ionized and are filled by electrons from the impurity bands (in an n-type device), leaving behind an equal concentration of ionized impurities.

2.2.2. Carriers in the conduction band

In a PEIR photoconductor, the carriers in the conduction band are produced by several generation or ionization effects that cause the carriers to be excited out of the impurity band into the conduction band. These are: 1) thermal generation, 2) generation due to the background or signal radiation, 3) thermal-field emission ionization (the Poole-Frenkel effect), 4) tunneling-field emission ionization (this is analogous to Zener tunneling), and 5) impact

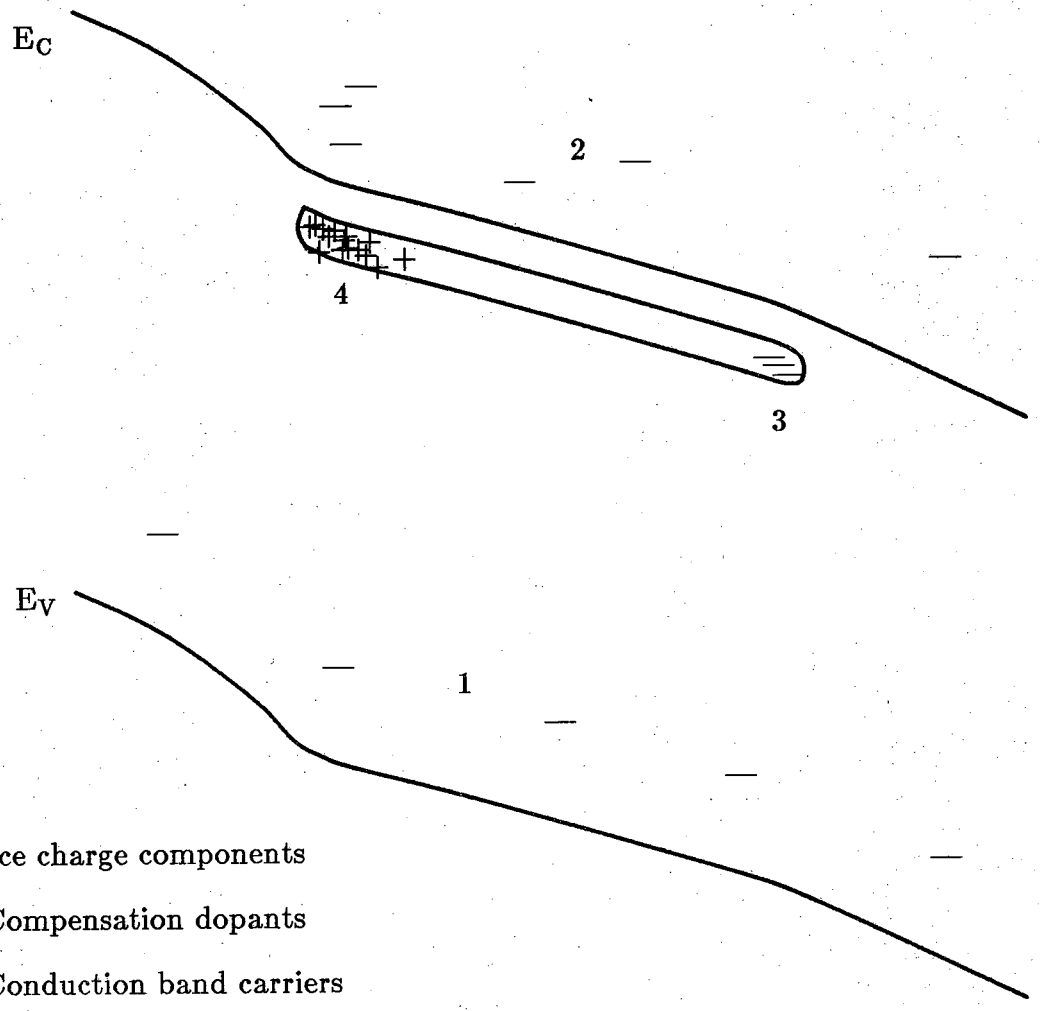

Space charge components

1) Compensation dopants

2) Conduction band carriers

3) Electron accumulation in the impurity band

4) Ionized impurities

Figure 2.1 The space charge components in a PEIR photoconductor

ionization.

If a PEIR photoconductor is operated in background limited conditions, the radiation generation process (process 2) in sec. 1.4.4 is most important. In this background limited condition, thermal generation will be smaller than background radiation generation (See app. B). The major noise source will be due to the background radiation.

As the temperature of operation increases, there will come a point when the thermal generation exceeds the generation due to background radiation. If this occurs in an extrinsic photoconductor with compensation dopants (See app. B) (and approximately in a PEIR photoconductor - because the carrier concentration may exceed the compensation dopant concentration), the major noise source will be due to the thermal generation [M.M. Blouke, C.B. Burgett, and R.L. Williams (1973)]. Consequently, thermal generation is important in a PEIR photoconductor because 1) it can be a factor in determining the carrier concentration in the active region (and the noise in the device) if it is comparable to the radiation generation and 2) the thermal generation places an upper limit on the temperature of operation.

Thermal-field emission ionization, tunneling-field emission ionization, and impact ionization can be neglected because if they exist at a certain electric field, the electric field throughout a PEIR photoconductor with ohmic contacts will decrease until these ionization processes are negligible. Of course, thermal-field emission ionization, tunneling-field emission ionization, and impact ionization can degrade the device because the detector might have to be biased to a less desirable operating point [Bratt 1977].

Finally, if the contacts are blocking and it is desired to collect charge and read out this charge (the normal mode in a detector array), impact ionization can amplify the signal. The field will still be smaller than that needed to prevent the other ionization processes from saturating the charge collection.

2.2.3. Excess carriers in the impurity band

The energy levels of the impurity band can be separated into two groups - the ground state energy levels and the excited state energy levels [Norton 1976]. As the doping concentration increases, the excited state energy levels broaden into an energy band (known as the upper Hubbard band [Thomas, Capizzi, DeRosa, Bhatt, & Rice 1981]) [Norton 1976, Dhariwal, Ojha, & Srivastava 1985]. If the doping is large enough, some of the excited states merge with the ground states (this is the Mott transition [Dhariwal, Ojha, & Srivastava 1985]).

There is an interesting effect that can occur if the temperature is low enough and the excited states are deep enough. The excited donor states can trap an extra electron [Norton 1976]. This has been labeled the D_2^- state [Norton 1976]. If clusters of 3, 4 or more impurity atoms form, D_3^-, D_4^-, or D_i^- states may form [Norton 1976, Thomas, Capizzi, DeRosa, Bhatt, & Rice 1981]. In an impurity band, many of these states could possibly form. If D_i^- states can form, it may be possible that electrons can accumulate at one end of the impurity band layer.

If electrons can accumulate, the impurity band layers will begin to resemble metals where electrons and "holes" will separate to opposite ends of the impurity band layer. The electric field in the impurity band layer will subsequently approach zero V/cm as this charge separation becomes more prevalent.

In addition to the field approaching zero V/cm in the impurity band layers, there is another problem with the D_i^- states. The D_i^- states will act like recombination centers [Rose 1963]. These centers will either be the extra ionized dopants caused by electron accumulation or the unoccupied D_i^- states. This increase in recombination centers will degrade the device, but if the concentration is less than $10^{14}cm^{-3}$, the device will still operate as well as an extrinsic photoconductor. This concentration is chosen because many extrinsic photoconductors operate with a compensation dopant concentration of $10^{14}cm^{-3}$ [Bratt 1977] and the recombination center concentration usually equals the compensation dopant concentration in an extrinsic photoconductor (See app. B).

2.2.4. Ionized impurities

The ionized impurities or "holes" will reside in the impurity band layers. Although some ionized impurities may be in the donor states that are located in the blocking layers, it will be assumed that their effect is negligible.

Since the "holes" in the impurity band can easily migrate from one impurity atom to another impurity atom, they will accumulate at one end of the impurity band layer. Consequently, the electric field will be larger in the blocking layers than in the impurity band layers (see Fig. 1.3).

2.3. Effect of the space charge formation on the performance of a PEIR photoconductor

Due to overall charge neutrality, the ionized impurity concentration equals the sum of the other three charge concentrations in a PEIR photoconductor. There are three possible cases to be considered for space charge formation in a

PEIR photoconductor. 1) If there is low compensation and the generation and ionization rates are small, there will be a small number of "holes" which equals the number of electrons in the conduction band. In this case, the band diagram looks like the one in Fig. 2.2 where there is hardly any space charge in a PEIR photoconductor. 2) As the compensation concentration, the generation rate or the ionization rate increases, the number of "holes" increases. The band diagram in this case will resemble the one in Fig. 1.3. Since the impurity band layers are so thin, an electric field will most probably exist throughout the impurity band layer which is better than what is shown in Fig. 1.3. 3) If the electrons begin to accumulate at one end of the impurity band layers, the band diagram will resemble the one in Fig. 1.4.

Consequently: 1) As the compensation dopant concentration and the carrier concentration in the conduction band increases, the electric field in the impurity band layers decreases slightly. 2) If electrons can accumulate at one end of the impurity band layers, the electric field in the impurity band layers decreases significantly. At first, this electron accumulation may appear to be a serious problem, but since the layers are so thin (on the order of 100 Å), the electrons excited into the conduction band can very likely escape from the impurity band layer into an adjacent blocking layer and be swept away by the electric field.

The performance of a PEIR photoconductor will depend upon the space charge formation in the device. It appears that the electric field distribution will not effect the performance near as much as the corresponding recombination centers produced by the space charge formation.

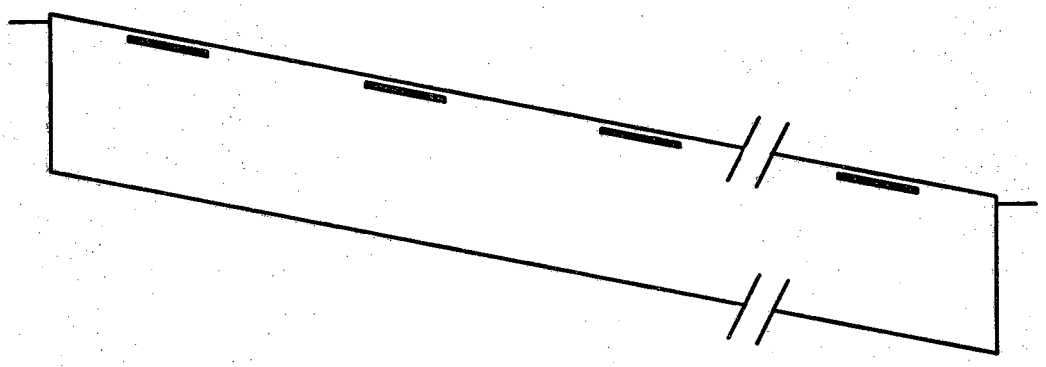

Figure 2.2 A PEIR photoconductor - low compensation or generation

3. DENSITY OF STATES IN THE PEIR PHOTOCONDUCTOR

3.1 Introduction

The density of states between the bottom of the impurity band and the conduction band influence the operation of the device. The density of states arises from three sources: 1) the conduction band energy levels, 2) the ground state energy levels of the impurity band, and 3) the excited state energy levels of the impurity band.

Sections 3.2 to 3.5 consider one method used [Lee & McGill 1975] to calculate the density of states of the first two sources (conduction band and ground state energy levels). These authors considered three parameters of interest: 1) The width of the impurity band (See sec. 3.2), 2) the density of states distribution and how it relates to the standard deviation σ_{dos} of the Gaussian potential distribution (See sec. 3.3), and 3) the relationship of the impurity level with respect to the conduction band edge (See sec. 3.4). Section 3.5 presents some numerical examples for a PEIR photoconductor when most of the carriers are produced by the background radiation and accompanying commentary on the results.

The most prominent unknown at this time is the excited state energy levels of the impurity band and how they will influence the operation of the device. A complete range of situations and their corresponding outcomes are presented in sec. 3.6.

Section 3.7 presents the important conclusions of the chapter.

3.2 Calculation of the impurity band width

To get an approximation of the width of the impurity band, the tight binding method can be used. The wavefunction ($\phi_{\mathbf{k}}$) used equals the wavefunction of the orbital (ϕ_a) which is assumed to be localized, times a phase constant ($e^{\mathbf{k}\cdot\mathbf{l}}$ which is a function of the central point of the orbital (not the distance r) or, mathematically [Ziman 1964],

$$\phi_{\mathbf{k}}(\mathbf{r}) = \sum_{\mathbf{l}} e^{\mathbf{k}\cdot\mathbf{l}} \phi_a(\mathbf{r}-\mathbf{l}) \ .$$

To find the total energy of the wavefunction $\phi_{\mathbf{k}}(\mathbf{r})$, one first assumes that the nearest neighbor atom orbitals overlap very little and that the potential of one locale is almost zero at the nearest neighbor locale. Then [Ziman 1964; Lee & McGill 1975]

$$E(\mathbf{k}) = \int \phi_{\mathbf{k}}^*(\mathbf{r}) [\frac{\hbar^2}{2m^*}\nabla^2 + V(\mathbf{r})]\phi_{\mathbf{k}}(\mathbf{r})d\mathbf{r} = E_o + J(|\mathbf{R}_i - \mathbf{R}_j|)e^{i\mathbf{k}\cdot(\mathbf{R}_i-\mathbf{R}_j)}$$

where $J(|\mathbf{R}_i-\mathbf{R}_j|)$ is presented in [Lee & McGill 1975] (In Ziman, when comparing equations (3.27), (3.28), and (3.29), $\int \phi_a^*(\mathbf{r})\phi_a(\mathbf{r})d\mathbf{r} = v_c$ - so v_c is a normalization factor).

To calculate the overall effect, one must calculate $E(\mathbf{k})$ at all points. This can be represented as

$$E(\mathbf{k}) = \frac{1}{N}\sum_{\mathbf{R}_i} E_i(\mathbf{k}) = E_o + \frac{1}{N}\sum_{\mathbf{R}_i} J(|\mathbf{R}_i-\mathbf{R}_j|)e^{i\mathbf{k}\cdot(\mathbf{R}_i-\mathbf{R}_j)}$$

where N is the number of impurity atoms in the material.

The width of the impurity band is approximated by merely replacing $e^{i\mathbf{k}\cdot(\mathbf{R}_i-\mathbf{R}_j)}$ with 2z where z is the number of nearest neighbors [Lee & McGill 1975]. It is speculated herein that the 2 factor comes about because $e^{i\phi}$ can vary from -1 to 1. Since there is only one nearest neighbor in a Poisson distribution, z equals one. Considering that the spacing between impurities follows a Poisson distribution if the impurities are absolutely randomly distributed [Lee & McGill 1975],

$$\frac{1}{N}\sum_{\mathbf{R}_i} J(|\mathbf{R}_i-\mathbf{R}_j|) = \int J(R) 4\pi N_D R^2 e^{-(4/3)\pi N_D R^3} dR$$

where $R = |\mathbf{R}_i-\mathbf{R}_j|$, $\mathbf{R}_j$ is the location of the nearest neighbor of $\mathbf{R}_i$, and $J(R) = \frac{q^2\xi}{4\pi\epsilon_s}(1+\xi R)e^{-\xi R}$ [Lee & McGill 1975]. The width of the impurity band, B_I, is [Lee & McGill 1975]

$$B_I = 2 \int J(R) 4\pi N_D R^2 e^{-4/3\pi N_D R^3} dR \ .$$

B_I depends upon ξ and N_D where $\xi = 1/r_{\sigma_{abs}}$ [Lee & McGill 1975]. $r_{\sigma_{abs}}$ can be thought of as related to the radius of the absorption cross section and is defined in sec. 4.4. Values of $B_I/2$ for various values of $r_{\sigma_{abs}}$ and N_D are shown in table 3.1. The static dielectric constant of the material is $\epsilon_s = \epsilon_o \epsilon_{sr}$, where ϵ_o is the dielectric constant of air. The values shown in table 3.1 are calculated using an integration program on a computer.

Table 3.1
$B_I/2$ for ϵ_{sr}=10.

N_I	$B_I/2$ (meV)					
	$r_{\sigma_{abs}}$=5Å	10Å	15Å	20Å	50Å	100Å
$10^{17}cm^{-3}$	.360	1.39	2.88	4.53	10.2	9.63
$2x10^{17}cm^{-3}$	.716	2.68	5.25	7.74	13.3	10.8
$5x10^{17}cm^{-3}$	1.76	6.11	10.7	14.2	17.4	12.1
$10^{18}cm^{-3}$	3.44	10.8	17.1	20.7	20.1	12.8
$2x10^{18}cm^{-3}$	6.58	18.1	25.4	28.2	22.4	13.2
$5x10^{18}cm^{-3}$	14.8	32.3	38.5	38.6	24.7	13.7
$10^{19}cm^{-3}$	25.8	46.2	48.9	45.9	25.9	14.0
$2x10^{19}cm^{-3}$	42.2	61.5	59.0	52.4		
$3x10^{19}cm^{-3}$	54.7	70.8	64.3	55.6		

3.3 Dependence of the density of states upon the Gaussian distribution of the potential

This section deals with the local variation of the density of states. This local variation arises because the impurities are randomly distributed and consequently, the impurities may have a high concentration in some places and a low concentration in other places. Section 3.3.1 describes how this local variation, which is a microscopic effect, is transformed into a macroscopic potential Gaussian distribution. Section 3.3.2 describes how the variance of the Gaussian will take on a different value depending upon whether the impurity band has merged with the conduction band (degenerately doped semiconductor) or it is separate from the conduction band (semiconductor with an impurity

band). Section 3.3.3 describes how the local variation will influence the operation of a PEIR photoconductor.

3.3.1 Density of states distribution

The simplest, most straightforward method of considering the effect of the changing potential on the density of states is to simply assume that the distribution of potential due to the ionized impurities (p(E)) has a Gaussian distribution [Kane 1963; Lee & McGill 1975] or

$$p(E) = \frac{1}{(2\pi)^{1/2}\sigma_{dos}} e^{\frac{-E^2}{2\sigma_{dos}^2}} .$$

This distribution of potential depends upon the compensating dopant concentration, the impurity band dopant concentration (both the total concentration and the ionized concentration), the dielectric constant, the carrier concentration, and the temperature.

The density of states are recalculated as the density of states at one location convoluted with the Gaussian distribution above [Lee & McGill 1975]. This will be used for the valence, conduction and impurity density of states [Lee & McGill 1975; Lee & Fossum 1983].

This method is known as the Thomas-Fermi method [Kane 1963; Kane 1985]. It has its limitations [Kane 1985], but is used here to determine the possible effects of the dopant impurities in a PEIR photoconductor.

3.3.2 Variation of the local electrostatic potential in degenerately doped semiconductors and semiconductors with impurity bands

Most authors consider the case where the impurity band has already merged with the conduction band. Consequently, the semiconductor becomes degenerately doped. In this case, the impurities can all be considered ionized and σ_{dos} is large.

In a degenerately doped semiconductor, it is assumed that the dopants are ionized because the impurity states are in the conduction band. Since the impurities are all ionized, the variation of impurity concentration remains the same as an electric field is applied in the semiconductor. Consequently, σ_{dos} will remain approximately the same as an electric field is applied.

In the impurity band layers of a PEIR photoconductor, the impurity band is separate from the conduction band. At the temperature of operation, only a small portion of the impurities are ionized. The remainder of the impurity ground state energy levels are occupied with electrons (n-type) and can be considered neutral. σ_{dos} is much smaller in this impurity band case.

As an electric field is applied in the impurity band layer of a PEIR photoconductor, electrons (holes) can move from one impurity atom to another. Consequently, the ionized impurities can reposition themselves in the impurity band. The movement of ionized impurities will also lower σ_{dos} throughout the impurity layer because the ionized dopants will accumulate at one end of the impurity band layer. Hence, σ_{dos} will be almost zero meV everywhere except at the end of the impurity band layer where the ionized dopants accumulate. As shown in sec. 2.2, it may be possible that the electric field in the impurity band layer approaches zero V/cm. In this case of electron accumulation, the electron need not be in its ground state (which is the same situation as degenerately doped semiconductors) but as shown in sec. 3.5, σ_{dos} will be reasonably small anyway.

3.3.3 The effect of bandtailing on the operation of a PEIR photoconductor

The conduction band and impurity band can form tails due to the value of σ_{dos}. The bandtailing effect can increase recombination, generation, and trapping. The bandtailing effect appears to be very small in a PEIR photoconductor, no matter what the situation (See sec. 3.5). As the performance of a PEIR photoconductor improves, the compensation dopant concentration and the accumulation of electrons will become negligible and subsequently the number of ionized impurities will become smaller (see sec. 2.3). Consequently, the bandtailing effect will decrease even further.

3.4 Energy separation between the donor level and the energy band edge

$E_C - E_D$ (E_I) is the energy difference between the conduction band and the donor level. There has been speculation that as the donor concentration increases, on one hand, the conduction band energy level is lowered toward the donor energy level [Mahan 1980] and on the other hand, the donor energy level is raised towards the conduction band energy level [Dhariwal, Ojha, & Srivastava 1985]. Whatever the case, the energy difference does appear to decrease and assuming the most recent analysis is the most accurate [Dhariwal, Ojha, & Srivastava 1985], the assumption will be that the donor level energy

increases towards the conduction band. This is actually the most ideal case for the PEIR photoconductor because there are no abrupt heterojunctions that cause reflection.

A rather straightforward description of the effect of ionized impurities upon the separation of the dopant level and the edge of the energy band has been presented by Lee and McGill [Lee & McGill 1975]. There are three effects that produce this shift: 1) The value of the dielectric constant will vary due to the absorption and must be calculated, 2) the shift of the impurity level due to screening, and 3) the average shift of the conduction band edge. These three effects are described in the next three subsections.

3.4.1 Determination of the dielectric constant

The dielectric constant to be considered is the relative static dielectric constant, ϵ_{sr} (it is assumed that the dielectric constant at the frequency of operation equals the static dielectric constant). The absorption coefficient (impurity band to conduction band) will most likely be $\tilde{}10^4 cm^{-1}$ only in a restricted energy range. Due to the Kramers-Kroenig relationship (See app. C) and $n_r^2 = \epsilon_{sr}$, the static dielectric constant ($\epsilon_{sr}\epsilon_o$) won't increase too much. The importance of the increase in the dielectric constant is that the donor ionization energy will decrease because the effective mass energy is proportional to the inverse of the dielectric constant squared.

One way to approximate the increase in the dielectric constant is to consider that the index of refraction increases by 2 for GaAs due to phonons (ϵ_{sr}=12.85 and $\epsilon_{\infty r}$=10.88 [Blakemore 1982]). The peak absorption coefficient is $5x10^4 cm^{-1}$ [Blakemore 1982]. If one assumes that the peak absorption coefficient due to impurity bands is $1x10^4 cm^{-1}$ ϵ_{sr} increases by 2/5 from 11.7 to 12.1. The effect of this increase upon the ionization energy is to decrease it from 45 meV to 42 meV. Since the dielectric constant increase is small for a peak absorption coefficient of $10^4 cm^{-1}$ and most peak absorption coefficients are less than this value, it will be assumed that the dielectric constant is approximately equal to the dielectric constant of an undoped material.

3.4.2 Shift due to screening

The impurity band can shift towards the conduction band due to the fact that the electrons in the conduction band can screen an electron attached to the donor. Lee and McGill have calculated the effect and stated it is negligible for low conduction band electron concentrations [Lee & McGill 1975].

3.4.3 Average shift of the conduction band edge

The overlap of ionized impurities will lower the conduction band. The shift is made up of two parts. One shift in potential is due to the overlap in potentials. In mathematical terms [Lee & McGill 1975],

$$\Delta E_{C1} = \frac{2q^2 e^{-d/2\lambda_D}}{4\pi\epsilon_{sr}(d/2)} - \frac{q^2 e^{-d/\lambda_D}}{4\pi\epsilon_{sr} d}$$

where the potential of the ionized impurity at its nearest neighbor ionized impurity equals $\frac{q^2 e^{-r/\lambda_D}}{4\pi\epsilon_{sr} r}$. $d = (N_D^+)^{-1/3}$ and N_D^+ is the number of ionized impurities. The equation to calculate λ_D, the screening length, is shown in sec. 3.5.

The other shift (ΔE_{C2}) is due to the fact that a bound excited state can propagate from ionized impurity to ionized impurity. Hence, it is conducting.

$$\Delta E_{C2} = \frac{2h^2}{m^* d^2} .$$

The total shift, ΔE_C, simply equals the sum of ΔE_{C1} and ΔE_{C2}. From sec. 3.5, it appears that ΔE_C is small enough such that its effect is minimal.

3.5 Numerical examples

This section now presents the heavy doping parameters that will normally be encountered in a PEIR photoconductor. An n-type photoconductor will be considered where N_A is the compensation dopant concentration (See sec. 2.2). In the analyses presented in this section, it is assumed that N_A and n are uniform throughout the active region. It is also assumed that the carriers are generated by radiation from the background (BLIP operation). For uniform

carrier concentration, the generation and recombination rates are approximated as uniform throughout the active layer (In reality, the generation occurs only in the impurity band layers).

The equations of interest are presented below. The generation rate (g) is calculated as

$$g = \phi\eta/d_{z2}$$

where ϕ is the photon flux, η is the quantum efficiency (assumed to be 100 %) and d_{z2} is the thickness of the active region.

For uniform generation and recombination, n can be approximated as (n-type)

$$n = \frac{g}{\sigma_{cap} v_{av}(n + N_A^-)} \quad .$$

In the equation above, it is assumed that there is a uniform concentration throughout the active region.

The ionized dopant concentration in the impurity band layers is

$$N_{DIL}^+ = (N_A^- + n)\frac{d_{BL} + d_{IL}}{d_{IL}} \quad .$$

where d_{BL} is the thickness of the blocking layer and d_{IL} is the thickness of the impurity band layer.

The other equations of interest are [Lee and McGill 1975]

$$a = \Gamma(4/3)[\frac{4}{3}\pi(N_D + N_A)]^{-1/3} \quad ,$$

$$\lambda_{Dio} = \left(\frac{\epsilon_s kT/q^2}{n + (N_A + n)(1 - \frac{N_A + n}{N_D})} \right)^{1/2} \quad ,$$

$$\lambda_{Di} = \lambda_{Dio} + a \quad ,$$

$$\lambda_{De} = \left(\frac{\epsilon_s kT}{q^2 n} \right)^{1/2} \quad ,$$

$$\frac{1}{\lambda_D^2} = \frac{1}{\lambda_{De}^2} + \frac{1}{\lambda_{Di}^2} \quad ,$$

$$d = (N_{DIL}^+)^{-1/3} \quad ,$$

$$\Delta E_{C1} = \frac{2q^2 e^{-d/2\lambda_D}}{4\pi\epsilon_s (d/2)} - \frac{q^2 e^{-d/\lambda_D}}{4\pi\epsilon_s d} \quad ,$$

$$\Delta E_{C2} = \frac{2h^2}{m^* d^2} \quad ,$$

and

$$\sigma_{dos} = \left(\frac{N_{DIL}^+ + N_A^-}{8\pi^2 \epsilon_s^2} q^4 \lambda_D \right)^{1/2} \quad .$$

Let

$$d_{BL} = d_{IL} \quad ,$$

$$d_{z2} = 5\mu m \quad ,$$

$$\sigma_{cap} = 10^{-12} cm^2 \quad ,$$

$$m_e^* = .5\ m_e \ ,$$

and

$$\epsilon_{sr} = 12 \ .$$

Some constants used are

$$\epsilon_s k/q^2 = 5.72\text{x}10^2\ (\text{Kcm})^{-1} \ ,$$

$$\frac{q^2}{4\pi\epsilon_s} = 1{,}190.\ \text{meV\AA} \ ,$$

$$\frac{q^4}{8\pi^2\epsilon_s} = 2.87\text{x}10^{-16}\text{cm}^2\text{eV}^2 \ .$$

Some examples are shown below that reveal how much the impurity band shifts towards the conduction band (n-type), how wide the impurity band becomes and the value of the standard deviation of the Gaussian distribution of potential. In addition, other important parameters are shown. In these examples, it is assumed that the radiation generation is much larger than the thermal generation. Four parameters are varied in these examples: 1) the majority dopant concentration, 2) the compensation dopant concentration, 3) the photon flux, and 4) the temperature of operation.

3.5.1 Influence of the majority dopant concentration on the heavy doping parameters

Tables 3.2 and 3.3 present several different parameters as the majority dopant concentration is varied. As can be seen in tables 3.2 and 3.3, B_I depends upon the majority dopant concentration. ΔE_C and σ_{dos} are essentially unchanged.

Table 3.2

Debye length parameters as the majority dopant concentration is varied. T=10 K, $N_A = 10^{12}(cm^{-3})$, $\phi_{ph} = 5x10^{17}(cm^{-2}sec^{-1})$

N_D (cm^{-3})	n (cm^{-3})	N^+_{DIL} (cm^{-3})	a (Å)	λ_{Dio} (Å)	λ_{Di} (Å)	λ_{De} (Å)
$5x10^{17}$	10^{13}	$2x10^{13}$	105.	1,650.	1,760.	2,390.
10^{18}	10^{13}	$2x10^{13}$	84.	1,650.	1,730.	2,390.
$2x10^{18}$	10^{13}	$2x10^{13}$	67.	1,650.	1,720.	2,390.

Table 3.3

Density of states parameters as the majority dopant concentration is varied. T=10 K, $N_A = 10^{12}(cm^{-3})$, $\phi_{ph} = 5x10^{17}(cm^{-2}sec^{-1})$

N_D (cm^{-3})	λ_D (Å)	d (Å)	ΔE_C (meV)	B_I (meV)	σ_{dos} (meV)
$5x10^{17}$	1,420.	3,690.	.415	10.7	.292
10^{18}	1,400.	3,690.	.412	17.1	.291
$2x10^{18}$	1,390.	3,690.	.409	25.4	.290

Table 3.4

Debye length parameters as the compensation dopant concentration is varied. T=10 K, $N_D = 10^{18}(cm^{-3})$, $\phi_{ph} = 5x10^{17}(cm^{-2}sec^{-1})$

N_A (cm^{-3})	n (cm^{-3})	N^+_{DIL} (cm^{-3})	a (Å)	λ_{Dio} (Å)	λ_{Di} (Å)	λ_{De} (Å)
10^{12}	10^{13}	$2x10^{13}$	84.	1,650.	1,730.	2,390.
10^{13}	$<10^{13}$	$>2x10^{13}$	84.	1,380.	1,460.	2,390.
10^{14}	10^{12}	$2x10^{14}$	84.	749.	833.	7,600.
10^{15}	10^{11}	$2x10^{15}$	84.	239.	323.	23,900.

3.5.2 Influence of the compensation dopant concentration on the heavy doping parameters

Tables 3.4 and 3.5 present several different parameters as the compensation dopant concentration is varied. From tables 3.4 and 3.5, B_I does not change when the dopant compensation concentration changes. ΔE_C and σ_{dos} increase as the dopant compensation concentration increases.

3.5.3 Influence of the photon flux on the heavy doping parameters

Tables 3.6 and 3.7 present several different parameters as the photon flux is varied. B_I is independent of the photon flux. As the photon flux decreases from $10^{15}cm^{-2}sec^{-1}$, ΔE_C and σ_{dos} increase because of the increase in the screening length. As the photon flux increases from $10^{15}cm^{-2}sec^{-1}$, ΔE_C increases because of the decrease in the distance between ionized majority impurities and σ_{dos} increases because of the increase of the ionized majority impurities.

3.5.4 Influence of the temperature on the heavy doping parameters

Tables 3.8 and 3.9 present several different parameters as the temperature is varied. n and N_{DIL}^{+} remain the same as the temperature is varied because it is assumed that the radiation generation is much larger than the thermal generation. B_I does not change when the temperature changes. ΔE_C and σ_{dos} increase as the temperature increases because the screening length increases.

3.6 Comparison of ground dopant states to excited dopant states

As stated in chap. 2, the energy levels of the impurity band can be separated into two groups - the ground state energy levels and the excited state energy levels. In addition to the space charge problems described in chap. 2, the wavelength response can increase because electrons can be excited by the radiation into the excited state and subsequently excited into the conduction band by another excitation process. This section describes how the wavelength response can increase and compares this result to the band diagrams shown in Figs. 1.3, 1.4, and 2.2. It is assumed in this section that the compensation dopant concentration is small enough such that the band diagram will resemble Fig. 2.2 and will begin to resemble Fig. 1.3 if the generation rate or ionization rate increases (See sec. 2.2) or will resemble Fig. 1.4 if the electrons can accumulate (See sec. 2.2).

Table 3.5

Density of states parameters as the compensation dopant concentration is varied. T=10 K, $N_D = 10^{18}(cm^{-3})$, $\phi_{ph} = 5x10^{17}(cm^{-2}sec^{-1})$

N_A (cm^{-3})	λ_D (Å)	d (Å)	ΔE_C (meV)	B_I (meV)	σ_{dos} (meV)
10^{12}	1,400.	3,690.	.412	17.1	.291
10^{13}	1,250.	3,690.	.366	17.1	.328
10^{14}	830.	1,710.	1.31	17.1	.844
10^{15}	323.	795.	3.52	17.1	1.67

Table 3.6

Debye length parameters as the photon flux is varied. T=10 K, $N_D = 10^{18}(cm^{-3})$, $N_A = 10^{12}(cm^{-3})$

ϕ_{ph} ($cm^{-2}sec^{-1}$)	n (cm^{-3})	N_{DIL}^{+} (cm^{-3})	a (Å)	λ_{Dio} (Å)	λ_{Di} (Å)	λ_{De} (Å)
10^{13}	$2x10^{9}$	$2x10^{12}$	84.	7,550.	7,630.	169,000.
10^{15}	$2x10^{11}$	$2x10^{12}$	84.	6,390.	6,480.	16,900.
10^{17}	$<4x10^{12}$	$\sim 8x10^{12}$	84.	2,520.	2,610.	3,780.
$5x10^{17}$	$<1x10^{13}$	$2x10^{13}$	84.	1,650.	1,730.	2,390.
10^{18}	$<1.4x10^{13}$	$3x10^{13}$	84.	1,490.	1,460.	2,020.

Table 3.7

Density of states parameters as the photon flux is varied. T=10 K, $N_D = 10^{18}(cm^{-3})$, $N_A = 10^{12}(cm^{-3})$

ϕ_{ph} ($cm^{-2}sec^{-1}$)	λ_D (Å)	d (Å)	ΔE_C (meV)	B_I (meV)	σ_{dos} (meV)
10^{13}	7,620.	7,940.	.322	17.1	.256
10^{15}	6,050.	7,940.	.289	17.1	.228
10^{17}	2,150.	5,000.	.321	17.1	.235
$5x10^{17}$	1,400.	3,690.	.412	17.1	.291
10^{18}	1,200.	3,220.	.476	17.1	.327

Table 3.8

Debye length parameters as the temperature is varied.
$N_D = 10^{18}(cm^{-3})$, $N_A = 10^{12}(cm^{-3})$ $\phi_{ph} = 5x10^{17}(cm^{-2}sec^{-1})$

T (K)	n (cm^{-3})	N^{+}_{DIL} (cm^{-3})	a (Å)	λ_{Dio} (Å)	λ_{Di} (Å)	λ_{De} (Å)
5	10^{13}	$2x10^{13}$	84.	1,170.	1,250.	1,690.
10	10^{13}	$2x10^{13}$	84.	1,650.	1,730.	2,390.
20	10^{13}	$2x10^{13}$	84.	2,330.	2,420.	3,380.
40	10^{13}	$2x10^{13}$	84.	3,300.	3,380.	4,780.

Table 3.9

Density of states parameters as the temperature is varied.
$N_D = 10^{18}(cm^{-3})$, $N_A = 10^{12}(cm^{-3})$ $\phi_{ph} = 5x10^{17}(cm^{-2}sec^{-1})$

T (K)	λ_D (Å)	d (Å)	ΔE_C (meV)	B_I (meV)	σ_{dos} (meV)
5	1,010.	3,690.	.286	17.1	.246
10	1,400.	3,690.	.412	17.1	.291
20	1,970.	3,690.	.544	17.1	.344
40	2,760.	3,690.	.666	17.1	.409

There are three possible effects on the wavelength response that can arise because of these excited states. For the first effect, there may be no change in the wavelength response because 1) the excited state concentration in the energy gap between the impurity band and the conduction band is negligible or 2) the electrons excited into an excited state recombine into the ground state before they can escape from the impurity potential. The excited state energy level concentration may become negligible because the excited states may spread out into the conduction or impurity band effectively lowering the concentration. The escape from the impurity potential is prevented because a) an electron cannot travel down the excited state band (no D_i^- states (n-type device, see sec. 2.2)) and b) the electrons are more likely to recombine than be excited into the conduction band by thermal generation, radiation generation, tunneling-field emission ionization, or thermal-field emission ionization. In this case, the wavelength response should not lengthen due to the excited states. The band diagram in the device should resemble the band diagram of Fig. 2.2 because there will be few carriers in the conduction band.

For the second effect, electrons in the excited states may be 1) more likely to be excited into the conduction band by thermal generation, radiation generation, tunneling-field emission ionization, or thermal-field emission ionization than recombine into the ground state energy levels or 2) swept away through the excited state energy level band and subsequently emitted into the conduction band. This effect will lengthen the wavelength response. This effect can improve, maintain or degrade the performance of the device depending upon whether the absorption cutoff is more sharp or more broad. The band diagram in the device will resemble the band diagram of Fig. 1.3 because the electron concentration will be much larger than for the first effect (See sec. 2.2).

The third possible effect may be that electrons can simultaneously occupy the ground state and the excited state at the same site (accumulation of electrons, see sec. 2.2). At this time, it is not verified whether this occurs. This third effect means that electrons can accumulate at one end of the impurity band layer. This process could seriously degrade the device because the electric field in the impurity band layers could be zero, as is shown in Fig. 1.4. The size of the decrease depends upon the thickness of the impurity band layer. The wavelength response will remain the same as a PEIR photoconductor with negligible excited states or increase only a portion of what is possible due to the second effect. This result is due to the fact that an electron in an excited state energy level can be excited into the conduction band only through thermal or radiation generation and not by thermal-field emission ionization or tunneling-field emission ionization since the electric field in the impurity band layer is

much smaller than the electric field in the impurity band layer for the second effect.

These several possibilities that can arise in a PEIR photoconductor depend upon the actual physics of the impurity band excited states. These possibilities are shown in table 3.10.

3.7 Conclusions

This chapter has considered the density of states in the conduction band and in the impurity band (both ground and excited states).

Sections 3.2 to 3.5 presented some important results for the conduction band states and the ground states in the impurity band. The important conclusions are that B_I is an unavoidable parameter that must be considered. ΔE_C and σ_{dos} can be neglected if the compensation doping concentration or the temperature is low. Since this is the desirable condition, it will be assumed that ΔE_C and σ_{dos} can be neglected for a PEIR photoconductor.

As for the excited states in the impurity band (See sec. 3.6), the major conclusion is that if electrons can accumulate in the impurity band, the band diagram will look like Fig. 1.4 while the wavelength response can increase very slightly. If electrons cannot accumulate, the band diagram will look like Fig. 1.3 and the wavelength response can increase.

Table 3.10
Various situations for the excited states of the impurities

Situation	Wavelength response	Fig.
I. Density of states are negligible in the gap between the impurity band and conduction band - due to the broadening of the states	no change	2.2
II. Density of states are not negligible in the gap between the impurity band and conduction band		
a. Electrons excited to a state and then excited to a band	increase	1.3
b. Electrons excited to a state and then fall back into the ground state	no change	2.2
c. Electrons excited to a state and then travel down a band		
1. Electrons excited into the conduction band	increase	1.3
2. Electrons trapped in the band at interface between the impurity band layers and the blocking layers	no change	1.4
3. Electrons prevented from traveling down the band and fall back into the ground state because electrons are not likely to exist in an excited state and a ground state at the same site	no change	2.2

4. ABSORPTION IN A PEIR PHOTOCONDUCTOR

4.1 Introduction

There are five types of absorption in a semiconductor: 1) valence band to conduction band absorption (electron), 2) impurity band to conduction band absorption (electron) for heavily doped semiconductors or dopant level to conduction band absorption (electron) for lightly doped semiconductors, 3) intraband or free carrier absorption (electron), 4) ground state of dopant level to excited state of dopant level (electron), and 5) phonon absorption (lattice). The electron in parentheses means that the electron absorbs most or all of the radiation energy and the lattice in parentheses means the lattice absorbs most or all of the radiation energy.

There are two possible beneficial absorption processes in a PEIR photoconductor. Absorption process 2 is considered in this chapter. Absorption process 4 is the other possible beneficial process in a PEIR photoconductor and has already been considered in depth [Thomas, Capizzi, DeRosa, Bhatt, & Rice 1981].

Section 4.2 presents the relative importance of the five absorption processes in a PEIR photoconductor. Section 4.3 relates the absorption coefficient to the absorption cross section. Section 4.4 describes a simple calculation for a theoretical absorption cross section and relates some of these values to some experimental absorption cross sections. Section 4.5 describes an approximate method used to calculate the absorption from the impurity band to the conduction band. Section 4.6 presents four host semiconductor:impurity atom systems suited for use in a PEIR photoconductor. Section 4.7 presents a method to determine the dopant concentration in the impurity band layers. Section 4.8 presents conclusions drawn from this chapter.

4.2 Absorption processes in a PEIR photoconductor

In a PEIR photoconductor: Absorption process 1 is not of interest because the energy of radiation producing this transition is in the optical range which is much larger than the infrared range of interest. Absorption process 2 produces the photoconductivity and is the most important absorption process in a PEIR

photoconductor. Absorption process 3 can be neglected because there are only a few free carriers in the conduction band. Absorption process 4 has been stated to be of importance [Thomas, Capizzi, DeRosa, Bhatt, & Rice 1981]. Depending upon which physical situation presented in sec. 3.6 actually occurs, this absorption process can have a range of effects on a PEIR photoconductor. Absorption process 4 can: a) produce photoconductivity (for situations IIa and IIc1 in table 3.10), or b) be of little effect (for situations I, IIb, IIc2 and IIc3 in table 3.10). Absorption process 5 is important in this device. For GaAs, this absorption occurs at 38 meV and will have to be taken into account when considering the design of a PEIR photoconductor. This absorption can be used as a filter and hence can be advantageous but it will also mean that the radiation energy at the optical phonon frequencies can not be detected. Since Si has a phonon energy at 62 meV, absorption process 5 can be neglected in Si because the phonon energy is too large. In any case, the phonon absorption in Si is too small to be important.

4.3 Relationship of the absorption coefficient to the absorption cross section

The rate of absorption, designated as $\frac{1}{\tau_{abs}}$, is related to the absorption cross section σ_{abs} by

$$\frac{1}{\tau_{abs}} = \sigma_{abs} N_I^o v_c$$

where v_c is the velocity of radiation in the medium and N_I^o is the concentration of neutral dopants.

Now it can be seen that for an absorption rate of $\frac{1}{\tau_{abs}}$,

$$\phi = \phi_o e^{\frac{-t}{\tau_{abs}}} = \phi_o e^{\frac{-v_c t}{v_c \tau_{abs}}}$$

$$= \phi_o e^{\frac{-x}{v_c \tau_{abs}}}$$

$$= \phi_o e^{-\alpha x}$$

where α is the absorption coefficient. Considering this last equation [Bratt 1977],

$$\alpha = \frac{1}{v_c \tau_{abs}} = \frac{\sigma_{abs} N_I^o v_c}{v_c} = \sigma_{abs} N_I^o \ .$$

As an example, consider the BIB detector (See sec. A.2.3). The cross section in Si:P is about 10^{-15}cm^2 and N_I^o=6.5x10^{17}cm^{-3}. The absorption coefficient is calculated as

$$\alpha = 650 \text{cm}^{-1}$$

which is close to the actual absorption coefficient [Walter & Dereniak 1986a].

4.4. Simple theoretical calculation of the absorption cross section and a comparison with experimental results

To calculate a theoretical cross section, one can look at the hydrogenic wave function [Kohn 1957]

$$F(r) \propto e^{\frac{-r}{a_H^*}} \ .$$

where a_H^* is the effective Bohr radius,

$$a_H^* = \frac{\hbar^2 4\pi\epsilon_s}{m^* e^2} = \frac{a_H^o}{m_r^*}\epsilon_{sr} \ ,$$

and a_H^o is the Bohr radius (.529 Å). ϵ_{sr} is the static dielectric constant.

This wave function is correct if the actual ionization energy E_I equals the ionization energy using the effective mass theory, E_{Ieff} [Kohn 1957],

$$E_{Ieff} = \frac{me^4}{(4\pi\epsilon_s)^2 2\hbar^2} = \frac{e^2}{8\pi\epsilon_s a_H^*} = \frac{E_{Hy} m_r^*}{\epsilon_{sr}^2} \quad .$$

where E_{Hy} is the ground state energy of the hydrogen atom and equals 13.6 eV.

If E_I doesn't equal E_{Ieff}, the wave function can be corrected as [Kohn 1957]

$$F(r) \propto e^{\frac{-r}{a_H^*}(\frac{E_I}{E_{Ieff}})^{1/2}} \quad .$$

Table 4.1 shows values for a_H^* and E_{Ieff} for GaAs, Ge, and Si. m^* is calculated from [Sze 1981]. ϵ_{sr} is found in [Sze 1981, Stillman, Wolfe, & Dimmock 1977, or Adachi 1985].

Table 4.2 shows a_H^* and E_{Ieff} for different compositions of $Al_xGa_{1-x}As$. For $Al_xGa_{1-x}As$, the electron density of states mass [Adachi 1985] is calculated from the Γ valley for Al compositions from 0 to .4 and from the X valley for Al compositions from .5 to 1.0 [Casey & Panish 1978]. The dielectric constant is assumed to vary linearly from GaAs to AlAs [Adachi 1985]. The hole density of states is calculated from the heavy and light hole Γ bands [Adachi 1985].

To calculate the theoretical cross section, consider

$$r_{\sigma_{abs}} = a_H^* \left(\frac{E_{Ieff}}{E_I}\right)^{1/2} = \frac{a_H^o}{\sqrt{m^*}} \left(\frac{E_{Hy}}{E_I}\right)^{1/2} \quad .$$

Where it can be noted that the relative dielectric constant, ϵ_{sr}, cancels out of this equation. The theoretical cross section will be approximated as

$$\sigma_{abs_{th}} = K\pi r_{\sigma_{abs}}^2$$

where K is a unitless empirical constant and

$$K = \frac{\sigma_{abs_{ex(Ge:Sb)}}}{\pi r_{\sigma_{abs_{ex(Ge:Sb)}}}^2} = \frac{16x10^{-15}cm^2}{\pi(42.5x10^{-8}cm)^2} = 2.82x10^{-2} \quad .$$

Various values for $\sigma_{abs_{th}}$ and $\sigma_{abs_{ex}}$ (the experimental cross section) are

Table 4.1
a_H^* and E_{Ieff} for GaAs, Ge, and Si

	m^* (unitless)	ϵ_{sr} (unitless)	a_H^* (Å)	E_{Ieff} (meV)
n - GaAs	.067	13.2	104.	5.83
p - GaAs	.45	13.2	15.5	39.2
n - Ge	.22	16.0	38.5	11.7
p - Ge	.29	16.0	29.1	15.4
n - Si	.33	11.8	18.9	32.2
p - Si	.55	11.8	11.3	53.7

Table 4.2
a_H^* and E_{Ieff} for $Al_xGa_{1-x}As$

	m^* (unitless)	ϵ_{sr} (unitless)	a_H^* (Å)	E_{Ieff} (meV)
n - GaAs	.067	13.18	104.	5.25
n - $Al_{.1}Ga_{.9}As$	.075	12.87	90.8	6.16
n - $Al_{.2}Ga_{.8}As$	.084	12.56	79.1	7.24
n - $Al_{.3}Ga_{.7}As$	.092	12.24	70.4	8.35
n - $Al_{.4}Ga_{.6}As$	.100	11.93	63.1	9.56
n - $Al_{.5}Ga_{.5}As$	.290	11.62	21.2	29.2
n - $Al_{.6}Ga_{.4}As$	.284	11.31	21.1	30.2
n - $Al_{.7}Ga_{.3}As$	.278	11.00	20.9	31.2
n - $Al_{.8}Ga_{.2}As$	.272	10.68	20.8	32.4
n - $Al_{.9}Ga_{.1}As$	.266	10.37	20.6	33.6
n - AlAs	.260	10.06	20.5	34.9
p - GaAs	.642	13.18	10.9	50.3
p - $Al_{.1}Ga_{.9}As$	.658	12.87	10.3	54.0
p - $Al_{.2}Ga_{.8}As$	.674	12.56	9.86	58.2
p - $Al_{.3}Ga_{.7}As$	.690	12.24	9.38	62.6
p - $Al_{.4}Ga_{.6}As$	.706	11.93	8.94	67.5
p - $Al_{.5}Ga_{.5}As$	.722	11.62	8.51	72.7
p - $Al_{.6}Ga_{.4}As$	.739	11.31	8.10	78.6
p - $Al_{.7}Ga_{.3}As$	.755	11.00	7.71	84.9
p - $Al_{.8}Ga_{.2}As$	.771	10.68	7.33	91.9
p - $Al_{.9}Ga_{.1}As$	.787	10.37	6.97	99.5
p - AlAs	.804	10.06	6.62	108.

compared in table 4.3. The experimental cross sections for the Si and Ge samples are from Bratt. E_I is also shown in table 4.3 [Sze 1981].

Table 4.4 presents some cross sections for $Al_xGa_{1-x}As$. E_I for n-type dopant Si [Lifshitz, Jayaraman, Logan, & Card 1980] and p-type dopant Be [Yang 1982; Yao 1985] are also presented in table 4.4. The experimental cross section for the GaAs sample is calculated as [Bosomworth, Crandall, & Enstrom 1968]

$$\sigma_{abs_{ex}} = \frac{75\ cm^{-1}}{1x10^{15}cm^{-3}} = 75x10^{-15}\ cm^2$$

where $1x10^{15}cm^{-1}$ is the neutral impurity concentration.

For deep and medium levels [Kohn 1957; Bebb and Chapman 1969; Bebb and Chapman 1967; Bebb 1969], the wave functions are not the hydrogenic wave functions. Consequently, the cross section will be smaller for larger E_I.

The results of table 4.3 are surprisingly consistent. Even for p-type materials, $\sigma_{abs_{th}}$ and $\sigma_{abs_{ex}}$ compare favorably, which indicates that the simple calculation of $r_{\sigma_{abs}}$ may be a reasonable approximation.

Tables 4.5 and 4.6 present some approximate values of $(E_C-E_D)_{min}$ or $(E_A-E_V)_{min}$ for certain absorption coefficients. The semiconductor materials used are the same ones as in tables 4.3 and 4.4 respectively. When examining these tables, it must be remembered that as the impurity band widens, the absorption spectrum also broadens. Hence, the absorption coefficients in tables 4.5 and 4.6 are optimum values. This effect is considered in the next section.

4.5 Impurity band to conduction band absorption

The theoretical absorption cross section as a function of energy has been considered for an electron excited out of a single discrete dopant level [Bebb and Chapman 1969; Bebb and Chapman 1967; Bebb 1969; Bratt 1977]. As long as these electron states remain spatially separated from one another, the absorption is simply the absorption cross section times the number of neutral dopant states.

When the electron states in the impurity atoms begin to overlap, two processes begin to occur: 1) The k states in the dopant levels may be altered by this overlap and 2) an impurity band begins to form and the ground state energy levels of the impurity atoms begin to take on a range of energies. For 1),

Table 4.3
Comparison of $\sigma_{abs_{th}}$ and $\sigma_{abs_{ex}}$

	dopant type	E_I (meV)	$r_{\sigma_{abs}}$ (Å)	$\sigma_{abs_{th}}$ ($10^{-15}cm^2$)	$\sigma_{abs_{ex}}$ ($10^{-15}cm^2$)
Si:P	n	45.	16.0	2.3	1.7
Si:As	n	54.	14.5	1.8	?
Si:Bi	n	69.	12.9	1.5	.70
Si:S	n	260.	6.65	.39	.06
Si:B	p	45.	12.3	1.3	1.4
Si:Al	p	67.	10.1	.90	.8
Si:Ga	p	72.	9.8	.85	.5
Si:In	p	160.	6.5	.37	.16
Ge:Sb	n	9.6	42.5	16.	16.
Ge:P	n	12.	38.0	15.	13.
Ge:Bi	n	~12.	38.0	15.	13.
Ge:As	n	13.	36.5	14.	12.
Ge:Tl	p	10.	36.1	12.	8.7
Ge:Cu	p	40.	18.1	2.9	1.0
Ge:Hg	p	87.	12.2	1.3	.39
GaAs:Si	n	5.8	99.0	87.	75.
GaAs:Te	n	30.	43.5	17.	?
GaAs:Be	p	26.	18.0	2.9	?

Table 4.4
Comparison of $\sigma_{abs_{th}}$ and $\sigma_{abs_{ex}}$

	dopant type	E_I (meV)	$r_{\sigma_{abs}}$ (Å)	$\sigma_{abs_{th}}$ ($10^{-15}cm^2$)	$\sigma_{abs_{ex}}$ ($10^{-15}cm^2$)
GaAs:Si	n	5.8	99.0	87.	75.
$Al_{.1}Ga_{.9}As$:Si	n	5.8	94.0	78.	?
$Al_{.2}Ga_{.8}As$:Si	n	8.0	75.3	50.	?
$Al_{.3}Ga_{.7}As$:Si	n	40.0	32.2	9.2	?
$Al_{.4}Ga_{.6}As$:Si	n	120.	17.8	2.8	?
$Al_{.5}Ga_{.5}As$:Si	n	105.	11.2	1.1	?
$Al_{.6}Ga_{.4}As$:Si	n	101.	11.5	1.2	?
$Al_{.7}Ga_{.3}As$:Si	n	101.	11.6	1.2	?
$Al_{.8}Ga_{.2}As$:Si	n	101.	11.8	1.2	?
$Al_{.9}Ga_{.1}As$:Si	n	101.	11.9	1.3	?
AlAs:Si	n	101.	12.0	1.3	?
GaAs:Be	p	28.	14.6	1.9	?
$Al_{.1}Ga_{.9}As$:Be	p	30.	13.9	1.7	?
$Al_{.2}Ga_{.8}As$:Be	p	32.	13.3	1.6	?
$Al_{.3}Ga_{.7}As$:Be	p	36.	12.4	1.4	?
$Al_{.4}Ga_{.6}As$:Be	p	39.	11.8	1.2	?
$Al_{.5}Ga_{.5}As$:Be	p	42.	11.2	1.1	?
$Al_{.6}Ga_{.4}As$:Be	p	50.	10.1	.90	?
$Al_{.7}Ga_{.3}As$:Be	p	66.	8.7	.67	?
$Al_{.8}Ga_{.2}As$:Be	p	90.	7.4	.49	?
$Al_{.9}Ga_{.1}As$:Be	p	110.	6.6	.39	?
AlAs:Be	p	140.	5.8	.30	?

Table 4.5
Calculation of $(E_C - E_D)_{min}$ or $(E_A - E_V)_{min}$
for various semiconductors and impurities

	E_I (meV)	$\sigma_{abs_{ex}}$ ($10^{-15}cm^2$)	$(E_C-E_D)_{min}$ or $(E_A-E_V)_{min}$ (meV)		
			(α=)$2.5x10^3(cm^{-1})$	$5x10^3(cm^{-1})$	$10^4(cm^{-1})$
Si:P	45.	1.7	22.4	13.4	3.6
Si:As	54.	~1.2	28.5	18.5	7.7
Si:Bi	69.	.70	37.4	25.8	13.6
Si:S	260.	.06	184.	160.	137.
Si:B	45.	1.4	24.3	14.2	2.3
Si:Al	67.	.8	42.5	30.4	16.0
Si:Ga	72.	.5	40.1	26.2	10.6
Si:In	160.	.16	114.	93.2	69.8
Ge:Sb	9.6	16.	<0.	<0.	<0.
Ge:P	12.	13.	<0.	<0.	<0.
Ge:Bi	~12.	13.	<0.	<0.	<0.
Ge:As	13.	12.	.2	<0.	<0.
Ge:Tl	10.	8.7	<0.	<0.	<0.
Ge:Cu	40.	1.0	9.7	1.1	<0.
Ge:Hg	87.	.39	47.	33.7	21.

Table 4.6
Calculation of $(E_C-E_D)_{min}$ or $(E_A-E_V)_{min}$
for $Al_xGa_{1-x}As$:Si and $Al_xGa_{1-x}As$:Be

	E_I (meV)	$\sigma_{abs_{ex}}$ ($10^{-15}cm^2$)	$(E_C-E_D)_{min}$ or $(E_A-E_V)_{min}$ (meV)		
			(α=)2.5x10^3(cm^{-1})	5x10^3(cm^{-1})	10^4(cm^{-1})
GaAs:Si	5.8	75.	<0.	<0.	<0.
$Al_{.1}Ga_{.9}As$:Si	5.8	~72.	<0.	<0.	<0.
$Al_{.2}Ga_{.8}As$:Si	8.0	~45.	<0.	<0.	<0.
$Al_{.3}Ga_{.7}As$:Si	40.0	~3.0	18.6	13.8	9.5
$Al_{.4}Ga_{.6}As$:Si	120.	~.5	81.0	72.4	64.7
$Al_{.5}Ga_{.5}As$:Si	105.	~.3	60.8	46.9	33.0
$Al_{.6}Ga_{.4}As$:Si	101.	~.2	48.	34.	22.
$Al_{.7}Ga_{.3}As$:Si	101.	~.2	48.	34.	22.
$Al_{.8}Ga_{.2}As$:Si	101.	~.2	48.	34.	22.
$Al_{.9}Ga_{.1}As$:Si	101.	~.2	48.	34.	22.
AlAs:Si	101.	.2	48.	34.	~22.
GaAs:Be	28.	1.7	6.7	<0.	~<0.
$Al_{.1}Ga_{.9}As$:Be	30.	~1.5	7.9	<0.	<0.
$Al_{.2}Ga_{.8}As$:Be	32.	~1.4	9.9	<0.	<0.
$Al_{.3}Ga_{.7}As$:Be	36.	~1.2	13.1	2.5	<0.
$Al_{.4}Ga_{.6}As$:Be	39.	~1.0	14.5	3.4	<0.
$Al_{.5}Ga_{.5}As$:Be	42.	~.8	15.3	3.4	<0.
$Al_{.6}Ga_{.4}As$:Be	50.	~.6	20.5	7.3	<0.
$Al_{.7}Ga_{.3}As$:Be	66.	~.3	26.9	10.7	<0.
$Al_{.8}Ga_{.2}As$:Be	90.	~.15	38.0	18.2	<0.
$Al_{.9}Ga_{.1}As$:Be	110.	~.10	50.4	28.0	4.2
AlAs:Be	140.	~.10	85.0	61.3	34.9

it is assumed that the k states in the dopant levels are hardly altered by the formation of an impurity band. This is justified in sec. 4.5.1. For 2), it is assumed that the absorption cross section has the same shape as a function of energy, no matter what the ground state energy level of the electron in the impurity band. The overall absorption then depends upon the density of states in the impurity band. This is explained more clearly in secs. 4.5.2 and 4.5.3.

4.5.1 Crystal momentum value for an electron in a dopant level

The crystal momentum in dopant states has been considered [Serre & Ghazali 1983; Gold, Serre, & Ghazali 1988; Ghazali & Serre 1982]. It has been stated that the k values for dopant states are spread out over a rather large range of values of k [Serre & Ghazali 1983; Gold, Serre, & Ghazali 1988; Ghazali & Serre 1982]. The argument is that the dopant states are localized in space and due to the Heisenberg principle, must be non-localized in k-space.

One could make an argument that when the impurity bands form that the electron wave function can be more compact in k-space. Yet even when the impurity band begins to form, the dopant states are non-localized in k-space [Serre & Ghazali 1983; Gold, Serre, & Ghazali 1988; Ghazali & Serre 1982]. The argument is that since the impurity atoms are randomly distributed in real space, the band formed by the impurities will be random in k-space. In addition, due to this random distribution, there is no periodic potential and the electrons in the impurity band energy levels should essentially maintain the same k-space spectral density. If the dopant atoms were precisely periodicly located, it seems reasonable to assume that the wave function would become more compact in k-space.

Impurity band to conduction band absorption is very similar to free carrier absorption because of the spread in k-space of the dopant electron state.

4.5.2 Absorption cross section as a function of energy

An example of the absorption cross section from a discrete dopant level is shown in Fig. 4.1 [Bratt 1977]. The absorption cross section increases at the ionization energy because of the increase in the density of states. It begins to decrease because of the decrease in the oscillator strength [Lax 1956].

The real unknown is the alteration of the absorption cross section as a function of energy as an impurity band is formed. Consider one electron and vary its dopant energy level. As the ionization energy changes, the absorption

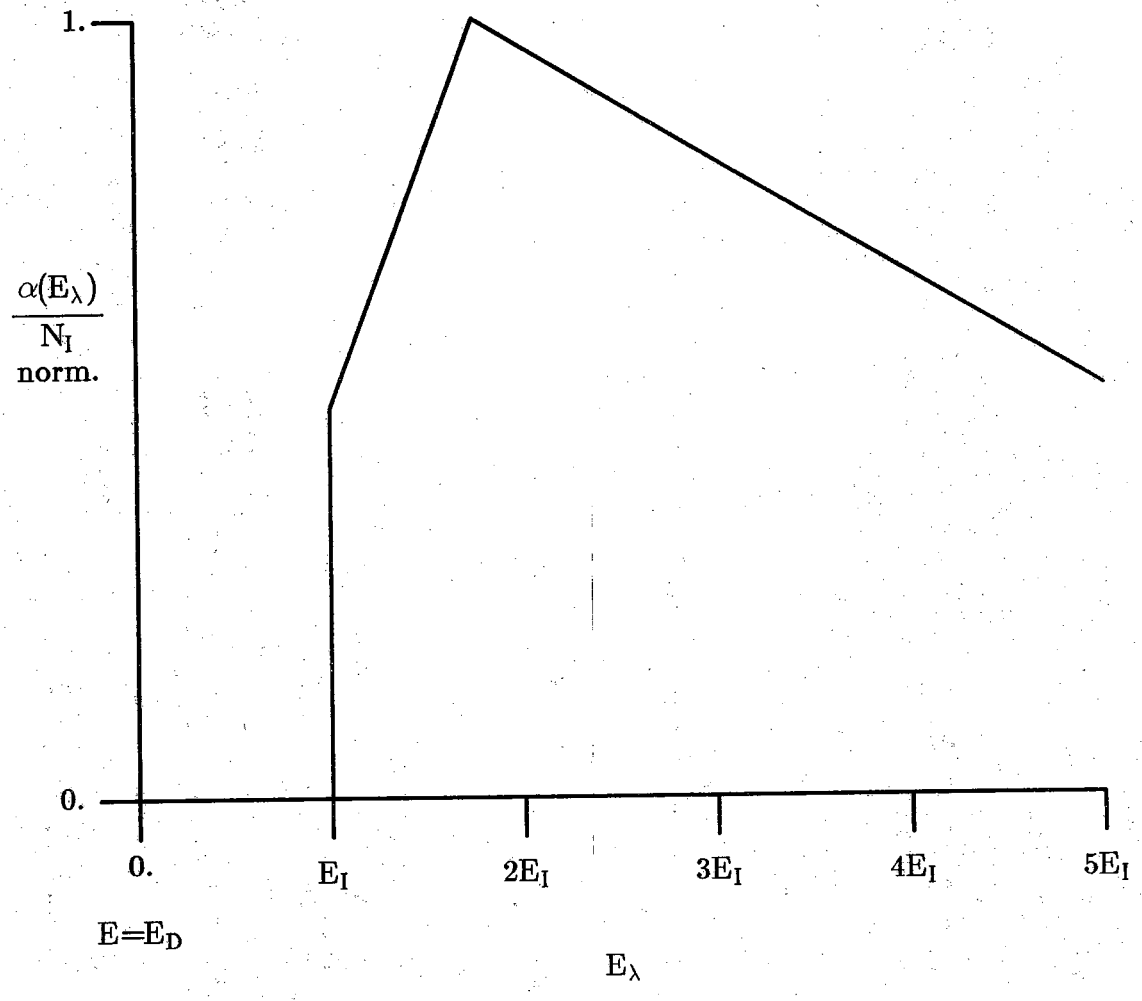

Figure 4.1 Schematic shape of a normalized absorption cross section vs. normalized energy curve - $B_I=0$

will correspondingly shift with the ionization energy. As is shown in sec. 4.5.3, this can be taken into account by integrating the impurity band density of states over the cross section.

If the shape of the absorption cross section as a function of energy also changes, the overall absorption will be difficult to calculate exactly. Yet the shape of the absorption cross section as a function of energy should change only slightly and the procedure shown in sec. 4.5.3 should still be a reasonable approximation.

4.5.3 Absorption as a function of energy

The absorption as a function of energy is assumed to be

$$\alpha(E_\lambda) = \int_{-\infty}^{+\infty} \sigma_{abs}(E) D_{B_I}(E-E_\lambda) dE \ .$$

where $D_{B_I}(E)$ is the density of states of the ground state energy levels in the impurity band. The assumption used for this equation is that $\sigma_{abs}(E)$ is independent of the doping concentration (ie., see sec. 4.5.2). If this assumption is reasonable, this equation can in theory be used to calculate the density of states in an impurity band.

For instance, one can consider a constant density of states in the impurity band. The absorption calculated using this density of states reveals an interesting result. The peak of the absorption increases in energy (See Fig. 4.2 and Fig. 4.3).

It appears that the density of states skews towards the conduction band [Serre & Ghazali 1983; Gold, Serre, & Ghazali 1988; Ghazali & Serre 1982]. In other words, there are more states in the upper part of the impurity band than the lower part (See Figs. 4.4 and 4.5). For this density of states, the peak of the absorption could stay approximately at the same energy and may actually shift downward.

In conclusion, one can get an idea of how the density of states changes in the impurity band as the dopant concentration is varied by looking at the location of the absorption peak. Of course, one must also take into account the radiation absorption corresponding to electrons being excited from the ground states of the impurity band to the excited impurity states [Thomas, Capizzi, DeRosa, Bhatt, & Rice 1981].

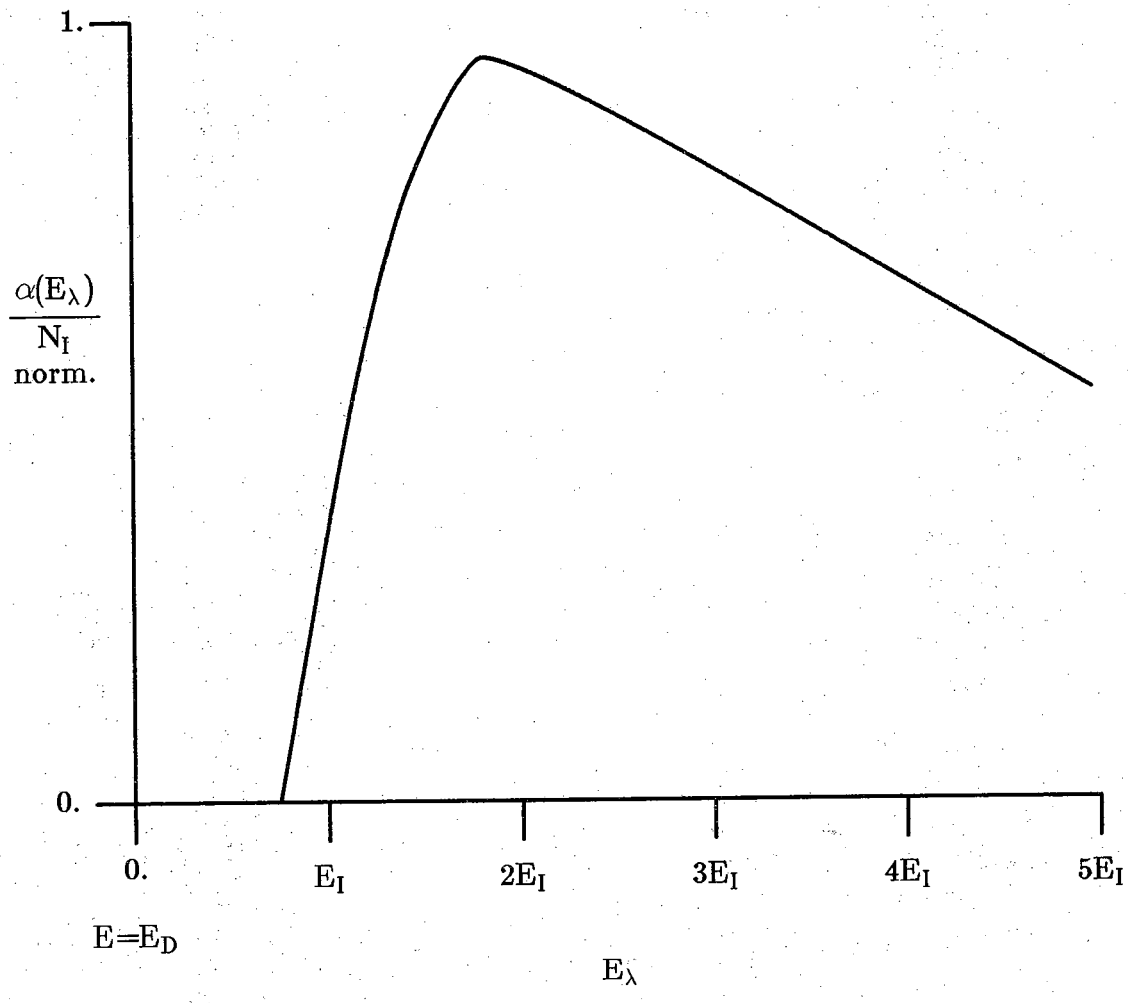

Figure 4.2 Schematic shape of a normalized absorption cross section vs. normalized energy curve - $B_I=.5E_I$

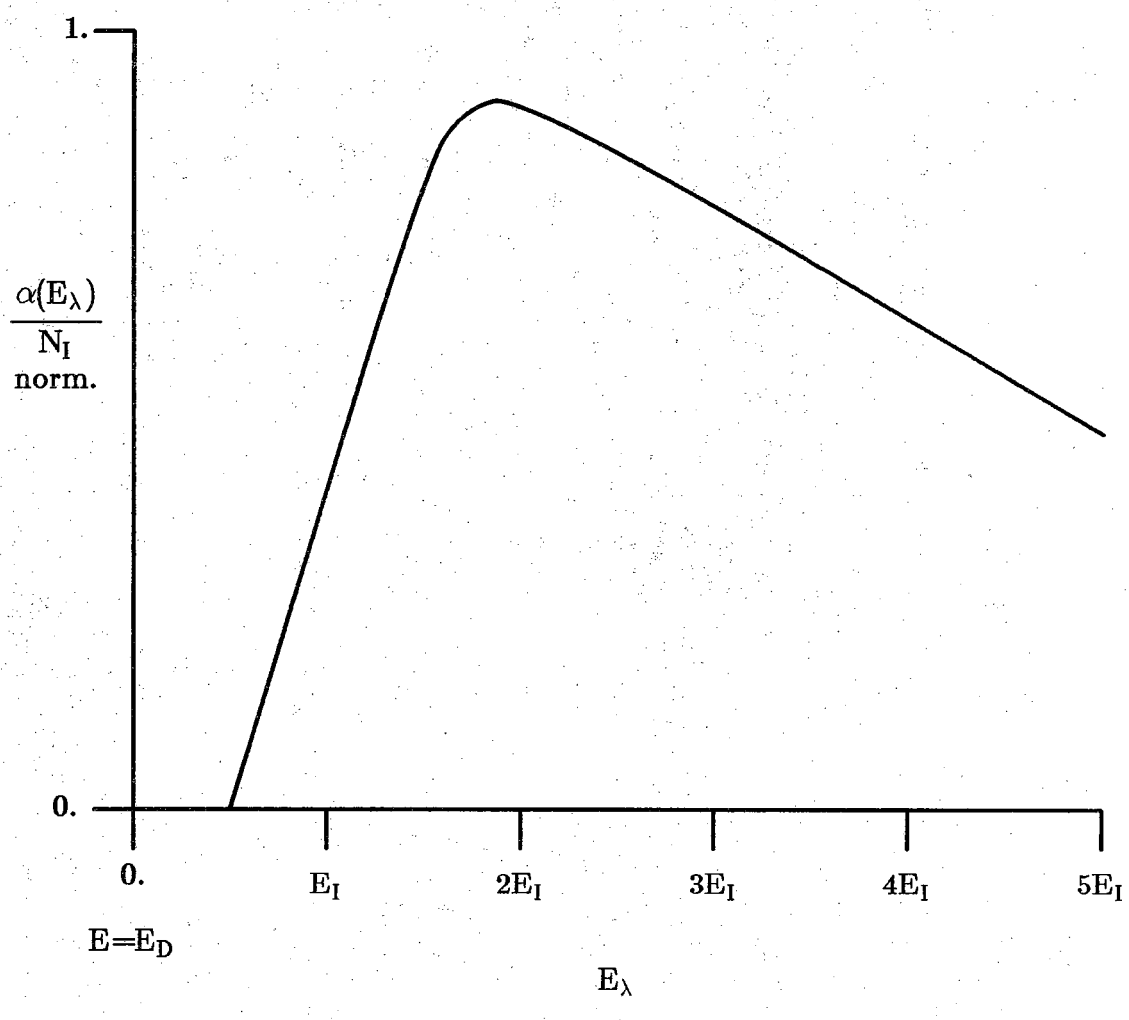

Figure 4.3 Schematic shape of a normalized absorption cross section vs. normalized energy curve - $B_I=1.0E_I$

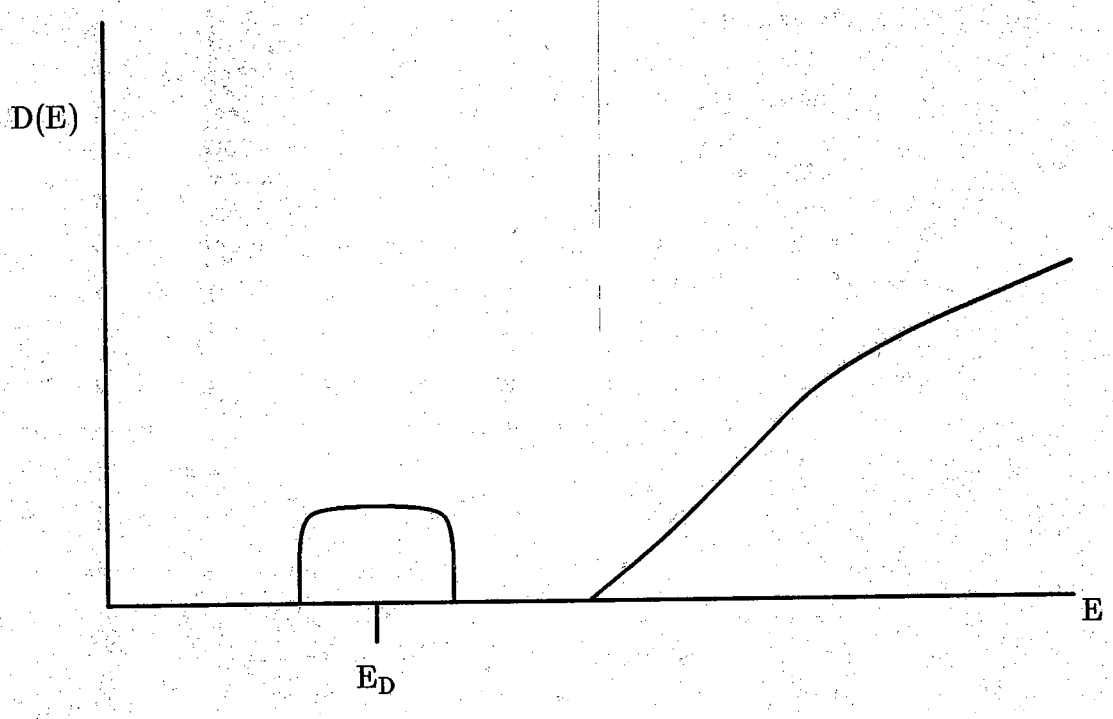

Figure 4.4 Density of states (D(E)) for a symmetric impurity band

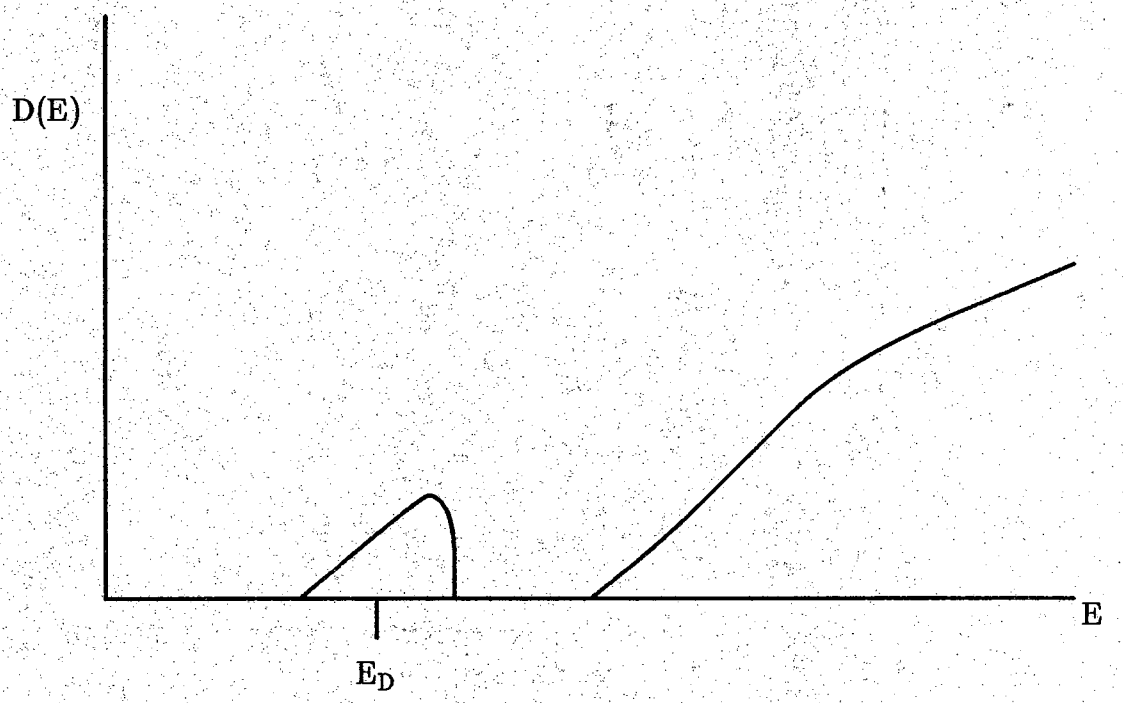

Figure 4.5 Density of states (D(E)) for a skewed impurity band

4.6 Four host semiconductor:impurity atom systems suited for use in a PEIR photoconductor

From this chapter and the calculation of B_I in sec. 3.2, it can be determined which semiconductor can have a large absorption and a reasonably large $(E_C-E_D)_{min}$ or $(E_A-E_V)_{min}$ (See Fig. 1.5 and tables 4.5 and 4.6). The host semiconductor:impurity atom system needs to have an ionization energy greater than the ionization energy using the effective mass theory. Comparing two dopant types with different ionization energies in the same semiconductor the argument is that the absorption cross section will be smaller in the deeper level but for the same absorption, $(E_C-E_D)_{min}$ or $(E_A-E_V)_{min}$ will be larger in the deeper level.

Another interesting result appears when looking at sec. 3.2 and B_I. In table 3.1, B_I for a specific impurity concentration peaks for a certain $r_{\sigma_{abs}}$ and decreases as $r_{\sigma_{abs}}$ increases or decreases in value from this peak value. It is questionable whether this phenomenon actually occurs, but it doesn't seem too unreasonable and consequently, a very promising type of semiconductor can be considered with a very large $r_{\sigma_{abs}}$. This will be the fourth host semiconductor:impurity atom system in this section.

The first host semiconductor:impurity atom system results when the actual ionization energy is much greater than the ionization energy using the effective mass theory. For instance, Si:P fits this category. On the other hand, GaAs:Be doesn't fit into this category, but there's still a possibility that even GaAs:Be can work. Hence, Si:P and similar semiconductor:dopant combinations will be very good materials to be incorporated into the impurity band layers.

The second host semiconductor:impurity atom system is one which has a very deep level and is doped extremely high. Due to the high doping problems in GaAs MBE processes, the high doping at this time is not be attainable. This host semiconductor:impurity atom system will be useful for detecting relatively short wavelengths (ie. around 10 μm). One possible reason to pursue this situation will be to consider absorption processes out of the extremely large and deep impurity band.

The third host semiconductor:impurity atom system can be seen when looking at the Si:P entry in table 4.3 and the $Al_{.4}Ga_{.6}As$:Si entry in table 4.4. E_I in Si:P is 45 meV and in $Al_{.4}Ga_{.6}As$:Si is 120 meV. Yet $\sigma_{abs_{th}}$ is larger for the $Al_{.4}Ga_{.6}As$ entry. This appears to be a very promising development but there are four notable considerations. 1) The absorption cross section may be much smaller because absorption out of a DX level may have a different cross section. 2) It may be very difficult to control the ionization energy because it

rapidly varies for different compositions around the Al_4Ga_6As:Si composition. 3) The DX center and the persistent photoconductivity could also be a problem, even at the high dopant concentrations that would be needed in a PEIR photoconductor. 4) The ionization energy using the effective mass theory is computed from the Γ valley while the valley the DX center is situated in is the X valley [Watanabe & Maeda 1984].

To detect longer wavelengths, the fourth host semiconductor:impurity atom system will utilize semiconductors with extremely small effective masses. In these semiconductors, $r_{\sigma_{abs}}$ becomes very large and considering table 3.1, it may be possible to find a high absorption coefficient with a small ionization energy (but larger than the ionization energy using the effective mass theory). The most likely materials will be InSb or InAs [Borrello, Roberts, Breazeale, & Pruett 1971] with impurity levels deeper than E_{Ieff}. A major problem is doping these narrow band gap materials.

4.7 Design of the active layer and the corresponding absorption coefficient

This section will briefly describe a procedure to determine what semiconductor:dopant combination will best be used in the active layers for a specific λ. Ideally, one will want B_I to be as small as possible to obtain a high absorption coefficient (See sec. 4.5). However, even if $B_I \simeq E_I$, the peak absorption coefficient can still be around 90% of the calculated peak value if B_I was assumed to be zero meV (Compare Figs. 4.1 and 4.3).

Considering these results, using Figs. 4.1, 4.2, and 4.3, and setting $B_I = E_I$, one can design the active layer to obtain a reasonably large absorption coefficient.

There are two design parameters in the impurity band layer needed to obtain an absorption coefficient - λ_d and the dopant concentration. λ_d is the wavelength that the detector is designed to detect and can be set equal to

$$\lambda_d = \frac{hc}{l_n E_{I_{th}}}$$

where $E_{I_{th}}$ is the theoretical ionization energy needed in the active layer to detect photons with a wavelength of λ_d. l_n is an empirical number that relates the radiation energy at the peak of the absorption cross section to the ionization energy. Based upon Fig. 4.1, n will be assumed herein to be 1.5.

The dopant concentration needs to be less than or equal to the amount that makes $B_I = E_I$. As shown in sec. 4.4, each semiconductor:dopant system has an $r_{\sigma_{abs}}$ value which can be used to find $B_I = E_I$. Some examples of B_I are shown in table 3.1. Consequently, the dopant concentration is found and in turn, the absorption coefficient.

As an example, table 4.7 shows three wavelengths to be detected, possible semiconductor:dopant systems, the associated dopant concentration and absorption coefficients.

4.8 Conclusions

Three major conclusions have arisen in this chapter. 1) The best semiconductor for incorporation in a PEIR photoconductor will be one in which the ionization energy is larger than the ionization energy using the effective mass theory 2) The absorption processes out of the impurity level can give some idea as to the distribution of the ground and excited states in the impurity band. 3) The absorption coefficients are reasonably large for certain host semiconductor:impurity atom combinations in a PEIR photoconductor.

Table 4.7
Design parameter examples in the active layer

λ_d (μm)	$E_{I_{th}}$ (meV)	System (unitless)	E_I (meV)	$r_{\sigma_{abs}}$ (Å)	N_I (cm^{-3})	α (cm^{-1})
10	82	Si:Ga	72	9.8	$6.0x10^{18}$	$5.1x10^{3}$
20	41	Si:P	45	16.0	$1.5x10^{18}$	$3.5x10^{3}$
30	27	GaAs:Te	30	43.5	$3.0x10^{17}$	$5.0x10^{3}$

5. NOISE AND D^*

5.1 Introduction

In this chapter, the determination of D^* for a PEIR photoconductor is discussed. D^* is a figure of merit in photodetectors and is defined in sec. 5.3. Since a PEIR photoconductor is operated in the infrared region, one of the most important noise sources will be due to the radiation produced by the background. This and other noise sources of interest are listed in sec. 5.2. Section 5.3 describes the Noise Equivalent Power (NEP) and D^* of a photodetector. One of the advantages of a PEIR photoconductor is the inherent filtering mechanisms in the device. These mechanisms are presented in sec. 5.4. Section 5.5 describes the D^* of a PEIR photoconductor.

5.2 Noise

Section 5.2.1 describes the noise terms and sec. 5.2.2 shows when the background noise is considered to be larger than the RG noise and the thermal noise[Seib & Aukerman 1973; Putley 1964; van Vliet 1967].

5.2.1 Noise terms

There are six noise terms of interest in an infrared photodetector - Recombination-generation (RG) noise, background noise, signal noise, shot noise, thermal noise, and amplifier noise [Putley 1964; Seib & Aukerman 1973]. Putley [Putley 1964] considers three more (for extrinsic photoconductors), but these will be neglected at this time.

RG noise is due to the randomness of recombination and generation. Conventionally, this generation is considered to be thermal generation [Kruse, McGlauchlin & McQuistan 1962; Kruse 1977] while the noise due to generation by photons is placed under signal or background noise. However, all these noise terms can be placed under RG noise because the noise depends on the generation itself, not on the type of generation [van Vliet 1967]. The rms current source for RG noise due only to thermal generation is (in an extrinsic photoconductor - See app. B)

$$\overline{(i_{RG}^2)}^{1/2} = (4eI_d G\Delta f)^{1/2}$$

where I_d is the dark current if the gain equals one and G is the gain.

Background noise is due to the radiation emitted from the background surrounding the object to be detected. The background noise can be represented by a background current [Long 1977] and can be placed with the other current terms in the RG noise factor. The rms current source for RG noise due only to background radiation generation is

$$\overline{(i_B^2)}^{1/2} = (4eGI_B G\Delta f)^{1/2}$$

where I_B is the current produced by the background radiation if the gain was equal to 1.

Signal noise is the noise produced by the random generation due to the signal. This noise is usually much smaller than the background or the other noise terms. The rms current source for RG noise due only to signal radiation generation is

$$\overline{(i_S^2)}^{1/2} = (4eGI_{op} G\Delta f)^{1/2}$$

where I_{op} is the current produced by the signal radiation if the gain was equal to 1.

Shot noise is due to the randomness of generation but not recombination. Shot noise is a special case of RG noise [Kruse, McGlauchlin & McQuistan 1962]. In a PEIR photoconductor with ohmic contacts, as in conventional photoconductors with ohmic contacts, there is no shot noise because the excited carriers have recombination processes in addition to generation processes. If one wanted to incorporate a PEIR photoconductor with a blocking contact in an array, shot noise will become more important than RG noise.

Thermal noise is due to the randomness of the collisions in a resistor. The rms current source for thermal noise is

$$\overline{(i_{Th}^2)}^{1/2} = (4\,\frac{kT}{R}\,\Delta f)^{1/2} \quad .$$

The thermal noise may be a factor in a PEIR photoconductor for the same

reason it is a factor in the intrinsic photoconductor - the device resistance is low [Blouke, Burgett, & Williams 1973]. Section 5.2.2 presents the equation that determines when the thermal noise is larger than the background noise.

5.2.2 Comparison of the background, RG due to thermal generation, and thermal noise

Ideally, an infrared detector will operate such that the the dominant noise term is the background noise. The optimum temperature of operation equals the point when the RG noise due to thermal generation, which increases with temperature, almost equals the background noise, which is independent of device temperature. The temperature will be low enough that the background noise is larger than the RG noise due to thermal generation.

Thermal and background noise can be compared in an extrinsic photoconductor [Long 1977] (and approximately in a PEIR photoconductor because the compensation dopant concentration is not necessarily greater than the carrier concentration (See app. B)). Using the proper relationships for GI_B and R [Long 1977],

$$\frac{\overline{i_B^2}}{\Delta f} = 4\, e^2 \mu_n n A_c (G\xi)$$

and

$$\frac{\overline{i_{Th}^2}}{\Delta f} = 4\, e^2 \mu_n n A_c \left(\frac{kT}{ed_c}\right)$$

where ξ is the electric field, A_c is the area of the contacts, and d_c is the distance between the contacts.

Table 5.1 shows some values of kT/ed_c for various values of d_c and T. Using the reasonable values of $\xi = 100V/cm$ [Bratt 1977] and $G \simeq 1$, it can be seen that the value of ξG is much larger than any of the kT/ed_c entries in table 5.1. Using this result and comparing the two previous equations, it can be seen that thermal noise will be smaller than the background noise for a PEIR photoconductor.

Table 5.1
Calculation of $\frac{kT}{ed_c}$

T (K)	d_c (μm)	$\frac{kT}{ed_c}$ (V/cm)
4	20	.172
10	20	.430
20	20	.862
40	20	1.72
80	20	3.45
4	100	.034
10	100	.086
20	100	.172
40	100	.345
80	100	.689

Using these comparisons, it will be assumed that the thermal noise and the RG noise due to thermal generation are much smaller than the background noise.

5.3 Noise Equivalent Power (NEP) and D^*

The figure of merit D^* depends on the wavelength, the frequency of modulation, and is defined to have a bandwidth of 1 Hz. The wavelength dependence of D^* is discussed in sec. 5.5. The modulation frequency is related to the response time.

D^* is calculated by finding the Noise Equivalent Power (NEP). NEP is defined as the minimum amount of radiation power incident on the detector needed to obtain a Signal to Noise ratio (S/N) equal to 1 [Sze 1981; Seib & Aukerman 1973; Kruse, McGlauchlin & McQuistan 1962; Kruse 1977].

To obtain NEP [Seib & Aukerman 1973],

$$I_s = I_{op} G = \sqrt{2(\bar{I}_n^2)}$$

and

$$\bar{I}_n^2 = 4\, e\, (I_d + I_{op} G + I_B G)\, G\, \Delta f + \frac{4kT\Delta f}{R}$$

where $I_{op}G$ is the current produced by the signal, hereafter known as the signal current or I_s. Δf is the bandwidth, and R is the resistance of the circuit. Using the results from sec. 5.2.2 and assuming Δf is small enough [Seib & Aukerman 1973] (This prevents I_s from getting too large),

$$I_s = \sqrt{8e\, (I_B)(G^2)\, \Delta f}\ .$$

Considering that [Seib & Aukerman 1973]

$$NEP = \frac{I_{op}}{\eta\sqrt{2}}(E_\lambda/q) = \frac{I_s}{\eta G\sqrt{2}}(E_\lambda/q)$$

and

$$D^* = \frac{\sqrt{A_D \Delta f}}{NEP} ,$$

$$D^* = \frac{(\frac{e}{E_\lambda})\, \eta \sqrt{A_D}}{\sqrt{4e\,(I_B)}}$$

where E_λ is the energy of the photon and A_D is the area of the detector (See sec. B.5). [Seib & Aukerman 1973]

5.4 Filtering of background radiation

There are two obvious inherent filtering mechanisms in a PEIR photoconductor. The first is due to impurity band to conduction band absorption while the second is due to phonon absorption.

As can be seen in sec. 4.5, impurity band to conduction band absorption peaks at a certain wavelength. Due to this peak, the background noise is collected only over a wavelength range about this peak. The importance of this phenomenon can be revealed when it is remembered that the background noise for a conventional photoconductor is calculated for all photons with energy less than the bandgap energy and that most of the blackbody radiation at 300 K occurs at wavelengths around 10 μm. If one designed a PEIR photoconductor for wavelengths around 30 μm or longer, some of the background noise around 10 μm will be effectively filtered out. For a description of how this phenomenon influences D^*, see sec. 5.5.

The other filtering mechanism is the absorption and reflection of radiation due to phonon emission alone. For GaAs, the phonon absorption exceeds $5x10^4 cm^{-1}$ [Blakemore 1982]. In the wavelength range this phonon absorption occurs, the photons can be effectively filtered out. Since the phonon energy changes as the composition in $Al_xGa_{1-x}As$ changes, there will be some freedom in filtering specific wavelengths. This filtering can take place in $Al_xGa_{1-x}As$ from .0354 eV (35 μm, 285 cm^{-1} - for GaAs) to .05 eV (24.8 μm, 403 cm^{-1} - for AlAs) [Adachi 1985]. Other compositions, such as InGaAs, can filter different wavelength ranges.

5.5 D^* of a PEIR photoconductor

D^*_{BLIP} (Background Limited Infrared Photodetector) is defined as the D^* value when the main source of noise is the background noise. For a background temperature of 300 K, a sufficiently low operating temperature, and a photodetector operating in the wavelength range greater than 3 μm, background noise becomes a major source of noise. In general (See sec. 5.3),

$$D^*_{BLIP} \propto \frac{\lambda}{\sqrt{I_B}}$$

where it is assumed that the quantum efficiency is one at the wavelength that the detector is designed to collect. This wavelength will be labeled λ_d.

In a conventional detector, the noise is due to all the photons with energies greater than the bandgap (for 2 carrier detectors). Since most of the background noise is in the 10 μm range for a background temperature of 300 K, the slope downward of D^*_{BLIP} as λ_d increases is due to the increase in noise (See Fig. 5.1). D^*_{BLIP} begins to increase when λ_d is greater than 20 μm because the photon wavelength is increasing. In this radiation wavelength range, the increase in the λ_d term in D^*_{BLIP} is larger than the increase in the I_B term (See sec. 5.3).

In a PEIR photoconductor, only radiation over a limited wavelength range is collected (See sec. 5.3). If wavelength to be detected is long enough (ie. greater than 30 μm), the major portion of background noise at 10 μm can be filtered out. Some examples of this filtering phenomenon is shown in table 5.2 and Fig. 5.1. It is assumed in table 5.2 that all the background radiation is collected if the wavelength range is between λ_{min} and λ_{max} and that none of the background radiation is not collected outside of this range. Fig. 5.1 contains the corresponding graphical description of table 5.2.

Table 5.2
Some parameters needed to calculate
D^* for some PEIR photoconductors

	N_I (cm^{-3})	$B_I/2$ (meV)	E_I (meV)	λ_{min} (μm)	λ_d (μm)	J_B (amps/cm^2)
Si:P	$2x10^{18}$	25.	45.	17.7	29.5	.179
GaAs:Te	$2x10^{17}$	13.	30.	28.8	38.8	.0754
GaAs:Te	$5x10^{17}$	17.	30.	26.4	44.3	.128

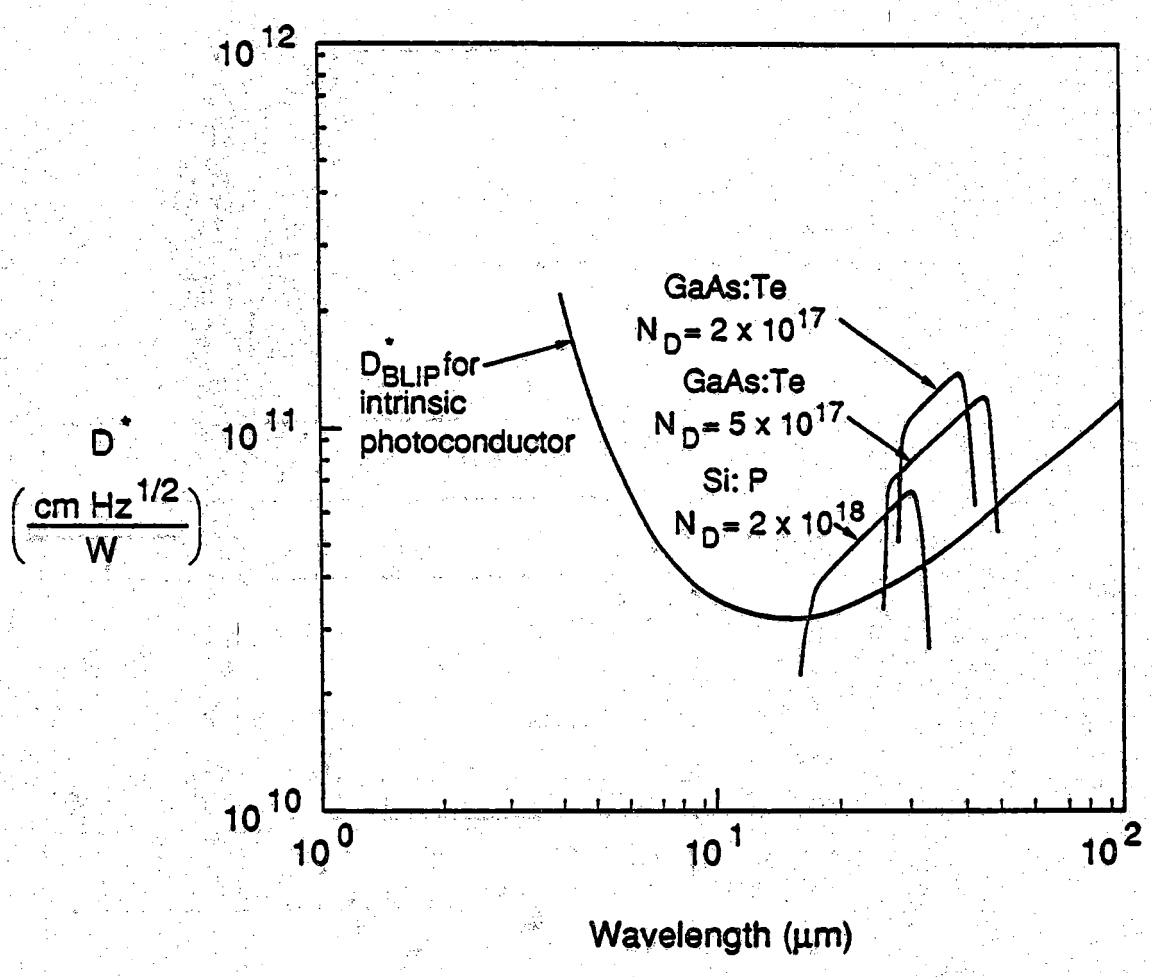

Figure 5.1 D^* for three theoretical PEIR photoconductors

6. DESIGN CONSIDERATIONS FOR THE FABRICATION OF THE PEIR PHOTOCONDUCTOR

6.1 Introduction

This chapter presents the design considerations when fabricating a PEIR photoconductor. As in most devices, the microscopic parameters can only be controlled by choosing certain macroscopic parameters. In a PEIR photoconductor, the macroscopic parameters are: 1) the semiconductor, 2) the types of impurity atoms, 3) the amount of impurity concentration, 4) the thickness of the layers, 5) the number of layers in the active region, 6) the arrangement of the layers, and 7) the temperature of the substrate when growing the epitaxial layers. The two PEIR photoconductor configurations being fabricated in this project are shown in Fig. 6.1 and Fig. 6.2. As can be seen in these figures, all the macroscopic parameters, except temperature, have been presented.

As a reference, the layers can be divided up into four parts: 1) the transparent contact layer, 2) the active region layers (both the impurity band layers and the blocking layers), 3) the epitaxial layer (otherwise known as the epilayer), and 4) the substrate-contact layer. All the layers are considered in the theoretical design of the device except the epilayer.

The optimization of macroscopic parameters and the corresponding experimental limitations in attaining the ideal parameters are presented in the remaining sections. Section 6.2 presents the ionization energy in the layers. Section 6.3 presents the doping concentration in the layers. Section 6.4 presents the design of the layers. Section 6.5 presents the temperature considerations when fabricating this device. Section 6.6 presents the conclusion of this chapter.

6.2 Ionization energy

The ionization energy needs to be considered in 1) the transparent contact layer, 2) the active region layers, 3) the epilayer, and 4) the substrate-contact layer.

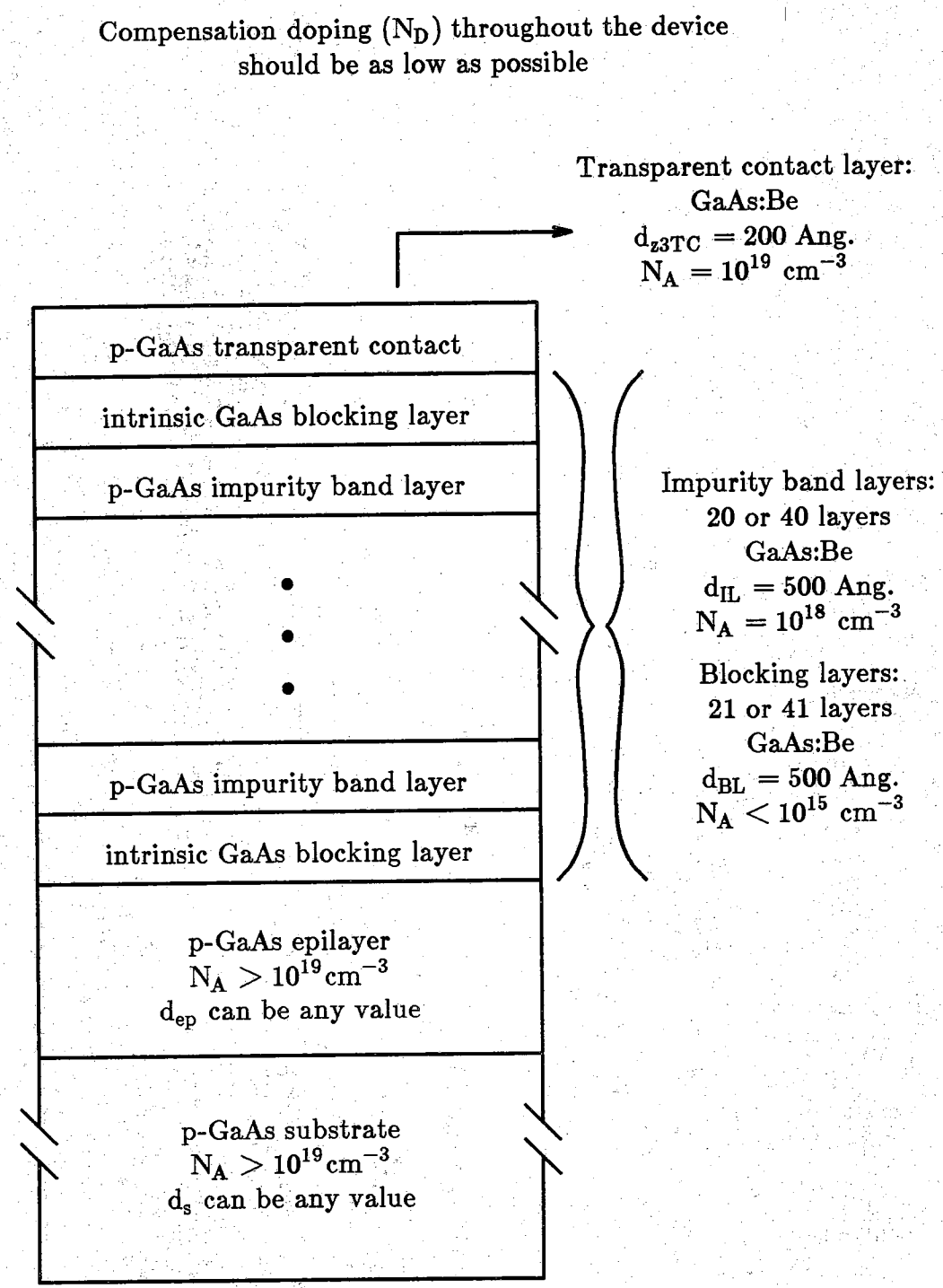

Figure 6.1 A GaAs:Be PEIR photoconductor

Compensation doping (N_A) throughout the device
should be as low as possible

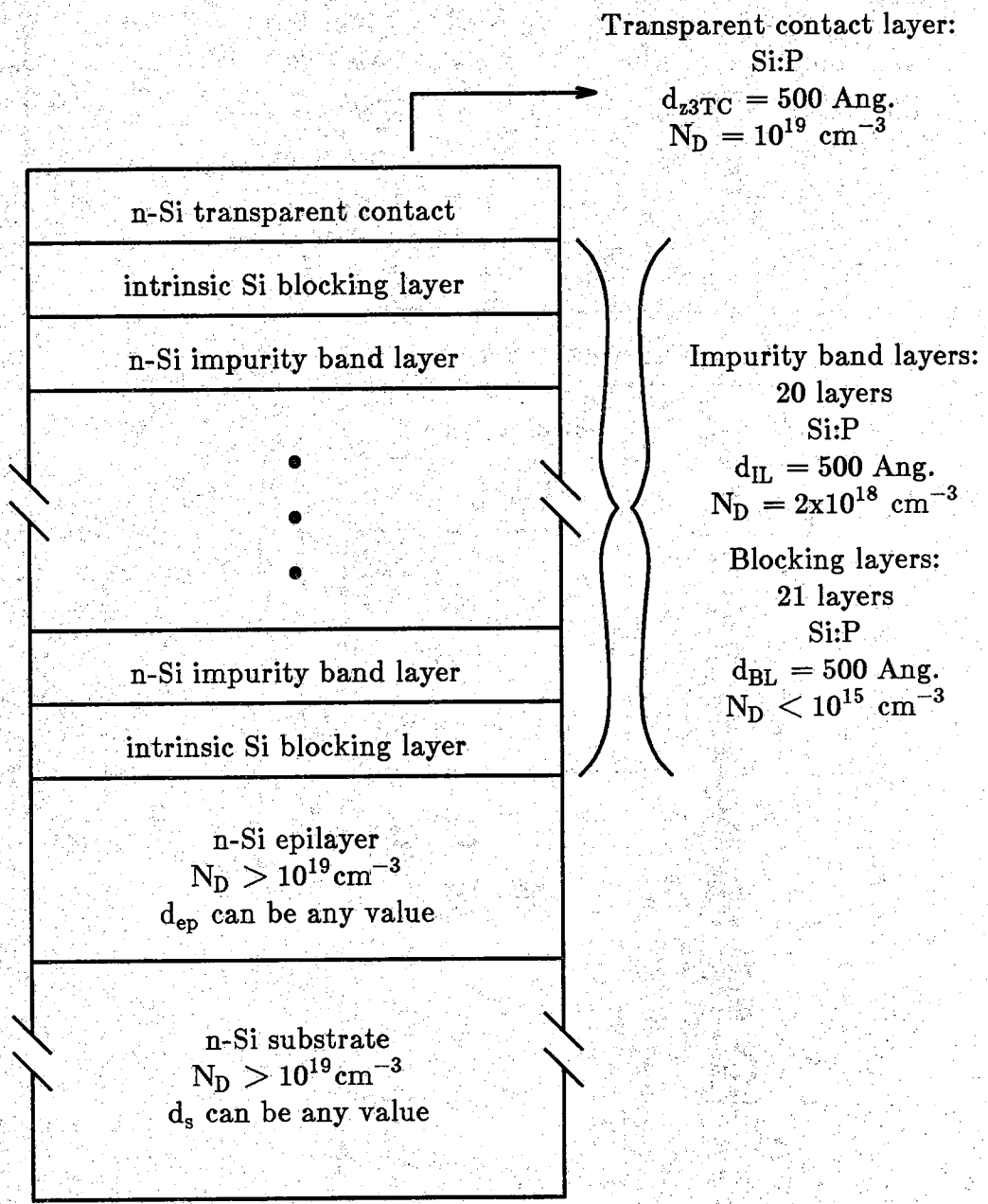

Figure 6.2 A Si:P PEIR photoconductor

6.2.1 Transparent contact layer

For the transparent contact layer, the ionization energy should be as small as possible. As the ionization energy becomes smaller, the dopant concentration needed to move the impurity band up into the conduction band (n-type device) decreases (When the impurity band merges with the conduction band, the semiconductor becomes degenerate). The smaller dopant concentration means that the free carrier concentration in the transparent contact layer becomes smaller, and as shown in app. E, the smaller the free carrier concentration, the more transparent the contact becomes. This problem of free carrier absorption in a transparent contact is briefly described. Infrared radiation in the wavelength range of interest can easily be absorbed due to free carrier absorption. This absorption is detrimental because the radiation can be absorbed in the contact before it reaches the active region and/or reflected due to the high imaginary part of the index of refraction (See app. E). Moreover, free carrier absorption is proportional to the free carrier concentration and the square of the wavelength. Consequently, transparent contacts become harder to make as the free carrier concentration increases or the wavelength increases.

It may be possible that the impurity band doesn't need to merge with the conduction band to make the contact ohmic. There will be two problems with this type of contact. First, the mobility in the impurity band may be too small. Of course, the mobility in a degenerately doped semiconductor is not that high so this may not be a problem. Second, there is the problem of freeze out of the carriers. It's reasonable to assume that the carriers will not freeze out if the depth of the impurity band is less than kT (This is a result for ohmic contacts). When considering the temperature of operation of a photoconductor (See app. B), it appears that the impurity band will not have to merge in a 300 K background source because a reasonable amount of carriers will be thermally generated into the conduction band. For a low background situation, however, the contact will most likely have to be degenerate. In any case, to be on the safe side, the contact is now designed to be degenerate.

One experimental consideration for the transparent contact layer is whether there can be two different impurity sources. An example of this would be to make a PEIR photoconductor using Si:As in the active region. The problem with Si:As is that a conservative estimate of the dopant concentration needed to make Si:As degenerate is around $2x10^{19}cm^{-3}$. For Si:P the concentration would be around $1x10^{19}cm^{-3}$. Hence, it would be better to make the contacts with Si:P than Si:As. The problem with this suggestion is that an epitaxial growth chamber may only have either a P source or a As source, but not both sources.

One important aside to this previous example is that even Si:P is not a good material to make a transparent contact layer. For n-type Si, though, Si:P is the most shallow dopant that one can realistically use and hence poses a problem in a PEIR photoconductor made with Si.

6.2.2 Active region layers

As shown in chap. 4, the best type of dopant to be used in the active region will be one where the actual ionization energy is larger than the effective mass ionization energy. The major consideration when choosing an ionization energy is that the diffusion of the impurity atom must be kept to a minimum.

6.2.3 Epilayer

The epilayer is grown on the substrate. The purpose of the epilayer is to grow a thin buffer film on the substrate to "cover up" the defects which may exist in the substrate. The active layer is then grown on the epilayer.

The epilayer can be grown two different ways - either degenerately doped or lightly doped. Degenerately doped would be the more preferable case, as then the interface between the substrate and the epilayer is not of much concern and the epilayer may be considered part of the contact. Unlike the transparent contact layer, it's not essential that the epilayer be transparent. In fact, this back contact will be reflecting. Hence, the ionization energy needs to only be shallow enough to fabricate a degenerate semiconductor at the highest attainable dopant concentration in the epitaxial growth system.

If the epilayer is lightly doped, the epilayer is considered part of the active region and the interface between the substrate contact and the epilayer needs to be carefully studied. The ionization energy will be of no importance in a lightly doped epilayer.

6.2.4 Substrate-contact layer

The ionization energy in the substrate-contact layer can be considered a secondary requirement. The primary requirement in this layer is that the substrate be degenerately doped. Most likely, this means that the impurity used in the substrate is shallow.

6.3 Doping concentration

The doping concentration in a PEIR photoconductor is far and away the most important macroscopic parameter. Doping concentration is a general term that has three particular terms: 1) the majority dopant concentration, 2) the compensation (minority) dopant concentration, and 3) the ability of the epitaxial system to change the dopant concentration. The doping concentration needs to be considered in 1) the transparent contact layer, 2) the active region layers, 3) the epilayer, and 4) the substrate-contact layer.

6.3.1 Transparent contact layer

In the transparent contact layer, the majority dopant concentration should be high enough to cause the semiconductor to become degenerate. As discussed in sec. 6.2.1, it may be possible that the impurity band can be separated from the conduction band (n-type device).

The compensation dopant concentration is not of importance in the transparent contact. It should be the same as the dopant concentration in the active region, which will be very small.

The two potential problems in the epitaxial growth system are 1) to change the dopant concentration from the value in the impurity band layer to the higher concentration in the transparent contact layer and 2) to attain a dopant concentration high enough to degenerately dope the contact (which shouldn't be a problem when considering sec. 6.2). In the MBE system, assuming there is only one dopant source, the concentration is altered by heating up the source container (If one wants an intrinsic layer, this source container is closed). It takes time and careful tuning to properly adjust the oven temperature. This is not a serious problem because the intrinsic layer adjacent to the transparent contact layer can be made wide enough to equal the time needed to alter the temperature of the source.

6.3.2 Active region layers

The active region is separated into two portions - the impurity band layers and the blocking layers. The majority dopant concentration in the impurity band layers needs to be less than the amount that causes the impurity band to merge with the conduction band yet large enough to fabricate a reasonably large absorption coefficient. A reasonable estimate is that the dopant concentration be high enough such that the energy width of the impurity band (B_I) equals the

ionization energy (E_I) (See sec. 4.7). It appears that the blocking layers can be doped with the limit being that an impurity band can't be formed. The advantage of doping the blocking layers is that impurity scattering lowers the impact ionization [Bratt 1977] which causes avalanching. Unfortunately, the MBE system is not designed to adjust quickly to two different dopant concentrations so it's easier to make the blocking layers lightly doped.

The problem with the epitaxial growth system is the only practical way to quickly change the doping concentration is to either have two sources at different temperatures or to use the shutter which when open dopes the layer and when closed doesn't dope the layer.

The compensation dopant concentration will be as small as possible in both the impurity band layers and the blocking layers. The only possible exception will be that if one wants to make a high speed detector [Bratt 1977], the compensation concentration can be made higher.

6.3.3 Epilayer

The same considerations in the transparent contact layer also exist in the degenerately doped epilayer. The same considerations in the blocking layer also exist in the lightly doped epilayer.

6.3.4 Substrate-contact layer

The substrate is degenerately doped when it is placed in the epitaxial growth chamber. Hence, the doping concentration in the substrate is already taken care of before fabrication.

6.4 Layers

The layer thickness needs to be considered in 1) the transparent contact layer, and 2) the active region layers.

In the transparent contact layer, the layer needs to be thin enough to allow the radiation to pass through. On the other hand, the layer needs to be thick enough for a low contact resistance. These tradeoffs are discussed in more depth in app. E.

In the active region layers, the sum of the impurity band layer thicknesses needs to be approximately equal to the inverse of the absorption coefficient. The experimental limit is that it may take a long time to grow the total thickness

desired and hence, one may have to settle for an active region that doesn't absorb all the possible radiation.

The most important requirement for the blocking layers is that they need to be wide enough to prevent the impurities from diffusing from one impurity band layer to another. If this were allowed to happen, an impurity band can form throughout the active layer, effectively transforming a PEIR photoconductor into a poor conventional extrinsic photoconductor.

Ideally, the number of layers that can be grown can be as large as desired. The limit is 1) the amount of time for growth and 2) if the shutters have to be manually controlled, the ability of the operator to efficiently open and close the shutter over a certain time period.

The important thing to note about the arrangement of the layers is that a blocking layer is adjacent to both of the contacts. This configuration is used because most likely, an impurity band layer adjacent to the contacts would be rendered useless at the best and could produce a leakage current through the adjacent impurity band at the worst.

6.5 Temperature

The important consideration for the temperature of the substrate during epitaxial growth is that the temperature must be low enough to hinder diffusion of the impurity atoms into the blocking layers.

6.6 Conclusion

This chapter has presented the important design considerations for a PEIR photoconductor. These considerations are straightforward, most likely because a PEIR photoconductor has a simple design.

7. CONCLUSIONS AND RECOMMENDATIONS

7.1 Conclusions

An infrared photoconductor, designated as the Periodic Extrinsic InfraRed (PEIR) photoconductor, has been analyzed. It will most likely be designed to detect wavelengths in a range from 7 μm to longer than 100 μm.

It has been proposed in this wavelength range because

1) conventional intrinsic photoconductors usually incorporate HgCdTe, which is very difficult to work with, in this wavelength range,

2) conventional extrinsic photoconductors have necessarily low absorption coefficients,

3) BIB detectors are limited by ionization problems and their relationship to the active region, and

4) superlattice photodetectors have serious problems with the gain, efficiency, and uniformity from layer to layer due to the necessary abrupt heterojunction.

Other important advantages in a PEIR photoconductor are:

1) The gain-bandwidth product will be large because the contacts are front to back and are closely spaced together because of the high absorption coefficient.

2) The response time in a PEIR photoconductor should be as fast as in an extrinsic photoconductor.

3) The temperature of operation in a PEIR photoconductor should be higher than in an extrinsic photoconductor.

4) The front to back contact configuration is ideal for incorporation into an array.

The major disadvantages in a PEIR photoconductor are:

1) Parasitic resistances are going to be a problem when detecting in a 300 K blackbody background.

2) Transparent contacts will be very difficult to make for wavelengths greater than 50μm.

Possible disadvantages in a PEIR photoconductor are:

3) Electrons may accumulate in the impurity band layers (n-type device) and the recombination could substantially increase.

4) Absorption could be smaller than expected due to the widening of the impurity band energy width.

A scheme has been found to determine the best host semiconductor:impurity atom combination in the impurity band layer (See chap. 4). It appears that the deeper the actual ionization energy is relative to the ionization energy calculated using the effective mass theory, the higher the absorption can be. To detect longer wavelengths, one needs to consider host semiconductors with smaller effective masses.

7.2 Recommendations

There are two recommendations. First, using the basic design procedures described in chap. 4, one can build and test the device. Some devices have already been built and are in the process of being tested. Unfortunately, the test procedure being used is for a large area detector operating in unfiltered 300 K blackbody radiation. If one can make the detector area smaller and/or the background radiation smaller, the detector will more likely be operational. This improved test procedure will also need to be considered. Second, once some of the results begin to be obtained, then a model can be developed to have a better idea of: 1) the operation of the device, 2) absorption, recombination, and the effect of space charge in the device, and 3) a procedure to optimize the performance of a PEIR photoconductor.

LIST OF REFERENCES

LIST OF REFERENCES

S. Adachi (1985), "GaAs, AlAs and $Al_xGa_{1-x}As$: Material parameters for use in research and device applications," Journal of Applied Physics, vol. 58, pp. R1-R29.

D.F. Barbe (1975), "Imaging devices using the charge-coupled concept," Proceedings of the IEEE, vol. 63, pp. 38-67.

H.B. Bebb (1969), "Application of quantum-defect method to optical transitions involving deep effective-mass-like impurities in semiconductors," Physical Review, vol. 185, pp. 1116-1126.

H.B. Bebb and R.A. Chapman (1967), "Application of quantum defect techniques to photoionization of impurities in semiconductors," Journal of Physics and Chemistry of Solids, vol. 28, pp. 2087-2097.

H.B. Bebb and R.A. Chapman (1969), "Theory of deep impurity centers in semiconductors," *Proceedings of the Third International Conference on Photoconductivity,* Ed. E.M. Pell, Pergammon Press, New York, pp. 245-251.

J.S. Blakemore (1982), "Semiconducting and other major properties of gallium arsenide," Journal of Applied Physics, vol. 53, pp. R123-R181.

H. Blauvelt, S. Margalit, and A. Yariv (1982), "Single-carrier-type dominated impact ionisation in multilayer structures," Electronics Letters, vol. 18, pp. 375-376.

M.M. Blouke, C.B. Burgett, and R.L. Williams (1973), "Sensitivity limits for extrinsic and intrinsic infrared detectors," Infrared Physics, vol. 13, pp. 61-71.

S.R. Borrello, C.G. Roberts, B.H. Breazeale, and G.R. Pruett (1971), "Cooling requirements for BLIP performance of intrinsic photoconductors," Infrared Physics, vol. 11, pp. 225-232.

D.R. Bosomworth, R.S. Crandall, and R.E. Enstrom (1968), "Donor spectroscopy in GaAs," Physics Letters, vol. 28A, pp. 320-321.

P.R. Bratt (1977), "Impurity germanium and silicon infrared detectors," *Semiconductors and Semimetals, vol. 12,* Eds. R.K. Willardson and A.C. Beer, Academic Press, New York, pp. 39-142.

N. Braslau (1983), "Ohmic contacts to GaAs," Thin Solid Films, vol. 104, pp. 391-397.

K. Brennan (1985a), "Theory of electron and hole impact ionization in quantum well and staircase superlattice avalanche photodiode structures," IEEE Transactions on Electron Devices, vol. ED-32, pp. 2197-2205.

K.F. Brennan (1985b), "Theory of the channeling avalanche photodiode," IEEE Transactions on Electron Devices, vol. ED-32, pp. 2467-2478.

K. Brennan (1986a), "Theory of the GaInAs/AlInAs-doped quantum well APD: A new low noise solid-state photodetector for lightwave communications systems," IEEE Transactions on Electron Devices, vol. ED-33, pp. 1683-1695.

K. Brennan (1986b), "Theory of the doped quantum well superlattice APD: A new solid-state photomultiplier," IEEE Journal on Quantum Electronics, vol. QE-22, pp. 1999-2016.

K. Brennan (1987a), "Comparison of multiquantum well, graded barrier, and doped quantum well GaInAs/AlInAs avalanche photodiodes: A theoretical approach," IEEE Journal on Quantum Electronics, vol. QE-23, pp. 1273-1282.

K. Brennan (1987b), "The p-n quantum well APD: A new solid-state photodetector for lightwave communications systems and on-chip detector applications," IEEE Transactions on Electron Devices, vol. ED-34, pp. 782-792.

K. Brennan (1987c), "The p-n heterojunction quantum well APD: A new high-gain low-noise high-speed photodetector suitable for lightwave communications and digital applications," IEEE Transactions on Electron Devices, vol. ED-34, pp. 793-803.

K.F. Brennan and C.J. Summers (1987), "The variably spaced superlattice energy filter quantum well avalanche photodiode: A solid state photomultiplier," IEEE Journal on Quantum Electronics, vol. QE-23, pp. 320-327.

K. Brennan, T. Wang, and K. Hess (1985), "Theory of electron impact ionization including a potential step: Application to GaAs-AlGaAs," IEEE Electron Device Letters, vol. EDL-6, pp. 199-201.

R.E. Burgess (1954), "Fluctuations in the number of charge carriers in a semiconductor," Physica, vol. 20, pp. 1007-1010.

R.E. Burgess (1956), "The statistics of charge carrier fluctuations in semiconductors," Proceedings of the Physical Society, vol. B69, pp. 1020-1027.

J.C. Campbell, A.G. Dentai, W.S. Holden, and B.L. Kasper (1983), "High-performance avalanche photodiode with separate absorption 'grading' and multiplication regions," Electronics Letters, vol. 19, pp. 818-820.

F. Capasso (1982), "The channeling avalanche photodiode: A novel ultra-low-noise interdigitated p-n junction detector," IEEE Transactions on Electron Devices, vol. ED-29, pp. 1388-1395.

F. Capasso (1982), "New ultra-low-noise avalanche photodiode with separated electron and hole avalanche regions," Electronic Letters, vol. 18, pp. 12-13.

F. Capasso (1983), "New device applications of bandedge discontinuities in multilayer heterojunction structures," Surface Science, vol. 132, pp. 527-539.

F. Capasso, J. Allam, A.Y. Cho, K. Mohammed, R.J. Malik, A.L. Hutchinson, and D. Sivco (1986), "New avalanche multiplication phenomenon in quantum well superlattices: Evidence of impact ionization across the band-edge discontinuity," Applied Physics Letters, vol. 48, pp. 1294-1296.

F. Capasso, A.Y. Cho, and P.W. Foy (1984), "Low-dark-current low-voltage 1.3-1.6 μm avalanche photodiode with high-low electric field profile and separate absorption and multiplication regions by molecular beam epitaxy," Electronics Letters, vol. 20, pp. 635-637.

F. Capasso, H.M. Cox, A.L. Hutchinson, N.A. Olsson, and S.G. Hummel (1984), "Pseudo-quaternary GaInAsP semiconductors: A new $Ga_{.47}In_{.53}As/InP$ graded gap superlattice and its applications to avalanche photodiodes," Applied Physics Letters, vol. 45, pp. 1193-1195.

F. Capasso, K. Mohammed, and A.Y. Cho (1985), "Quantum photoconductive gain by effective mass filtering and negative conductance in superlattice pn junctions," Physica, vol. 134B, pp. 487-493.

F. Capasso, K. Mohammed, and A.Y. Cho (1986), "Resonant tunneling through double barriers, perpendicular quantum transport phenomena in superlattices, and their device applications," IEEE Journal on Quantum Electronics, vol. QE-22, pp. 1853-1869.

F. Capasso, K. Mohammed, A.Y. Cho, R. Hull, and A.L. Hutchinson (1985a), "Effective mass filtering: Giant quantum amplification of the photocurrent in a semiconductor superlattice," Applied Physics Letters, vol. 47, pp. 420-422.

F. Capasso, K. Mohammed, A.Y. Cho, R. Hull, and A.L. Hutchinson (1985b), "New quantum photoconductivity and large photocurrent gain by effective-mass filtering in a forward-biased superlattice p-n junction," Physical Review Letters, vol. 55, pp. 1152-1155.

F. Capasso and W.T. Tsang (1982), "Superlattice, graded band gap, channeling and staircase avalanche photodiodes towards a solid-state photomultiplier," IEDM Technical Digest, pp. 334-337.

F. Capasso, W.T. Tsang, A.L. Hutchinson, and P.W. Foy (1982), "The graded bandgap avalanche photodiode: A new molecular beam epitaxial structure with a large ionization rates ratio," Institute of Physics Conference Series, No. 63, pp. 473-478.

F. Capasso, W.T. Tsang, A.L. Hutchinson, and G.F. Williams (1982), "Enhancement of electron impact ionization in a superlattice: A new avalanche photodiode with a large ionization rate ratio," Applied Physics Letters, vol. 40, pp. 38-40.

F. Capasso, W.-T. Tsang, and G.F. Williams (1983), "Staircase solid-state photomultipliers and avalanche photodiodes with enhanced ionization rates ratio," IEEE Transactions on Electron Devices, vol. ED-30, pp. 381-390.

H.C. Casey, Jr. and M.B. Panish (1978), *Heterostructure Lasers,* Academic Press, New York.

P. Chakrabarti and B.B. Pal (1987), "Optical characteristics of a superlattice avalanche photodiode," Solid State Electronics, vol. 30, pp. 675-679.

R. Chin, N. Holonyak, Jr., G.E. Stillman, J.Y. Tang, and K. Hess (1980), "Impact ionisation in multilayered heterojunction structures," Electronics Letters, vol. 16, pp. 467-469.

L.C. Chiu, J.S. Smith, S. Margalit, and A. Yariv (1983), "Internal photoemission from quantum well heterojunction superlattices by phononless free-carrier absorption," Applied Physics Letters, vol. 43, pp. 331-332.

L.C. Chiu, J.S. Smith, S. Margalit, A. Yariv, and A.Y. Cho (1983), "Application of internal photoemission from quantum-well and heterojunction superlattices to infrared photodetectors," Infrared Physics, vol. 23, pp. 93-97.

K.K. Choi, B.F. Levine, C.G. Bethea, J. Walker, and R.J. Malik (1987), "Multiple quantum well 10 micron $GaAs/Al_xGa_{1-x}As$ infrared detector with improved responsivity," Applied Physics Letters, vol. 50, pp. 1814-1816.

K.K. Choi, B.F. Levine, R.J. Malik, J. Walker, and C.G. Bethea (1987), "Periodic negative conductance by sequential resonant tunneling through an expanding high-field superlattice domain," Physical Review B, vol. 35, pp. 4172-4175.

D.D. Coon, S.D. Gunapala, R.P.G. Karunasiri, and H.-M. Muehlhoff (1983), "Integrating infra-red detector with electronically modulated response," Electronics Letters, vol. 19, pp. 1070-1071.

D.D. Coon, S.D. Gunapala, R.P.G. Karunasiri, and H.-M. Muehlhoff (1984), "IR detection by depletion of trapped charge in localized impurity of an extrinsic semiconductor," International Journal of Infrared and Millimeter Waves, vol. 5, pp. 197-205.

D.D. Coon, S.D. Gunapala, R.P.G. Karunasiri, and H.-M. Muehlhoff (1985), "A high-sensitivity sampling IR detector," Infrared Physics, vol. 25, pp. 323-325.

D.D. Coon and R.P.G. Karunasiri (1983a), "Photoionization of impurity atoms in semiconductors in the presence of an applied electric field," Solid State Electronics, vol. 26, pp. 1151-1155.

D.D. Coon and R.P.G. Karunasiri (1983b), "Effect of electric fields on long-wavelength response of infra-red detectors," Electronics Letters, vol. 19, pp. 284-287.

D.D. Coon and R.P.G. Karunasiri (1984), "New mode of IR detection using quantum wells," Applied Physics Letters, vol. 45, pp. 649-651.

D.D. Coon, R.P.G. Karunasiri, and H.C. Liu (1986), "Fast response quantum well photodetectors," Journal of Applied Physics, vol. 60, pp. 2636-2638.

D.D. Coon, R.P.G. Karunasiri, and L.Z. Liu (1985), "Narrow band infrared detection in multiquantum well structures," Applied Physics Letters, vol. 47, pp. 289-291.

D.D. Coon and A.G.U. Perera (1986), "Spectral information coding by infrared photoreceptors," International Journal of Infrared and Millimeter Waves, vol. 7, pp. 1571-1583.

J. Conradi (1972), "The distribution of gains in uniformly multiplying avalanche photodiodes: Experimental," IEEE Transactions on Electron Devices, vol. ED-19, pp. 713-718.

P.N.J. Dennis (1986), *Photodetectors - An introduction to current technology,* Plenum, New York.

S.R. Dhariwal, V.N. Ojha, and G.P. Srivastava (1985), "On the shifting and broadening of impurity bands and their contribution to the effective electrical bandgap narrowing in moderately doped semiconductors," IEEE Transactions on Electron Devices, vol. ED-32, pp. 44-48.

C.T. Elliott (1981), "Infrared detectors," *Handbook on Semiconductors, vol. 4,* Ed. T.S. Moss, North Holland Publishing Company, Amsterdam, pp. 727-798.

L. Esaki, L.L. Chang, and E.E. Mendez (1981), "Polytype superlattices and multi-heterojunctions," Japanese Journal of Applied Physics, vol. 20, pp. L529-L532.

S.R. Forrest (1986), "Optical detectors: Three contenders" Spectrum, vol. 23, pp. 76-84 (May).

S.R. Forrest, O.K. Kim, and R.G. Smith (1982), "Optical response time of $In_{53}Ga_{47}As/InP$ avalanche photodiodes," Applied Physics Letters, vol. 41, pp. 95-98.

S.R. Forrest, G.F. Williams, O.K. Kim, and R.G. Smith (1981), "Excess-noise and receiver sensitivity measurements of $In_{53}Ga_{47}As/InP$ avalanche photodiodes," Electronics Letters, vol. 17, pp. 917-919.

A. Ghazali and J. Serre (1982), "Multiple-scattering approach to the formation of the impurity band in semiconductors," Physical Review Letters, vol. 48, pp. 886-889.

A. Gold, J. Serre, and A. Ghazali (1988), "Density of states in a two-dimensional electron gas: Impurity bands and band tails," Physical Review B, vol. 37, pp. 4589-4603.

K.W. Goossen, S.A. Lyon, and K. Alavi (1988a), "Photovoltaic quantum well infrared detector," Applied Physics Letters, vol. 52, pp. 1701-1703.

K.W. Goossen, S.A. Lyon, and K. Alavi (1988b), "Grating enhancement of quantum well detector response," Applied Physics Letters, vol. 53, pp. 1027-1029.

K.W. Goossen and S.A. Lyon (1985), "Grating enhanced quantum well detector," Applied Physics Letters, vol. 47, pp. 1257-1259.

K.W. Goossen and S.A. Lyon (1988), "Performance aspects of a quantum well detector," Journal of Applied Physics, vol. 63, pp. 5149-5153.

S.D. Gunapala and D.D. Coon (1988), "High-performance integrating infrared detector," Infrared Physics, vol. 28, pp. 61-65.

M.A. Green (1982), *Solar Cells,* Prentice Hall, Englewood Cliffs, N.J.

V. Hadek, J. Farhoomand, C.A. Beichman, D.M. Watson, and M.D. Jack (1985), "Extension of long wavelength response by modulation doping in extrinsic germanium infrared detectors," Applied Physics Letters, vol. 46, pp. 403-405.

W.S. Holden, J.C. Campbell, and A.G. Dentai (1985), "Gain uniformity of InP/InGaAsP/InGaAs avalanche photodiodes with separate absorption, grading, and multiplication regions," IEEE Journal of Quantum Electronics, vol. QE-21, pp. 1310-1313.

Z. Ikonic, V. Milanovic, and D. Tjapkin (1988), "On the design of tunable quantum well infrared photodetectors," Solid State Electronics, vol. 31, pp. 1447-1449.

B. Jenson (1978), "The infrared absorption spectrum of n-type GaAs," Physica Status Solidi B, vol. 86, pp. 291-301.

Y.K. Jhee, J.C. Campbell, W.S. Holden, A.G. Dentai, and J.K. Plourde (1985), "The effect of nonuniform gain on the multiplication noise of InP/InGaAsP/InGaAs avalanche photodiodes," IEEE Journal of Quantum Electronics, vol. QE-21, pp. 1858-1861.

F.-Y. Juang, U. Das, Y. Nashimoto, and P.K. Bhattacharya (1985), "Electron and hole impact ionization coefficients in GaAs—$Al_xGa_{1-x}As$ superlattices," Applied Physics Letters, vol. 47, pp. 972-974.

E.O. Kane (1959), "Zener tunneling in semiconductors," Journal of Physics and Chemistry of Solids, vol. 12, pp. 181-188.

E.O. Kane (1961), "Theory of tunneling," Journal of Applied Physics, vol. 32, pp. 83-91.

E.O. Kane (1963), "Thomas-Fermi approach to impure semiconductor band structure," Physical Review, vol. 131, pp. 79-88.

E.O. Kane (1985), "Band tails in semiconductors," Solid State Electronics, vol. 28, pp. 3-10.

A. Kastalsky, T. Duffield, S.J. Allen, and J. Harbison (1988), "Photovoltaic detection of infrared light in a GaAs/AlGaAs superlattice," Applied Physics Letters, vol. 52, pp. 1320-1322.

O.K. Kim, S.R. Forrest, W.A. Bonner, and R.G. Smith (1981), "A high gain $In_{.53}Ga_{.47}As/InP$ avalanche photodiode with no tunneling leakage current," Applied Physics Letters, vol. 39, pp. 402-404.

W. Kohn (1957), "Shallow impurity states in silicon and germanium," Solid State Physics, vol. 5, pp. 258-321.

S.V. Kozyrev and A.Ya. Shik (1985), "Capture of carriers by quantum wells in heterostructures," Soviet Physics-Semiconductors, vol. 19, pp. 1024-1025.

P.W. Kruse, L.D. McGlauchlin, and R.B. McQuistan (1962), *Elements of Infrared Technology: Generation, Transmission and Detection,* John Wiley, New York.

P.W. Kruse (1977), "The photon detection process," *Topics in Applied Physics, vol. 19,* Ed. R.J. Keyes, Springer Verlag, Berlin, pp. 5-69.

S.R. Kurtz, R.M. Biefeld, L.R. Dawson, I.J. Fritz, and T.E. Zipperian (1988), "High photoconductive gain in lateral InAsSb strained-layer superlattice infrared detectors," Applied Physics Letters, vol. 53, pp. 1961-1963.

S.R. Kurtz, L.R. Dawson, T.E. Zipperian, and S.R. Lee (1988), "Demonstration of an InAsSb strained-layer superlattice photodiode," Applied Physics Letters, vol. 52, pp. 1581-1583.

S.R. Kurtz, G.C. Osbourn, R.M. Biefeld, L.R. Dawson, and H.J. Stein (1988), "Extended infrared response of InAsSb strained-layer superlattices," Applied Physics Letters, vol. 52, pp. 831-833.

S.R. Kurtz, G.C. Osbourn, R.M. Biefeld, and S.R. Lee (1988), "Photoluminescence and the band structure of InAsSb strained-layer superlattices," Applied Physics Letters, vol. 53, pp. 216-218.

M. Lax (1956), "The influence of lattice vibrations on electronic transitions in solids," *Photoconductivity Conference,* Ed. R.G. Breckenbridge, John Wiley, New York, pp. 111-145.

M. Lax (1959), "Giant traps," Journal of Physics and Chemistry of Solids, vol. 8, pp. 66-73.

M. Lax (1960), "Cascade capture of electrons in solids," Physical Review, vol. 119, pp. 1502-1523.

D.S. Lee and J.G. Fossum (1983), "Energy-band distortion in highly doped silicon," IEEE Transactions on Electron Devices, vol. ED-30, pp. 626-634.

T.F. Lee and T.C. McGill (1975), "Variation of impurity-to-band activation energies with impurity density," Journal of Applied Physics, vol. 46, pp. 373-380.

B.F. Levine, C.G. Bethea, K.K. Choi, J. Walker, and R.J. Malik (1988), "Tunneling lifetime broadening of the quantum well intersubband photoconductivity spectrum," Applied Physics Letters, vol. 53, pp. 231-233.

B.F. Levine, K.K. Choi, C.G. Bethea, J. Walker, and R.J. Malik (1987a), "Quantum well avalanche multiplication initiated by 10 μm intersubband absorption and photoexcited tunneling," Applied Physics Letters, vol. 51, pp. 934-936.

B.F. Levine, K.K. Choi, C.G. Bethea, J. Walker, and R.J. Malik (1987b), "New 10 μm infrared detector using intersubband absorption in resonant tunneling GaAsAs superlattices," Applied Physics Letters, vol. 50, pp. 1092-1094.

B.F. Levine, R.J. Malik, J. Walker, K.K. Choi, C.G. Bethea (1987), D.A. Kleinman, and J.M. Vandenberg, "Strong 8.2 μm infrared intersubband absorption in doped GaAs/AlAs quantum well waveguides," Applied Physics Letters, vol. 50, pp. 273-275.

B.F. Levine, C.G. Bethea, G. Hasnain, J. Walker, and R.J. Malik (1988), "High-detectivity $D^* = 1.0 \times 10^{10}$ cmHz$^{1/2}$/W GaAs/AlGaAs multiquantum well λ=8.3μm infrared detector," Applied Physics Letters, vol. 53, pp. 296-298.

N. Lifshitz, A. Jayaraman, R.A. Logan, and H.C. Card (1980), "Pressure and compositional dependences of the Hall coefficient in $Al_xGa_{1-x}As$ and their significance," Physical Review B, vol. 21, pp. 670-678.

D. Long (1977), "Optical and infrared detectors," *Topics in Applied Physics, vol. 19,* Ed. R.J. Keyes, Springer Verlag, Berlin, pp. 101-147.

G.D. Mahan (1980), "Energy gap in Si and Ge: Impurity dependence," Journal of Applied Physics, vol. 51, pp. 2634-2646.

R.J. McIntyre (1966), "Multiplication noise in uniform avalanche diodes," IEEE Transactions on Electron Devices, vol. ED-13, pp. 164-168.

R.J. McIntyre (1972), "The distribution of gains in uniformly multiplying avalanche photodiodes: Theory," IEEE Transactions on Electron Devices, vol. ED-19, pp. 703-713.

A.F. Milton (1977), "Optical and infrared detectors," *Topics in Applied Physics, vol. 19,* Ed. R.J. Keyes, Springer Verlag, Berlin, pp. 197-228.

T.N. Morgan (1965), "Broadening of impurity bands in heavily doped semiconductors," Physical Review, vol. 139, pp. A343-A348.

T.S. Moss (1959), *Optical Properties of Semiconductors,* Academic Press, New York.

R.D. Nelson (1974), "Accumulation-mode charge-coupled device," Applied Physics Letters, vol. 25, pp. 568-570.

K. Nishida, K. Taguchi, and Y. Matsumoto (1979), "InGaAsP heterostructure avalanche photodiodes with high avalanche gain," Applied Physics Letters, vol. 35, pp. 251-253.

P. Norton (1976), "Photoconductivity from shallow negative donor ions in silicon: A new far-infrared detector," Journal of Applied Physics, vol. 47, pp. 308-320.

G.C. Osbourn (1984), "InAsSb strained-layer superlattices for long wavelength detector applications," Journal of Vacuum Science and Technology, vol. B2, pp. 176-178.

G.C. Osbourn, L.R. Dawson, R.M. Biefeld, T.E. Zipperian, I.J. Fritz, and B.L. Doyle (1987), "III-V strained layer superlattices for long-wavelength detector applications: Recent progress," Journal of Vacuum Science and Technology, vol. A5, pp. 3150-3152.

A. Otto (1968), "Excitation of nonradiative surface plasma waves in silver by the method of frustrated total reflection," Zeitschrift fur Physik, vol. 216, pp. 398-410.

J.I. Pankove (1971), *Optical Processes in Semiconductors,* Dover, New York.

M.D. Petroff and M.G. Stapelbroek (1984), "Responsivity and noise models of blocked impurity band detectors," IRA-IRIS Specialty group on IR Detectors, Meeting in Seattle, Wash., vol. 2, pp 43-61 (August).

M.D. Petroff and M.G. Stapelbroek (1986), "Blocked impurity band detectors," US Patent No. 4,568,960 (4 February 1986).

M.D. Petroff, M.G. Stapelbroek, and W.A. Kleinhans (1987), "Detection of individual .4-28 μm wavelength photons via impurity-impact ionization in a solid state photomultiplier," Applied Physics Letters, vol. 51, pp. 406-408.

A. Piotrowska, A. Guivarc'h, and B. Pelous (1983), "Ohmic Contacts to III-V Compound Semiconductors: A review of fabrication techniques," Solid State Electronics, vol. 26, pp. 179-197.

E.H. Putley (1960), "Impurity photoconductivity in n-type InSb," Proceedings of the Physical Society (London), vol. 76, 802-805.

E.H. Putley (1964), "Far infra-red photoconductivity," Physica Status Solidi, vol. 6, pp. 571-614.

E.H. Putley (1977), "InSb submillimeter photoconductive detectors," *Semiconductors and Semimetals, vol. 12,* Eds. R.K. Willardson and A.C. Beer, Academic Press, New York, pp. 143-168.

S. Ramo, J.R. Whinnery, and T. van Duzer (1965), *Fields and Waves in Communications Electronics,* John Wiley and Sons, New York.

R.A. Reynolds, M.J. Brau, H. Kraus, and R.T. Bate (1969), "Mixed Conduction in $Hg_{1-x}Cd_xTe$ having a bandgap near 0.1 eV (x=0.20 to 0.21)," *Proceedings of the Third International Conference on Photoconductivity,* Ed. E.M. Pell, Pergammon Press, New York, pp. 511-521.

V.L. Rideout (1975), "A review of the theory and technology for ohmic contacts to group III-V compound semiconductors," Solid State Electronics, vol. 18, pp. 541-550.

A. Rose (1963), *Concepts in Photoconductivity and Allied Problems,* Interscience Publishers, New York.

C.L. Roy (1986), "Carrier concentrations in impure semiconductors in the presence of an electric field," Journal of Physics and Chemistry of Solids, vol. 47, pp. 375-379.

N.S. Rytova (1967), "Resonance absorption of electromagnetic waves in a thin film," Soviet Physics-Solid State, vol. 8, pp. 2136-2140.

D.K. Schroder and D.L. Meier (1984), "Solar cell contact resistance - A review," IEEE Transactions on Electron Devices, vol. ED-31, pp. 637-647.

D.H. Seib and L.W. Aukerman (1973), "Photodetectors for the .1 to 1. micrometer spectral region," *Advances in Electronics and Electron Physics, vol. 34,* Ed. L. Marton, Academic Press, New York, 95-221.

J. Serre and A. Ghazali (1983), "From band tailing to impurity-band formation and discussion of localization in doped semiconductors: A multiple-scattering approach," Physical Review B, vol. 28, pp. 4704-4715.

A.Ya. Shik (1969), "Anisotropy of the high frequency conductivity of size-quantized films," Soviet Physics JETP, vol. 29, pp. 931-933.

A.Ya. Shik (1973), "Optical properties of semiconductor superlattices with complex band structures," Soviet Physics-Semiconductors, vol. 6, pp. 1110-1117.

A.Ya. Shik (1975), "Superlattices - periodic semiconductor structures (review)," Soviet Physics-Semiconductors, vol. 8, pp. 1195-1209.

A.Ya. Shik (1986), "Intraband photoconductivity of quantum-well heterostructures," Soviet Physics-Semiconductors, vol. 20, pp. 1002-1006.

F. Sibille (1986), "Infrared detection and imaging," Reports on the Progress in Physics, vol. 49, pp. 1197-1242.

J.S. Smith, L.C. Chiu, S. Margalit, A. Yariv, and A.Y. Cho (1983), "A new infrared detector using electron emission from multiple quantum wells," Journal of Vacuum Science and Technology, vol. B1, pp. 376-378.

R.A. Smith (1978), *Semiconductors,* 2nd. ed., Cambridge University Press, Cambridge.

G.E. Stillman, V.M. Robbins, and N. Tabatabaie (1984), "III-V compound semiconductor devices: Optical detectors," IEEE Transactions on Electron Devices, vol. ED-31, pp. 1643-1655.

G.E. Stillman, C.M. Wolfe, and J.O. Dimmock (1977), "Far infrared photoconductivity in high purity GaAs," *Semiconductors and Semimetals, vol. 12,* Eds. R.K. Willardson and A.C. Beer, Academic Press, New York, pp. 169-290.

C.J. Summers and K.F. Brennan (1987), "New resonant tunneling superlattice avalanche photodiode device structure for long-wavelength infrared detection," Applied Physics Letters, vol. 51, pp. 276-278.

N. Susa, H. Nakagome, O. Mikami, H. Ando, and H. Kanbe (1980), "New InGaAs/InP avalanche photodiode structure for the 1-1.6 micron wavelength region," IEEE Journal of Quantum Electronics, vol. QE-16, pp. 864-869.

S.M. Sze (1981), *Physics of Semiconductor Devices,* 2nd ed., Wiley Interscience, New York.

F. Szmulowicz and F.L. Madarsz (1987), "Blocked impurity band detectors - An analytical model: Figures of merit," Journal of Applied Physics, vol. 62, pp. 2533-2540.

M.C. Teich, K. Matsuo, and B.E.A. Saleh (1986), "Excess noise factors for conventional and superlattice avalanche photodiodes and photomultiplier tubes," IEEE Journal of Quantum Electronics, vol. QE-22, pp. 1184-1193.

G.A. Thomas, M. Capizzi, F. DeRosa, R.N. Bhatt and T.M. Rice (1981), "Optical study of interacting donors in semiconductors," Physical Review B, vol. 23, pp. 5472-5494.

A. van der Ziel (1976), *Noise in Measurements,* Wiley Interscience, New York.

K.M. van Vliet (1958), "Noise in semiconductors and photoconductors," Proceedings of the IRE, vol. 46, pp. 1004-1018.

K.M. van Vliet (1967), "Noise limitation in solid state photodetectors," Applied Optics, vol. 6, pp. 1145-1169.

K.M. van Vliet and J.R. Fassett (1965), "Fluctuations due to electronic transitions and transport in solids," *Fluctuation Phenomena in Solids,* Ed. R.E. Burgess, Academic Press, New York, pp. 267-354.

G.A. Walter and E.L. Dereniak (1986a), "Photodetectors for focal plane arrays. Part 1: Extrinsic silicon," Laser Focus/Electro-Optics, vol. 22, pp. 108-118 (March).

G.A. Walter and E.L. Dereniak (1986b), "Photodetectors for focal plane arrays. Part 2: HgCdTe," Laser Focus/Electro-Optics, vol. 22, pp. 86-96 (April).

J-Q. Wang, P.L. Richards, J.W. Beeman, N.M. Haegel, and E.E. Haller (1986), "Optical efficiency of far-infrared photoconductors," Applied Optics, vol. 25, pp. 4127-4134.

M.O. Watanabe and H. Maeda (1984), "Electron activation energy in Si-doped AlGaAs grown by MBE," Japanese Journal of Applied Physics, vol. 23, pp. L734-L736.

D.M. Watson and J.E. Huffman (1988), "Germanium blocked-impurity-band far-infrared detectors," Applied Physics Letters, vol. 52, pp. 1602-1604.

P.P. Webb, R.J. McIntyre, and J. Conradi (1974), "Properties of avalanche photodiodes," RCA Review, vol. 35, pp. 234-278.

P.E. Welsh and R.J. Schwartz (1988), "Final Report on NASA Grant NAG 3-433. Solar energy conversion through the interaction of plasmons with tunnel junctions. Part A Solar cell analysis. Part B Photoconductor analysis." Technical Report TR-EE 88-37, Purdue University (July).

L.C. West and S.J. Eglash (1985), "First observation of an extremely large-dipole infrared transition within the conduction band of a GaAs quantum well," Applied Physics Letters, vol. 46, pp. 1156-1158.

Z. Wiley (1975), "Transport in III-V semiconductors," *Semiconductors and Semimetals, vol. 10,* Eds. R.K. Willardson and A.C. Beer, Academic Press, New York, pp. 91.

G.F. Williams, F. Capasso, and W.T. Tsang (1982), "The graded bandgap multilayer avalanche photodiode: A new low-noise detector," IEEE Electron Device Letters, vol. EDL-3, pp. 71-73.

C-L. Yang and D-S. Pan (1988), "Intersubband absorption of silicon-based quantum wells for infrared imaging," Journal of Applied Physics, vol. 64, pp. 1573-1575.

C-L. Yang, D-S. Pan, and R. Somoano (1989), "Advantages of an indirect semiconductor quantum well system for infrared detection," Journal of Applied Physics, vol. 65, pp. 3253-3258.

J.J. Yang, W.I. Simpson, and L.A. Moudy (1982), "Electrical properties of Zn in metalorganic chemical vapor deposition $Ga_{(1-x)}Al_xAs$," Journal of Applied Physics, vol. 53, pp. 771-773.

T. Yao, S. Matsui, H. Nagase, and K. Ishida (1985), "Comparative study of the binding energy of shallow impurities in GaAs/AlAs superlattices and AlGaAs mixed alloys," Institute of Physics Conference Series, vol. 79, pp. 469-474.

S.Y. Yuen (1983), "Fast relaxing absorptive nonlinear refraction in superlattices," Applied Physics Letters, vol. 43, pp. 813-815.

J.M. Ziman (1964), *Principles of the Theory of Solids,* Cambridge University Press, London.

APPENDICES

Appendix A.

Survey of the competing photodetectors

A.1 Introduction

This chapter surveys the literature on some of the devices which have been proposed to compete with conventional photodetectors. These novel devices are not described in depth. Only the basic physical processes are described. The pertinent experimental results are listed (if there are any) and possible problems and advantages are presented. A set of references accompanies each section.

These proposed photodetectors can be grouped under two different areas - 1) photoconductors and pin photodiodes and 2) avalanche photodiodes. For simplicity photoconductors and pin photodiodes have been merged into one area because only one proposed detector resembles a photodiode.

The conventional pin photodiode has the best combination of low noise and a large bandwidth [Forrest 1986]. Due to these inherent advantages and its simple design, the pin photodiode is the most common of the three [Forrest 1986]. At long wavelengths though, the pin photodiode has some serious limits because of the narrow gap materials problems. The strained-layer superlattice photodiode described in sec. A.2.13 can be considered in many ways a novel photodiode for infrared wavelengths.

There have been several novel one carrier photoconductors that, like the PEIR photoconductor, attempt to compete with the conventional photoconductors. These novel photoconductors, along with the conventional photoconductors, the submillimeter photoconductor, the two carrier effective mass filter intersubband photoconductor, and the strained-layer superlattice photodetectors, are described in sec. A.2.

Many publications have described novel devices designed to replace the APD. This is due to the avalanching and the associated problems of excess noise. The small band gap requirement for long wavelengths limits these new devices to wavelengths less than 7 microns unless there is an improvement in HgCdTe fabrication. The important problems, considerations and alternative devices are presented in sec. A.3.

Section A.4 lists the novel devices which are most promising. The PEIR photoconductor is then compared directly with the blocked impurity band (BIB) photodetector, which appears to be one of the best (if not the best) of the novel photodetectors which have been proposed.

A.2 Conventional and novel photoconductors

The PEIR photoconductor, the submillimeter photoconductor and the novel photoconductors presented below are in essence extrinsic photoconductors (except the two carrier effective mass filter intersubband photoconductor). The main advantage of the proposed detectors is the same as the extrinsic photoconductor - they avoid using HgCdTe (See sec. 1.2). The main advantage of the proposed detectors over the extrinsic photoconductor is absorption. The absorption coefficients in these devices have been proposed to be from 10^4 cm^{-1} to 10^6 cm^{-1}. Hence, they could have a high absorption coefficient and use materials with relatively desirable properties (compared to HgCdTe).

Section A.2.1 briefly describes the conventional photoconductors. Section A.2.2 briefly describes the submillimeter photoconductor. The proposed photoconductors (and photodiode) are briefly described in secs. A.2.3 to A.2.13. The noise in all these devices is the same as in a conventional photoconductor except the strained-layer superlattice photodiode, which should have the same noise characteristics as in a conventional photodiode.

A.2.1 Conventional photoconductors

There are two conventional photoconductors. The first is the intrinsic photoconductor and is described in sec. A.2.1.1. The second is the extrinsic photoconductor and is described in sec. A.2.1.2. The advantages and disadvantages of both these photodetectors are described in sec. A.2.1.3.

A.2.1.1 Intrinsic photoconductor

The intrinsic photoconductor is shown in Fig. A.1. Intrinsic means that the absorption is valence band to conduction band absorption and doesn't have anything to do with doping (most intrinsic photoconductors are doped). To operate the device, the radiation is directed into the photoconductor and excites an electron from the valence band to the conduction band. The change in the carrier concentration changes the resistance which changes the output signal. The carriers either recombine through recombination centers or when the minority carriers reach the contact (this is known as the sweepout effect).

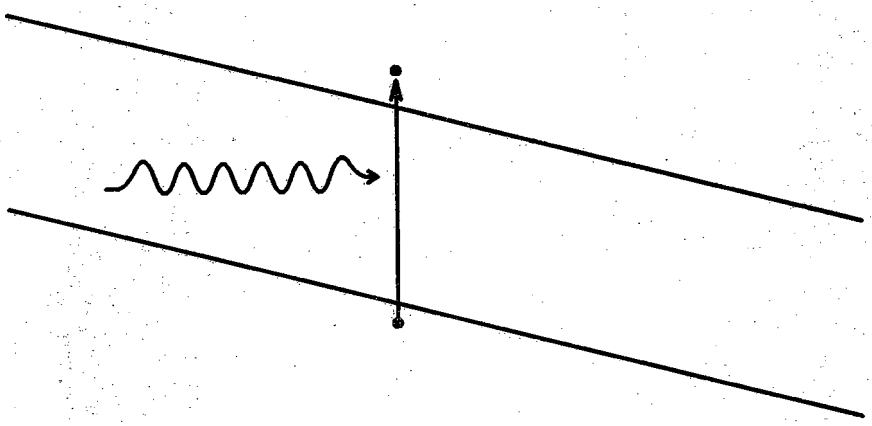

Figure A.1 Intrinsic photoconductor

A.2.1.2 Extrinsic photoconductor

The extrinsic photoconductor is shown in Fig. A.2. Extrinsic means that the absorption is from a dopant level to the conduction (n-type) or valence (p-type) band. To operate the device, the radiation is directed into the photoconductor and excites an electron (hole) from the donor (acceptor) level to the conduction (valence) band. The change in the carrier concentration changes the resistance which changes the output signal. The carriers recombine through the excited dopant states [Lax 1959; Lax 1960].

A.2.1.3 Advantages and disadvantages of conventional photoconductors

The intrinsic photoconductor has a very large absorption coefficient ($>10^4 cm^{-1}$), which is the primary prerequisite for making a good photoconductor. The problem with the intrinsic photoconductor is that for wavelengths longer than 7 μm, the band gap becomes very narrow. Hence, there are only two materials suitable for use as an intrinsic photoconductor - HgCdTe and the lead salts. HgCdTe is undesirable because of the serious fabrication difficulties encountered when using Hg. The lead salts have a large dielectric relaxation time. Due to these materials problems, extrinsic photoconductors begin to compete favorably with intrinsic photoconductors when the wavelength to be detected is longer than 7 μm.

The major advantage of the extrinsic photoconductor is that the material is stable which means that an array with a uniform response can be fabricated much easier than an array with HgCdTe. The problem with the extrinsic photoconductor is the low absorption coefficient ($\simeq 10^2$ cm^{-1} [Elliott 1981]). The inherent problems associated with a low absorption coefficient are 1) lower operating temperatures [Blouke, Burgett, & Williams 1973; Elliott 1981; Long 1977] (See app. B), 2) lower quantum efficiencies [Long 1977], and 3) optical crosstalk problems [Sibille, 1986].

A.2.2 Submillimeter photoconductor

The free carrier absorption photoconductor, otherwise known as the submillimeter photoconductive detector [Putley 1977], is shown in Fig. A.3. This device was first experimentally verified in 1960 [Putley 1960]. To operate the device, radiation enters the device. Through free carrier absorption, the electron is excited into a higher part of the conduction band (n-type device). This excitation produces a change in the carrier distribution as a function of energy. Since mobility and in turn, conductivity are energy dependent, the

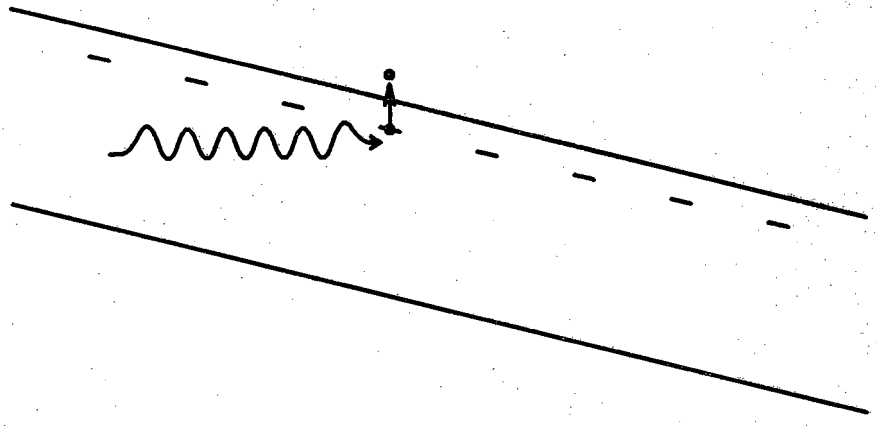

Figure A.2 Extrinsic photoconductor

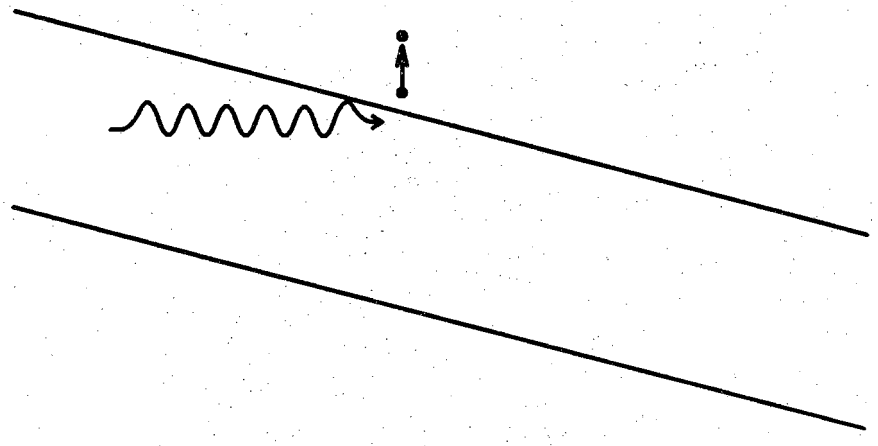

Figure A.3 Submillimeter photoconductor

current depends upon the radiation intensity [Putley 1977]. The major problem with this device is that the free carrier concentration must be small to limit the dark current. Since free carrier absorption is proportional to the free carrier concentration times the wavelength squared, this device will work if the wavelength becomes long enough. Unfortunately, the wavelengths to be detected in a submillimeter photoconductor must be greater than 100 μm.

A.2.3 Blocked impurity band (BIB) detector

The blocked impurity band (BIB) detector [Petroff & Stapelbroek 1986; Petroff & Stapelbroek 1984; Walter & Dereniak 1986a; Szmulowicz & Madarsz 1987; Hadek, Farhoomand, Beichman, Watson, & Jack 1985; Watson & Huffman 1988] is shown in Fig. A.4 (unbiased) and Fig. A.5 (biased). It was conceived in 1977 [Szmulowicz & Madarsz 1987; Petroff & Stapelbroek 1986] and experimentally verified in 1978 [Szmulowicz & Madarsz 1987; Petroff & Stapelbroek 1986]. It can be considered the best of the novel photodetectors and for this reason, it is compared with the PEIR photoconductor in sec. A.4.2.

A BIB detector is made up of two layers. The first layer is the impurity band layer. The second layer is a blocking layer which blocks conduction in the impurity band. Unlike an extrinsic photoconductor, where the dopant concentration must be less than the amount that will form an impurity band [Bratt 1977], the dopant concentration in the impurity band layer in a BIB detector is not similarly limited because of the blocking layer. The blocking layer has the same purpose as the blocking layer in a PEIR photoconductor.

For the device to operate, it is assumed that the radiation or thermal generation rate is small enough that the carrier concentration in the conduction band (in an n-type device) is smaller than the compensation dopant concentration (See chap. 2). Due to the low temperature of operation, the compensation dopants will be ionized. The impurity band layer will contain a concentration of ionized impurity band dopants that will be equal to this compensation dopant concentration.

Several possible modes of operation of a BIB detector have been considered but this discussion only considers the mode shown in Fig. A.5. As a potential is applied across the device, the ionized impurities in the impurity band will begin to drift towards the cathode. The impurities remain in the same location, but electrons can easily flow from one impurity atom to an ionized impurity atom, producing the effect of an ionized impurity moving towards the anode. The only space charge remaining in the device will be the ionized compensation dopants (excluding electron accumulation in an n-type impurity band (See chap. 2)).

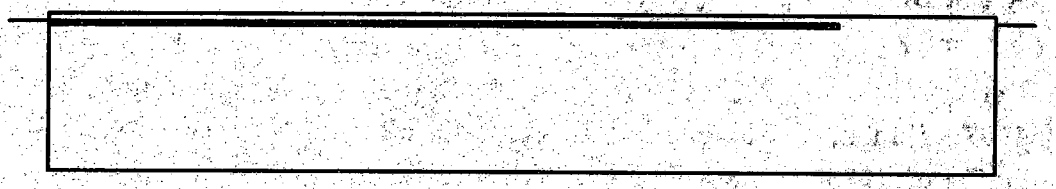

Figure A.4 The BIB detector - unbiased

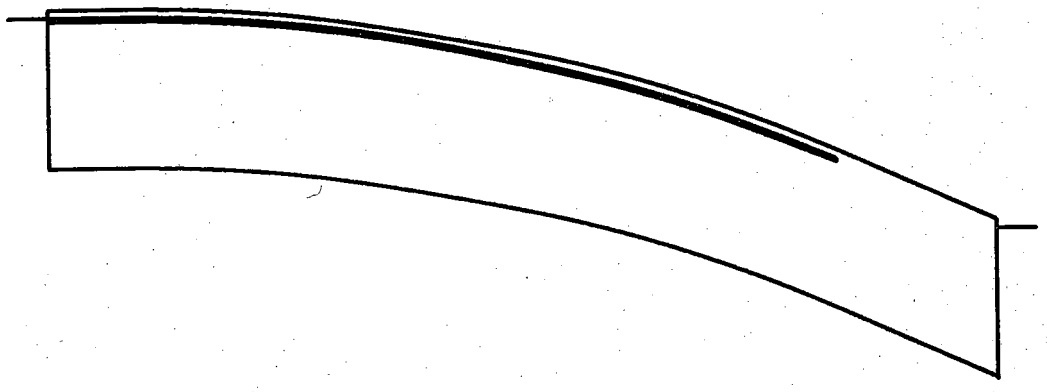

Figure A.5 The BIB detector - biased

These ionized compensation impurities produce a variation of the electric field throughout the device.

The operation of the device is straightforward. The radiation enters the device and excites an electron from the donor band to the conduction band. The electron drifts towards the anode (the right contact in Fig. A.5) while the ionized donor drifts towards the cathode. Since the temperature of operation is low enough to make the cathode a blocking contact to the electrons, electrons recombine with the ionized donors at the cathode.

The variation of the electric field in the impurity band layer is a detriment in a BIB detector. The electric field in the impurity band layer varies from 0 V/cm at some point in the impurity band layer to a maximum value at the impurity band layer-blocking layer interface. This maximum value is defined as ξ_d. The depletion region in a BIB detector is the region between the point where the electric field is almost 0 V/cm to the end of the impurity band layer where the electric field is ξ_d. This depletion region is the active region of the device and as the active region thickness decreases, the percentage of radiation collected can decrease substantially. Consequently, the depletion region should be as wide as possible.

Unfortunately, ξ_d is limited by either thermal-field emission ionization or tunneling-field emission ionization (See sec. 1.4.4 and app. F). The important relationship in this limitation is that as $(E_C - E_D)_{min}$ decreases (either through widening of the impurity band or through the band moving closer to the conduction band (n-type) (See Fig. 1.5)) ξ_d and in turn, the depletion region width must decrease. Consequently, 1) the longer the wavelength to be detected, the more difficult it is to build a BIB detector and 2) the absorption coefficient will be limited because of this limit on the energy width of the impurity band, B_I.

A.2.4 SuperLattice Intraband-absorption Photodetector (SLIP)

The SuperLattice Intraband-absorption Photodetector (SLIP) was first proposed in 1988 [Welsh & Schwartz 1988]. The only experimental study published has been on the graded well SLIP discussed in the next section. As will be shown below, the graded well SLIP is a variation of one of the five possible modes in the SLIP.

The SLIP incorporates a superlattice made up of quantum wells and barriers (See Fig. A.6 and Fig. A.7). The wells contain a large amount of free carriers and the barriers have a minimal amount of free carriers. Consequently,

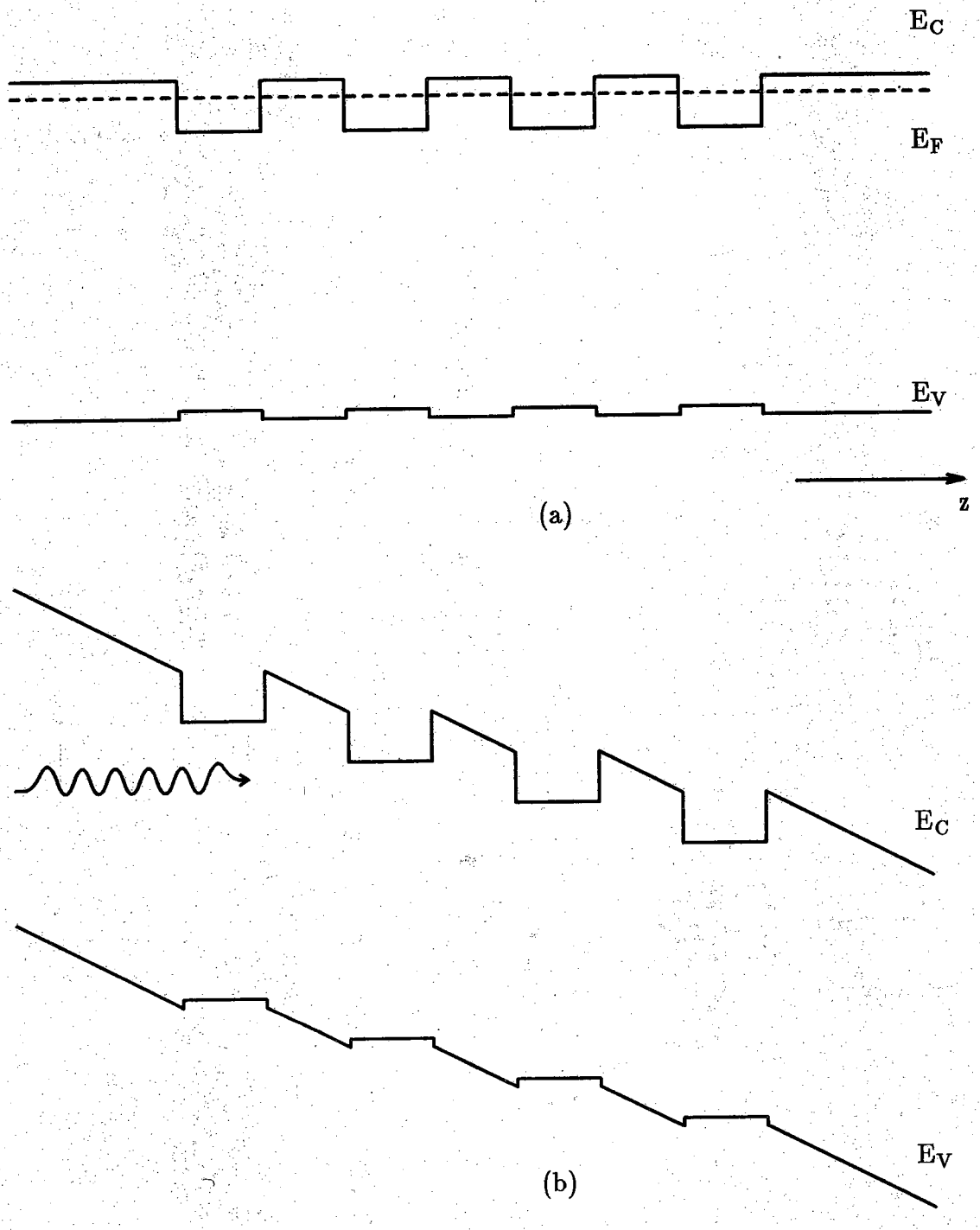

Figure A.6 The SLIP. (a) Unbiased. (b) Biased.

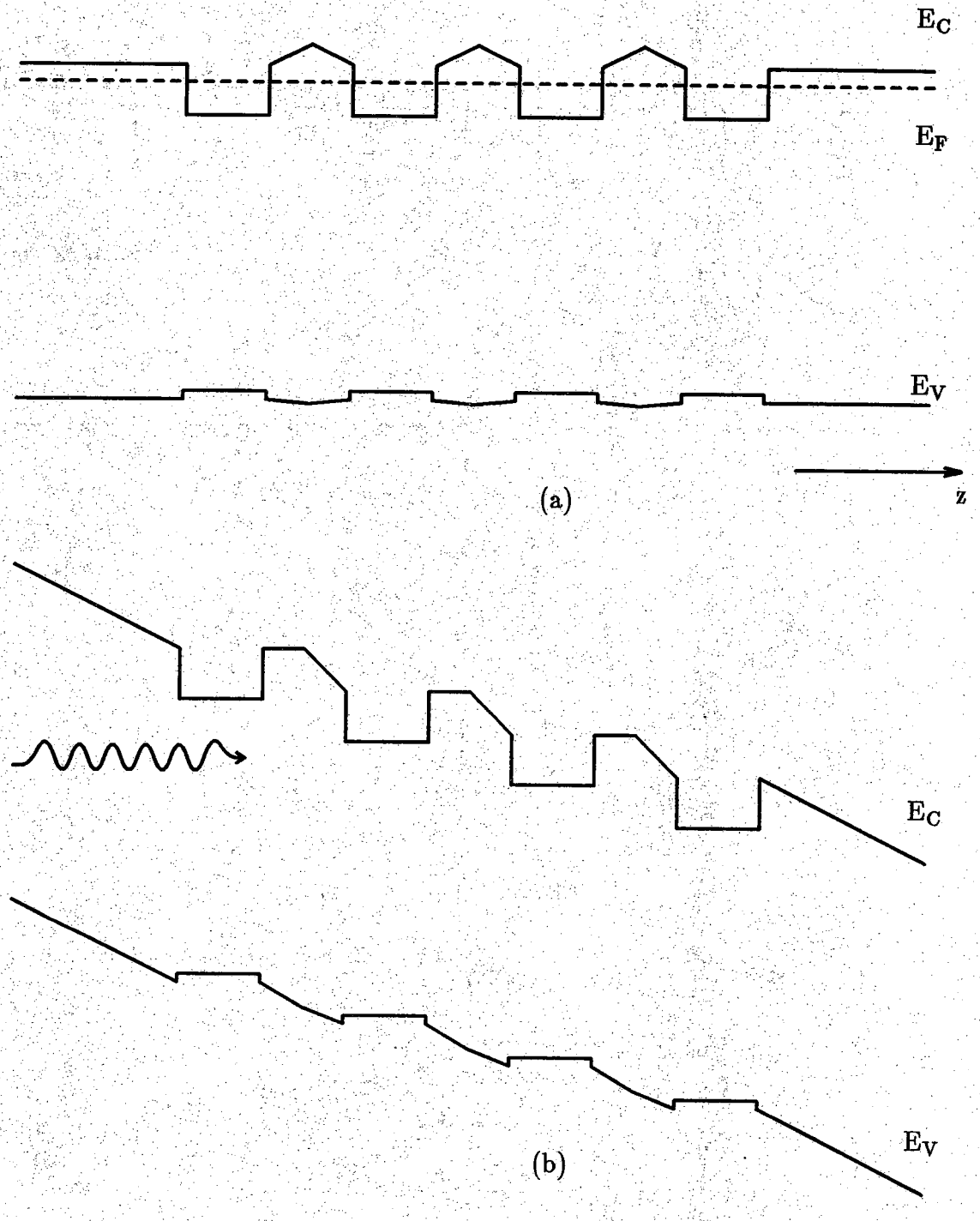

Figure A.7 The SLIP which prevents tunneling. (a) Unbiased. (b) Biased.

the applied electric field will be much larger in the barriers than in the quantum wells. Radiation enters the device and through intraband-absorption (free carrier absorption - FCA) excites the carriers in the wells to energies greater than the barrier height. These carriers have a probability (which equals the quantum efficiency) of surmounting the barrier height and being swept by the electric field through the barrier region (See Fig. A.8).

The SLIP operates like an extrinsic photoconductor, where the analog of the donor levels are the total free carrier energy levels less than the barrier height energy level (The carrier cannot escape out of the well without excitation) and the analog of the conduction band energy levels are the total free carrier energy levels above the barrier height energy level. Since it has been calculated to be rather easy for the carrier to get trapped in a well, the SLIP should be as fast as a conventional photoconductor.

The location of the Fermi level in the quantum well in the SLIP can be separated into two cases. One is the partly closed well case and the other is the open well case. For the partly closed well case (See Fig. A.9), $E_{Cb}-E_F$ (See Fig. A.8) is less than the optical and intervalley phonon energies. For the open well case (See Fig. A.10), $E_{Cb}-E_F$ is greater than the optical and intervalley phonon energies.

There are five modes of operation. The partly closed well case has three different modes (See Fig. A.9): 1) the radiation can be incident perpendicular to the device layers, 2) the radiation can be incident parallel to the device layers, and 3) the radiation can be incident at an oblique angle to the device layers. All should have high efficiencies. The temperature of operation will have to be around 10 K. The open well case has the other two modes (See Fig. A.10): 1) the radiation can be incident parallel to the device layers and 2) the radiation can be incident at an oblique angle to the device layers. The temperature of operation in the open well case can be higher than the partly closed well case (due to thermionic emission), but the efficiency will be lower.

The materials used in this system can be either a system like GaAs-$Al_xGa_{1-x}As$ or a superlattice that has alternating layers of a degenerately doped and a lightly doped semiconductor of the *same* material. This second possibility can occur if the conduction band in the degenerately doped semiconductor decreases faster than the Fermi level in the degenerately doped semiconductor increases with respect to the conduction band in the degenerately doped semiconductor [Mahan 1980]. If this were the case, the barrier will be the lightly doped semiconductor.

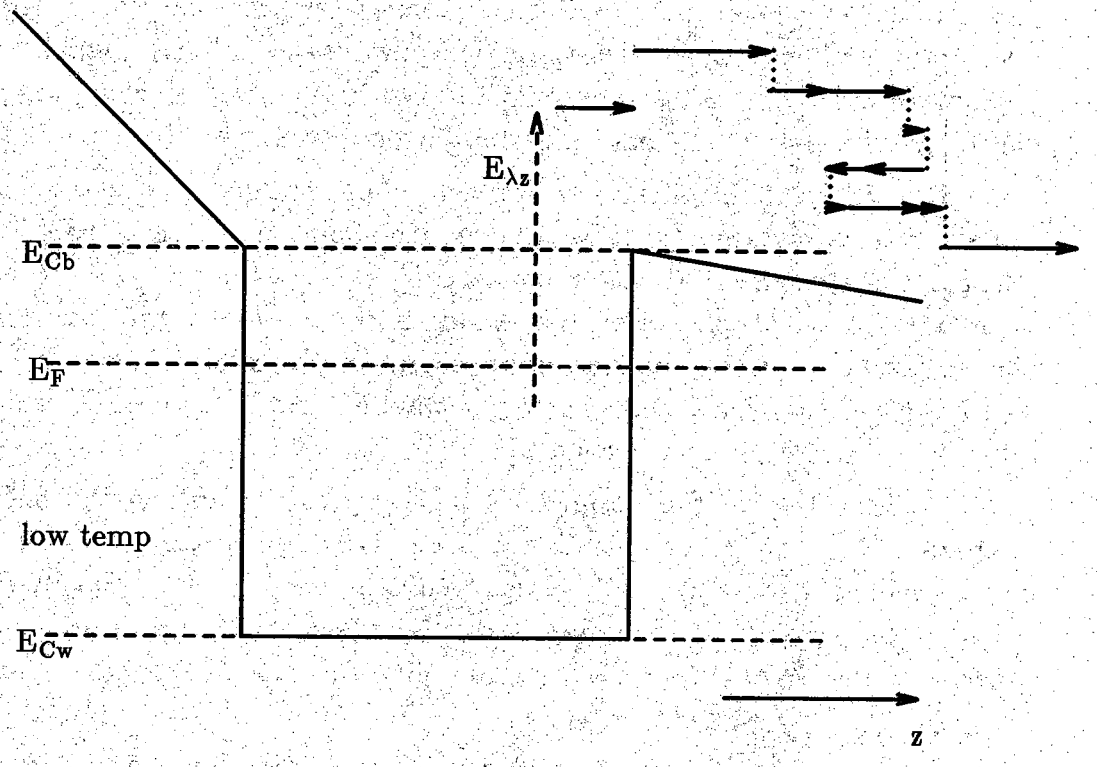

Figure A.8 Trajectory of an electron excited by a photon with energy E_λ

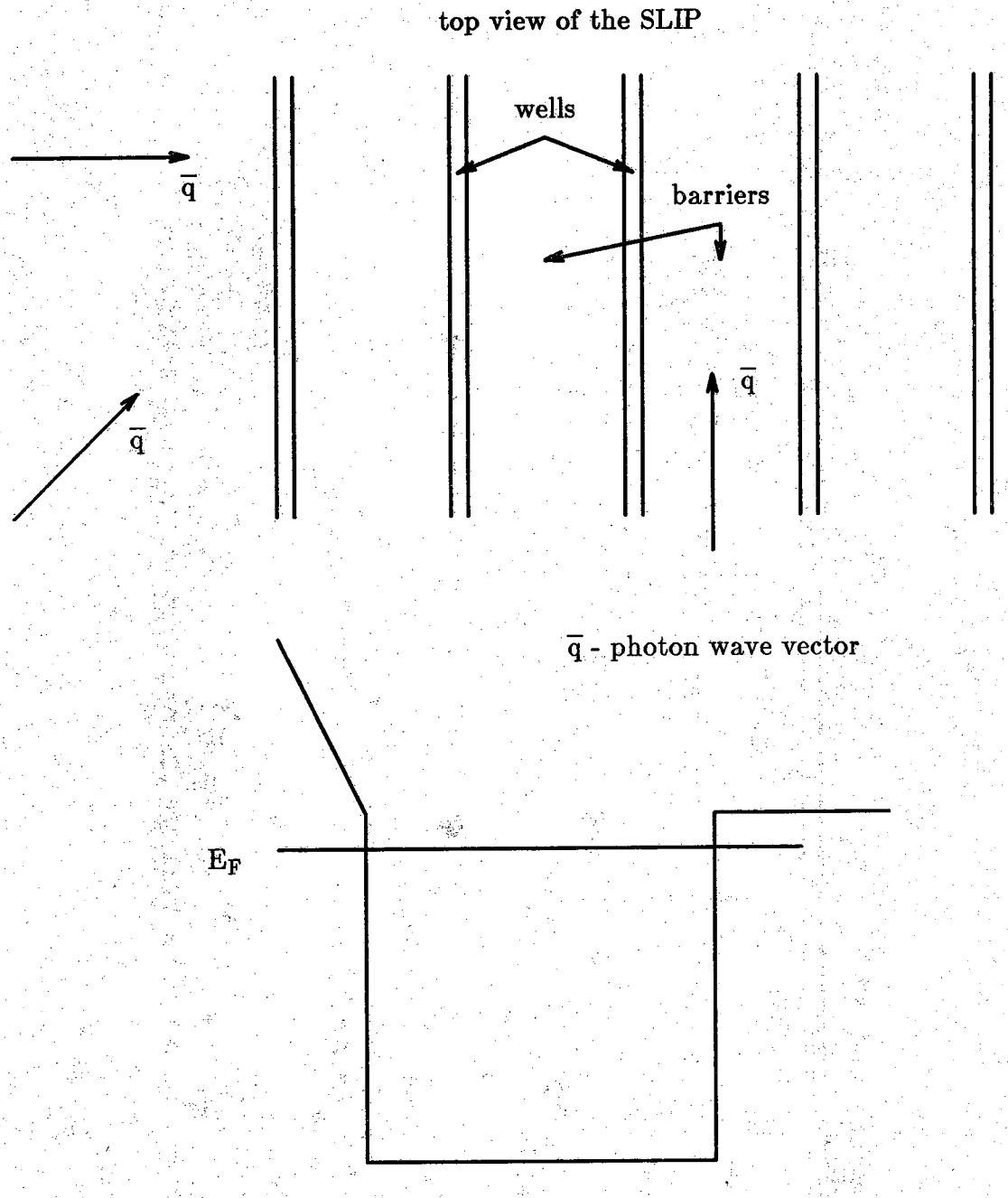

Figure A.9 The three modes in the partly closed well case

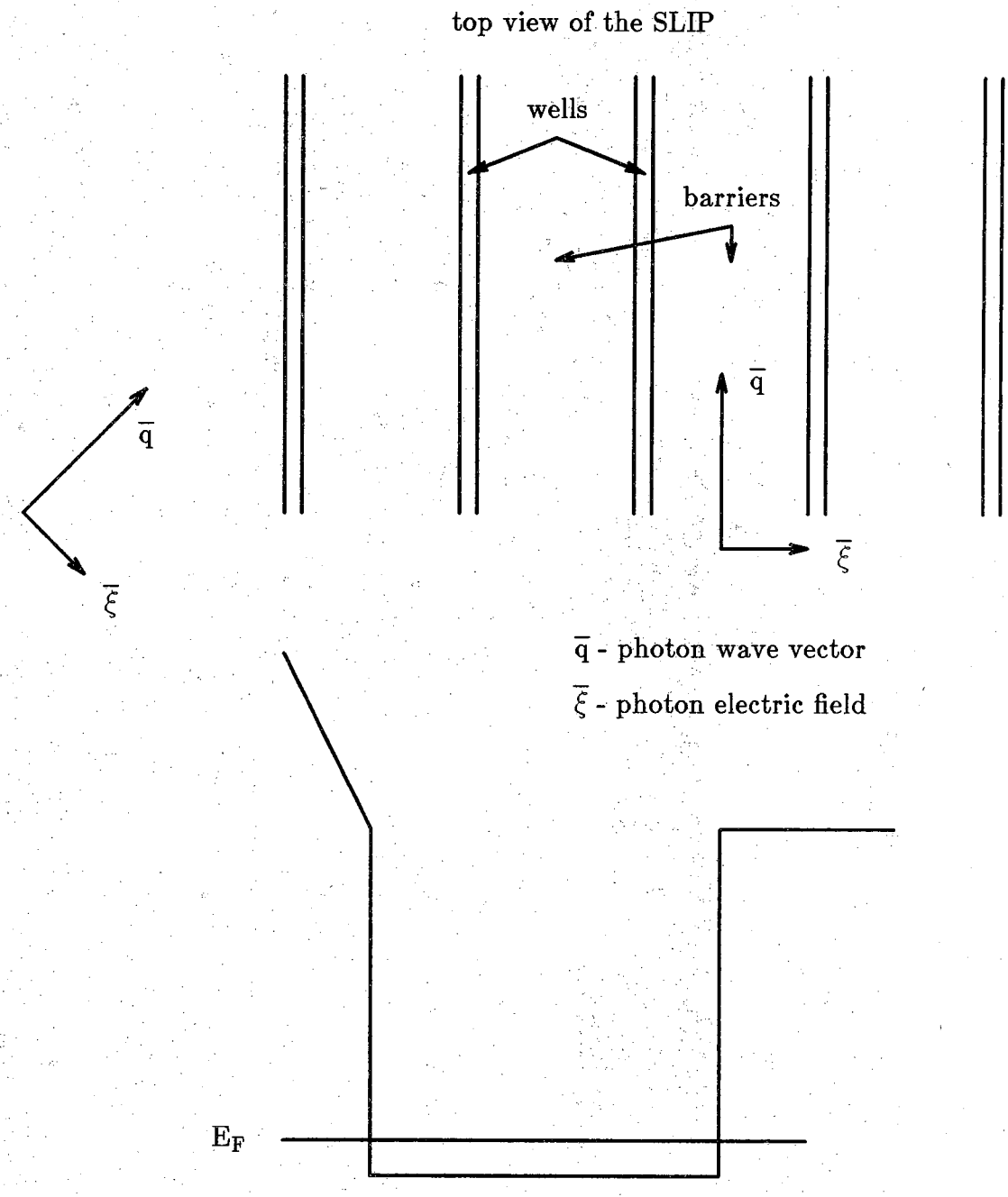

Figure A.10 The two modes in the open well case

The problem with this detector and the other detectors incorporating quantum wells is the high recombination rates associated with the high concentration of empty states (recombination centers) in the quantum well. This will reduce the gain and the efficiency. The only detector that attempts to overcome this problem is the SLIP using the partially closed well case. The solution is to almost fill the well with occupied states, greatly reducing the concentration of empty states.

A.2.5 Graded well SLIP

The graded well SLIP [Kozyrev & Shik 1985; Smith, Chiu, Margalit, Yariv & Cho 1983; Shik 1986; Chiu, Smith, Margalit, Yariv, & Cho 1983; Chiu, Smith, Margalit, & Yariv 1983; Capasso, Allam, Cho, Mohammed, Malik, Hutchinson, & Sivco 1986] was first proposed and experimentally verified in 1983 [Smith, Chiu, Margalit, Yariv & Cho 1983; Chiu, Smith, Margalit, Yariv, & Cho 1983]. It is operated in the same manner as the parallel incidence-open well case mode in the SLIP. Important differences are: 1) The authors [Smith, Chiu, Margalit, Yariv & Cho 1983; Chiu, Smith, Margalit, Yariv, & Cho 1983] don't consider the importance of the Fermi level position with respect to the barrier height energy. 2) They consider it imperative that the well have a built-in electric field (See Fig. A.11). Consequently, the quantum wells are graded because of this electric field. 3) The barriers and the wells are doped. Also, since E_F is much lower than E_{Cb}, tunneling is not considered much of a problem.

The experimental results [Smith, Chiu, Margalit, Yariv & Cho 1983; Chiu, Smith, Margalit, Yariv, & Cho 1983] are not very promising. The response time is 1 sec.. The blackbody source used in these experiments was at 2700 C, which is very large. The radiation from this source between 1 and 10 μm will produce a radiation current density of 14.8 A/cm^2 assuming a quantum efficiency of 1. The actual radiation current density at 1.3 V [Chiu, Smith, Margalit, Yariv, & Cho 1983] is .0222 A/cm^2. For the dark current to be this small at 77 K, the Fermi level will have to be at least .1 eV below E_{Cb}. If one assumes a gain of 10,000 [Smith, Chiu, Margalit, Yariv & Cho 1983] and compares the current densities, the efficiency is 1.5 x 10^{-5}%. For the experiment, the direction of propagation of radiation was parallel to the layers. The barrier is $Al_{.3}Ga_{.7}As$.

The authors assumed that the electrons were excited out of the well, but considering the long response time and the position of the Fermi level, the electrons might have been excited out of the deep dopant levels in the barrier layers [Lifshitz, Jayaraman, Logan, & Card 1980] and subsequently trapped in the wells.

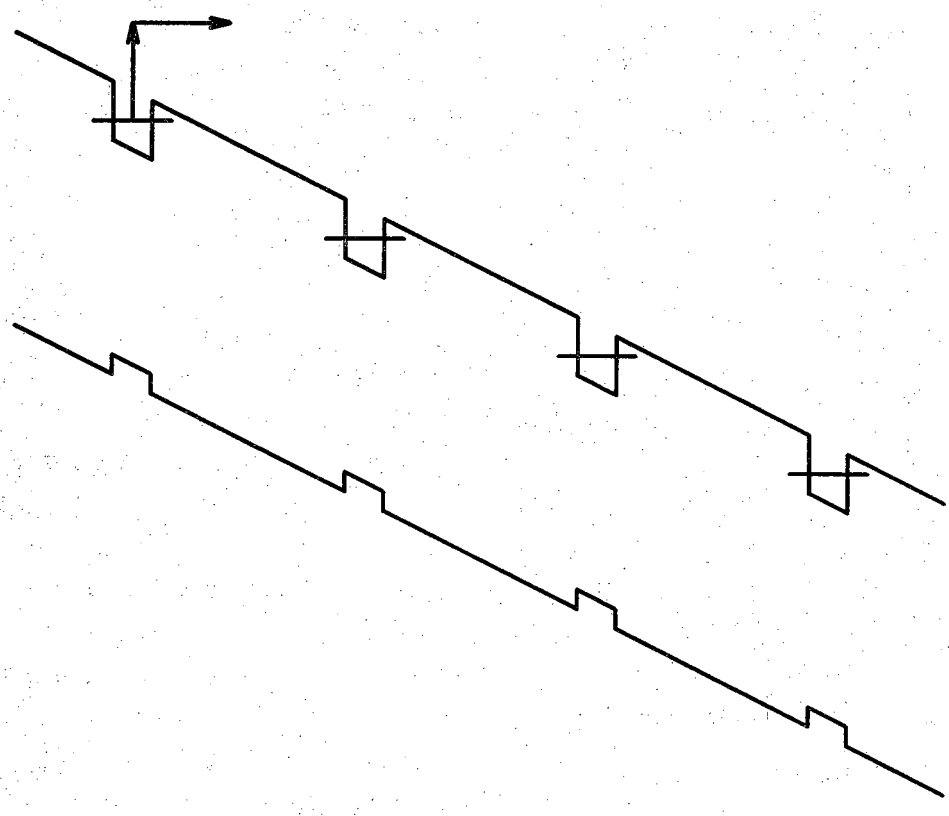

Figure A.11 Graded well SLIP

A.2.6 Intersubband photoconductor (IS-PC)

A.2.6.1 Intersubband absorption

Intersubband absorption [Kozyrev & Shik 1985; Shik 1986; Chiu, Smith, Margalit, & Yariv 1983; Rytova 1967; Shik 1969; Shik 1973; Shik 1975; Yuen 1983] occurs without involving a phonon. It is a direct transition between two energy levels produced by the periodic potential of the superlattice. These energy levels are formed in the direction perpendicular to the superlattice layers and are analogous to the energy levels in a potential well. One requirement for this type of transition is that the radiation must be polarized in the same direction as these energy levels.

In a 1D potential well along the z-direction, the electron can only exist at certain energies in the z-direction. The same is true for a superlattice or any variation of the quantum well. Ideally, these energy levels are discrete and only exist at a specific value of energy. Due to interactions with other particles though, these levels broaden. In turn, the density of states decreases as the width of the energy level increases.

A photon is absorbed by exciting an electron from an initial energy level to a final energy level. The absorption coefficient is related to the density of states in these levels. For all the variations of the IS-PC presented below, their proponents argue that there is little broadening of the energy levels, which produces a large density of states, which in turn causes a large absorption.

Consider a superlattice at flat band condition (No potential is applied across the superlattice). In the well, the energy level broadens due to interaction with carriers [Rytova 1967] and the fact that it can tunnel to other wells [Esaki & Tsu 1970]. Hence as the final energy level increases, the interaction between the wells increases and the width of the levels increases [Shik 1975; Esaki & Tsu 1970]. The absorption decreases as the energy in the well is increased (See Fig. 3 in [Shik 1975]).

As the energy level is raised above the wells, the energy width of the level increases. In turn, resonant absorption will decrease as the energy increases [Shik 1975]. A special case occurs when the energy of the electron is just above the well and approaches the energy value of the conduction band of the barrier layers. If the width and the depth of the well are of the proper dimensions [Shik 1986; Shik 1975], it is possible to have a level at that energy and only that energy. Hence, one would have a delta function for the density of states and the absorption will be infinite. Collisions broaden this level so it's not infinite [Shik 1986; Rytova 1967; Shik 1969; Shik 1973; Shik 1975; Yuen 1983] but the

absorption can, in theory, be very large.

This is the argument for resonant absorption. This argument is only correct for superlattices at the flat band condition. When an electric field is applied, the levels broaden [Shik 1986] and the absorption will decrease.

Some people have suggested this can work for a single quantum well (See secs. A.2.10 and A.2.11). For flat band conditions and infinitely wide barrier layers, this will be the same situation as the superlattice, but as the field is applied or the barrier is made thinner, the levels will subsequently widen. The problem with an applied electric field will be the same as the superlattice at high electric fields because the superlattice becomes a set of noncoherent quantum wells. At low electric fields though, the levels should widen more for the quantum well device.

A.2.6.2 Intersubband photoconductor (IS-PC)

The IS-PC [Kozyrev & Shik 1985; Shik 1986; Chiu, Smith, Margalit, & Yariv 1983; Capasso, Allam, Cho, Mohammed, Malik, Hutchinson, & Sivco 1986; Shik 1973; Shik 1975; Yuen 1983] was first proposed in 1983 [Chiu, Smith, Margalit, & Yariv 1983]. The final energy level is just above the well for this device (See Fig. A.12). The corresponding absorption process was introduced in 1973 [Shik 1973]. No experimental results have been published. The direction of the propagation of radiation is very important for these intersubband processes [Shik 1986, Shik 1973; Shik 1975; Yuen 1983].

These transitions are largest when the radiation propagates parallel to the layers [Shik 1986]. The device is operated in the same way that a PEIR photoconductor is operated. There are two differences from a PEIR photoconductor. 1) The absorption is due to intersubband absorption. 2) The radiation must be partially polarized in the direction perpendicular to the layers to cause this intersubband absorption. In addition, unlike the SLIP (See sec. A.2.4), the location of the Fermi level with respect to the barrier height energy level is explicitly considered.

A.2.7 Tunneling IS-PC

The tunneling IS-PC [Levine, Choi, Bethea, Walker & Malik 1987b; West & Eglash 1985; Levine, Malik, Choi, Bethea, Kleinman & Vanderberg 1987; Choi, Levine, Malik, Walker, & Bethea 1987; Levine, Choi, Bethea, Walker & Malik 1987a; Choi, Levine, Bethea, Walker & Malik 1987; Levine, Bethea, Choi,

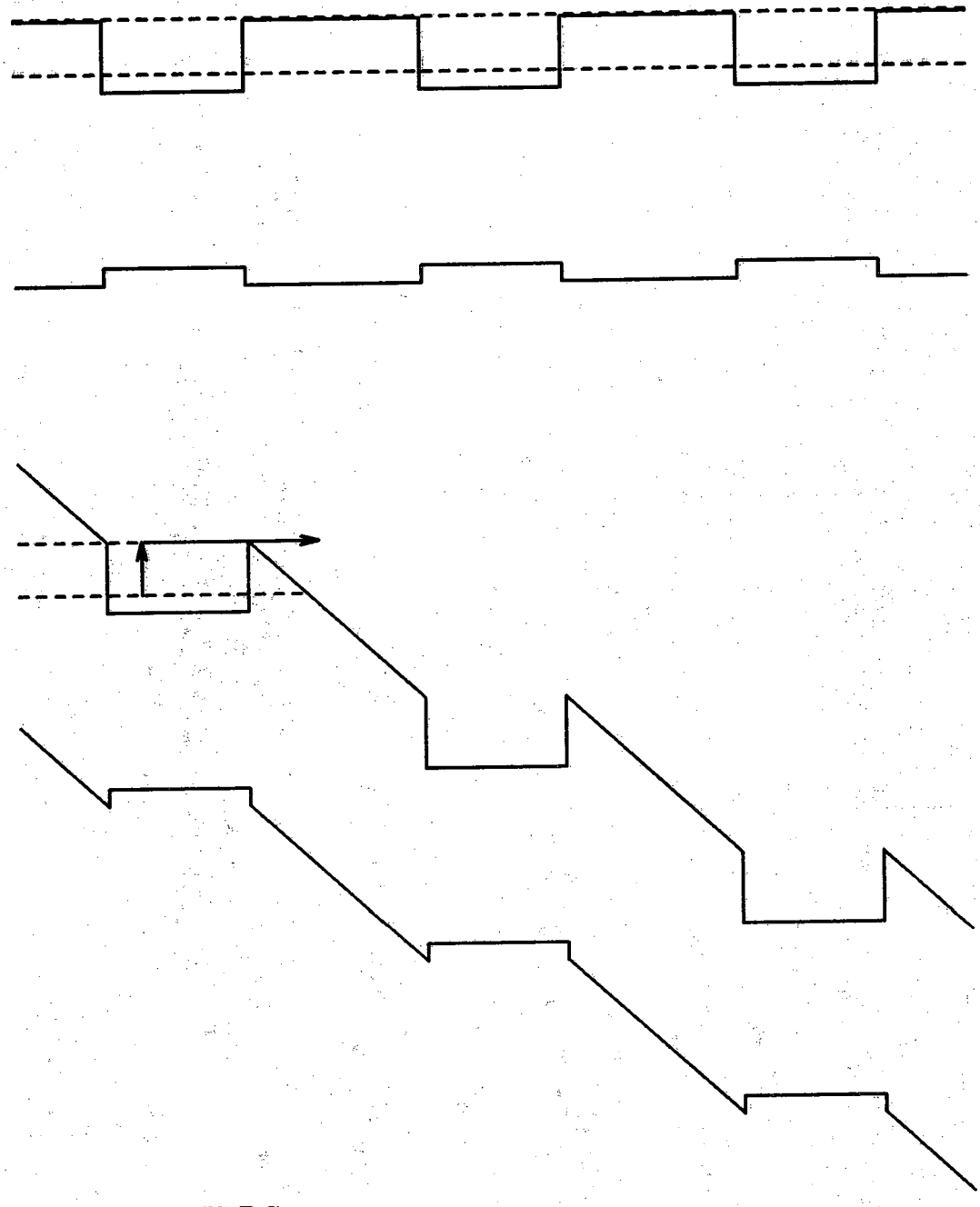

Figure A.12 IS-PC

Walker & Malik 1988; Levine, Bethea, Hasnain, Walker & Malik 1988; Ikonic, Milanovic & Tjapkin 1988; Yang & Pan 1988; Yang, Pan, & Somoano 1989] was first proposed and experimentally tested in 1987 [Levine, Choi, Bethea, Walker & Malik 1987a]. It operates under the same principle as the IS-PC except that the final energy level is still in the well. The excited electron tunnels through the barrier (See Fig. A.13). The dopant concentration in the well is 10^{18} cm^{-3} and the barriers are undoped [Levine, Choi, Bethea, Walker & Malik 1987b; Levine, Choi, Bethea, Walker & Malik 1987a; Choi, Levine, Bethea, Walker & Malik 1987].

The device was operated at 15 K. The radiation entered the detector at an oblique angle to the layers. The efficiency is about 25% [Levine, Choi, Bethea, Walker & Malik 1987b; Choi, Levine, Bethea, Walker & Malik 1987]. This efficiency demonstrates that there is promise for this type of device.

Impact ionization has been shown to occur in this type of device [Levine, Choi, Bethea, Walker & Malik 1987b]. The authors apparently believe this is an advantage because in this paper, the gain is incorporated into the quantum efficiency (The efficiency becomes 84% [Levine, Choi, Bethea, Walker & Malik 1987b]). Impact ionization is only an advantage in this device for two reasons. First, the temperature is so low that the dark current, even with impact ionization, is not large. Second, there must be some type of blocking contact (as in a CCD array [Sibille 1986; Milton 1977; Barbe 1975]) that prevents injection of electrons from the cathode.

Another mode of operation is to consider the flat band condition and to use an asymmetric device [Kastalsky, Duffield, Allen, & Harbison 1988]. One contact is connected to the superlattice and the other contact is separated from the superlattice. The radiation enters the device and excites the carriers, which then diffuse to the separated contact, producing a potential across the contacts. This device with no bias should be much slower than the tunneling IS-PC with bias because of the fact that the transport of carriers is due to diffusion. It is stated that this mode of operation will be less noisy than the photoconductive mode, but the photoconductive mode should be faster and more efficient. In addition, the noise advantage disappears if one uses a blocking contact for the tunneling IS-PC because the noise in both cases is shot noise (as compared to RG noise). It is also stated that since there is no power source [Kastalsky, Duffield, Allen, & Harbison 1988], the noise problems will be much smaller than in the tunneling IS-PC. The authors [Kastalsky, Duffield, Allen, & Harbison 1988] present experimental results but there is no mention of efficiency. The response is in arbitrary units.

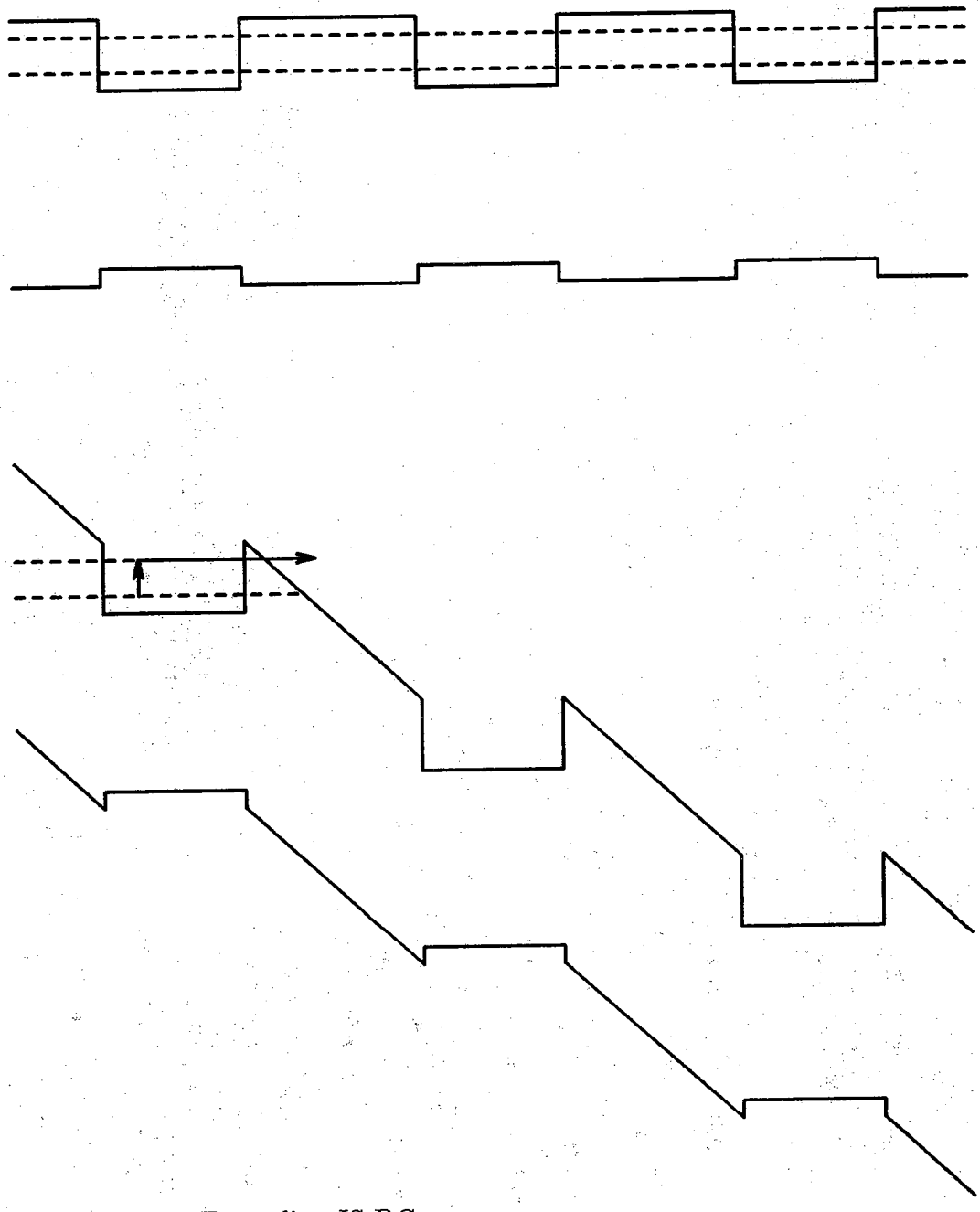

Figure A.13 Tunneling IS-PC

A.2.8 Resonant IS-PC

The resonant IS-PC [Capasso, Mohammed, & Cho 1986] was first described in 1986 [Capasso, Mohammed, & Cho 1986]. No experimental results have been published.

This device is similar to the tunneling IS-PC except instead of tunneling into the conduction band of the adjacent barrier, the electron in the resonant IS-PC tunnels from a quantum level in one well to another quantum level in the adjacent well (See Fig. A.14). There are two problems with this type of device. 1) In every well, the electron must recombine from the third level into the second level and tunnel before recombining into the lowest level. Since the lowest level has a larger number of states, this may lower the gain drastically. 2) The electric field in the photoconductor depends upon the radiation intensity. This changing electric field appears to be a large obstacle in aligning the quantum levels to cause resonant tunneling.

A.2.9 Effective mass filter IS-PC

This effective mass filter IS-PC [Capasso, Mohammed, & Cho 1986; Capasso, Mohammed, Cho, Hull, & Hutchinson 1985a; Capasso, Mohammed, Cho, Hull, & Hutchinson 1985b; Capasso, Mohammed, & Cho 1985] was first proposed and experimentally tested in 1985 [Capasso, Mohammed, Cho, Hull, & Hutchinson 1985a]. It does appear to be a very viable photoconductor, except that the absorption is band to band. Which in turn means that one must deal with HgCdTe at sufficiently long wavelengths.

The device is a superlattice with direct band to band absorption. The initial electron state is in the valence band well and the final electron state is in the conduction band well. If the electron has a much smaller effective mass than the hole, it is possible to choose a correct barrier width and electric field such that the electrons are not localized in the wells and easily pass through the barriers and the holes are localized in the wells and do not pass through the barriers. This is analogous to an intrinsic photoconductor with no sweepout effects.

A.2.10 Quantum well IS-PC

The first variation of the quantum well IS-PC [Coon & Karunasiri 1984; Coon, Karunasiri, & Liu 1985; Coon, Karunasiri, & Liu 1986] was proposed in 1984 [Coon & Karunasiri 1984]. The most recent variation was presented in

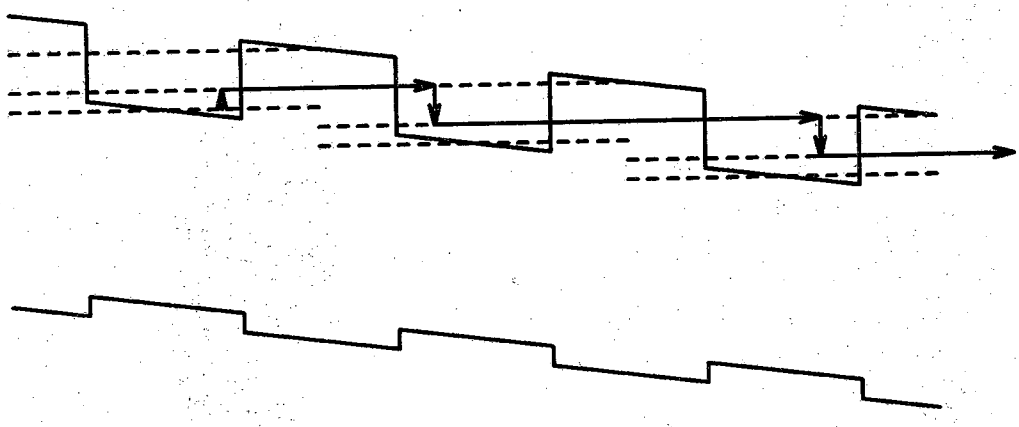

Figure A.14 Resonant IS-PC

1986 [Coon, Karunasiri, & Liu 1986]. No experimental results have been published. This device operates in the same manner as the IS-PC except, instead of a superlattice, there is one quantum well.

The main assumptions in these papers is that the absorption is calculated using a flat band situation and is assumed to be very high. When a field is applied, the levels will widen. At wavelengths with a calculated high absorption, this will pose a problem because the levels are assumed to be very narrow. If one lowers these absorption peaks, the quantum efficiency will be approximately 20 % at best for concentrations of 10^{18} cm^{-3} [Coon, Karunasiri, & Liu 1986]. Additionally, the high absorption is necessarily accompanied by high reflection (See app. E). One possible solution to this problem is to redirect the radiation such that it propagates in the plane of the quantum well. This process and the coupling procedure will be similar to what occurs in surface plasmon propagation [Otto 1968].

A.2.11 Grating IS-PC

The grating IS-PC [Goossen and Lyon 1985; Goossen and Lyon 1988; Goossen, Lyon, & Alavi 1988a; Goossen, Lyon, & Alavi 1988b] was first proposed in 1985 [Goossen and Lyon 1985]. The device was first experimentally tested in 1988 [Goossen, Lyon, & Alavi 1988a]. The device is a variation of the quantum well IS-PC. The only difference is that in a quantum well IS-PC, the quantum well has barriers on both sides and the contacts are placed on the ends of these barriers. In the grating IS-PC, a grating is inserted at one of these contact-barrier interfaces. The experimental detector had one contact in the quantum well and the other contact was the grating (or in one paper, was a flat metal contact). The purpose of this grating is to redirect the radiation so that more of the electric field is directed perpendicular to the quantum well layers which will increase the probability of collisionless escape.

The authors [Goossen and Lyon 1985] do not state an absorption coefficient. If it is large, the problem of the level widening as the electric field is applied would be a major problem. For instance, the efficiency they obtain is 1% [Goossen, Lyon, & Alavi 1988a], which means the absorption is reasonably small.

A.2.12 Sampling IR detector

The sampling IR detector [Coon & Karunasiri 1983a; Coon, Gunapala, Karunasiri, & Muehlhoff 1983; Coon & Karunasiri 1983b; Coon, Gunapala, Karunasiri, & Muehlhoff 1984; Coon, Gunapala, Karunasiri, & Muehlhoff 1985; Coon & Perera 1986; Gunapala & Coon 1988] was first proposed in 1983 [Coon & Karunasiri 1983a] and experimentally verified in 1983 [Coon, Gunapala, Karunasiri, & Muehlhoff 1983]. The radiation enters the device and excites carriers from impurity potentials in the intrinsic region of a pin diode. This device acts as a integrating detector where the refresh is caused by forward biasing the device until the impurities in the intrinsic region are neutral. The thermal generation and background radiation generation must be very low to prevent saturation of the detector. This requirement signifies that this device will not be a serious contender when it comes to optical communications or detection with a normal amount of background radiation or signal radiation. In addition, the efficiency is only about 4.5% [Coon, Gunapala, Karunasiri, & Muehlhoff 1985] which is much less than the tunneling IS-PC [Levine, Choi, Bethea, Walker & Malik 1987b; Choi, Levine, Bethea, Walker & Malik 1987] It has been shown that the absorption cross section can be increased enough to cause the efficiency to rise to as high as 16% [Gunapala & Coon 1988].

A.2.13 InAsSb strained-layer superlattice infrared detectors

This detector incorporates a strained-layer superlattice for use as an infrared detector [Osbourn 1984; Osbourn, Dawson, Biefeld, Zipperian, Fritz, & Doyle 1987; Kurtz, Biefeld, Dawson, Fritz, & Zipperian 1988; Kurtz, Dawson, Zipperian, & Lee 1988; Kurtz, Osbourn, Biefeld, Dawson, & Stein 1988; Kurtz, Osbourn, Biefeld, & Lee 1988]. The concept was first proposed in 1984 [Osbourn 1984]. Experimental results have been found in both a photodiode (See Fig. A.15) [Kurtz, Dawson, Zipperian, & Lee 1988] and a photoconductor (See Fig. A.16) [Kurtz, Biefeld, Dawson, Fritz, & Zipperian 1988]. The carriers in a photodiode tunnel from well to well while the carriers in a photoconductor are separated into different wells and subsequently drift towards opposite contacts. At this time, the wavelength response can go out to around 8 μm. These strained-layer superlattice detectors and the PEIR photoconductor appear to be the major competitors with HgCdTe for wavelengths out to 15 μm. Strained-layer superlattice photodetectors could possibly be superior to the PEIR photoconductor in this wavelength range, depending upon the absorption as a function of energy in both devices. This superiority would be a moot point though if HgCdTe is shown to be superior to either of these. For longer

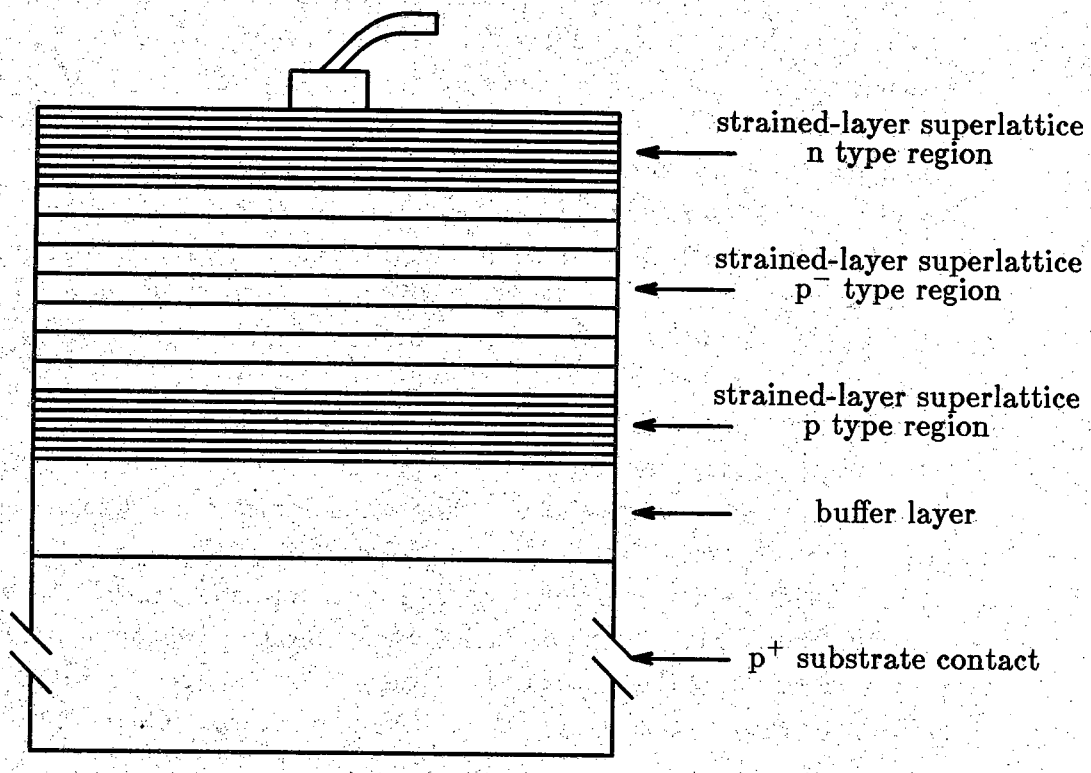

Figure A.15 Strained-layer superlattice photodiode

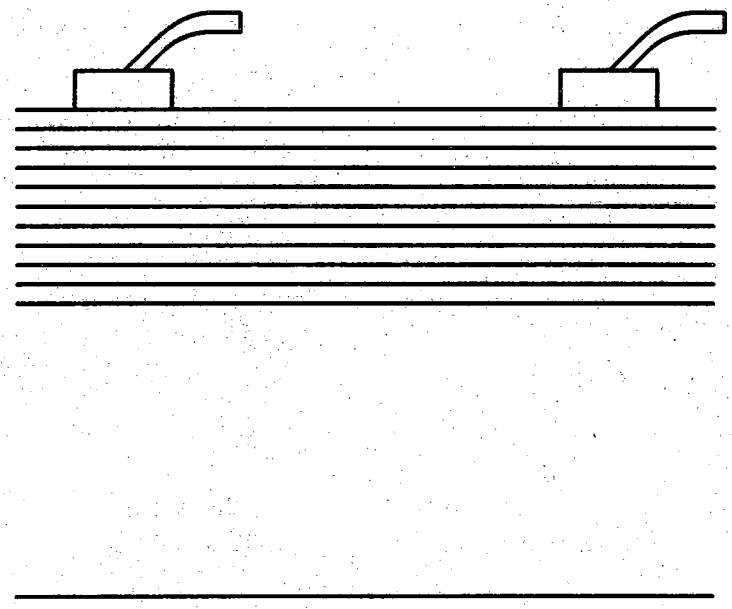

Figure A.16 Strained-layer superlattice photoconductor

wavelengths, a PEIR photoconductor should be superior because the energy difference between the conduction band and the impurity band (n-type device) in a PEIR photoconductor should be much easier to control than the heterojunction barrier heights required in strained-layer superlattice photodetectors and the increasingly small band gap needed for HgCdTe.

A.3 Conventional and novel avalanche photodiodes (APDs)

There are four important physical requirements that should be met for an APD designed to detect radiation longer than 7 μm. First, a narrow gap semiconductor must be fabricated. Second, one disadvantage with the conventional APD is that for long wavelengths, Zener tunneling [Kane 1959; Kane 1961] becomes a problem. As the band gap decreases, the tunneling current becomes too large and the conventional APD is no longer a viable device. The devices presented in this section represent attempts to overcome this obstacle. Third, to make the response time as fast as possible, the absorption should take place in a region that has an electric field. Diffusion makes the response time too sluggish [Sze 1981; Seib & Aukerman 1973]. Fourth, to make the noise as small as possible, the electron's rate of ionization β_e should be much larger or smaller than the hole's rate of ionization β_h [McIntyre 1966; McIntyre 1972; Webb, McIntyre, & Conradi 1974]. For instance the ionization ratio, β_e/β_h, is approximately thirty five for silicon [Conradi 1972]. All of the novel devices try to approach or better this ionization ratio.

The increase in the rms noise current caused by avalanching is always greater than the increase of the signal current. This extra increase in noise is related to the excess noise factor [McIntyre 1966; Teich, Matsuo, & Saleh 1986]. If other noise terms, which also includes any amplifier noise, are greater than this avalanching noise, the signal can be increased more rapidly than the overall noise [Forrest 1986; Seib & Aukerman 1973; Teich, Matsuo, & Saleh 1986]. This increase is beneficial until the avalanching noise becomes comparable to all other noise terms.

There has been a study [Teich, Matsuo, & Saleh 1986] that compares the excess noise factors of the photomultiplier, the APD and a group of novel photodiodes. The authors concur with a previous conclusion [Capasso, Tsang, & Williams 1983] that the novel photodiodes would always have lower excess noise factors than APDs with the same ionization ratios. If the ionization ratio is infinite and multiplication occurred at every stage, it would have a minimum excess noise factor of 1. It is pointed out though that as the ionization ratio approaches one and the number of multiplication stages increases, the excess

noise factor increases accordingly.

A.3.1 Separate absorption and multiplication region APD (SAM-APD)

The SAM-APD [Nishida, Taguchi, & Matsumoto 1979; Susa, Nakagome, Mikami, Ando, & Kanbe 1980; Kim, Forrest, Bonner, & Smith 1981; Forrest, Kim, Smith, & Williams 1981; Forrest, Kim, & Smith 1982; Campbell, Dentai, Holden, & Kasper 1983; Capasso, Cho, & Foy 1984; Stillman, Robbins, & Tabatabaie 1984; Capasso, Cox, Hutchinson, Olsson, & Hummel 1984; Holden, Campbell, & Dentai 1985; Jhee, Campbell, Holden, Dentai, & Plourde 1985; Petroff, Stapelbroek, & Kleinhans 1987] was first proposed and experimentally tested in 1979 [Nishida, Taguchi, & Matsumoto 1979]. Of all the novel devices, this is the one that has been considered most seriously. As stated before, the main problem with an APD with a thin gap is that the Zener current is too large. The SAM-APD is divided into two regions. A narrow band gap absorption region that has an electric field small enough to prevent avalanching and a wide band gap multiplication (or avalanche) region where the electric field is large enough to cause avalanching. An idealized band diagram of this device is presented in Fig. A.17. A more realistic band diagram is presented in [Stillman, Robbins, & Tabatabaie 1984] and the corresponding electric field is in [Holden, Campbell, & Dentai 1985]. The problem with the abrupt junction is that the notch (See Fig. A.17) traps electrons (holes in [Stillman, Robbins, & Tabatabaie 1984]) which lowers the bandwidth.

There have been several suggested improvements of the SAM-APD. One has been to grade the junction [Forrest, Kim, & Smith 1982]. An ideal graded SAM-APD is shown in Fig. A.18 (See [Forrest, Kim, & Smith 1982] for a more realistic band diagram). This will solve the electron (hole in [Forrest, Kim, & Smith 1982]) trapping problem. Other suggestions have been to use a doping spike to better control the electric fields in the absorption and multiplication regions [Capasso, Cho, & Foy 1984] and to grade the gap by using a superlattice [Capasso, Cox, Hutchinson, Olsson, & Hummel 1984].

Another new device with the same operating principles has been presented in [Petroff, Stapelbroek, & Kleinhans 1987]. Instead of holes, one considers the ionized donor states as being the holes. The time response is about a μsec. This detector is very promising for one simple reason. It is a wide band gap, two carrier detector for long wavelengths.

These devices are being seriously considered, but there are three problems at present. First, the slow response due to hole trapping at the abrupt junction [Forrest, Kim, & Smith 1982]. Second, it is hard to fabricate the graded

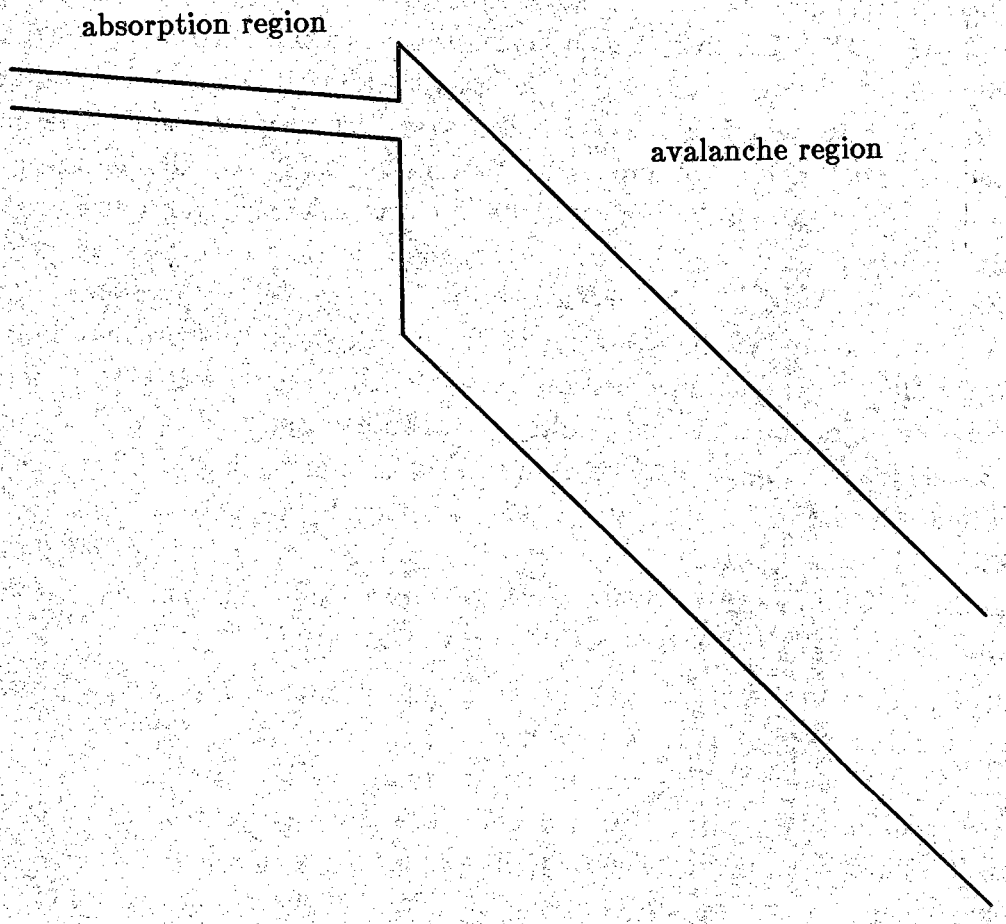

Figure A.17 SAM-APD

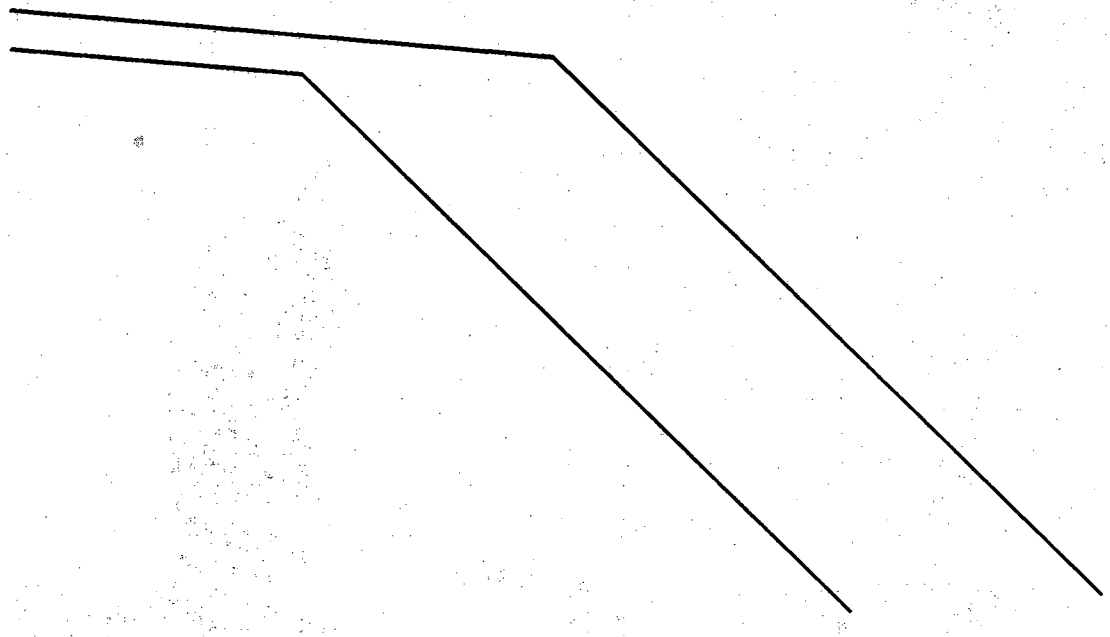

Figure A.18 Graded SAM-APD

junction SAM-APD without having large leakage currents [Forrest 1986]. Third, the ionization ratio in most of the III-V materials is about equal to 1 which causes noise problems (See sec. A.3 or [McIntyre 1966]). The devices presented in secs. A.3.2 to A.3.7 try to increase this ionization ratio. In fact, the devices presented in secs. A.3.2 to A.3.7 are SAM-APDs with more exotic avalanche regions.

The noise in these devices will be the same as the conventional APDs with similar ionization ratios.

A.3.2 Superlattice APD

The superlattice APD [Capasso, Tsang, & Williams 1983; Chin, Holonyak, Stillman, Tang, & Hess 1980; Capasso, Tsang, Hutchinson, Williams 1982; Capasso 1983; Brennan, Wang, & Hess 1985; Juang, Das, Nashimoto, & Bhattacharya 1985; Brennan 1985a; Chakrabarti & Pal 1987; Brennan 1987a] was first proposed in 1980 [Chin, Holonyak, Stillman, Tang, & Hess 1980]. The first experimental results were presented in 1982 [Capasso, Tsang, Hutchinson, Williams 1982]. The first theoretical calculation of ionization rates was presented in 1985 [Brennan, Wang, & Hess 1985].

Most papers describing this device don't discuss where the absorption is taking place. Some papers show absorption in a flat band region [Brennan, Wang, & Hess 1985; Brennan 1985a; Brennan 1987a]. This would greatly lower the response time due to diffusion and is avoided in conventional APDs (See sec. A.3 and [Sze 1981; Seib & Aukerman 1973]). This type of diffusion limited superlattice APD is shown in Fig. A.19.

A practical device will be something like the SAM-APD (See Fig. A.17) with the multiplication region being the superlattice APD. A major problem occurs with this configuration though. To get impact ionization, an electric field larger than 100,000 V/cm is needed in the avalanche region [Capasso, Tsang, Hutchinson, Williams 1982].

In [Capasso, Tsang, Hutchinson, Williams 1982], it is assumed that the electrons are not trapped in the well because the average electron energy in the electric field is greater than the conduction band height. One way to overcome this trapping problem is presented in [Capasso 1983]. The material must be of high quality because of the large number of heterointerfaces and the large electric field [Capasso, Tsang, Hutchinson, Williams 1982].

The excess noise factor of this device will be better than the conventional APDs [Teich, Matsuo, & Saleh 1986; Capasso, Tsang, & Williams 1983].

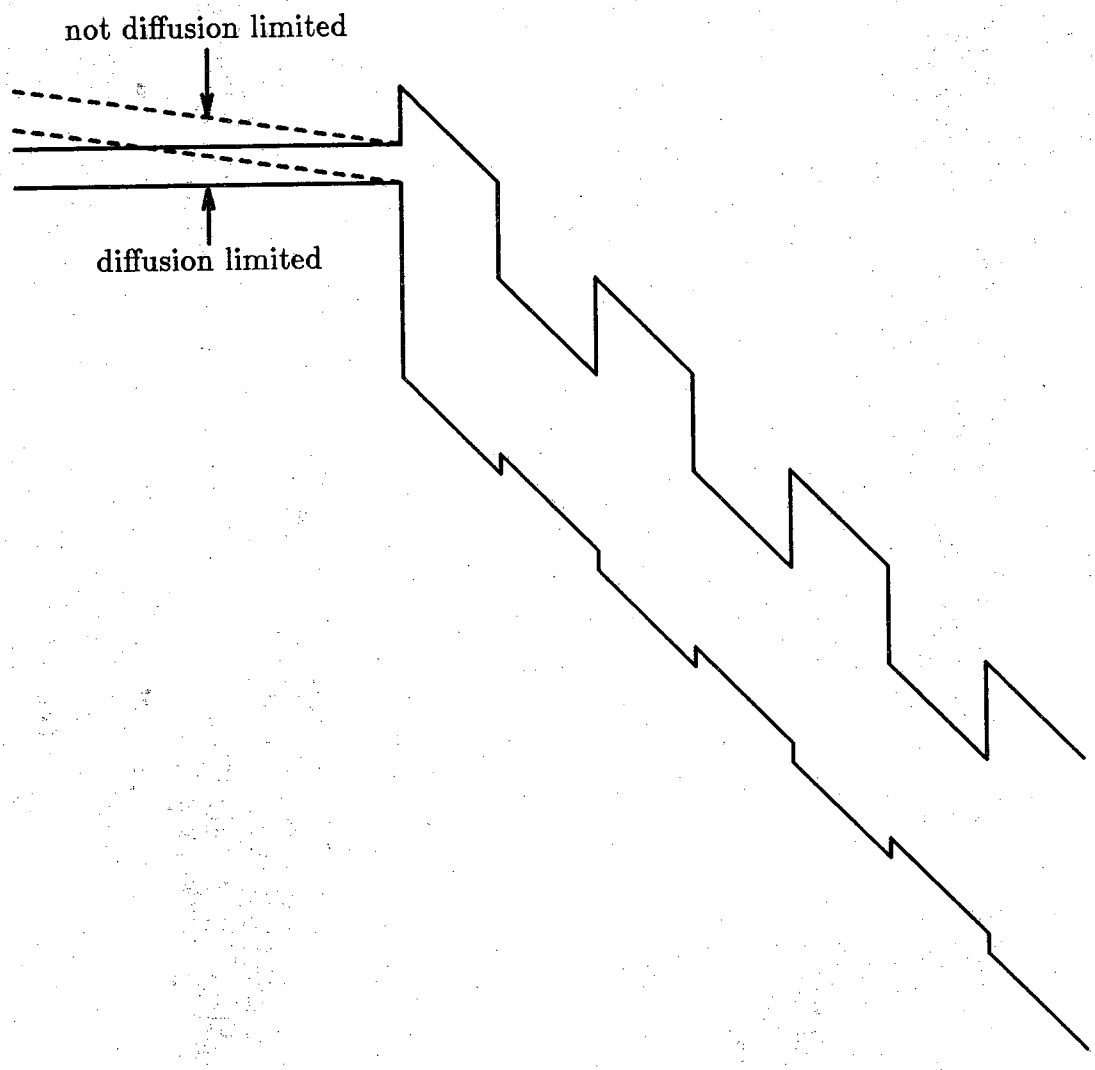

Figure A.19 Superlattice APD

A.3.3 Staircase APD

The Staircase APD [Capasso, Tsang, & Williams 1983; Brennan 1985a; Brennan 1987a; Capasso & Tsang 1982; Williams, Capasso, & Tsang 1982] is an alternative to the superlattice APD. It was first proposed in 1982 [Capasso & Tsang 1982]. No experimental results have been presented at this time [Forrest 1986].

The multiplication region of the device is shown in Fig. A.20. A modification of this design is shown in [Capasso, Tsang, & Williams 1983]. The ionization ratio should increase because the electron has a high kinetic energy when it enters the narrow band gap region. The electric field is much smaller than the superlattice APD - around 10,000 V/cm [Williams, Capasso, & Tsang 1982].

The reason for no reported results may be the difficulty in grading the gap for such a large conduction band difference. One proposed material composition requires a conduction band change of .8 eV (the ionization energy) in a layer thickness of 3000 Å [Williams, Capasso, & Tsang 1982]. These requirements may be too difficult to achieve. A similar problem occurs for the graded SAM-APD [Forrest 1986].

The excess noise factor is the same as the superlattice APD [Teich, Matsuo, & Saleh 1986; Capasso, Tsang, & Williams 1983].

A.3.4 Quantum well APD

The quantum well APD [Brennan 1987a; Blauvelt, Margalit, & Yariv 1982; Brennan 1986b; Brennan 1986a; Brennan 1987b; Brennan 1987c] was first proposed in 1982 [Blauvelt, Margalit, & Yariv 1982]. No experimental results have been published. Other than the SAM-APD papers, this is the first paper [Blauvelt, Margalit, & Yariv 1982] that explicitly considers the separation of the absorption and avalanche regions.

This device is the same as the superlattice APD except that the doping profile is adjusted in the barriers to increase the electric field at certain points (See Fig. A.21).

The excess noise factor is the same as the superlattice APD [Teich, Matsuo, & Saleh 1986; Capasso, Tsang, & Williams 1983].

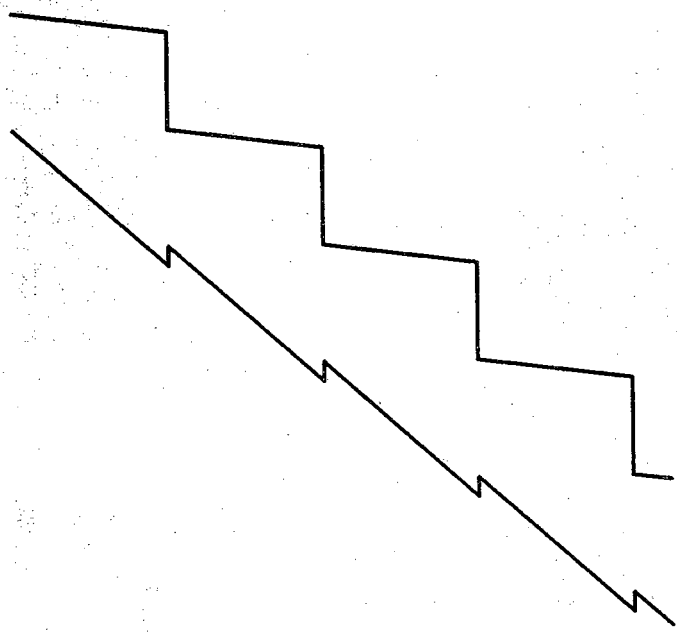

Figure A.20 Multiplication region of the staircase APD

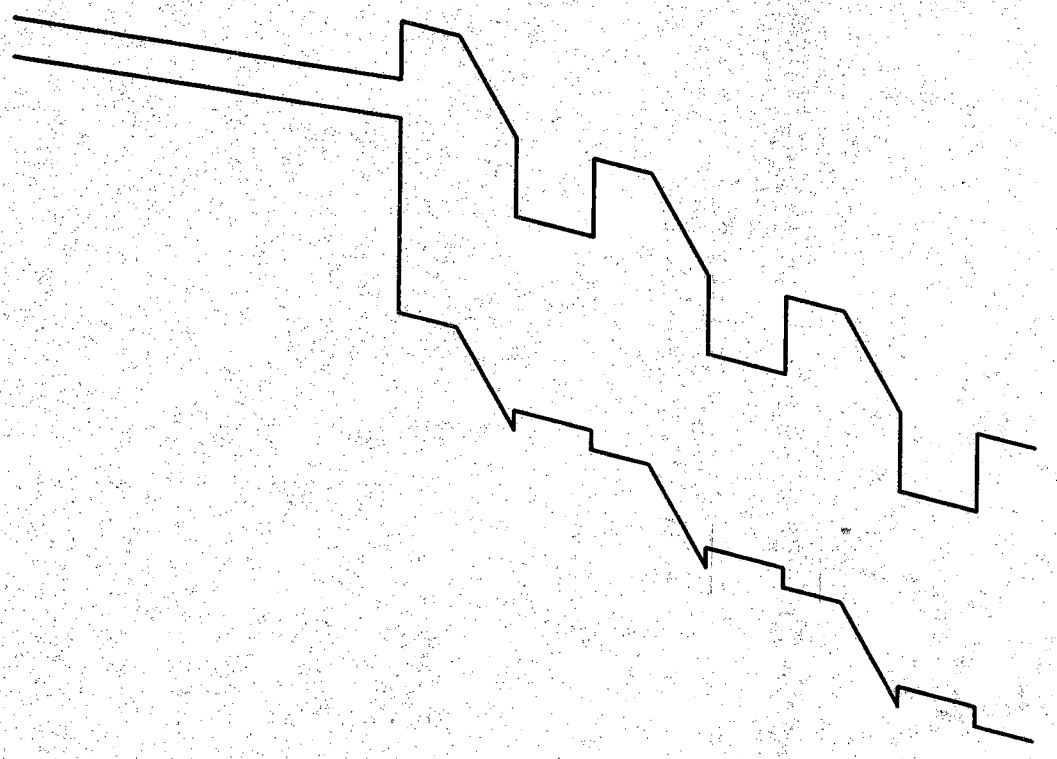

Figure A.21 Quantum well APD

A.3.5 Graded Gap APD

The graded gap APD [Capasso, Tsang, & Williams 1983; Capasso, Tsang, Hutchinson, & Foy 1982] was first proposed and experimentally tested in 1982 [Capasso, Tsang, Hutchinson, & Foy 1982]. A representation of the graded gap APD is shown in Fig. A.22.

As can be seen in Fig. A.22, the effective electric field in the device is larger for the electron than the hole. If only one layer is used, the gain will be around 5 at best [Capasso, Tsang, Hutchinson, & Foy 1982]. Matching this device to a compatible absorption region will be much more difficult than the SAM-APD (See Fig. A.22).

The excess noise factor is the same as the conventional APD [Teich, Matsuo, & Saleh 1986; Capasso, Tsang, & Williams 1983].

A.3.6 Resonant tunneling superlattice APD (RTS-APD)

The RTS-APD [Summers & Brennan 1987; Brennan & Summers 1987] was first proposed in 1987 [Summers & Brennan 1987]. It operates by aligning quantum levels in adjacent wells such that resonant tunneling can occur. This is a revision of another novel APD [Brennan & Summers 1987]. No experimental results have been published.

This paper [Summers & Brennan 1987] explicitly discusses absorption in the flat band region and diffusion currents. The band diagram is shown in [Summers & Brennan 1987]. For the device to be competitive, an electric field must exist in an absorbing region.

The RST-APD is proposed as an alternative to the SAM-APD. This is due to the slower response caused by the trapped charge at the notch of the abrupt junction. It seems that there can possibly be similar trapping problems in the valence band of the RST-APD. In addition, the voltage in conventional photodiodes and APDs changes when the radiation intensity varies. It seems reasonable to assume the voltage in the RTS-APD will also change. This change in voltage appears to be a large obstacle in aligning the quantum levels to cause resonant tunneling. These problems appear to be more difficult to solve than the grading problems of the SAM-APD.

The excess noise factor is the same as the superlattice APD [Teich, Matsuo, & Saleh 1986; Capasso, Tsang, & Williams 1983].

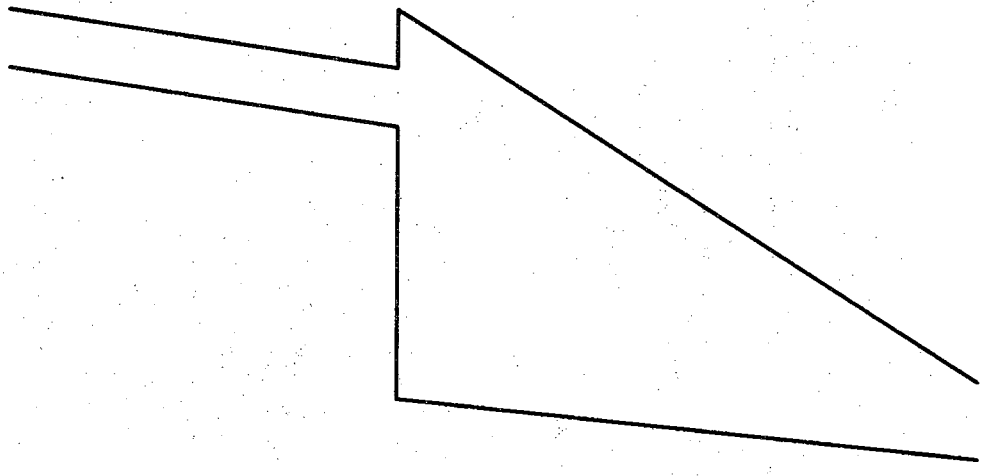

Figure A.22 Graded gap APD

A.3.7 Channeling APD

The channeling APD [Capasso, Tsang, & Williams 1983; Capasso 1982a; Capasso 1982b; Brennan 1985b] was first proposed in 1982 [Capasso 1982a]. No experimental results on the device have been published.

As shown in [Capasso 1982a], this device is very complicated. The major problem with this device is that for wavelengths of interest, one needs small band gap. With such a small band gap and a high electric field needed for ionization, Zener tunneling would be a serious obstacle.

The excess noise factor is the same as the conventional APD [Teich, Matsuo, & Saleh 1986; Capasso, Tsang, & Williams 1983].

A.4 Conclusion

Section A.4.1 lists the most promising detectors presented in this appendix. Section A.4.2 compares the PEIR photoconductor with the most promising detector to date - the BIB detector.

A.4.1 Promising novel detectors

Of the novel devices presented in this appendix, only a few are promising. The novel one carrier photoconductors are more promising at long wavelengths because of the small band gap problems in the novel APDs.

For one carrier detectors (the submillimeter photoconductor is not considered to be novel), the BIB detector, the SLIP, the IS-PC and the tunneling IS-PC are the most promising.

The most promising two carrier detectors are the strained-layer superlattice photodetectors described in sec. A.2.13. the SAM-APD, the superlattice APD, the staircase APD, the quantum well APD, the graded gap APD, and the effective mass filter PC in A.2.5.

A.4.2 Comparison of a BIB detector and a PEIR photoconductor

There are two disadvantages in a PEIR photoconductor compared to a BIB detector. First, it acts like a photoconductor, which is more noisy than the shot noise that exists in a BIB detector. Second, it is a more complex structure than a BIB detector. This will become less of a problem as the science of epitaxial growth matures. The biggest concerns are uniformity throughout the layers, uniformity from layer to layer, and the accuracy of calibrating the dopant

concentration.

There are three advantages in a PEIR photoconductor compared to a BIB detector. First, the temperature of operation will be much higher because the contacts can be ohmic in a PEIR photoconductor while the cathode needs to be blocking in a BIB detector. This advantage is closely tied to the first disadvantage of the previous paragraph. Second, a BIB detector has ionization problems (thermal-field emission ionization, tunneling-field emission ionization - see sec. 1.4.4) that the PEIR photoconductor does not have. In a PEIR photoconductor, the active region is from front contact to back contact regardless of the electric field while the active region in a BIB detector is only the depletion region. This depletion region depends upon the electric field in the impurity band layer of a BIB detector and the electric field is limited by the ionization effects. As the energy difference between the conduction band and the top of the impurity band ($(E_C-E_D)_{min}$) gets smaller, these ionization problems become more severe (See app. F). Third, a PEIR photoconductor can be doped at a higher dopant concentration because $(E_C-E_D)_{min}$ gets smaller as the dopant concentration in the impurity band layers increases.

In conclusion, less serious problems exist in a PEIR photoconductor than in a BIB detector because a depletion region must exist in a BIB detector. Consequently: 1) The impurity band dopant concentration (and the absorption coefficient) can be larger in a PEIR photoconductor. 2) It will be easier to build a PEIR photoconductor as the wavelength to be detected increases.

Appendix B.

Calculation of D^* due to thermal generation in photoconductors

B.1 Introduction

This appendix briefly describes how to obtain D^* from the fluctuations in the number of carriers in the photoconductors. In this appendix, D^* is calculated due only to thermal generation (the dark current term in the RG noise), not photon generation and will be defined as D^*_{RG}.

One important point to be considered is that the terms equilibrium (See eqn (25) in [van Vliet 1958]) and steady state are intermixed [van Vliet 1958] when calculating the variance in the number of carriers (ie. $\Delta n^2(t) = (n(t) - \langle n(t) \rangle)^2$). In the photoconductor, the case of interest is the steady state case. The way this discrepancy is reconciled is to realize that the statistical approach solves the steady state case [Burgess 1954] and if the generation and recombination rates (g and r, respectively) are known, the variance can be solved (This is discussed at the end of [Burgess 1954]). It appears to be assumed [van Vliet 1958] that the dependence of the generation and recombination rate on the number of carriers (at all energy levels) is the same in either the equilibrium or steady state case. For simplicity, the case throughout this appendix will be considered to be steady state but for a more rigorous approach, the reader is advised to consult the literature (van Vliet [van Vliet 1958] is a good beginning).

Section B.2 presents the variance of the number of carriers ($\langle \Delta n^2(t) \rangle$) and calculates the spectral noise density ($S_i(f)$) for a photoconductor in general. Section B.3 presents the recombination and generation rates and calculates $S_i(f)$ for four specific photoconductor cases. Section B.4 calculates the noise current due to thermal generation for two specific photoconductor cases. Section B.5 calculates D^*_{RG} due to thermal generation for two specific photoconductor cases and discusses the physical significance of D^*_{RG}. Section B.6 presents how to obtain numerical values of D^*_{RG} due to thermal generation (RG noise) for two specific photoconductor cases.

B.2 Spectral noise density ($S_i(f)$) of a photoconductor in general

The current is defined as [van Vliet 1958]

$$i(t) = \frac{e\xi}{L}(\mu_n \hat{n}(t) + \mu_p \hat{p}(t))$$

where it is emphasized that $\hat{n}(t)$ and $\hat{p}(t)$ are numbers, not densities. L is the distance between the contacts and $L=d_x$ (See Fig. D.1).

The spectral density function $S_k(f)$ is defined as [van Vliet 1958]

$$\langle \Delta k^2(t) \rangle = \int_{-\infty}^{\infty} \Delta k^2(t) p(t) dt = \int_{0}^{\infty} S_k(f) df$$

where $\Delta k^2(t) = (k(t) - \langle k(t) \rangle)^2$ and $p(t)$ is the probability density function. The brackets signify that the quantity in the brackets is the mean average over time.

Rearranging some of the terms in the current eqn.,

$$i^2(t) = \mu_p^2 \frac{e^2 \xi^2}{L^2}(b\hat{n}(t) + \hat{p}(t))^2$$

$$= \mu_p^2 \frac{e^2 \xi^2}{L^2}(b^2 \hat{n}^2(t) + 2b\hat{n}(t)\hat{p}(t) + \hat{p}^2(t))$$

where $b = \frac{\mu_n}{\mu_p}$. Defining

$$I_{DC}^2 = \frac{e^2 \xi^2}{L^2}(\mu_n \hat{n}_o + \mu_p \hat{p}_o)^2$$

$$= \frac{e^2 \xi^2}{L^2} \mu_p^2 (b\hat{n}_o + \hat{p}_o)^2 \quad ,$$

then [van Vliet 1958]

$$S_i(f) = \frac{I_{DC}^2}{(b\hat{n}_o + \hat{p}_o)^2}(b^2 S_{nn}(f) + 2bS_{np}(f) + S_{pp}(f)) .$$

The subscript o stands for the value at steady state [van Vliet 1958]. $S_{nn}(f)$, $S_{np}(f)$, and $S_{pp}(f)$ are defined as

$$\int_0^\infty S_{nn}(f)df = <\Delta\hat{n}^2(t)> ,$$

$$\int_0^\infty S_{np}(f)df = <\Delta\hat{n}(t)\Delta\hat{p}(t)> ,$$

and

$$\int_0^\infty S_{pp}(f)df = <\Delta\hat{p}^2(t)> .$$

There are two specific cases of interest. First, if $\hat{p}_o = 0$,

$$S_i(f) = \frac{I_{DC}^2}{\hat{n}_o^2} S_{nn}(f) .$$

This is the case for extrinsic photoconductors [van Vliet 1958]. Second, if $\Delta\hat{n}(t) = \Delta\hat{p}(t)$,

$$S_i(f) = I_{DC}^2 \left(\frac{b+1}{b\hat{n}_o + \hat{p}_o}\right)^2 S_{nn}(f) .$$

This is the case for intrinsic photoconductors when recombination centers are neglected [van Vliet 1958].

Using the Langevin equation and the Wiener-Khintchine theorem [van Vliet 1958],

$$S_{nn}(f) = 4<(\Delta\hat{n}(t))^2> \frac{\tau}{1 + \omega^2\tau^2}$$

and

$$\tau = \frac{1}{(\frac{dr}{d\hat{n}})_o - (\frac{dg}{d\hat{n}})_o} \ .$$

The subscript o stands for taking the derivative at steady state [van Vliet 1958; Burgess 1954]. It can be shown that [van Vliet 1958; Burgess 1954 Burgess 1956; van der Ziel 1976],

$$<(\Delta\hat{n}(t))^2> = g_o\tau \ .$$

Combining these equations,

$$S_i(f) = 4\,\frac{I_{DC}^2}{\hat{n}_o^2}\,g_o\tau\,\frac{\tau}{1+\omega^2\tau^2} \qquad (B.1)$$

for extrinsic photoconductors and

$$S_i(f) = 4\,I_{DC}^2(\frac{b+1}{b\hat{n}_o+\hat{p}_o})^2 g_o\tau\,\frac{\tau}{1+\omega^2\tau^2} \qquad (B.2)$$

for intrinsic photoconductors (with no recombination centers).

B.3 Calculation of the spectral noise density for specific photoconductor cases

The analysis for this section can be found in [van Vliet 1958; van der Ziel 1976, van Vliet 1967, van Vliet & Fassett 1965].

B.3.1 Extrinsic photoconductor, no compensation doping

Assume an n-type photoconductor where $\hat{p}_o=0$ and no compensation doping, then [van Vliet 1958]

$$g(\hat{n}) = \gamma(\hat{N}_D - \hat{n})$$

where, keeping with convention, $\hat{N}_D$ is the total number (not density) of donors.

$$r(\hat{n}) = \delta \hat{n}^2$$

where it has been assumed that the only levels of interest are the donor levels and the conduction band.

At steady state [van Vliet 1958],

$$g_o = \gamma(\hat{N}_D - \hat{n}_o) = \delta \hat{n}_o^2 = r_o$$

and

$$\tau = \frac{1}{2\delta \hat{n}_o + \gamma} = \frac{1}{\delta(2\hat{n}_o + \frac{\gamma}{\delta})} .$$

Using the steady state values,

$$\tau = \frac{1}{\delta(2\hat{n}_o + \frac{\hat{n}_o^2}{\hat{N}_D - \hat{n}_o})} .$$

Defining $\theta = \frac{\hat{n}_o}{\hat{N}_D}$,

$$\tau = \frac{1-\theta}{\delta \hat{N}_D \theta(2-\theta)}$$

and

$$<\Delta \hat{n}^2(t)> = g_o \tau = \hat{N}_D \frac{\theta(1-\theta)}{2-\theta} .$$

Consequently [van Vliet 1958],

$$S_i(f) = 4\frac{I_{DC}^2}{\hat{n}_o^2}\,\hat{N}_D\,\frac{\theta(1-\theta)}{2-\theta}\,\frac{\tau}{1+\omega^2\tau^2}$$

$$= 4\frac{I_{DC}^2}{\hat{n}_o}\,\frac{1-\theta}{2-\theta}\,\frac{\tau}{1+\omega^2\tau^2} \quad .$$

B.3.2 Extrinsic photoconductor, compensation doping

It is assumed all the compensated levels are ionized and that the two levels of interest are the donor levels and conduction band levels. In this situation [van Vliet 1958],

$$g(\hat{n}) = \gamma(\hat{N}_D - \hat{m}_o - \hat{n})$$

and

$$r(\hat{n}) = \delta\hat{n}_o(\hat{m}_o + \hat{n})$$

where $\hat{m}_o$ is the compensation doping value. If $\hat{m}_o \gg \hat{n}$,

$$g(\hat{n}) = \gamma(\hat{N}_D - \hat{m}_o) \quad ,$$

$$r(\hat{n}) = \delta\hat{n}\hat{m}_o \quad ,$$

$$\tau = \frac{1}{(\frac{dr}{d\hat{n}})_o - (\frac{dg}{d\hat{n}})_o} = \frac{1}{\delta\hat{m}_o} \quad ,$$

and

$$<\Delta\hat{n}^2(t)> = g_o\tau = \frac{\delta\hat{n}_o\hat{m}_o}{\delta\hat{m}_o} = \hat{n}_o \quad .$$

Combining these previous equations,

$$S_i(f) = 4\frac{I_{DC}^2}{\hat{n}_o}\frac{\tau}{1+\omega^2\tau^2} \quad .$$

B.3.3 Intrinsic and near intrinsic photoconductors, no recombination centers

There are only two levels, $\Delta\hat{p}(t) = \Delta\hat{n}(t)$. Consequently [van Vliet & Fassett 1965],

$$g(\hat{n}) = \varsigma$$

and

$$r(\hat{n}) = \beta\hat{n}\hat{p}$$

where

$$\hat{n}-\hat{p} = \hat{N}_D-\hat{N}_A \quad .$$

The thing to remember about $g(\hat{n})$ is that ς depends on the lifetime of the carrier.

Looking at the three previous equations,

$$r(\hat{n}) = \beta\hat{n}(\hat{n}-\hat{N}_D+\hat{N}_A) \quad ,$$

$$g_o = \beta\hat{n}_o\hat{p}_o \quad ,$$

$$\tau = \frac{1}{(\frac{dr}{d\hat{n}})_o-(\frac{dg}{d\hat{n}})_o} = \frac{1}{\beta(\hat{p}_o+\hat{n}_o)} \quad ,$$

and

$$<\Delta\hat{n}^2(t)> = g_o\tau = \frac{\hat{n}_o\hat{p}_o}{\hat{n}_o + \hat{p}_o} \simeq \hat{p}_o$$

for an n-type material.

From these equations,

$$S_i(f) = 4\, I_{DC}^2 \left(\frac{b+1}{b\hat{n}_o + \hat{p}_o}\right)^2 \frac{\hat{n}_o\hat{p}_o}{\hat{n}_o + \hat{p}_o} \frac{\tau}{1+\omega^2\tau^2} \quad .$$

B.3.4 Intrinsic and near intrinsic photoconductors, recombination centers

For this situation, $\tau \longrightarrow \tau_{SR}$ [van Vliet 1967; van Vliet & Fassett 1965] (where τ_{SR} is the Shockley-Read lifetime) and

$$S_i(f) = 4\, I_{DC}^2 \left(\frac{b+1}{b\hat{n}_o + \hat{p}_o}\right)^2 \frac{\hat{n}_o\hat{p}_o}{\hat{n}_o + \hat{p}_o} \frac{\tau_{SR}}{1+\omega^2\tau_{SR}^2} \quad .$$

B.3.5 Consolidation of this section's results

The overall results are presented in a concise form in table B.1. The second way of looking at the noise spectral density is to incorporate the τ into the gain - G_p, G_n, or G. In addition, in the extrinsic cases in the table, it is assumed to be n-type, but to get the p-type equations, simply change the notation from n to p wherever there is an n.

One of the interesting results of table B.1 appears in the last row. In this row, it can be seen that for the worst case RG noise situation,

$$S_i(f) = (4eG_n I_{DC}) \quad .$$

Consequently, the thermal generation needs to exceed the background radiation generation to become the dominant noise factor. Although thermal generation can be less noisy than background radiation generation, it can never be more noisy and in its worst case, will be equally noisy.

Table B.1

$S_i(f)$ for some photoconductors

	extrinsic PC (no compensation doping)	extrinsic PC (compensation doping)	intrinsic PC (no recombination centers)
g r τ	$\gamma(\hat{N}_D-\hat{n})$ $\delta(\hat{n}^2)$ $\dfrac{1-\theta}{\delta\hat{N}_D\theta(2-\theta)}$	$\gamma(\hat{N}_D-\hat{m}_o-\hat{n})$ $\delta\hat{n}(\hat{m}_o+\hat{n})$ $\dfrac{1}{\delta\hat{m}_o}$	ς $\beta\hat{n}\hat{p}$ $\dfrac{1}{\beta(\hat{p}_o+\hat{n}_o)}$
$<\Delta n^2(t)>$ I_{DC} G_n G	$\hat{N}_D\dfrac{\theta(1-\theta)}{2-\theta}$ $\dfrac{e^2\xi^2}{d_z^2}\mu_n^2\hat{n}_o^2$ $\dfrac{\mu_n\xi\tau}{d_z}$ -	$\hat{n}_o$ $\dfrac{e^2\xi^2}{d_z^2}\mu_n^2\hat{n}_o^2$ $\dfrac{\mu_n\xi\tau}{d_z}$ -	$\dfrac{\hat{n}_o\hat{p}_o}{\hat{n}_o+\hat{p}_o}$ $\dfrac{e^2\xi^2}{d_z^2}\mu_p^2(b\hat{n}_o+\hat{p}_o)^2$ - $\dfrac{\mu_p\xi\tau(1+b)}{d_z}$
$S_i(f)$	$4\dfrac{I_{DC}^2}{\hat{n}_o}\dfrac{1-\theta}{2-\theta}\dfrac{\tau}{1+\omega^2\tau^2}$	$4\dfrac{I_{DC}^2}{\hat{n}_o}\dfrac{\tau}{1+\omega^2\tau^2}$	$4I_{DC}^2\left(\dfrac{b+1}{b\hat{n}_o+\hat{p}_o}\right)^2\dfrac{\hat{n}_o\hat{p}_o}{\hat{n}_o+\hat{p}_o}\dfrac{\tau}{1+\omega^2\tau^2}$
$S_i(f)$ $(\omega\tau\ll 1)$	$(4eG_nI_{DC})\dfrac{1-\theta}{2-\theta}$	$4eG_nI_{DC}$	$(4eGI_{DC})\left(\dfrac{b+1}{b\hat{n}_o+\hat{p}_o}\right)\dfrac{\hat{n}_o\hat{p}_o}{\hat{n}_o+\hat{p}_o}$

B.4 Calculation of noise current

This section calculates the noise current for two specific photoconductors already considered [Blouke, Burgett, & Williams 1973]. There are two important equations in this section. First, the noise current is [Blouke, Burgett, & Williams 1973]

$$i_{RG}^2 = S_i(f)\Delta f \ .$$

Second, the number of carriers ($\hat{n}_o$) is related to the density (n_o) by

$$n_o d_x d_y d_z = \hat{n}_o$$

where $d_x d_y d_z$ is the volume of the photoconductor.

B.4.1 Extrinsic photoconductor (compensation doping)

Placing the result for $S_i(f)$ in sec. B.3.2 into the noise current equation in sec. B.4,

$$i_{RG_e}{}^2 = 4\frac{I_{DC_e}{}^2}{n_o}\ \frac{\tau}{1+\omega^2\tau^2}\ \frac{\Delta f}{d_x d_y d_z}$$

$$= 4\frac{q^2\mu_n^2\xi^2}{L^2}\ \frac{n_o^2(d_x d_y d_z)^2}{n_o}\ \frac{\tau}{1+\omega^2\tau^2}\ \frac{\Delta f}{d_x d_y d_z}$$

$$= 4\frac{q^2\mu_n^2\xi^2}{L^2} n_o \tau (d_x d_y d_z)\Delta f$$

$$= 4q^2 G_n^2 \frac{n_o}{\tau}(d_x d_y d_z)\Delta f$$

where it is assumed that $\omega^2\tau^2 \ll 1$ and that the detector is n-type.

B.4.2 Intrinsic photoconductor (recombination centers)

Placing the result for $S_i(f)$ in sec. B.3.4 into the noise current equation in sec. B.4,

$$i_{RG_i}{}^2 = 4\,q^2 \frac{\xi^2 \mu_p^2}{L^2} (b+1)^2 (d_x d_y d_z)^2 \frac{n_o p_o}{n_o + p_o} \frac{\tau_{SR}}{1+\omega^2 \tau_{SR}^2} \frac{\Delta f}{d_x d_y d_z}$$

$$= 4\,q^2 G_p^2 \frac{(b+1)^2}{\tau_{SR}^2} \frac{n_o p_o}{n_o + p_o} \frac{\tau_{SR}}{1+\omega^2 \tau_{SR}^2} (d_x d_y d_z) \Delta f \ .$$

For n-type material ($p_o \ll n_o$),

$$i_{RG_i}{}^2 = 4\,q^2 G_p^2 \frac{(b+1)^2}{\tau_{SR}} p_o (d_x d_y d_z) \Delta f$$

where $\omega^2 \tau_{SR}^2 \ll 1$. Since [Blouke, Burgett, & Williams 1973]

$$g_o = \frac{p_o}{\tau} = r_o = \beta n_o p_o = \beta n_i^2 \ ,$$

$$i_{RG_i}{}^2 = 4\,q^2 G_p^2 (b+1)^2 (\beta n_i^2)(d_x d_y d_z) \Delta f \ .$$

B.5 Calculation of D^*_{RG}

The AC signal current produced by the radiation is (assuming 100% modulation) [Seib & Aukerman 1973],

$$I_s^2 = 2\left(\frac{q\eta P_d G_p (1+b)}{h\nu}\right)^2$$

where $G_p(1+b)$ is the gain and P_d is the radiation power that enters the detector.

Considering when RG noise is the major noise term [Blouke, Burgett, & Williams 1973],

$$I_s^2 = 2 i_{RG}^2$$

so

$$NEP = P_d\left(\frac{I_s^2}{2i_{RG}^2} = 1\right) = \frac{hc}{\lambda q \eta G_p (1+b)} \sqrt{i_{RG}^2}$$

$$= \frac{E_\lambda}{q \eta G_p (1+b)} \sqrt{i_{RG}^2} \quad .$$

D^*_{RG} is defined as [Seib & Aukerman 1973]

$$D^*_{RG} = \frac{\sqrt{A_d \Delta f}}{NEP} = \frac{q \eta G_p (1+b)}{E_\lambda} \frac{\sqrt{A_d \Delta f}}{\sqrt{i_{RG}^2}}$$

where A_d is the area of the detector.

B.5.1 Extrinsic photoconductor (compensation doping)

Combining the results of sec. B.4.1 and sec. B.5,

$$D^*_{RG_e} = \frac{\eta}{2E_\lambda} \frac{1}{\sqrt{\frac{n_o}{\tau_e} d_{z_e}}} \qquad \text{(n–type)}$$

or

$$D^*_{RG_e} = \frac{\eta}{2E_\lambda} \frac{1}{\sqrt{\frac{p_o}{\tau_e} d_{z_e}}} \qquad \text{(p–type)}$$

where

$$\tau_e = \frac{1}{\sigma_{cap_e} v_{av} m_o} \quad .$$

σ_{cap} is defined as the capture cross section, v_{av} is the average velocity of the electron, and m_o is the compensation dopant density. This is a combination of

equations (13) and (16) in [Blouke, Burgett, & Williams 1973].

B.5.2 Intrinsic photoconductor (recombination centers)

Combining the results of sec. B.4.2 and sec. B.5,

$$D^*_{RG_i} = \frac{\eta}{2E_\lambda} \frac{1}{\sqrt{\beta n_i^2 d_{z_i}}}$$

$$D^*_{RG_i} = \frac{\eta}{2E_\lambda} \frac{1}{\sqrt{\frac{p_o}{\tau_i} d_{z_i}}} \quad \text{(n–type)}$$

where

$$\tau_i = \frac{1}{\sigma_{cap_i} v_{av} n_o} = \frac{1}{\beta n_o} .$$

This is equation (22) in Blouke.

B.5.3 Important physical parameters in D^*

Looking at secs. B.5.1 and B.5.2, D^* depends on three parameters. 1) D^* decreases as the product of the carrier concentrations in both levels increase. 2) D^* decreases as σ_{cap} increases. 3) D^* decreases as d_z increases.

The carrier concentration in both levels depends upon Fermi-Dirac statistics. In other words, the thermal generation rate changes to maintain the carrier concentration Fermi-Dirac statistics. As the temperature increases, the product of the carrier concentrations increases. For a specific temperature and an excitation gap, the product of the carrier concentrations is approximately the same, whether the photoconductor is extrinsic or intrinsic.

σ_{cap} is the carrier cross section. As σ_{cap} decreases, the thermal generation rate decreases. If there are less carriers generated over an amount of time, there is a smaller amount of noise.

d_z is approximately equal to the inverse of the absorption constant. Hence, as the absorption increases, the RG noise will decrease. This relationship reveals that the background radiation generation depends upon the radiation flux. The detector is built to detect this fixed radiation flux and hence, as the absorption coefficient decreases, the volume of the detector increases. The noise due to

radiation generation remains the same in both cases (the light generates the same number of carriers). On the other hand, the noise due to the thermal generation depends upon the volume of the detector and the larger the volume, the greater the thermal generation.

B.5.4 Comparison of D^* in extrinsic and intrinsic photoconductors

When comparing a p-type extrinsic PC and an n-type intrinsic PC, the product of the carrier concentrations at the same temperature are approximately the same while

$$\sigma_{cap_e} \gg \sigma_{cap_i}$$

and

$$d_{z_e} \gg d_{z_i} .$$

Hence,

$$D^*_{iRG} \gg D^*_{eRG}$$

if i_{RG} is the dominant noise mechanism.

Numerical analysis of Blouke's results are presented in the next section.

B.6 Numerical analysis of extrinsic and intrinsic photoconductors

The analysis for this section can be found in [Blouke, Burgett, & Williams 1973].

B.6.1 Ge:Hg and Ge:Cu extrinsic photoconductors

To calculate the generation rate, one must know the carrier concentration at steady state in the dark. It is assumed that the steady state distribution resembles a Fermi-Dirac distribution. In analogy with Smith [Smith 1978] (who looked at electrons),

$$\#\ \text{of holes} = \text{total}\ \#\ \text{of acceptors} - \#\ \text{of donors} - \#\ \text{of neutral acceptors}$$

or

$$p = N_A - N_D - N_A^o$$

$$= N_A\left(\frac{1}{1+ge^{\frac{E_A-E_F}{kT}}}\right) - N_D$$

where g equals 4 for acceptors (See [Sze 1981]) and keeping in mind that E_F depends upon N_A and N_D. Multiplying the previous equation by the denominator and p/p where

$$p = N_V e^{\frac{E_V-E_F}{kT}} ,$$

then

$$p^2 4\frac{e^{\frac{\epsilon_A}{kT}}}{N_V} + p\left(1 + 4\frac{e^{\frac{\epsilon_A}{kT}}}{N_V}N_D\right) - N_A + N_D = 0$$

where

$$\epsilon_A = E_A - E_V .$$

Dividing by $4\frac{e^{\frac{\epsilon_A}{kT}}}{N_V}$,

$$p^2 + p\left(\frac{N_V e^{\frac{-\epsilon_A}{kT}}}{4} + N_D\right) + (N_D - N_A)\frac{N_V e^{\frac{-\epsilon_A}{kT}}}{4} = 0 .$$

The solution to this equation is

$$p = -\left(\frac{N'_v + N_D}{2}\right) + 1/2\sqrt{(N'_v + N_D)^2 + 4(N_A - N_D)N'_v}$$

where

$$N'_v = \frac{N_V e^{\frac{-\epsilon_A}{kT}}}{4} .$$

If $N'_v \ll N_D$ (ie. $p_o \ll N_D = m_o$),

$$p \simeq \frac{N'_v(N_A - N_D)}{N_D} = \frac{(N_A - N_D)}{4N_D} N_V e^{\frac{-\epsilon_A}{kT}} .$$

In Blouke, $N_D \simeq N^-$ and if $N_A \gg N_D$, $N_A \simeq N^o$. Consequently,

$$p \simeq \frac{N_A}{4N_D} N_V e^{\frac{-\epsilon_A}{kT}} .$$

For an extrinsic, compensation doped PC,

$$\tau = \frac{1}{\delta m_o} = \frac{1}{\sigma_{cap_e} v_{av} m_o}$$

where $m_o = N_D$. Subsequently,

$$\frac{p_o}{\tau} \simeq \frac{N_A}{4} N_V \sigma_{cap_e} v_{av} e^{\frac{-\epsilon_A}{kT}}$$

and

$$D^*_{eRG} = \frac{\eta}{2E_\lambda} \frac{1}{\sqrt{\frac{N_A}{4} N_V \sigma_{cap_e} v_{av} e^{\frac{-\epsilon_A}{kT}} d_{z_e}}} .$$

The important parameters needed to solve this equation are listed in table B.2.

In table B.2, p_o in the Ge:Cu is too large for the assumption used when solving the quadratic equation.

Table B.2
Numerical analysis of two extrinsic photoconductors

parameters T	Ge:Hg $\epsilon_A = .089$ eV 40K	Ge:Cu $\epsilon_A = .044$ eV 40K
N_A	$2.x10^{15}cm^{-3}$	$2.x10^{15}cm^{-3}$
N_D	$10^{13}cm^{-3}$	$10^{13}cm^{-3}$
σ_{cap_e}	$10^{-13}cm^2$	$10^{-13}cm^2$
v_{av}	$10^7 \frac{cm}{sec}$	$10^7 \frac{cm}{sec}$
d_z	.55cm	.55cm
N_V	$2.9x10^{17}cm^{-3}$	$2.9x10^{17}cm^{-3}$
p_o	$8.9x10^7cm^{-3}$	$4.2x10^{13}cm^{-3}$
g_{th}	$8.9x10^{14}cm^{-3}sec^{-1}$	$4.2x10^{20}cm^{-3}sec^{-1}$
D^*_{eRG}	$1.5x10^{12}cmHz^{1/2}/W$	$4.7x10^{09}cmHz^{1/2}/W$

B.6.2 HgCdTe intrinsic photoconductors

For HgCdTe [Reynolds, Brau, Kraus, & Bate 1969], the intrinsic carrier concentration is calculated as

$$n_i = 6.96 \times 10^{13} T^{3/2} e^{-\frac{\Delta E_G}{2kT}}$$

where one can multiply by 1.5 to take nonparabolicity into account [Reynolds, Brau, Kraus, & Bate 1969].

For $Hg_{1-x}Cd_xTe$ @ 40 K, x=.20, ΔE_G=.089eV,

$$n_i = 4.33 \times 10^{10} cm^{-3} .$$

For $Hg_{1-x}Cd_xTe$ @ 40 K, x=.175, ΔE_G=.044eV,

$$n_i = 2.97 \times 10^{13} cm^{-3} .$$

From Blouke [Blouke, Burgett, & Williams 1973] and Van Vliet [van Vliet 1958] ($n_o \gg p_o$)

$$\beta = \frac{1}{n_o \tau} = \frac{\sigma_{cap_i} v_{av}}{n_o} n_o = \sigma_{cap_i} v_{av}$$

where σ_{cap_i} is the collision cross section and the thermal velocity is assumed to be

$$v_{av} \simeq 10^7 \frac{cm}{sec} .$$

Using these results,

$$D^*_{iRG} = \frac{\eta}{2E_\lambda} \frac{1}{\sqrt{\sigma_{cap_i} v_{av} n_i^2 d_{z_i}}} .$$

Table B.3 presents some important parameters and solutions to this equation.

Table B.3
Numerical analysis of two intrinsic photoconductors

parameters T	x=.204 ΔE_G = .089 eV 40K	x=1.75 ΔE_G = .044 eV 40K
σ_{cap_i}	$1.2x10^{-17}cm^2$	$1.2x10^{-17}cm^2$
v_{av}	$10^7 \frac{cm}{sec}$	$10^7 \frac{cm}{sec}$
n_i	$4.3x10^{10}cm^{-3}$	$3.0x13^{13}cm^{-3}$
d_z	$10^{-3}cm$	$10^{-3}cm$
g_{th}	$2.3x10^{11}cm^{-3}sec^{-1}$	$1.1x10^{17}cm^{-3}sec^{-1}$
D^*_{iRG}	$2.3x10^{15}cmHz^{1/2}/W$	$6.8x10^{12}cmHz^{1/2}/W$

Appendix C.

Parameters of a PEIR photoconductor

σ_{abs} - absorption cross section (cm^{-2})

The absorption coefficient, α, is related to the absorption cross section by the equation

$$\alpha = \sigma_{abs} N \quad .$$

In a PEIR photoconductor, σ_{abs} should be as large as possible (See chap. 4).

α - absorption coefficient (cm^{-1})

To produce photoconductivity in a PEIR photoconductor, the electron will be excited from the donor impurity band into the conduction band (n-type device). Since the $\hbar k$ value (crystal momentum) between the initial and final state is different, this absorption will be similar to free carrier absorption.

σ_{cap} - capture cross section (cm^{-2})

The capture cross section is related to the lifetime by

$$\tau = \frac{1}{\sigma_{cap} N_T v_{av}} \quad .$$

In a PEIR photoconductor, σ_{cap} should be as small as possible. This will consequently lower the RG noise due to thermal generation and the Johnson noise. As shown in app. D though, the capture cross section may become small enough such that parasitic resistances become a serious problem.

It appears that the worst case scenario is that the capture cross section in a PEIR photoconductor equals the capture cross section in a corresponding extrinsic photoconductor. In addition, it may be possible to lower the capture cross section just due to the freedom one has when using the MBE machine.

For instance, one could possibly construct a donor band such as that shown in Fig. C.1. Since the center is deeper at the upper end of the impurity band and since the "holes" will migrate to the upper end, it is possible to make the capture cross section smaller. This decrease in capture cross section is known to occur in DX centers in $Al_xGa_{1-x}As$ and produces what is defined as persistent photoconductivity [Lifshitz, Jayaraman, Logan, & Card 1980].

Of course, if one wants a very fast detector, a PEIR photoconductor can be compensated to increase the number of "holes" in the impurity band.

E_I - ionization energy (meV)

In the active region, E_I should be larger than the ionization energy calculated using the effective mass theory, E_{Ieff}. This is discussed more in depth in chap. 4.

In the transparent contact layer in a PEIR photoconductor, E_I should be as shallow as possible. The more shallow the doping level, the smaller the number of dopants needed to produce a degenerate semiconductor. This smaller number of dopants means that the number of free carriers is smaller and in turn, the free carrier absorption is smaller. Consequently, the transparent contact is more transparent as the dopant level in the contact is more shallow (See app. E).

ϵ_{sr} - relative static dielectric constant (unitless)

ϵ_{sr} is related to the static dielectric constant (ϵ_s) by

$$\epsilon_s = \epsilon_{sr}\ \epsilon_o \ .$$

To make the impurity band energy width as small as possible, ϵ_{sr} should be as large as possible. Conversely, as ϵ_{sr} increases, E_I decreases and the dielectric relaxation time increases.

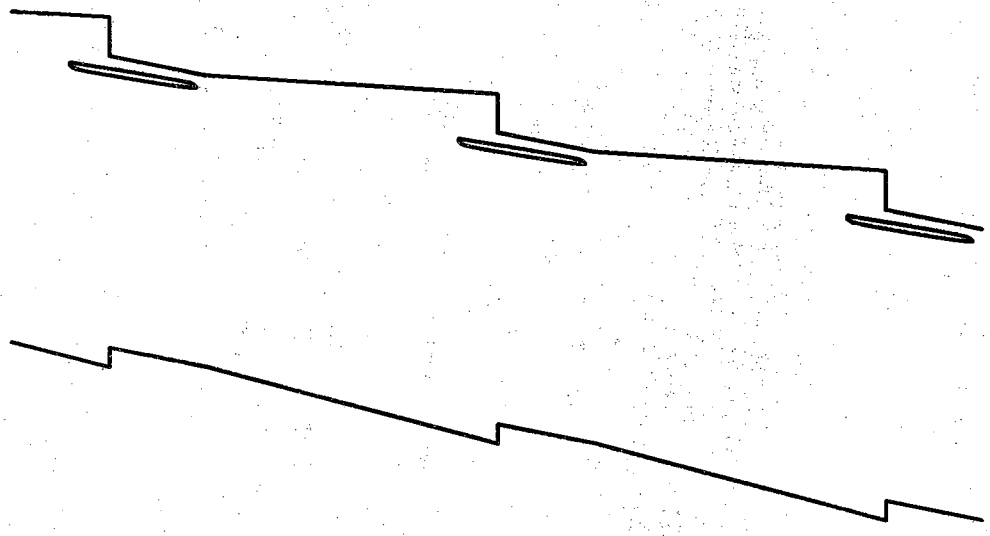

Figure C.1 One procedure how deep levels can alter capture cross sections

n_c - complex index of refraction

The complex index of refraction is related to the relative static dielectric constant by the equation

$$n_c^2 = \epsilon_{sr} \quad .$$

The complex index of refraction can be separated into a real part (n_r) and an imaginary part (κ) where

$$n_c = n_r - j\kappa \quad .$$

κ is related to the absorption (α) by

$$\kappa = \frac{\alpha\lambda}{4\pi}$$

where λ is the wavelength of radiation. Using the Kramers-Kroenig relation, n_r is related to the absorption by [Moss 1959, Pankove 1971]

$$n_r(E) = 1 + \frac{ch}{2\pi^2} P\int_0^\infty \frac{\alpha(E')}{(E')^2 - E^2}\, dE'$$

where E is the energy and P designates the Cauchy principal value of the integral [Pankove 1971].

μ - mobility (cm^2/Vsec)

In the contact layers, the mobility will approximately equal 50 (cm^2/Vsec). In the active layers in a PEIR photoconductor, the mobility will approximately equal 10^5 (cm^2/Vsec).

m_r^* - relative effective mass (unitless)

m_r^* is the relative effective mass in the conduction band (n-type device). When looking at free carrier absorption, the absorption coefficient is fairly independent of the value of m_r^*. This is due to the other terms that offset the effect of m_r^*.

The ionization energy using the effective mass theory depends directly upon the relative effective mass. E_{Ieff} becomes more shallow as m_r^* decreases.

T - temperature (K)

The temperature of operation needs to be small enough such that the background noise is the major source of noise. It appears that the temperature of operation will be higher than the temperature of operation of an extrinsic photoconductor and lower than the temperature of operation of an intrinsic photoconductor.

When growing the epitaxial layers, the growth temperature needs to be small enough to prevent diffusion of the impurity dopants.

$d_x d_y$ - area of the detector (cm^2)

Unlike conventional photoconductors, all the resistances in a PEIR photoconductor are inversely proportional to $d_x d_y$. Hence, the resistance problem discussed in app. D always exists.

d_z - depth of the photoconductor (cm)

d_z is related to $1/\alpha$. The smaller d_z becomes, the better the operation of the device. Parasitic resistances limit this type of optimization in the PEIR photoconductor.

ϕ_B - background photon flux (ph/(cm^2sec))

The smaller ϕ_B (ie., through filtering), the better the D^* becomes in a photodetector. However, as ϕ_B gets smaller, other noise terms increase in importance.

N_D - majority dopant concentration (n-type device) (cm^{-3})

In an n-type device, N_D is the majority dopant. N_D must be large enough to produce a large α.

N_A - compensation dopant concentration (n-type device) (cm^{-3})

In an n-type device, N_A is the compensation dopant. Usually N_A will be as small as possible. An exception will be if one wants a faster response [Bratt 1977].

n - free carrier concentration (n-type) (cm^{-3})

n equals the number of carriers in the conduction band. In a background limited photodetector, the value of n depends mainly upon the background photon flux.

v_{av} - average velocity of the electron (cm/sec)

At low temperatures, v_{av} approximately equals the drift velocity of the electron. In most cases, v_{av} is between 10^6 cm/sec and 10^7 cm/sec.

τ - lifetime (sec)

The lifetime is the amount of time an excess electron is in the conduction band before any electron in the conduction band recombines into its initial state before the excitation.

g - generation rate

In a PEIR photoconductor, the generation rate is the rate that an electron will be excited from the impurity band to the conduction band. The major source of generation will most likely be the background photon flux, although if the temperature is high enough, thermal generation will become the major source. In a photodetector, the generation due to the signal is usually much smaller than these generation terms.

N_D^+ - ionized majority dopant concentration (n-type) (cm^{-3})

N_D^+ should be as small as possible. The larger this concentration, the larger σ_{dos} and ΔE_C.

λ_{Di} - intrinsic Debye length (cm)

λ_{Di} becomes smaller as 1) T decreases, 2) n increases (n-type), 3) N_A increases (n-type), and 4) ϵ_s decreases. In the case of interest, the physical explanation of λ_{Di} is that it is the screening length when the acceptor impurities are taken into account.

λ_{De} - extrinsic Debye length (cm)

λ_{De} becomes smaller as 1) T decreases and 2) n increases, and 3) ϵ_s decreases. λ_{De} is the screening length due to the free carriers.

λ_D - overall screening length (cm)

λ_D is defined by the equation

$$(\lambda_D)^{-2} = (\lambda_{Di})^{-2} + (\lambda_{De})^{-2} \quad .$$

ΔE_{C1} (meV)

ΔE_{C1} is the lowering of the ionization energy due to the overlap of the ionized donor potentials.

ΔE_{C2} (meV)

ΔE_{C2} is the lowering of ionization energy due to the tunneling of a bound electron from one ionized donor to another.

ΔE_C (meV)

ΔE_C is the total lowering of the ionization energy.

σ_{dos} - Gaussian standard deviation (meV)

σ_{dos} is the standard deviation of the Gaussian potential distribution. σ_{dos} increases as 1) compensation dopants increase, 2) ionized majority dopants increase, 3) the total Debye length increases, and 4) ϵ_s decreases.

B_I - energy width of the impurity band (meV)

B_I depends upon 1) the majority dopant concentration, 2) the dielectric constant, 3) the effective mass, and 4) the ionization energy.

a_H^* - effective Bohr radius (cm)

a_H^* depends upon the dielectric constant and the inverse of the effective mass.

E_{Ieff} - Ionization energy due to the effective mass theory (meV)

E_{Ieff} is only really correct for Γ valley n-type dopants but can be extended to other electron (not hole) valleys. E_{Ieff} increases as 1) m_e^* increases and 2) ϵ_{sr} decreases. As a rough approximation, E_{Ieff} is also considered for p-type semiconductors in chap. 4.

impact ionization

Impact ionization is the ionization caused by free carriers colliding with carriers in the neutral dopants (carriers at the dopant levels) or carriers in other bands.

Zener tunneling

Zener tunneling can be thought of as field assisted tunneling. Zener tunneling can be labeled as tunneling-field emission ionization [Rideout 1975]. In reverse-biased diodes, the electron tunnels from the valence band to the conduction band. In a BIB detector or a PEIR photoconductor, the carrier would tunnel from the impurity band to the conduction band (n-type device). For an impurity potential, this type of ionization is shown in Fig. C.2. The electric field in the impurity band layer of the BIB detector or the PEIR photoconductor must be less than that needed to induce Zener tunneling.

Poole-Frenkel effect

In a BIB detector or a PEIR photoconductor, the Poole-Frenkel effect can be approximately labeled as thermal-field emission ionization [Rideout 1975]. Its effect is due to the lowering of the impurity potential and subsequent ionization because of thermal generation over the lowered barrier. For an impurity

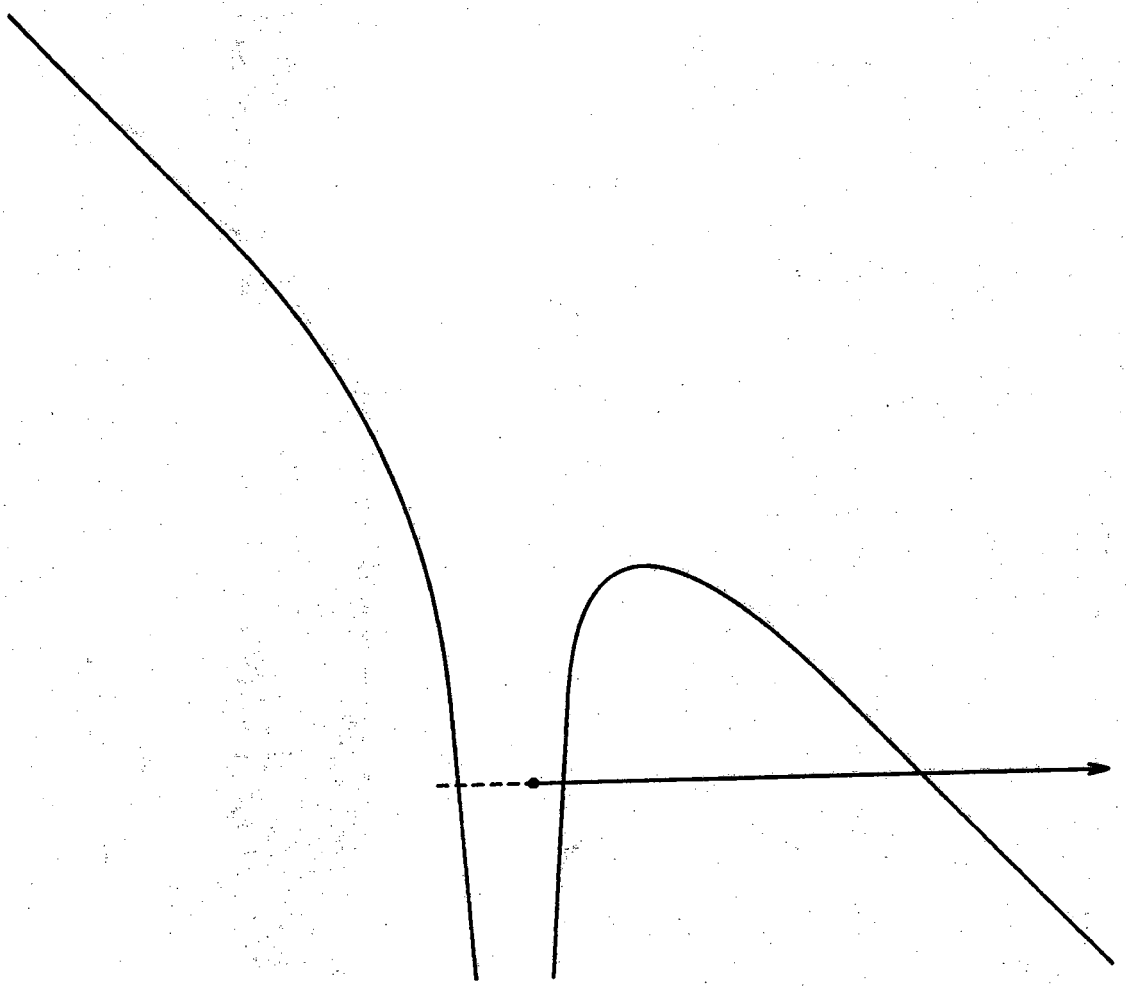

Figure C.2 Zener tunneling

potential, this type of ionization is shown in Fig. C.3. The electric field in the impurity band layer of the BIB detector or the PEIR photoconductor must be less than that needed to induce the Poole-Frenkel effect.

R - resistance (Ω)

The resistance is discussed extensively in app. D.

η - efficiency (unitless)

η should be as high as possible in a PEIR photoconductor.

$(\overline{I_n^2})^{1/2}$ - noise current (amps)

$(\overline{I_n^2})^{1/2}$ is the current due to the noise.

I_s - signal current (amps)

The signal current is the current produced by the signal radiation.

I_{op} - optical current (amps)

The optical current is the current produced by the signal radiation if the gain of the photoconductor was equal to one.

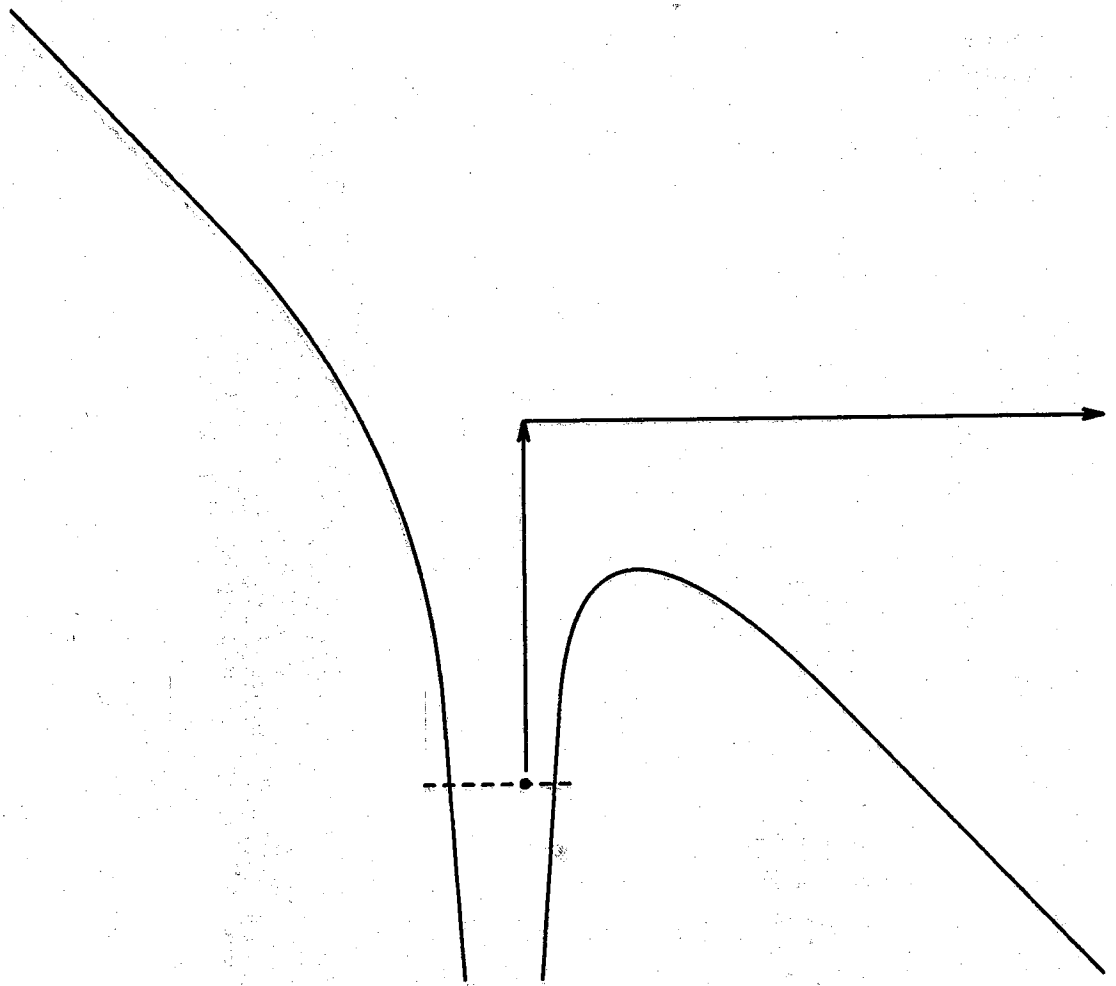

Figure C.3 Poole-Frenkel effect

I_B - background current (amps)

The background current is the current produced by the background radiation if the gain of the photoconductor was equal to one.

G - gain (unitless)

The gain is defined as the ratio of the lifetime of the electron to the time it takes the electron to traverse the photoconductor.

ξ - electric field (V/cm)

The electric field should be as large as possible in a photoconductor. The limiting factors on the electric field would be impact ionization, space charge limited current, or drift velocity saturation.

NEP - Noise equivalent power (watts)

The NEP is the amount of radiation power needed to produce a signal to noise ratio (S/N) equal to 1.

D^* - D-star ($cmHz^{1/2}$/watts)

D^* is a figure of merit that compares detectors that have different detector areas and bandwidths.

Appendix D.

Calculation of the resistance in photoconductors

There are five resistance terms of interest in the photoconductor [Schroder & Meier 1984]. These resistances are shown in Fig. D.1 for a conventional photoconductor and in Fig. D.2 for a PEIR photoconductor. R_1 is the contact resistance at one of the contacts. For a conventional photoconductor, the contacts are symmetric and R_1 should equal R_4. For a PEIR photoconductor, R_1 is the contact resistance for the back contact. Another resistance in a PEIR photoconductor not considered by [Schroder & Meier 1984] will be the resistance due to the substrate. This will be labeled the R_{1sub} and lumped with R_1. R_2 is the resistance of the active area. This resistance depends upon how far the carriers travel to reach the contacts and the area these carriers flow through. R_3 is the lateral resistance of the transparent contact and is closely related to the sheet resistance. This resistance does not exist in conventional photoconductors. It is due to the transparent contact (TC) in a PEIR photoconductor. R_4 is the contact resistance for the other contact. For a PEIR photoconductor, the resistance depends upon the shape of the metal contact connected to the front transparent contact layer. R_5 is the resistance of the metallic contacts. As shown in D.6.4, R_5 is not necessarily negligible in this device.

R_1 is calculated in sec. D.1. R_2 is calculated in sec. D.2. R_3 is calculated in sec. D.3. R_4 is calculated in sec. D.4. Some numerical examples accompany each section. Section D.5 compares each resistance in conventional photoconductors and PEIR photoconductors. The conventional photoconductor resistances are calculated from actual cases. The PEIR photoconductor resistances are then calculated as certain parameters are varied. These parameters are 1) detector area and contact area, 2) concentration, 3) background photon flux, 4) layer thickness, and 5) efficiency. Section D.6 presents a set of resistance equations based upon the results of the previous sections and the resistance values of a practical PEIR photoconductor that will be tested.

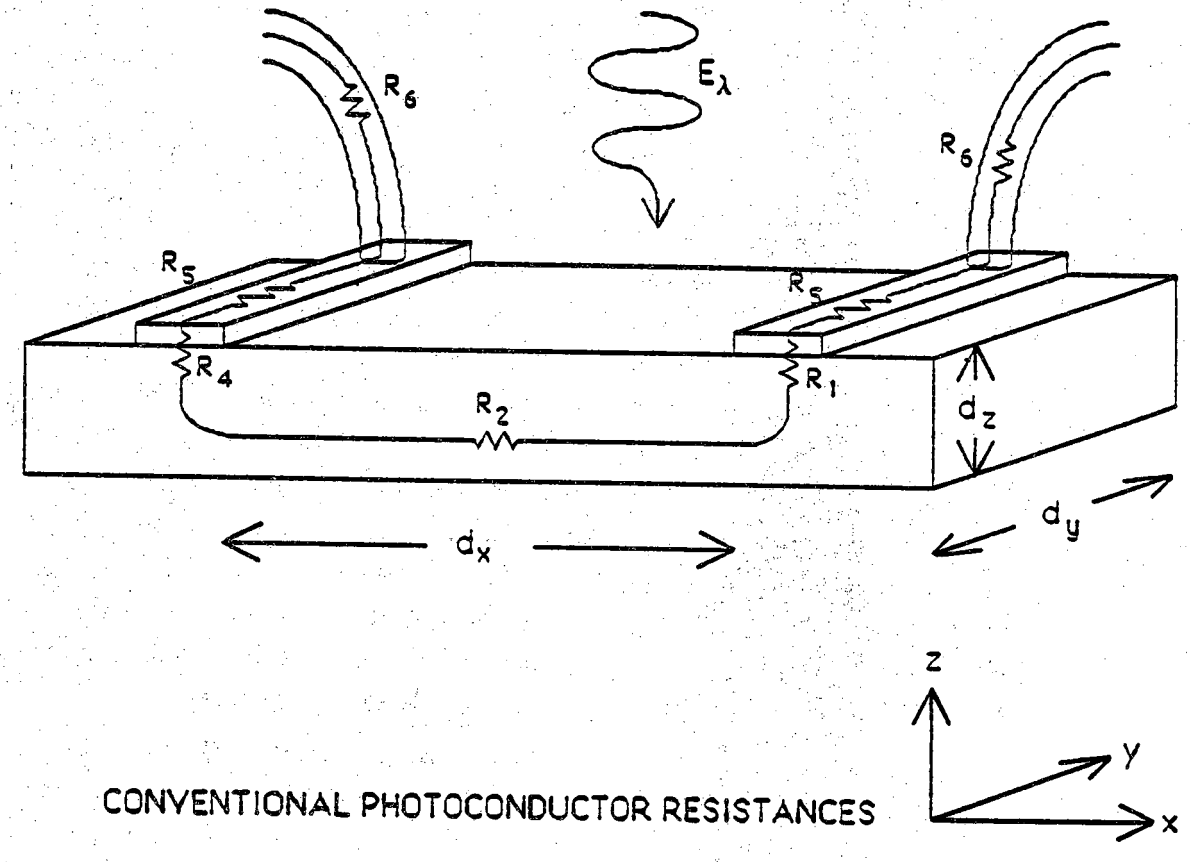

Figure D.1 Resistances in a conventional photoconductor

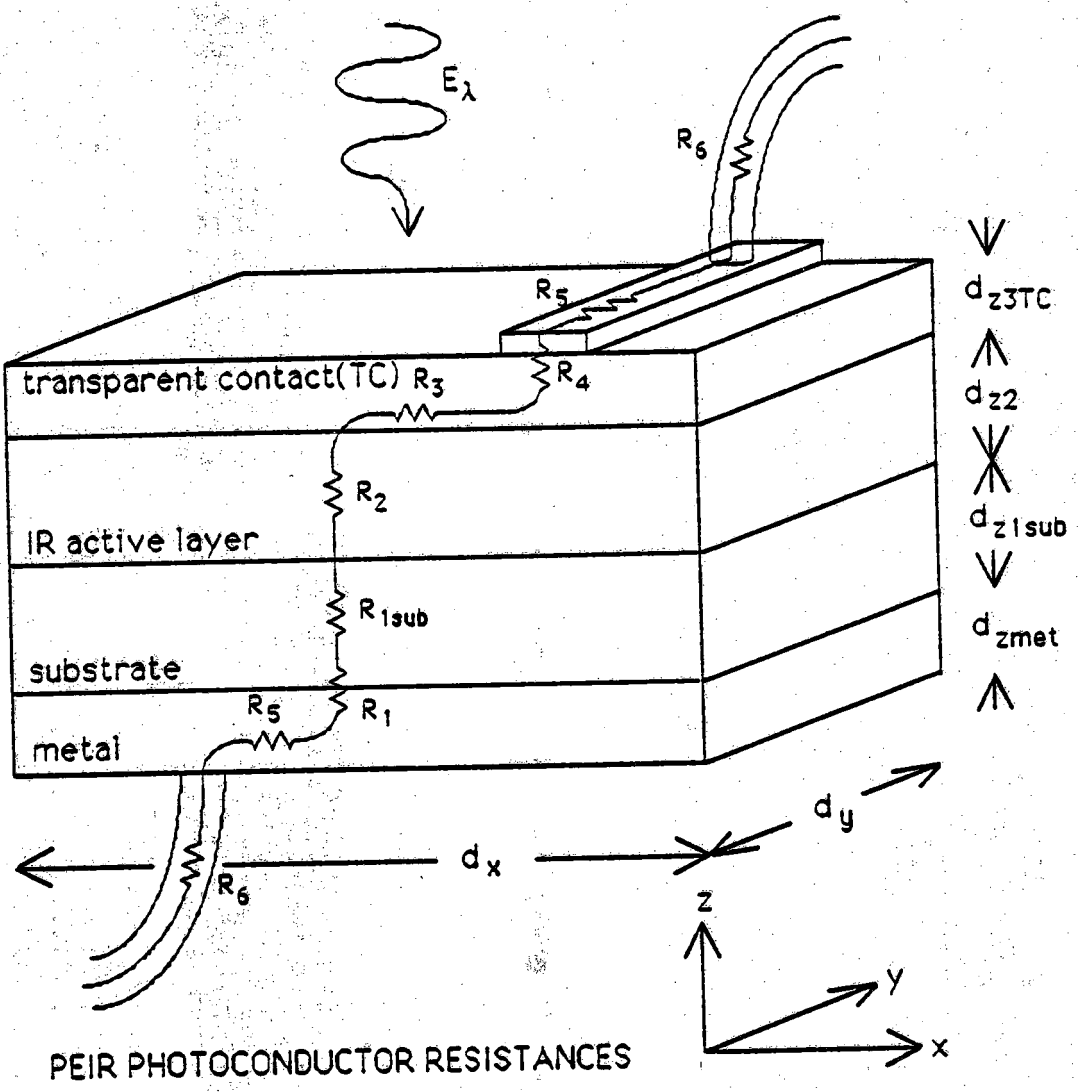

Figure D.2 Resistances in a PEIR photoconductor

D.1. R_1 - The contact resistance of the back contact

The calculation of the contact resistance, R_1, is straightforward if one knows the contact resistivity. The contact resistivity is defined as [Schroder & Meier 1984; Brauslau 1983; Piotrowska, Guivarc'h, & Pelous 1983]

$$r_c = \left(\frac{\partial J}{\partial V} \right)^{-1}_{V=0}$$

where r_c is in units of Ωcm^2. R_1 can then be approximated as

$$R_1 = \frac{r_{c1}}{A_{c1}}$$

where r_{c1} is the value of r_c at the contact with the resistance label R_1 and A_{c1} is the metal contact area through which the current flows. It is assumed in this equation that the current is approximately the same over A_{c1} [Piotrowska, Guivarc'h, & Pelous 1983].

D.1.1 Conventional photoconductor

A_{c1} can have two possible values for a conventional photoconductor (See Fig. D.1). A_{c1} will equal the smaller of the areas Ld_y or $L_T d_y$ [Schroder & Meier 1984] where L is the actual width of the metal strip (See Fig. D.1) and [Schroder & Meier 1984]

$$L_{T1} = (r_{c1}/R_\square)^{1/2} \quad .$$

$R_\square$ is known as the sheet resistance and is defined as [Green 1982]

$$R_\square = \frac{\rho}{d_T}$$

where ρ is the resistivity and d_T is the thickness of the layer through which the current is flowing. In Fig. D.1, d_T equals d_z. L_T can be thought of as the distance under the metal the current in the semiconductor layer travels before the current is redirected into the metal [Schroder & Meier 1984].

Representative values of $R_\square$ for extrinsic and intrinsic photoconductors are shown in table D.1 for a 300 K background. With the low temperature of operation, the free carrier concentration, n, will be due to the 300 K blackbody photon flux. The values of the mobility, μ, n and d_z are taken from sec. D.2. The best way to make an ohmic contact is to degenerately dope the semiconductor directly under the metal. It will be assumed that the semiconductor is doped enough such that $r_{c1} = 10^{-5}\Omega cm^2$ [Schroder & Meier 1984].

Assuming the metal contact is wider than L_{T1},

$$R_1 = \frac{r_{c1}}{L_{T1} d_y} = 1.0\Omega$$

where $d_y = 100\ \mu m$ for the representative intrinsic photoconductor and

$$R_1 = 3.6\Omega$$

where $d_y = 100\ \mu m$ for the representative extrinsic photoconductor.

D.1.2 PEIR photoconductor

The resistance due to the substrate can be calculated as

$$R_{1sub} = \frac{1}{q\mu_{p1sub} n_{1sub}} \frac{d_{z1sub}}{d_x d_y} \qquad \text{(n—type)} \ ,$$

$$R_{1sub} = \frac{1}{q\mu_{p1sub} p_{1sub}} \frac{d_{z1sub}}{d_x d_y} \qquad \text{(p—type)} \ .$$

The substrate is degenerately doped so that at low temperatures there is no freeze out of carriers. Assuming a p-type detector, Let $\mu_{p1sub} = 50 cm^2/V—sec$ (The mobility is being limited by carrier-carrier scattering), $d_{z1sub} = 300\mu m$, $d_x = d_y = 100\mu m$ and $p_{1sub} = 10^{19} cm^{-3}$,

Table D.1.
Some representative values of $R_{\square}$ and L_{T1}

	μ_{n2} (cm^2/V–sec)	n_2 (cm^{-3})	d_z (μm)	$R_{\square}$ ($\Omega/\square$)	L_{T1} (μm)
extrinsic PC	10^5	$5x10^{12}$	500.	125.	2.8
intrinsic PC	10^5	$3x10^{15}$	10.	10.4	9.8

$$R_{1sub} = 3.75\Omega \ .$$

The area for R_1 will be assumed to be the detector area $d_x d_y$. Letting $r_{c1} = 10^{-5}\Omega cm^2$, a representative value is

$$R_1 = 10^{-1}\Omega \ .$$

D.2. R_2 - The resistance of the IR active area

The resistance of the active layer is

$$R_2 = \frac{1}{q(\mu_{n2} n_2 + \mu_{p2} p_2)} \frac{L}{d_T W}$$

where L is the length of the active layer that the electrons traverse. $d_T W$ is the area through which the electrons travel.

If the background photon flux is large enough and depending upon the type of photoconductor,

$$n_2 = g\tau$$

or

$$p_2 = g\tau$$

where τ is the carrier lifetime and

$$g = \frac{\phi_B \eta}{d_\alpha} \ .$$

d_α is the active area thickness in the direction of propagation and η is the quantum efficiency. This thickness must be wide enough to collect most of the radiation.

These three equations in this section are now defined for the conventional photoconductor shown in Fig. D.1 and for the PEIR photoconductor shown in Fig. D.2.

D.2.1 Conventional photoconductors

The resistance of the IR active layer is

$$R_2 = \frac{1}{q(\mu_{n2} n_2 + \mu_{p2} p_2)} \frac{d_x}{d_y d_z} .$$

For a 300 K blackbody background and an n-type extrinsic or a p-type intrinsic photoconductor,

$$n = g\tau$$

where

$$g = \frac{\phi_B \eta}{d_z} .$$

Some representative values are now calculated for extrinsic and intrinsic photoconductors.

D.2.1.1 Intrinsic photoconductor

For T_B=300K, $\lambda \leq 13\mu$m, and assuming η=100%,

$$\phi_B = 10^{18} \text{cm}^{-2}\text{sec}^{-1} .$$

Additionally, it will be assumed in this section that

$$\eta = 100\%$$

$$v_{av} = 10^7 \frac{cm}{sec} \quad ,$$

$$\sigma_{cap_i} = 10^{-17} cm^2 \quad ,$$

$$\mu_{n2} = \mu_{p2} = 10^5 \frac{cm^2}{V-sec} \quad ,$$

$$d_x \text{ X } d_y \text{ X } d_z = 100\mu m \text{ X } 100\mu m \text{ X } 10\mu m \quad .$$

For these numbers, the generation rate becomes

$$g = \frac{\phi_B \eta}{d_z} \simeq 10^{21} cm^{-3} sec^{-1} \quad .$$

For an n-type intrinsic photoconductor with no Shockley-Hall-Read (SHR) recombination [Borrello, Roberts, Breazeale, & Pruett 1971],

$$p_2 = g\tau = \frac{g}{\sigma_{cap_i} v_{av} n_2} \quad .$$

Similarly, for p-type,

$$n_2 = g\tau = \frac{g}{\sigma_{cap_i} v_{av} p_2} \quad .$$

Using the numbers shown above,

$$n_2 \simeq 3x10^{15} cm^{-3}$$

for FOV = 180° and

$$n_2 \simeq 2x10^{15}cm^{-3}$$

for FOV = 60° where FOV is an abbreviation for field of view [Kruse 1977].

For simplicity, assume that $\mu_{n2}n_2 = \mu_{p2}p_2$, then for the case of interest,

$$R_2 = 10.4\Omega \qquad FOV = 180°$$

and

$$R_2 = 15.7\Omega \qquad FOV = 60° \ .$$

D.2.1.2 Extrinsic photoconductor

For T_B=300K, $\lambda \leq 13\mu m$, and assuming η=100%,

$$\phi_B = 10^{18}cm^{-2}sec^{-1} \ .$$

In reality, ϕ_B is less than this value because the absorption cross section out of a dopant level peaks at a certain energy approximately equal to the ionization energy. Additionally, it will be assumed in this section that

$$\eta = 100\%$$

$$v_{av} = 10^7 \frac{cm}{sec} \ ,$$

$$\sigma_{cap_e} = 10^{-13}cm^2 \ ,$$

$$\mu_{n2} = 10^5 \frac{cm^2}{V-sec} \qquad (n-type) \ ,$$

$$\mu_{p2} = 10^5 \frac{cm^2}{V-sec} \qquad (p-type) \ ,$$

and

$$d_x \ X \ d_y \ X \ d_z = 100\mu m \ X \ 100\mu m \ X \ 500\mu m \ .$$

For these numbers, the generation rate becomes

$$g = \frac{\phi_B \eta}{d_z} \simeq \ 2x10^{19} cm^{-3} sec^{-1} \ .$$

The concentration depends upon how much the material is compensated. For n-type,

$$n = g\tau = \frac{g}{\sigma_{cap} v_{av} (n_2 + N_{A2}^-)}$$

where N_A^- is the compensation dopant concentration. For p-type,

$$p = g\tau = \frac{g}{\sigma_{cap} v_{av} (p_2 + N_{D2}^+)}$$

where N_D^+ is the compensation dopant concentration. The resistance for an extrinsic detector is

$$R_2 = \frac{1}{q\mu_{n2} n_2} \frac{d_x}{d_y d_z} \qquad (n-type)$$

or

$$R_2 = \frac{1}{q\mu_{p2} p_2} \frac{d_x}{d_y d_z} \qquad (p-type) \ .$$

Carrier concentrations and resistances are shown in table D.2 as the compensation and field of view are varied for several extrinsic photoconductors.

D.2.2 PEIR photoconductors

The resistance of the IR active layer is

$$R_2 = \frac{1}{q\mu_{n2} n_2} \frac{d_{z2}}{d_x d_y} \qquad \text{(n—type)}$$

or

$$R_2 = \frac{1}{q\mu_{p2} p_2} \frac{d_{z2}}{d_x d_y} \qquad \text{(p—type)} \ .$$

For a 300 K blackbody background,

$$n_2 = g\tau \qquad \text{(n—type)}$$

or

$$p_2 = g\tau \qquad \text{(p—type)}$$

where

$$g = \frac{\phi_B \eta}{d_{z2}} \ .$$

When these sets of equations are compared with the equations in sec. D.2.1 and the geometries of the devices in Figs. D.1 and D.2 are considered, it can be seen that the resistance in a PEIR photoconductor will be much smaller than the resistance in conventional extrinsic photoconductors. A representative value is now calculated for PEIR photoconductor to show how the resistance compares with the conventional photoconductors in sec. D.2.1.

For T_B=300K, $\lambda \leq 13\mu$m, and assuming η=100%,

Table D.2
$R_2(\Omega)$ for some extrinsic photoconductors

N_{A2}^- (cm^{-3})	FOV	n_2 (cm^{-3})	R_2 (Ω)
$\leq 10^{10}$	180°	4.5×10^{12}	278.
$\leq 10^{10}$	60°	3.2×10^{12}	391.
10^{13}	180°	2×10^{12}	625.
10^{13}	60°	1.4×10^{12}	893.
10^{14}	180°	2×10^{11}	6,250.
10^{14}	60°	1.4×10^{11}	8,930.

$$\phi_B = 10^{18} cm^{-2} sec^{-1} \quad .$$

In a similar manner as extrinsic photoconductors, ϕ_B is less than this value because the absorption cross section out of a dopant level peaks at a certain energy approximately equal to the ionization energy. Additionally, it will be assumed in this section that

$$v_{av} = 10^7 \frac{cm}{sec} \quad ,$$

$$\sigma_{cap_e} = 10^{-13} cm^2 \quad ,$$

$$\mu_{n2} = 10^5 \frac{cm^2}{V-sec} \qquad (n-type) \quad ,$$

$$\mu_{p2} = 10^5 \frac{cm^2}{V-sec} \qquad (p-type) \quad ,$$

$$d_x \text{ X } d_y \text{ X } d_{z2} = 100\mu m \text{ X } 100\mu m \text{ X } 2\mu m \quad .$$

For these numbers, the generation rate becomes

$$g = \frac{\phi_B \eta}{d_{z2}} \simeq 5x10^{21} cm^{-3} sec^{-1} \quad .$$

Carrier concentrations and resistances are shown in table D.3 as the compensation and field of view are varied for several PEIR photoconductors.

D.3. R_3 - The lateral resistance of the contact

R_3 exists only in detectors which have a transparent contact. Hence, conventional photoconductors don't have an R_3 while a PEIR photoconductor does.

Table D.3
$R_2(\Omega)$ for some PEIR photoconductors

N_{A2}^{-} (cm^{-3})	FOV	n_2 (cm^{-3})	R_2 (Ω)
$\leq 10^{11}$	180°	$7x10^{13}$	1.8
$\leq 10^{11}$	60°	$5x10^{13}$	2.5
10^{14}	180°	$<5x10^{13}$	2.5
10^{14}	60°	$<3.5x10^{13}$	3.6
10^{15}	180°	$5x10^{12}$	25.
10^{15}	60°	$3.5x10^{12}$	36.

R_3 depends upon 3 parameters: 1) The shape and spacing of the metal grid that contacts to the transparent contact; 2) the dopant concentration of the degenerately doped transparent contact and 3) the thickness of the transparent contact.

The last two parameters are incorporated into the sheet resistance

$$R_{\square} = \frac{\rho}{d_{z3TC}} = \frac{1}{q\mu_n n_{3TC} d_{z3TC}}$$

for n-type transparent contacts and

$$R_{\square} = \frac{1}{q\mu_p p_{3TC} d_{z3TC}}$$

for p-type transparent contacts. For degenerately doped contacts, the carrier concentration is equal to the dopant concentration.

The shape of the grid and the spacing between the metal strips affect R_3. There are two ways to calculate an effective resistance R_3 for the transparent contact and a specific metal grid. One is to calculate an effective voltage

$$V_{eff} = \int I \, dR$$

and the other is to calculate an effective power loss [Green 1982]

$$P_{eff} = \int I^2 \, dR \ .$$

R_3 is larger when the effective voltage method is used. In addition, it appears the effective voltage method more correctly compares R_3 with R_2 for a current. Consequently, the effective voltage method is presented.

The rectangular grid is considered first. This grid is made up of parallel contacts that can be connected at the ends by what are defined as busbars [Green 1982]. The area of the transparent contact between the grids will be a rectangle (See Fig D.3). The length of the contact will be set equal to b and the width will equal S. The current through the transparent contact can be calculated as

$d_y \gg S$

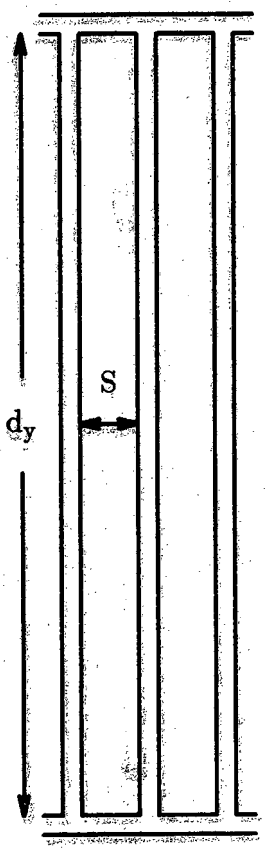

Figure D.3 Rectangular grid schematic

$$I(y) = \int_0^y J\, b\, dy' = Jby$$

where J is the current density flowing into the transparent contact and is assumed to be constant, y = 0 at the midpoint between the metal grids and increases to S/2 at the metal grids.

The effective voltage is calculated as

$$V_{eff} = \int_0^{S/2} I(y)dR = \int_0^{S/2} Jby \frac{R_\square dy}{b}$$

$$= Jb\frac{S}{2}\left(\frac{R_\square S}{4b}\right) .$$

This value presented for an effective voltage can now be used to calculate an effective resistance R_3. To properly compare the voltages and subsequently, the resistances between the IR active layer and the transparent contact layer, the effective voltage should be multiplied by the area of the IR active layer through which the current flows. In the case of a PEIR photoconductor shown in Fig. D.2 this area equals $d_x d_y$ and

$$V_{eff} = [Jd_x d_y]\frac{bS}{2d_x d_y}\left(\frac{R_\square S}{4b}\right) .$$

From this equation,

$$R_3 = \frac{V_{eff}}{Jd_x d_y} = \left(\frac{R_\square S^2}{8d_x d_y}\right) .$$

For the square grid with a spacing SxS (See Fig. D.4),

$$I(y) = \int_0^y J\, y' dy' = J\frac{y^2}{2} .$$

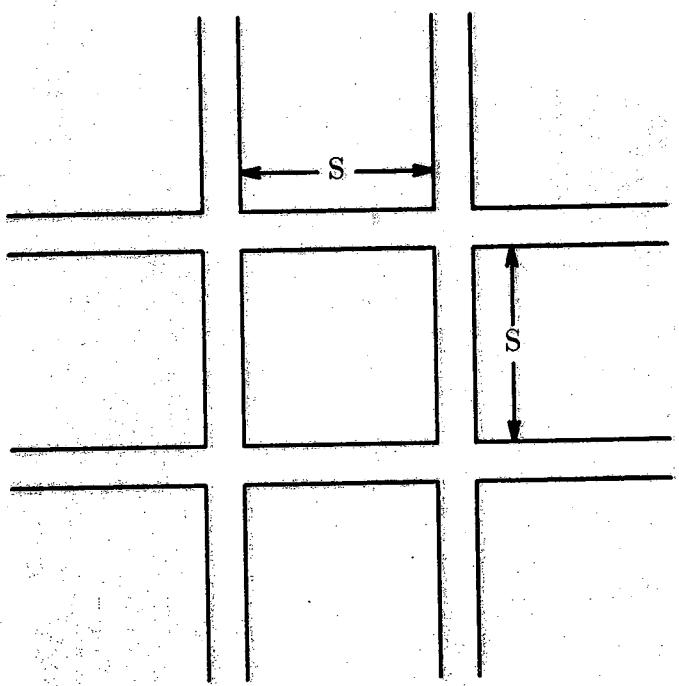

Figure D.4 Square grid schematic

The effective voltage becomes

$$V_{eff} = \int_0^{S/2} I(y)dR = \int_0^{S/2} J\frac{y^2}{2}\,\frac{R_\square dy}{b}$$

$$= \frac{J}{2}\,\frac{S^2}{4}\left(\frac{R_\square}{6}\right) .$$

Using the same procedure as for the rectangular grid,

$$V_{eff} = [Jd_x d_y]\,\frac{S^2}{8d_x d_y}\left(\frac{R_\square}{6}\right) .$$

From this equation,

$$R_3 = \frac{V_{eff}}{Jd_x d_y} = \left(\frac{R_\square S^2}{48 d_x d_y}\right) .$$

Some R_3 values for n-type and p-type transparent contacts are shown in table D.4 and table D.5, respectively. The grids will be assumed to be square. d_{z3TC} must be thin enough to let the radiation through, yet thick enough to produce a small resistance. The mobilities are found in [Sze 1981]. These are room temperature mobilities. For lower temperatures, the mobilities will be approximately the same. It is assumed that the material is degenerately doped. $S=d_x=d_y=100\mu m$. In this case, $R_3 = R_\square/48$ and the area equals $d_x d_y$.

D.4. R_4 - Contact resistance for contacts to the front contact

Most of the theory for this section has already been presented in sec. D.1. Section D.4.1 briefly discusses the second contact for a conventional photoconductor. Section D.4.2 discusses the contact to the transparent layer for a PEIR photoconductor.

Table D.4.
$R_3(\Omega)$ for n-type
GaAs transparent contacts

d_{z3TC}(Å)	$R_3(\Omega)$ $n_{3TC}=10^{18}cm^{-3}$ $\mu_{n3TC} \simeq 3x10^3 \frac{cm^2}{V-sec}$	$3x10^{18}cm^{-3}$ $2x10^3 \frac{cm^2}{V-sec}$
100.	43.	22.
300.	14.	7.2
500.	8.7	4.3
1000.	4.3	2.2

Table D.5.
$R_3(\Omega)$ for p-type
GaAs transparent contacts

d_{z3TC}(Å)	$R_3(\Omega)$ $p_{3TC}=7x10^{18}cm^{-3}$ $\mu_{p3TC} \simeq 80 \frac{cm^2}{V-sec}$	$10^{19}cm^{-3}$ $50 \frac{cm^2}{V-sec}$
100.	-	260.
300.	77.	87.
500.	46.	52.
1000.	23.	-

D.4.1 Conventional photoconductors

Since the contacts are symmetric for the conventional photoconductor presented in Fig. D.1, $R_1=R_4$. For different contacts, the theory presented in sec. D.1 should be adequate.

D.4.2 PEIR photoconductors

Using the results of sec. D.1, R_4 for a rectangular grid is (approximation assumes the metal width is negligible)

$$R_4 = \frac{r_{c4}}{(\frac{d_y}{S}d_x)(2L_{T4})} = \frac{r_{c4}S}{2L_{T4}(d_x d_y)} \qquad (L>2L_{T4})$$

or

$$R_4 = \frac{r_{c4}S}{L(d_x d_y)} \qquad (L<2L_{T4})$$

where S is the distance between the fingers.

R_4 for a square grid is

$$R_4 = \frac{r_{c4}}{(\frac{d_x}{S}d_y + \frac{d_y}{S}d_x)(2L_{T4})} = \frac{r_{c4}S}{4L_{T4}(d_x d_y)} \qquad (L>2L_{T4})$$

or

$$R_4 = \frac{r_{c4}S}{2L(d_x d_y)} \qquad (L<2L_{T4})$$

where S is the width of the square metal grid. If the metal strip thickness L is more thin than twice the thickness L_{T4}, L_{T4} will be replaced by L. The factor 2 is used assuming that photocurrent is generated on both sides of the metal strips causing the current to flow through both sides.

Tables D.6 and D.7 present R_4 values for a PEIR photoconductor for metal contacts to n-type and p-type GaAs. The r_c values can be found in [Schroder & Meier 1984]. $S=d_x=d_y=100\mu m$.

D.5. Comparison of resistances for different situations

This section compares the resistances for different situations. Section D.5.1 presents the important equations for the conventional photoconductors (intrinsic and extrinsic) and several tables that compare the resistances for these equations. Section D.5.2 presents the important equations for a PEIR photoconductor and several tables that compare the resistances for these equations.

D.5.1 Conventional photoconductor

D.5.1.1 Intrinsic photoconductor

The important auxiliary equations are

$$g = \phi_B \eta / d_z \ ,$$

$$p_2 = \frac{g}{\sigma_{cap} v_{av} n_2} \qquad \text{(n–type)} \ ,$$

$$n_2 = \frac{g}{\sigma_{cap} v_{av} p_2} \qquad \text{(p–type)} \ .$$

Assume most of the carriers are generated by background radiation, then

$$\mu_{n2} n_2 = \mu_{p2} p_2 \ ,$$

or

$$\mu_{n2} n_2 + \mu_{p2} p_2 = 2\mu_{n2} n_2 \ ,$$

Table D.6.
$R_4(\Omega)$ for metal contacts
to n-type GaAs transparent contacts

N_{D3TC} (cm^{-3})	d_{z3TC} (Å)	$R_\square$ ($\frac{\Omega}{\square}$)	r_{c4} (Ωcm^2)	L_{T4} (cm)	R_4 (Ω)
$1x10^{18}$	100.	2,080.	$1x10^{-5}$	$6.9x10^{-5}$	3.6
	300.	694.	$1x10^{-5}$	$1.2x10^{-4}$	2.1
	500.	416.	$1x10^{-5}$	$1.6x10^{-4}$	1.6
	1000.	208.	$1x10^{-5}$	$2.2x10^{-4}$	1.1
$3x10^{18}$	100.	1,040.	$3x10^{-6}$	$5.4x10^{-5}$	1.4
	300.	347.	$3x10^{-6}$	$9.3x10^{-5}$	.81
	500.	208.	$3x10^{-6}$	$1.2x10^{-4}$	.63
	1000.	104.	$3x10^{-6}$	$1.7x10^{-4}$	.44

Table D.7.
$R_4(\Omega)$ for metal contacts
to p-type GaAs transparent contacts

N_{A3TC} (cm^{-3})	d_{z3TC} Å	$R_\square$ ($\frac{\Omega}{\square}$)	r_{c4} (Ωcm^2)	L_{T4} (cm)	R_4 (Ω)
$7x10^{18}$	300.	3,700.	$2x10^{-4}$	$2.3x10^{-4}$	22.
	500.	2,200.	$2x10^{-4}$	$3.0x10^{-4}$	17.
	1000.	1,100.	$2x10^{-4}$	$4.3x10^{-4}$	12.
$1x10^{19}$	100.	12,500.	$1x10^{-5}$	$2.8x10^{-5}$	8.9
	300.	4,170.	$1x10^{-5}$	$4.9x10^{-5}$	5.1
	500.	2,500.	$1x10^{-5}$	$6.3x10^{-5}$	4.0

$$R_{\square} = \frac{1}{2q\mu_{n2}n_2 d_z} \quad ,$$

and

$$L_{T1} = L_{T4} = (r_{c1}/R_{\square})^{1/2} \quad .$$

The resistance equations are (assuming $d_x = d_y$)

$$R_1 = r_{c1}/L_{T1}d_y \quad ,$$

$$R_2 = \frac{1}{2q\mu_{n2}n_2 d_z} \quad ,$$

and

$$R_4 = R_1 \quad .$$

Tables D.8 and D.9 present the resistance values in some intrinsic photoconductors as d_z and λ_d (the wavelength the detector is designed to detect) is varied. The parameters used in tables D.8 and D.9 are as follows.

d_x X d_y – .1mm X .1mm

d_z – See tables D.8 & D.9

ϕ_B – See tables D.8 & D.9

$\sigma_{cap_i} = 10^{-17}$ cm^2

$v_{av} = 10^7$ cm/sec

$p_2 = n_2$ – See tables D.8 & D.9

$\mu_{p2} = 10^5$ cm^2/(V–sec)

Table D.8
Resistance values for
several HgCdTe photoconductors where $d_z = 10\mu m$

λ_d (μm)	ϕ_B ($cm^{-2}sec^{-1}$)	n_2 (cm^{-3})	$R_\square$ ($\Omega/\square$)	L_{T1} (μm)	R_1 (Ω)	R_2 (Ω)
10.6	$4.6x10^{17}$	$2.1x10^{15}$	15.	8.2	1.2	15.
12.0	$6.0x10^{17}$	$2.4x10^{15}$	13.	8.8	1.1	13.
13.5	$8.5x10^{17}$	$2.9x10^{15}$	11.	9.5	1.1	11.
14.5	$9.3x10^{17}$	$3.0x10^{15}$	10.	10.	1.0	10.
4.5	$4.9x10^{15}$	$2.2x10^{14}$	142.	2.6	3.9	142.

Table D.9
Resistance values for
several HgCdTe photoconductors where $d_z = 5\mu m$

λ_d (μm)	ϕ_B ($cm^{-2}sec^{-1}$)	n_2 (cm^{-3})	$R_\square$ ($\Omega/\square$)	L_{T1} (μm)	R_1 (Ω)	R_2 (Ω)
10.6	$4.6x10^{17}$	$3.0x10^{15}$	21.	6.9	1.4	21.
12.0	$6.0x10^{17}$	$3.5x10^{15}$	18.	7.5	1.3	18.
13.5	$8.5x10^{17}$	$4.1x10^{15}$	15.	8.1	1.2	15.
14.5	$9.3x10^{17}$	$4.3x10^{15}$	15.	8.3	1.2	15.
4.5	$4.9x10^{15}$	$3.1x10^{14}$	202.	2.2	4.5	202.

$\mu_{n2} = 10^5$ cm^2/(V–sec)

$r_{c1} = r_{c4} = 10^{-5}$ Ωcm^2

$R_\square$ – See tables D.8 & D.9

$L_{T1} = L_{T4}$ – See tables D.8 & D.9

$\eta = 100\%$

FOV = 60°

λ_{max} is the wavelength at which D^* has its maximum value. These numbers compare well with the Santa Barbara Research Center (SBRC) catalog.

D.5.1.2 Extrinsic photoconductors

The important auxiliary equations are

$$g = \phi_B \eta / d_z = \phi_B \eta \alpha \ ,$$

where α is the absorption coefficient and equals the absorption cross section [Bratt 1977] times the maximum impurity dopant that can be incorporated without impurity conduction [Bratt 1977] or

$$\alpha \simeq N_i(\max)\, \sigma_{abs} \ ,$$

$$n_2 = \frac{g}{\sigma_{cap} v_{av} (n_2 + N_A^-)} \qquad \text{(n–type)} \ ,$$

$$p_2 = \frac{g}{\sigma_{cap} v_{av} (p_2 + N_D^+)} \qquad \text{(p–type)} \ ,$$

$$R_\square = \frac{\alpha}{q \mu_{n2} n_2} \qquad \text{(n–type)} \ ,$$

$$R_{\square} = \frac{\alpha}{q\mu_{p2}p_2} \qquad \text{(p—type)} \ ,$$

and

$$L_{T1} = L_{T4} = (r_{c1}/R_{\square})^{1/2} \ .$$

The resistance equations are (assuming $d_x = d_y$)

$$R_1 = r_{c1}/L_{T1}\, d_y \ ,$$

$$R_2 = \frac{\alpha}{q\mu_{n2}n_2} \qquad \text{(n—type)} \ ,$$

$$R_2 = \frac{\alpha}{q\mu_{p2}p_2} \qquad \text{(p—type)} \ ,$$

and

$$R_4 = R_1 \ .$$

Tables D.10 and D.11 present the resistance values in extrinsic photoconductors utilizing several host semiconductor:impurity dopant systems. The parameters used in tables D.10 and D.11 are as follows.

d_x X d_y — .1mm X .1mm

$d_z = \frac{1}{\alpha}$ — See tables D.10 & D.11

ϕ_B — See table D.10

$N_D^+ = 10^{13}\text{cm}^{-3}$ (p—type)

$N_A^- = 10^{13}\text{cm}^{-3}$ (n—type)

Table D.10
Parameter values for several extrinsic photoconductors

	λ_d (μm)	σ_{cap_e} (cm^2)	α (cm^{-1})	N_i(max) (cm^{-3})	ϕ_B ($cm^{-2}sec^1$)	n_2, p_2 (cm^{-3})
Ge:Au	5.0	10^{-13}	8.	10^{17}	$1.2x10^{16}$*	$9.6x10^9$
Ge:Hg	10.6	$3.6x10^{-12}$	24.	$6x10^{16}$	$1.5x10^{17}$	10^{10}
Ge:Cu	21.0	$5x10^{-12}$	10.	10^{16}	$4.3x10^{17}$	$8.6x10^9$
Ge:Zn	37.0	~$6x10^{-12}$	~30.	$3x10^{16}$	$6.0x10^{17}$	$3x10^{10}$
Si:Ga	15.5	~$5x10^{-12}$	~20.	$4x10^{16}$	$4.1x10^{17}$	$1.6x10^{10}$
Si:As	23.5	10^{-11}	~30.	$3x10^{16}$	$4.6x10^{17}$	$1.4x10^{10}$
Si:Sb	27.0	10^{-11}	~20.	$2x10^{16}$	$5.1x10^{17}$	$1.0x10^{10}$

* - FOV =180°

Table D.11
Resistance values for
several extrinsic photoconductors

	n_2, p_2 (cm^{-3})	$R_\square$ (k$\Omega/\square$)	L_{T1} (μm)	R_1 (Ω)	R_2 (kΩ)
Ge:Au	$9.6x10^9$	52.	.14	71.	52.
Ge:Hg	10^{10}	150.	.082	122.	150.
Ge:Cu	$8.6x10^9$	73.	.12	83.	73.
Ge:Zn	$3x10^{10}$	63.	.13	77.	63.
Si:Ga	$1.6x10^{10}$	78.	.11	91.	78.
Si:As	$1.4x10^{10}$	134.	.086	116.	134.
Si:Sb	$1.0x10^{10}$	125.	.089	112.	125.

σ_{cap_e} = See table D.10

$v_{av} = 10^7$ cm/sec

p_2, n_2 – See table D.10

$\mu_{p2} = 10^5$ cm^2/(V–sec)

$\mu_{n2} = 10^5$ cm^2/(V–sec)

$r_{c1} = r_{c4} = 10^{-5}$ Ωcm^2

$R_\square$ – See table D.11

$L_{T1} = L_{T4}$ – See table D.11

$\eta = 25\%$

FOV = 60°

λ_{max} is the wavelength at which D^* has its maximum value. N_i(max) is defined at the beginning of this section.

These numbers compare well with the SBRC catalog. Potential differences from the SBRC catalog are: 1) Probably the compensation can be made lower. 2) For high speed devices, compensation is made higher. 3) η could be higher. 4) ϕ_B is also affected by the fact that only the radiation with wavelengths around λ_{max} is efficiently collected.

D.5.2 PEIR photoconductor

The important auxiliary equations are

$$g = \phi_B \eta / d_{z2} \quad ,$$

$$n_2 = \frac{g}{\sigma_{cap} v_{av} (n_2 + N_A^-)} \qquad \text{(n–type)} \quad ,$$

$$p_2 = \frac{g}{\sigma_{cap} v_{av} (p_2 + N_D^+)} \qquad \text{(p–type)} \ ,$$

$$R_\square = \rho_{3TC}/d_{z3TC} = \frac{1}{q\mu_{n3TC} n_{3TC} d_{z3TC}} \qquad \text{(n–type)} \ ,$$

$$R_\square = \rho_{3TC}/d_{z3TC} = \frac{1}{q\mu_{p3TC} p_{3TC} d_{z3TC}} \qquad \text{(p–type)} \ ,$$

and

$$L_{T4} = (r_{c4}/R_\square)^{1/2} \ .$$

The resistance equations are (assuming that $A_D = A_C$)

$$R_1 = r_{c1}/d_x d_y \ ,$$

$$R_{1sub} = \frac{1}{q\mu_{n1sub} n_{1sub}} \frac{d_{z1sub}}{d_x d_y} \qquad \text{(n–type)} \ ,$$

$$R_{1sub} = \frac{1}{q\mu_{p1sub} p_{1sub}} \frac{d_{z1sub}}{d_x d_y} \qquad \text{(p–type)} \ ,$$

$$R_2 = \frac{1}{q\mu_{n2} n_2} \frac{d_{z2}}{d_x d_y} \qquad \text{(n–type)} \ ,$$

$$R_2 = \frac{1}{q\mu_{p2} p_2} \frac{d_{z2}}{d_x d_y} \qquad \text{(p–type)} \ ,$$

$$R_3 = R_\square/48 \qquad \text{(squaregrid)} \ ,$$

and

$$R_4 = \frac{r_{c4}}{4L_{T4}d_x}$$

where it is assumed $d_x = d_y = S$. S is the grid spacing (See Fig. D.4).

D.5.2.1 Variation of the area

Table D.12 presents the resistance values in a PEIR photoconductor as the area, d_x X d_y, is varied. The parameters used in table D.12 are as follows.

d_x X d_y — See table D.12

$d_{z3TC} = 300\text{Å} = 300\text{x}10^{-8}\text{cm}$

$d_{z2} = 5\ \mu\text{m}$

$d_{z1sub} = 400\ \mu\text{m}$

$\phi_B = 5\text{x}10^{17}\ \text{ph}/(\text{cm}^2\text{sec})$

$p_{3TC} = N_{A3TC} = 10^{19}\ \text{cm}^{-3}$

$p_{1sub} = N_{A1sub} = 10^{19}\ \text{cm}^{-3}$

$N_D^+ < 10^{12}\ \text{cm}^{-3}$

$g = 10^{21}\ \text{cm}^{-3}\text{sec}^{-1}$

$\sigma_{cap} = 10^{-12}\ \text{cm}^2$

$v_{av} = 10^7\ \text{cm/sec}$

$p_2 = 10^{13}\ \text{cm}^{-3}$

$\mu_2 = 10^5\ \text{cm}^2/(\text{V—sec})$

$\mu_{p3TC} = 50\ \text{cm}^2/(\text{V—sec})$

$\mu_{p1sub} = 50\ \text{cm}^2/(\text{V—sec})$

$r_{c1} = r_{c4} = 10^{-5}\ \Omega\text{cm}^2$

Table D.12
The resistances as the area is varied

$d_x(=d_y)$ (cm)	d_x (μm)	R_1 (Ω)	R_{1sub} (Ω)	R_2 (Ω)	R_3 (Ω)	R_4 (Ω)
.005	50	.4	20.	125.	86.9	10.2
.01	100	.1	5.	31.3	86.9	5.1
.05	500	.004	.20	1.25	86.9	1.02
.1	1000	.001	.05	.313	86.9	.51

$R_{\square} = 4{,}170\ \Omega/\square$

$L_{T4} = 4.9\text{x}10^{-5}$ cm

$\eta = 100\%$

The resistances depend upon the area as follows. R_1, R_{1sub}, and R_2 are proportional to the inverse of the area. R_3 is a constant of the area. R_4 is proportional to the inverse of the square root of the area. If the grid size (SxS) stayed the same (ie., did not vary with the area), R_3 and R_4 will also be proportional to the inverse of the area (See sec. D.6)

D.5.2.2 Variation of the thicknesses

Table D.13 presents the resistance values in a PEIR photoconductor as the thicknesses throughout the device are varied. The parameters used in table D.13 are as follows.

d_x X d_y = 100μm X 100μm

d_{z3TC} — See table D.13

d_{z2} — See table D.13

d_{z1sub} — See table D.13

$\phi_B = 5\text{x}10^{17}$ ph/(cm^{2}sec)

$p_{3TC} = N_{A3TC} = 10^{19}$ cm^{-3}

$p_{1sub} = N_{A1sub} = 10^{19}$ cm^{-3}

$N_D^+ < 10^{12}$ cm^{-3}

$g = 2.5\text{x}10^{21}$ cm^{-3}sec^{-1} when d_{z2}=2μm

$g = 5.\text{x}10^{20}$ cm^{-3}sec^{-1} when d_{z2}=10μm

$\sigma_{cap} = 10^{-12}$ cm^2

Table D.13
The resistances as
the layer thicknesses are varied

d_{z3TC} (Å)	d_{z2} (μm)	d_{z1sub} (μm)	R_1 (Ω)	R_{1sub} (Ω)	R_2 (Ω)	R_3 (Ω)	R_4 (Ω)
300	2	400	.1	5.	7.9	86.9	5.1
500	2	400	.1	5.	7.9	52.1	4.0
300	10	400	.1	5.	88.	86.9	5.1
300	2	600	.1	7.5	7.9	86.9	5.1

$v_{av} = 10^7$ cm/sec

$p_2 = 1.58 \times 10^{13}$ cm^{-3} when $d_{z2}=2\mu$m

$p_2 = 7.1 \times 10^{12}$ cm^{-3} when $d_{z2}=10\mu$m

$\mu_{p2} = 10^5$ cm^2/(V–sec)

$\mu_{p3TC} = 50$ cm^2/(V–sec)

$\mu_{p1sub} = 50$ cm^2/(V–sec)

$r_{c1} = r_{c4} = 10^{-5}$ Ωcm^2

$R_\square = 4{,}170$ $\Omega/\square$ when $d_{z3TC}=300$Å

$R_\square = 2{,}500$ $\Omega/\square$ when $d_{z3TC}=500$Å

$L_{T4} = 4.9 \times 10^{-5}$ cm when $d_{z3TC}=300$Å

$L_{T4} = 6.3 \times 10^{-5}$ cm when $d_{z3TC}=500$Å

$\eta = 100\%$

The resistances depend upon the thicknesses as follows. R_1 is independent of any of the layer thicknesses R_{1sub} is proportional to the substrate thickness. For no compensation, R_2 is proportional to the active region thickness to the 3/2 power. For compensation, R_2 is proportional to the active region thickness squared. R_3 is inversely proportional to the transparent contact thickness. R_4 is inversely proportional to the square root of the transparent contact thickness.

D.5.2.3 Variation of the photon flux

Tables D.14 and D.15 present the resistance values in a PEIR photoconductor as the photon flux is varied. The parameters used in tables D.14 and D.15 are as follows.

d_x X $d_y = 100\mu$m X 100μm

$d_{z3TC} = 300\text{Å} = 300\text{x}10^{-8}\text{cm}$

$d_{z2} = 5\ \mu\text{m}$

$d_{z1sub} = 400\ \mu\text{m}$

ϕ_B — See tables D.14 & D.15

$p_{3TC} = N_{A3TC} = 10^{19}\ \text{cm}^{-3}$

$p_{1sub} = N_{A1sub} = 10^{19}\ \text{cm}^{-3}$

N_D^+ — See tables D.14 & D.15

g — See tables D.14 & D.15

$\sigma_{cap} = 10^{-12}\ \text{cm}^2$

$v_{av} = 10^7\ \text{cm/sec}$

p_2 — See tables D.14 & D.15

$\mu_{p2} = 10^5\ \text{cm}^2/(\text{V—sec})$

$\mu_{p3TC} = 50\ \text{cm}^2/(\text{V—sec})$

$\mu_{p1sub} = 50\ \text{cm}^2/(\text{V—sec})$

$r_{c1} = r_{c4} = 10^{-5}\ \Omega\text{cm}^2$

$R_\square = 4{,}170\ \Omega/\square$

$L_{T4} = 4.9\text{x}10^{-5}\ \text{cm}$

$\eta = 100\%$

As the background photon flux decreases, R_2 increases. The other resistances are independent of the photon flux.

Table D.14
The resistances as the photon flux
is varied for $N_{D2}^{+}=10^{12}cm^{-3}$

ϕ_B ($cm^{-2}sec^{-1}$)	g ($cm^{-3}sec^{-1}$)	p_2 (cm^{-3})	R_1 (Ω)	R_{1sub} (Ω)	R_2 (Ω)	R_3 (Ω)	R_4 (Ω)
10^{11}	$2x10^{14}$	$2x10^{7}$	.1	5.	$1.6x10^{7}$	86.9	5.1
10^{13}	$2x10^{16}$	$2x10^{9}$	.1	5.	$1.6x10^{5}$	86.9	5.1
10^{15}	$2x10^{18}$	$>2x10^{11}$	.1	5.	$1.6x10^{3}$	86.9	5.1
10^{17}	$2x10^{20}$	$>4.5x10^{12}$	.1	5.	$7.1x10^{1}$	86.9	5.1
$5x10^{17}$	10^{21}	$>10^{13}$	.1	5.	$3.2x10^{1}$	86.9	5.1
10^{18}	$2x10^{21}$	$>1.4x10^{13}$	.1	5.	$2.3x10^{1}$	86.9	5.1

Table D.15
The resistances as the photon flux
is varied for $N_{D2}^{+}=10^{14}cm^{-3}$

ϕ_B ($cm^{-2}sec^{-1}$)	g ($cm^{-3}sec^{-1}$)	p_2 (cm^{-3})	R_1 (Ω)	R_{1sub} (Ω)	R_2 (Ω)	R_3 (Ω)	R_4 (Ω)
10^{11}	$2x10^{14}$	$2x10^{5}$	.1	5.	$1.6x10^{9}$	86.9	5.1
10^{13}	$2x10^{16}$	$2x10^{7}$	.1	5.	$1.6x10^{7}$	86.9	5.1
10^{15}	$2x10^{18}$	$2x10^{9}$	.1	5.	$1.6x10^{5}$	86.9	5.1
10^{17}	$2x10^{20}$	$2x10^{11}$	.1	5.	$1.6x10^{3}$	86.9	5.1
$5x10^{17}$	10^{21}	10^{12}	.1	5.	$3.2x10^{2}$	86.9	5.1
10^{18}	$2x10^{21}$	$2x10^{12}$	.1	5.	$1.6x10^{2}$	86.9	5.1

D.5.2.4 Variation of the dopant concentration in the contacts

Tables D.16 and D.17 present the resistance values in a PEIR photoconductor as the dopant concentration is varied. The parameters used in tables D.16 and D.17 are as follows.

d_x X d_y = 100μm X 100μm

d_{z3TC} = 300Å = 300x10^{-8}cm

d_{z2} = 5 μm

d_{z1sub} = 400 μm

ϕ_B = 5x10^{17} ph/(cm^{2}sec)

p_{3TC} = N_{A3TC} – See tables D.16 & D.17

p_{1sub} = N_{A1sub} – See tables D.16 & D.17

$N_D^+ < 10^{12}$cm^{-3}

$N_A^- < 10^{12}$cm^{-3}

g = 10^{21} cm^{-3}sec^{-1}

σ_{cap} = 10^{-12} cm^2

v_{av} = 10^7 cm/sec

p_2 or n_2 – 10^{13}cm^{-3}

μ_{p2} = 10^5 cm^2/(V–sec) (p–type)

μ_{n2} = 10^5 cm^2/(V–sec) (n–type)

μ_{p3TC}, μ_{p1sub}(cm^2/(V–sec)) – See table D.16

μ_{n3TC}, μ_{n1sub}(cm^2/(V–sec)) – See table D.16

r_{c1}, r_{c4} – See table D.16

$R_\square$ – See table D.16

Table D.16
The parameters that depend upon the change
in concentration in the substrate or transparent contact

type	N_{i1sub} (cm^{-3})	N_{i3TC} (cm^{-3})	μ_{i1sub}	μ_{i3TC}	r_{c1} (Ωcm^2)	r_{c4} (Ωcm^2)	$R_\square$ ($\Omega/\square$)	L_{T4} (μm)
p	10^{19}	$8x10^{18}$	50.	70.	10^{-5}	$5x10^{-4}$	3720.	3.7
p	10^{19}	10^{19}	50.	50.	10^{-5}	10^{-5}	4170.	.49
p	10^{19}	$3x10^{19}$	50.	45.	10^{-5}	$7x10^{-6}$	1540.	.67
p	$5x10^{19}$	10^{19}	40.	50.	$2x10^{-6}$	10^{-5}	4170.	.49
n	$3x10^{18}$	$8x10^{17}$	2000.	3000.	$5x10^{-6}$	$2x10^{-5}$	868.	$1.5x10^{-4}$
n	$3x10^{18}$	10^{18}	2000.	2800.	$5x10^{-6}$	$8x10^{-6}$	745.	$1.0x10^{-4}$
n	$3x10^{18}$	$2x10^{18}$	2000.	2300.	$5x10^{-6}$	$2x10^{-6}$	453.	$6.6x10^{-5}$
n	$8x10^{18}$	10^{18}	1300.	2800.	$6x10^{-7}$	$8x10^{-6}$	745.	$1.0x10^{-4}$

Table D.17
The resistances as the concentrations
in the substrate and the transparent layer are varied

type	N_{i1sub} (cm^{-3})	N_{i3TC} (cm^{-3})	R_1 (Ω)	R_{1sub} (Ω)	R_2 (Ω)	R_3 (Ω)	R_4 (Ω)
p	10^{19}	$8x10^{18}$	.1	5.	31.	77.5	34.
p	10^{19}	10^{19}	.1	5.	31.	86.9	5.1
p	10^{19}	$3x10^{19}$	.1	5.	31.	32.1	2.6
p	$5x10^{19}$	10^{19}	.02	1.25	31.	86.9	5.1
n	$3x10^{18}$	$8x10^{17}$	.05	.42	31.	18.1	3.3
n	$3x10^{18}$	10^{18}	.05	.42	31.	15.5	2.0
n	$3x10^{18}$	$2x10^{18}$	.05	.42	31.	9.4	.76
n	$8x10^{18}$	10^{18}	.006	.24	31.	15.5	2.0

L_{T4} — See table D.16

$\eta = 100\%$

p-GaAs mobilities are from Wiley [Wiley 1976]. n-GaAs mobilities are from Sze [Sze 1981]. r_c values are from Schroder [Schroder & Meier 1984].

D.5.2.5 Variation of the efficiency

Tables D.18 and D.19 present the resistance values in a PEIR photoconductor as the efficiency is varied. The parameters used in tables D.18 and D.19 are as follows.

d_x X d_y = 100μm X 100μm

d_{z3TC} = 300Å = 300x10^{-8}cm

d_{z2} = 5 μm

d_{z1sub} = 400 μm

ϕ_B = 5x10^{17} ph/(cm^{2}sec)

$p_{3TC} = N_{A3TC} = 10^{19}$ cm^{-3}

$p_{1sub} = N_{A1sub} = 10^{19}$ cm^{-3}

N_D^+ — See tables D.18 & D.19

$g = \eta 10^{21}$ cm^{-3}sec^{-1} — See tables D.18 & D.19

$\sigma_{cap} = 10^{-12}$ cm^2

$v_{av} = 10^7$ cm/sec

p_2 — See tables D.18 & D.19

$\mu_{p2} = 10^5$ cm^2/(V—sec)

$\mu_{p3TC} = 50$ cm^2/(V—sec)

$\mu_{p1sub} = 50$ cm^2/(V—sec)

Table D.18
The resistances as the efficiency is varied
where $N_{D2}^{+}=10^{12}cm^{-3}$

η (%)	g ($cm^{-3}sec^{-1}$)	p_2 (cm^{-3})	R_1 (Ω)	R_{1sub} (Ω)	R_2 (Ω)	R_3 (Ω)	R_4 (Ω)
1.	10^{19}	$<10^{12}$	.1	5.	313.	86.9	5.1
10.	10^{20}	$<3.2x10^{12}$	.1	5.	98.	86.9	5.1
30.	$3.x10^{20}$	$<5.5x10^{12}$	.1	5.	57.	86.9	5.1
50.	$5.x10^{20}$	$<7.1x10^{12}$	.1	5.	44.	86.9	5.1
75.	$7.5x10^{20}$	$<8.7x10^{12}$	.1	5.	36.	86.9	5.1

Table D.19
The resistances as the efficiency is varied
where $N_{D2}^{+}=10^{13}cm^{-3}$

η (%)	g ($cm^{-3}sec^{-1}$)	p_2 (cm^{-3})	R_1 (Ω)	R_{1sub} (Ω)	R_2 (Ω)	R_3 (Ω)	R_4 (Ω)
1.	10^{19}	10^{11}	.1	5.	3,130.	86.9	5.1
10.	10^{20}	10^{12}	.1	5.	313.	86.9	5.1
30.	$3.x10^{20}$	$<3x10^{12}$	.1	5.	104.	86.9	5.1
50.	$5.x10^{20}$	$<5x10^{12}$	.1	5.	63.	86.9	5.1
75.	$7.5x10^{20}$	$<7.5x10^{12}$	.1	5.	42.	86.9	5.1

$r_{c1} = r_{c4} = 10^{-5}\ \Omega cm^2$

$R_{\square} = 4{,}170\ \Omega/\square$

$L_{T4} = 4.9x10^{-5}$ cm

η = See tables D.18 & D.19

As the efficiency decreases, R_2 increases. The other resistances are independent of the frequency.

D.6. Resistance equations for a general PEIR photoconductor

Unlike the first five sections in which the grid spacing (SxS) equaled the detector area, this section will consider the case when SxS doesn't equal $d_x x d_y$.

Assuming that the grid spacings (S) are uniform and that the widths of the metal are negligibly small,

$$R_1 = \frac{r_{c1}}{d_x d_y} \ ,$$

$$R_{1sub} = \frac{1}{q\mu_{n1sub} n_{1sub}} \frac{d_{z1sub}}{d_x d_y} \qquad \text{(n—type)} \ ,$$

$$R_{1sub} = \frac{1}{q\mu_{p1sub} p_{1sub}} \frac{d_{z1sub}}{d_x d_y} \qquad \text{(p—type)} \ ,$$

$$R_2 = \frac{1}{q\mu_{n2} n_2} \frac{d_{z2}}{d_x d_y} \qquad \text{(n—type)} \ ,$$

$$R_2 = \frac{1}{q\mu_{p2} p_2} \frac{d_{z2}}{d_x d_y} \qquad \text{(p—type)} \ ,$$

$$R_3 = \left(\frac{R_\square S^2}{8 d_x d_y}\right) \qquad \text{(rect. grid)} \ ,$$

$$R_3 = \left(\frac{R_\square S^2}{48 d_x d_y}\right) \qquad \text{(square grid)} \ ,$$

$$R_4 = \frac{r_{c4} S}{(2L_{T4})(d_x d_y)} \qquad \text{(rect. grid} - L > 2L_{T4}) \ ,$$

$$R_4 = \frac{r_{c4} S}{L(d_x d_y)} \qquad \text{(rect. grid} - L < 2L_{T4}) \ ,$$

$$R_4 = \frac{r_{c4} S}{4L_{T4}(d_x d_y)} \qquad (\square \text{ grid} - L > 2L_{T4}) \ ,$$

$$R_4 = \frac{r_{c4} S}{2L(d_x d_y)} \qquad (\square \text{ grid} - L < 2L_{T4}) \ ,$$

where

$$g = \phi_B \eta / d_{z2} \ ,$$

$$n_2 = \frac{g}{\sigma_{cap} v_{av} (n_2 + N_A^-)} \qquad \text{(n–type)} \ ,$$

$$p_2 = \frac{g}{\sigma_{cap} v_{av} (p_2 + N_D^+)} \qquad \text{(p–type)} \ ,$$

$$R_\square = \rho_{3TC} / d_{z3TC} = \frac{1}{q \mu_{n3TC} n_{3TC} d_{z3TC}} \qquad \text{(n–type)} \ ,$$

$$R_{\square} = \rho_{3TC}/d_{z3TC} = \frac{1}{q\mu_{p3TC}p_{3TC}d_{z3TC}} \qquad \text{(p-type)} \ ,$$

and

$$L_{T4} = (r_{c4}/R_{\square})^{1/2} \ .$$

These equations are acceptable as a simple approximation but if one wants to get a more physically reliable set of equations, one must consider three factors: 1) The distribution of potential in the device affects the resistances. 2) The finite width of the metal will necessarily cause a change in some of the resistances. 3) The non-uniformity in grid widths over the area of device will cause a change in some of the resistances. The next three subsections describe how the resistances will change due to these effects. Subsection D.6.4 presents the configuration and the corresponding resistances of a PEIR photoconductor that is being tested.

D.6.1 The effect of distribution of potential on the resistances

The potential in the IR active layer will not be uniform because the metal is not uniform over the transparent contact. This nonuniformity in potential will redirect the carriers in the direction parallel to the layers. Consequently, the carriers should flow towards the metal and away from the center part of the grid. These effects on the resistances are now described.

For R_1 and R_{1sub}, there should be no real change because the part of the device where these resistances exist are considered to be contacts and in contacts it can be assumed that the potential is necessarily uniform. For R_2, it appears that the potential distribution will alter the concentration but since R_2 depends upon the concentration times the area ($d_x d_y$), R_2 should not change much for a change in potential distribution.

R_3 will decrease due to this variation in potential because more of the current will be directed away from the middle of the grid opening to the metal contact. Hence, the constant J assumed over the grid opening used to determine R_3 in sec. D.3 is not correct and when considering the integration dependence, R_3 will necessarily decrease. Physically, this can be explained by the fact that there are not as many excess carriers attracted towards the surface under the grid opening. Since the space charge from the excess carriers determines the

potential along the transparent layer, the potential will necessarily decrease due to the variation of the potential.

R_4 will most likely decrease because the effective contact area in the metal will become larger. It becomes larger because electrons will more easily flow to the central portion of the metal strip. As stated in sec. D.4, if the actual thickness is more than $2L_{T4}$ (The 2 is needed for current flow from grid openings on both sides of the metal strips), the effective area depends upon L_{T4}. This assumes that the current is constant flowing toward the grid surface. For a redirection of the current towards the metal contacts, the effective area should increase because the effective thickness should be larger than L_{T4}.

If the actual thickness of the metal strips is less than $2L_{T4}$, R_4 should not change that much from the equations above.

D.6.2 The effect of finite metal widths on the resistances

The metal strips must have a certain width. Assuming it is capable to make a strip any width, the requirement is that the width of the metal strips must be wide enough to make the resistance in the strips negligible. The first effect of this finite metal strip is to decrease the efficiency in the active region (See app. E). The second effect is that in some of the resistances, the actual area is not $d_x d_y$, but a smaller area. These effects on the resistances are now described.

R_1 and R_{1sub} should not be effected by the metal strip thickness or how the metal is arranged. As in sec. D.6.1, these contacts are assumed to be of constant composition over the area and so the $d_x d_y$ term in these resistances should stay the same.

R_2 will increase because as the efficiency decreases the carrier concentration due to the background decreases. It is assumed that the carriers in the active layer are produced by the background radiation. If this is the case, R_2 will increase. After considering sec. D.6.1, it appears that the $d_x d_y$ term will stay about the same.

R_3 will change because in the calculation in sec. D.3, it is assumed that all the current flows to the surface under the grid opening. When the metal obtains a finite thickness, the sum of the grid opening areas is actually smaller than the detector area. This effectively increases R_3. In other words, when calculating R_3, one cannot merely take $d_x d_y$ to be the value of the denominator.

R_4 will change because R_4 calculated in sec. D.4 is really too simplified. It was assumed that the number of metal strips equaled d_x/S in the x-direction

and d_y/S in the y-direction. Let the actual number of strips in the x and y-direction be n_{xm} and n_{ym} respectively (See sec. E.2 for a calculation of n_{xm} and n_{ym}).

For the rectangular grid,

$$R_4 = \frac{r_{c4}}{(2L_{T4}n_{ym})(d_x)} \qquad (L>2L_{T4})$$

$$R_4 = \frac{r_{c4}}{Ln_{ym}(d_x)} \qquad (L<2L_{T4})$$

where is it assumed that the strips are directed along the x-direction.

For the square grid, the change is more complicated because one also needs to take the overlap of the metal strips into account. R_4 then becomes

$$R_4 = \frac{r_{c4}}{(2n_{ym}L_{T4})(d_x-n_{xm}(L-2L_{T4}))+(2n_{xm}L_{T4})(d_y-n_{ym}L)} \qquad (L>2L_{T4})$$

$$R_4 = \frac{r_{c4}}{(Ln_{ym})d_x+(Ln_{xm})(d_y-n_{ym}L)} \qquad (L<2L_{T4}) \ .$$

Since

$$n_{ym} \leq d_y/S \ ,$$

R_4 will remain the same or more likely increase for the rectangular grid. For the square grid, R_4 will necessarily increase.

D.6.3 Non-uniformity of grid widths

If the grids are not uniform, the resistances can vary. The non-uniformity most likely encountered would be a finger that has been damaged, hence making the spacing bigger or a spacing that has been covered with metal. This section presents how the resistances would depend upon these two situations.

R_1 and R_{1sub} should remain the same.

R_2 and R_3 should increase due to the damaged finger. The enlarged area's resistance increases, slightly increasing the overall resistance. The larger R_2 is with respect to R_3, the smaller the resistance will increase. The effect of this increased resistance is to make a dead space out of the enlarged area.

R_2 and R_3 should decrease due to the spacing covered with metal. The larger R_2 is with respect to R_3, the smaller the resistance will decrease. The reason behind the decrease is that the area under any metal should have a smaller resistance than R_2 plus R_3, effectively decreasing any resistance. The photodetector becomes less sensitive due to this added parallel resistance.

R_4 should vary in a similar matter that R_2 and R_3 varies.

It is believed that although these resistances can vary due to these metal problems, that the overall effect will be reasonably small.

D.6.4 Example

A GaAs:Be PEIR detector has been built. The resistances are calculated in this section. It is assumed that the background radiation is produced by a 300 K blackbody with no filtering. For a 5 mm. x 5 mm. detector, the following numbers are calculated for a 100 x 100 μm grid, $p_{1sub}=3x10^{19}cm^{-1}$, $d_{z2}=1.3\mu m$, $R_{\square}=4180\Omega/\square$, $\rho_{metal}=10^{-6}\Omega cm$, and R_4 is found with the aid of table D.13. For R_5, L/A = 1000 μm / (.5 μm 20 μm) and for R_6, L = 300 cm and the radius of the wire is .051 cm. The resistance values are shown in table D.20. As can be seen in this table, the parasitic resistances can be much larger than R_2.

Table D.20
Resistances for a GaAs:Be PEIR photoconductor
with an area of 5 x 5 mm

	Resistance (mΩ)
R_1	~0.
R_{1sub}	1.39
R_2	2.5
R_3	34.
R_4	2.0
R_5	100.
R_6	3.7
R_{TOT}	150.

Appendix E.

Degradation of efficiency due to the transparent contact and the metal grid

The purpose of this section is to compare how the efficiency changes as the transparent layer thickness changes and as the amount of metal changes. Section E.1 describes how the efficiency changes due to the change in the transparent layer. Section E.2 describes how the efficiency depends upon the amount of metal contacting to the transparent contact.

E.1. The dependence of efficiency upon the transparent contact - η_{TC}

The transparent contact must be doped enough to cause the impurity band in the semiconductor to merge with the conduction or valence band. This merging will effectively make the layer a conductor at low temperatures. Unfortunately, due to free carrier absorption, this degenerate doping does not make the transparent layer very transparent. In addition, the longer the wavelength, the less transparent the contact.

The transparent layer affects the efficiency in two ways. First, the absorption of radiation itself decreases the efficiency. The second and more serious problem is that the absorption times the wavelength is proportional to the imaginary part of the index of refraction - κ. κ is closely related to the amount of reflection of radiation at the interface of two materials - the larger κ, the larger the reflection.

This section is split into three parts. The first part presents some calculations for the reflection from a thin epitaxial layer grown on a semi-infinite substrate of GaAs. The radiation is assumed to strike this structure normal to the surface with the incident material being air. The second part presents the efficiency for these values of reflection. The third part shows why a thicker transparent contact layer with a lower free carrier concentration is superior to a thinner transparent contact layer with a higher free carrier concentration.

Four types of transparent contact layers will be considered in this section: 1) n-type GaAs with a concentration of $5\text{x}10^{17}\text{cm}^{-3}$, 2) n-type GaAs with a concentration of 10^{18}cm^{-3}, 3) p-type GaAs with a concentration of $5\text{x}10^{18}\text{cm}^{-3}$, and 4) p-type GaAs with a concentration of 10^{19}cm^{-3}. It is reasonable to assume that these concentrations are high enough to cause the impurity band to

merge into the conduction or valence band (See chapter 3).

E.1.1 Calculation of the reflection

This section will present four sets of two tables. The first table presents the complex index of refraction, the absorption and the reflectivity for two semi-infinite layers as the energy of the incident radiation is varied. The absorption, α, is calculated from the classical equation for free carrier absorption. κ is related to α by the equation

$$\kappa = \alpha\lambda/4\pi \ .$$

It is assumed that the index of refraction varies as it has been presented in [Jenson 1978]. This assumption appears to be acceptable since the absorption is approximately the same for either p-type or n-type GaAs and since n depends upon the absorption. R_{2l} is the reflection coefficient for 2 semi-infinite layers where one of the layers is made up of the degenerately doped semiconductor and [Pankove 1971]

$$R_{2l} = \frac{(n-1)^2 + \kappa^2}{(n+1)^2 + \kappa^2} \ .$$

The second table presents the calculated reflection from the computer - $R_{em} = |\rho_{em}|^2$ where ρ_{em} is defined in app. G. The reflection is calculated for the radiation incident in air striking an epitaxial layer of thickness d_{z3TC} which has been grown on a substrate of intrinsic GaAs. The substrate is assumed to be infinite in length. Although this is not the exact situation as what will appear in the photoconductor, it should be a good indicator as to the actual value of reflection.

E.1.1.1 Reflection values for n-GaAs, $n=5x10^{17}cm^{-3}$

The reflection values for n-GaAs where $n=5x10^{17}cm^{-3}$ are shown in tables E.1 and E.2. One interesting entry to note is the 4 μm column where the reflection coefficients are almost equivalent to the reflection coefficient from two semi-infinite materials, R_{2l}, where one of the materials is the transparent contact material and the other is air.

Table E.1
Index and absorption parameters for
n-GaAs $n = 5x10^{17} cm^{-3}$

E_λ (meV)	n_{r2} (unitless)	α (cm^{-1})	κ_2 (unitless)	R_{2l} (%)
6.	3.9	$1.7x10^4$	30.6	98.
12.	1.5	$1.1x10^4$	10.1	94.
18.	.84	$9.6x10^3$	5.3	89.
24.	.56	$7.6x10^3$	3.3	83.

Table E.2
Reflection coefficients for
n-GaAs $n = 5x10^{17} cm^{-3}$

E_λ (meV)	R_{em}(%)						
	d_{z3TC}=400Å	800Å	1200Å	1600Å	2000Å	2400Å	4μm
6.	38.	48.	57.	64.	71.	75.	98.
12.	33.	35.	37.	38.	40.	42.	94.
18.	33.	33.	34.	34.	35.	36.	87.
24.	32.	33.	33.	33.	34.	34.	79.

Table E.3
Index and absorption parameters for
n-GaAs $n = 10^{18} cm^{-3}$

E_λ (meV)	n_{r2} (unitless)	α (cm^{-1})	κ_2 (unitless)	R_{2l} (%)
6.	6.1	$2.8x10^4$	48.1	99.
12.	2.1	$2.x10^4$	17.8	97.
18.	1.1	$1.8x10^3$	9.9	96.
24.	.7	$1.5x10^3$	6.6	94.

E.1.1.2 Reflection values for n-GaAs, $n=10^{18}cm^{-3}$

The reflection values for n-GaAs where $n=10^{18}cm^{-3}$ are shown in tables E.3 and E.4.

E.1.1.3 Reflection values for p-GaAs, $p=5x10^{18}cm^{-3}$

The reflection values for p-GaAs where $p=5x10^{18}cm^{-3}$ are shown in tables E.5 and E.6.

E.1.1.4 Reflection values for p-GaAs, $p=10^{19}cm^{-3}$

The reflection values for p-GaAs where $p=10^{19}cm^{-3}$ are shown in tables E.7 and E.8.

E.1.2 Calculation of the efficiency due to the transparent contact - η_{TC}

The efficiency due to the transparent contact is calculated using the equation

$$\eta_{TC} = (1-R_{em})e^{-\alpha d_{z3TC}} \quad .$$

This equation is an optimum value because the light that enters the device is assumed to pass through the contact layer once. As the absorption (and κ_2) decreases, the equation above becomes very accurate. Tables E.9 to E.12 present the values of η_{TC} for the parameters in tables E.1 to E.8.

E.1.3 Comparison of η_{TC} for different transparent contacts

From section D.3, one can see that R_3 decreases as the product $\mu_n n_{3TC} d_{z3TC}$ increases. The comparison made in this section is that as n_{3TC} is varied while R_3 is kept constant, what is the effect on η_{TC}. There is one simplification made in this comparison - μ_n is kept independent of carrier concentration. In other words, as n_{3TC} is varied while $n_{3TC}d_{z3TC}$ is kept constant, what is the effect on η_{TC}. In reality, μ_n increases with decreasing carrier concentration, which means that R_3 will be slightly lower (and more advantageous) as the carrier concentration increases.

Table E.4
Reflection coefficients for
n-GaAs $n = 10^{18}cm^{-3}$

E_λ (meV)	R_{em}(%) d_{z3TC}=200Å	400Å	600Å	800Å	1000Å	1200Å
6.	40.	52.	62.	70.	76.	80.
12.	34.	36.	38.	42.	42.	48.
18.	33.	34.	34.	36.	36.	38.
24.	33.	33.	33.	34.	34.	35.

Table E.5
Index and absorption parameters for
p-GaAs $p = 5x10^{18}cm^{-3}$

E_λ (meV)	n_{r2} (unitless)	α (cm^{-1})	κ_2 (unitless)	R_{2l} (%)
6.	14.9	$7.2x10^4$	127.	100.
12.	10.	$2.7x10^4$	23.7	94.
18.	4.3	$3.0x10^4$	16.5	94.
24.	2.3	$2.9x10^4$	12.7	95.

Table E.6
Reflection coefficients for
p-GaAs $p = 5x10^{18}cm^{-3}$

E_λ (meV)	R_{em}(%) d_{z3TC}=200Å	400Å	600Å	800Å	1000Å	1200Å
6.	83.	93.	96.	97.	98.	98.
12.	39.	45.	51.	55.	60.	63.
18.	35.	39.	44.	48.	52.	55.
24.	34.	37.	40.	43.	47.	50.

Table E.7
Index and absorption parameters for
p-GaAs $p = 10^{19} cm^{-3}$

E_λ (meV)	n_{r2} (unitless)	α (cm^{-1})	κ_2 (unitless)	R_{21} (%)
6.	29.	$1.2x10^5$	215.	100.
12.	12.	$7.5x10^4$	66.	99.
18.	6.	$7.1x10^4$	39.	98.
24.	3.5	$6.4x10^4$	28.	98.

Table E.8
Reflection coefficients for
p-GaAs $p = 10^{19} cm^{-3}$

E_λ (meV)	R_{em}(%)					
	d_{z3TC}=100Å	200Å	300Å	400Å	500Å	600Å
6.	89.	95.	97.	98.	98.	99.
12.	51.	68.	77.	83.	87.	89.
18.	41.	52.	62.	70.	75.	79.
24.	37.	45.	53.	60.	66.	71.

Table E.9
η_{TC} for
n-GaAs $n = 5x10^{17} cm^{-3}$

E_λ (meV)	η_{TC}(%)						
	d_{z3TC}=400Å	800Å	1200Å	1600Å	2000Å	2400Å	4μm
6.	59.	48.	38.	30.	23.	19.	.096
12.	64.	60.	55.	52.	48.	45.	.287
18.	64.	62.	59.	57.	54.	51.	.621
24.	66.	63.	61.	59.	57.	55.	1.00

Table E.10
η_{TC} for
n-GaAs $n = 10^{18}cm^{-3}$

E_λ (meV)	$\eta_{TC}(\%)$ d_{z3TC}=200Å	400Å	600Å	800Å	1000Å	1200Å
6.	57.	43.	32.	24.	18.	14.
12.	63.	59.	55.	49.	45.	41.
18.	65.	61.	59.	55.	53.	50.
24.	65.	63.	61.	59.	57.	54.

Table E.11
η_{TC} for
p-GaAs $p = 5x10^{18}cm^{-3}$

E_λ (meV)	$\eta_{TC}(\%)$ d_{z3TC}=200Å	400Å	600Å	800Å	1000Å	1200Å
6.	15.	5.2	2.6	1.7	.97	.84
12.	58.	49.	42.	36.	31.	27.
18.	61.	54.	47.	41.	36.	31.
24.	62.	56.	50.	45.	40.	35.

Table E.12
η_{TC} for
p-GaAs $p = 10^{19}cm^{-3}$

E_λ (meV)	$\eta_{TC}(\%)$ d_{z3TC}=100Å	200Å	300Å	400Å	500Å	600Å
6.	9.8	3.9	2.1	1.2	1.1	.49
12.	45.	28.	18.	13.	8.9	7.0
18.	55.	42.	31.	23.	18.	14.
24.	59.	48.	39.	31.	25.	20.

There will be three comparisons between the results in tables E.9 to E.12. First, when comparing the results of tables E.9 and E.10, it can be seen that η_{TC} for $5x10^{17}cm^{-13}$ concentration is always greater than or equal to the values for $1x10^{18}cm^{-13}$ when the layer thickness is twice as much for the $5x10^{17}cm^{-13}$ entry. Another interesting result of the first table is that if the transparent contact is made more thick than 1 μm, the contact is not very transparent.

Second, when comparing the fifth column entry of table E.10 and the first column entry of table E.11, it can be seen that for photon energies of 6 meV, the lower concentration case is the better choice, but for the higher photon energies, the higher concentration case is the superior case. This discrepancy arises because table E.10 is for the n-type case while table E.11 is for the p-type case and that the free carrier absorption coefficient in the n-type case is assumed to be a little higher. If the absorption was the same, the lower carrier concentration will be the superior choice.

Third, when comparing the proper entries in tables E.11 and E.12, the lower concentration, thicker transparent contact case is superior for all layer thicknesses and photon energies.

E.2. The dependence of efficiency upon the amount of metal - η_{metal}

The efficiency of the metal is simply calculated as the percentage of metal that covers the front part of the photodetector. One other effect that might be considered but is not here is the effect of diffraction of radiation. Briefly, this second effect is minimized if the wavelength to be detected is less than twice the spacing between the metals. This diffraction problem is analogous to transmission in a waveguide where the cutoff wavelength is related to twice the spacing of the waveguide.

The number of contacts must be calculated to determine the percentage of metal used. The simplest way to approximate this is to take the ratio of the width of the area of the detector divided by the grid spacing or d_y/S. For $d_y = 5mm$ and the six values of S considered in this section, these ratios are shown in table E.13.

The actual number of metal strips, n_{ym} depends upon the width of the detector - d_y, the grid spacing - S, and the width of the metal - W_m. The requirements to find n_{ym} is that the metal strips be placed upon the detector such that the grid spacing is S throughout the area and that the distance between the edge of the detector and the nearest parallel strip is less than S/2. With these requirements,

Table E.13
Ratio of d_y/S

S (mm)	d_y/S (unitless)
1.0	5
.5	10
.408	13
.25	20
.167	30
.1	50

$$n_{ym} = \text{integer}\left(\frac{d_y - S/2}{S+W_m} + 1\right)$$

where the integer operator means that the real number is converted to an integer and the fraction is neglected.

Section E.2.1 presents η_{metal} for rectangular grids and sec. E.2.2 presents η_{metal} for square grids.

E.2.1 η_{metal} for a rectangular grid

The efficiency due to the metal for a rectangular grid is calculated as

$$\eta_{metal} = \frac{d_x - n_{xm}(W_m)}{d_x} .$$

Table E.14 presents the corresponding values for certain grid spacings and metal thicknesses.

E.2.2 η_{metal} for a square grid

The efficiency due to the metal for a square grid is calculated as

$$\eta_{metal} = \frac{d_x d_y - n_{xm}(W_m) d_y - n_{ym}(W_m)(d_x - n_{xm} W_m)}{d_x d_y} .$$

Table E.15 presents the corresponding values for certain grid spacings and metal thicknesses. It is assumed that $d_x = d_y$.

E.3. Conclusions

There are five conclusions revealed during this study. 1) η is higher if one tries to lower R_s by applying more metal. 2) As the wavelength gets shorter, the TC layer can be made thicker. 3) There will be a wavelength of radiation where applying more metal or making d_{z3TC} thicker produces the same drop in efficiency. For the contacts presented, this wavelength will be shorter than 50 μm. 4) The real effectiveness of widening d_{z3TC} can best be determined by the

Table E.14

η_{metal} values for a rectangular grid

S (mm)	W_m = .15mm n_f (unitless)	W_m = .15mm η_{metal} (%)	W_m = .05mm n_f (unitless)	W_m = .05mm η_{metal} (%)	W_m = .02mm n_f (unitless)	W_m = .02mm η_{metal} (%)
1.	4	88.	5	95.	5	98.
.5	8	76.	9	91.	10	96.
.408	9	73.	11	89.	12	95.
.25	13	61.	17	83.	19	92.
.167	16	52.	23	77.	27	89.
.1	20	40.	34	66.	42	83.

Table E.15

η_{metal} values for a square grid

S (mm)	W_m = .15mm n_f (unitless)	W_m = .15mm η_{metal} (%)	W_m = .05mm n_f (unitless)	W_m = .05mm η_{metal} (%)	W_m = .02mm n_f (unitless)	W_m = .02mm η_{metal} (%)
1.	4	77.	5	90.	5	96.
.5	8	58.	9	83.	10	92.
.408	9	53.	11	79.	12	91.
.25	13	37.	17	69.	19	85.
.167	16	27.	23	59.	27	80.
.1	20	16.	34	44.	42	69.

layer reflectivity

$$R_{2l} = \frac{(n-1)^2 + \kappa^2}{(n+1)^2 + \kappa^2} \quad .$$

The lower this value is, the more likely widening d_{z3TC} will be a proper option. 5) Another implicit physical result is that $\kappa = \alpha\lambda/4\pi$. The longer the wavelength, the higher R_{2l}, the less effective it is to widen d_{z3TC}.

Because of these five results, detectors operating at 20 μm will most likely use a thick d_{z3TC} while detectors designed to detect wavelengths greater than 50μm will have a thin d_{z3TC} and a large amount of metal.

Appendix F.

Ionization effects in a Blocked Impurity Band (BIB) detector

This appendix presents some possible disadvantages due to compensation dopants in a BIB detector (See chap. 2). The four components of space charge that exist in a PEIR photoconductor also exist in a BIB detector. Ideally, it is assumed that the ionized impurities are swept out into the contact fast enough such that the ionized impurity concentration is much smaller than the compensation dopant concentration [Petroff & Stapelbroek 1984]. Consequently, the carrier concentration in the conduction band is also negligible, since they are swept out much faster than the ionized impurities [Petroff & Stapelbroek 1984]. This assumption will be true only if radiation and thermal generation are low enough. If one follows this assumption, the only space charge components that may exist are compensation dopants and electron accumulation. The effect of the compensation dopants is now discussed in detail.

Three ionization effects exist in a BIB detector: 1) impact ionization, 2) the Poole-Frenkel effect, and 3) tunneling-field emission ionization. The Poole-Frenkel effect is temperature dependent, while the other two effects are fairly independent of temperature and cannot be mitigated by lowering the temperature. All three are electric field dependent.

This appendix is separated into five sections: Section F.1 presents the electric field in an impurity band layer. Section F.2 presents the critical electric field for impact ionization to occur. Section F.3 calculates the current due to the Poole-Frenkel effect. Section F.4 calculates the tunneling current from electrons tunneling from an impurity band to the conduction band. Section F.5 presents the conclusions of this appendix.

F.1 Electric field in an impurity band layer

In a BIB detector (n-type), the impurity band is occupied, the electric field at one end of the impurity band is zero V/cm, and there are no carriers in the conduction band. For these requirements, the depletion region is due only to the compensation dopants and the maximum electric field in the impurity band layer is

$$\xi_d = \frac{-qN_A l_d}{\epsilon} = -\frac{1,800}{\epsilon_{sr}}\left(\frac{N_A}{10^{13}\text{cm}^{-3}}\right)\left(\frac{l_d}{1\mu\text{m}}\right) \text{ [V/cm]}$$

where ϵ_{sr} is the relative static dielectric constant, N_A is the compensation charge, and l_d is the width of the depletion region.

Table F.1 presents some ξ_d values in Si and Ge for various values of N_A and $l_d = 20\mu$m.

The importance of ξ_d arises due to the field dependence of impact ionization, thermal-field emission ionization, and tunneling-field emission ionization.

F.2 Impact ionization and the associated critical electric field

Impact ionization has already been considered in depth in a BIB detector [Szmulowicz & Madarsz 1987] and only impact ionization with respect to the ionization energy is considered in this section [Bratt 1977].

Impact ionization in a n-type extrinsic photoconductor, BIB detector, or PEIR photoconductor is defined as the ionization of an electron out of a donor level into the conduction band after colliding with an energetic electron in the conduction band. After the collision, there are two carriers in the conduction band which then have the capability of impact ionizing other electrons in the donor levels.

The critical electric field is defined as the electric field where impact ionization noticeably increases the number of carriers in the conduction band (in n-type devices). In shallow extrinsic photoconductors, the electric field needed to cause impact ionization is very small (on the order of 100 V/cm).

The critical electric field can be increased by increasing the dopant concentration. The increase in dopant concentration increases impurity scattering which helps to prevent the electron from attaining an energy high enough to impact ionize.

As discussed at the beginning of this appendix, a BIB detector can be limited by impact ionization. The rest of this section presents the critical electric field which must be greater than or on the order of ξ_d presented in sec. F.1.

The critical electric field (ξ_c) increases empirically 1:1 (approx.) as $N_D + N_A$ increase [Bratt 1977]. Some breakdown fields are listed in table F.2 below [Bratt 1977]

Table F.1
ξ_d for various values
of N_A and $l_d = 20\mu m$

	$N_A(cm^{-3})$	$\xi_d(V/cm)$
Si	$2x10^{12}$	-616.
	$5x10^{12}$	-1540.
	$1x10^{13}$	-3080.
	$1x10^{14}$	-30,800.
Ge	$2x10^{12}$	-442.
	$5x10^{12}$	-1105.
	$1x10^{13}$	-2210.
	$1x10^{14}$	-22,100.

Table F.2
Impact ionization critical fields

semi:dopant	E_I[eV]	ξ_c[V/cm]	dopant[cm^{-3}]
Ge:In	.01	100	10^{16}
Ge:Zn	.03	405	10^{16}
Ge:Cu	.042	630	$2x10^{16}$
Ge:Cd	.054	900	10^{16}
Si:P	.045	~200	$3x10^{16}$
Si:As	.054	~300	$3x10^{16}$

Table F.3
ξ_c for various E_I [Bratt 1977]
(N_i=$5x10^{17}cm^{-3}$)

semi:dopant	E_I[eV]	ξ_c[V/cm]
Ge:In	.01	3300.
Ge:Zn	.03	20,000.
Ge:Cu	.042	30,000.
Ge:Cd	.054	45,000.
Si:P	.045	3200
Si:As	.054	5000

Using the 1:1 empirical relationship, table F.3 presents the extrapolated critical fields for the materials in table F.2. The number of impurities, N_I, is set at $5x10^{17}cm^{-3}$. This high concentration can be attained in BIB detectors. To prevent the other ionization problems, the impurity concentration will have to be smaller for the more shallow dopant levels.

When comparing the results from tables F.1 and F.3, it appears that impact ionization will not occur for compensation dopant concentrations below $5x10^{12}cm^{-3}$ for a depletion region of 20 μm.

F.3 Poole-Frenkel effect and the associated thermionic emission current

The current due to the Poole-Frenkel effect depends on the lowering of the barrier height [Roy 1986] as an electric field is applied (See Fig. C.3). The barrier is due to the sum of the potential of the impurity atom and the potential due to the electric field [Roy 1986]. This potential can be written as [Roy 1986]

$$V(r) = -\frac{q^2}{4\pi\epsilon r} - q\xi x$$

where the electric field is applied in the x-direction and

$$V_\xi(r) = -q\xi x \ .$$

This potential is a minimum when [Roy 1986]

$$r_o = (\frac{e}{4\pi\epsilon\xi})^{1/2}$$

and

$$V_\xi(r_o) = -(\frac{e^3\xi}{4\pi\epsilon})^{1/2}$$

Some values of r_o and the lowering of the potential are shown in table F.4.

If one assumes that the energy width of the barrier is very small (the lowest leakage current case), one can calculate the lowering of the barrier by subtracting the barrier lowering above from the ionization energy. This is

Table F.4
$V(r_o)/q$ for various ξ

ξ (V/cm)	r_o (Å)	$V_\xi(r_o)/q$ (meV)	$V(r_o)/q$ (meV)
0	∞	0	0
100	1095	-1.10	-1.10
200	774	-1.54	-3.14
500	489	-2.45	-4.85
1000	346	-3.46	-7.0
2000	245	-4.9	-9.7
5000	155	-7.8	-15.3
10000	110	-11.	-22.

Table F.5
Impurity potential barrier height due to an applied electric field

ξ	ΔE_{te}(meV)				
(V/cm)	$E_I = 45$meV	35 meV	25 meV	15 meV	10 meV
100	44	34	24	14	9
200	42	32	22	12	7
500	40	30	20	10	5
1000	38	28	18	8	
2000	35	25	15	5	
5000	30	20	10		
10,000	23	13			

shown for several ionization energies in table F.5. The barrier height, ΔE_{te}, equals the ionization energy, E_I, minus the lowering of the potential, $V(r_o)/q$.

Considering this barrier lowering effect, the current can be calculated as [Sze 1981]

$$J_{te} = (\frac{A^*}{A})120T^2 e^{\frac{-\Delta E_{te}}{kT}} \ [A/cm^2]$$

where T is the temperature (K), A is the Richardson constant, A^* is the effective Richardson constant, and ΔE_{te} is the barrier height.

Figures F.1 and F.2 show approximate J_{te} values for different values of ξ_d in some BIB detectors (See sec. A.2.3) for ionization energies of 45 meV and 10 meV respectively. In these figures, it is assumed that $A^*/A = .5$.

F.4 Zener tunneling and the associated tunnel current

The Zener tunneling effect is shown in Fig. C.2. The current due to tunneling-field emission ionization (J_{tun}) can be roughly approximated as [Kane 1959]

$$J_{tun} = qn_{tun}l_{tun} \ [A/cm^2] \ .$$

l_{tun} is the length over which the field is applied and

$$n_{tun} = \frac{q^2\xi^2 m_r^{1/2}}{18\pi\hbar^2 \Delta E_{te}^{1/2}} \ e^{(\frac{-\pi m_r^{1/2}\Delta E_{te}^{3/2}}{2\hbar q|\xi|})} [cm^{-3}sec^{-1}]$$

where for simplicity, ΔE_{te} as defined above is approximated as the energy gap [Kane 1959] from the impurity band to the conduction band (n-type). In a BIB detector, ξ can be set approximately equal to ξ_d. It is assumed herein that the mass is isotropic and the mass in the donor band equals the conduction band mass (Consequently, $m_r = m_e/2$ [Kane 1959]). Figures F.1 and F.2 present approximate tunnel currents in some BIB detectors for different electric fields and ionization energies. For the calculations shown in Figs. F.1 and F.2, it is assumed that $l_{tun} = 1.$ μm and m_e^*=.50.

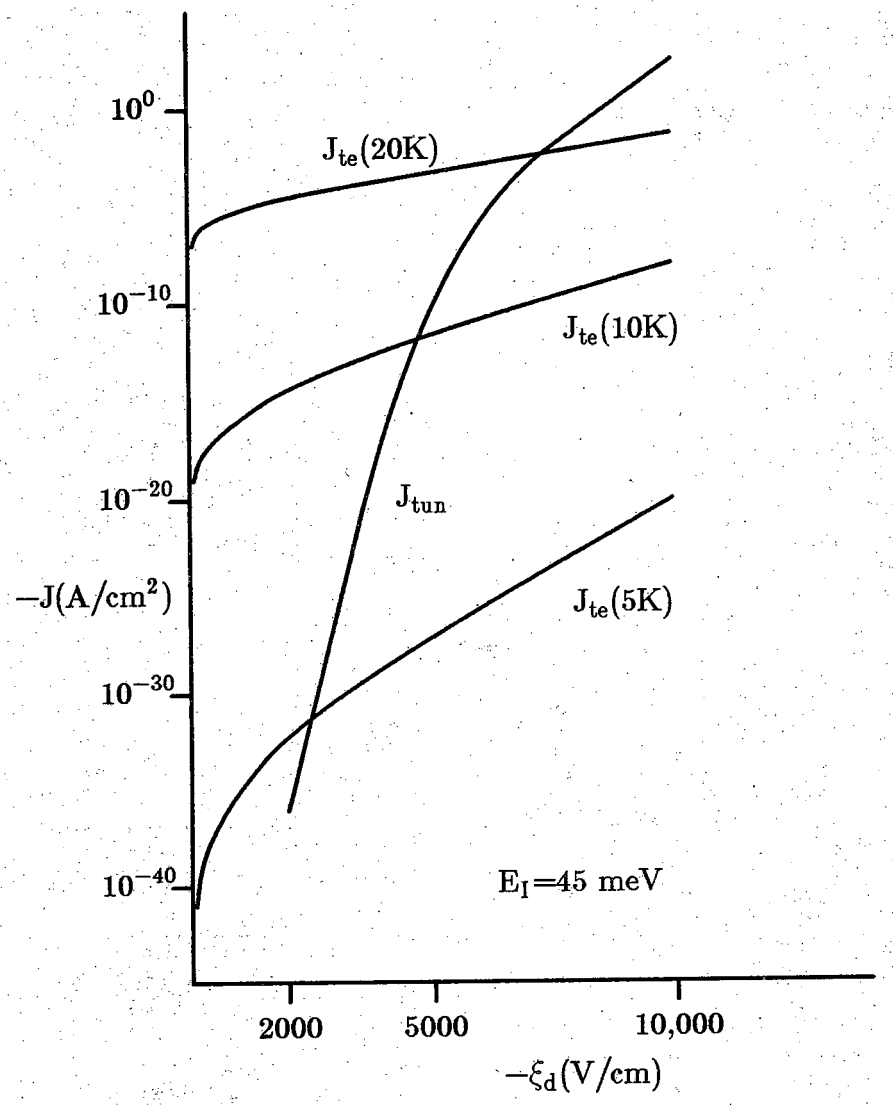

Figure F.1 Theoretical J_{te} and J_{tun} from the impurity band of a BIB detector. $E_I = 45$ meV.

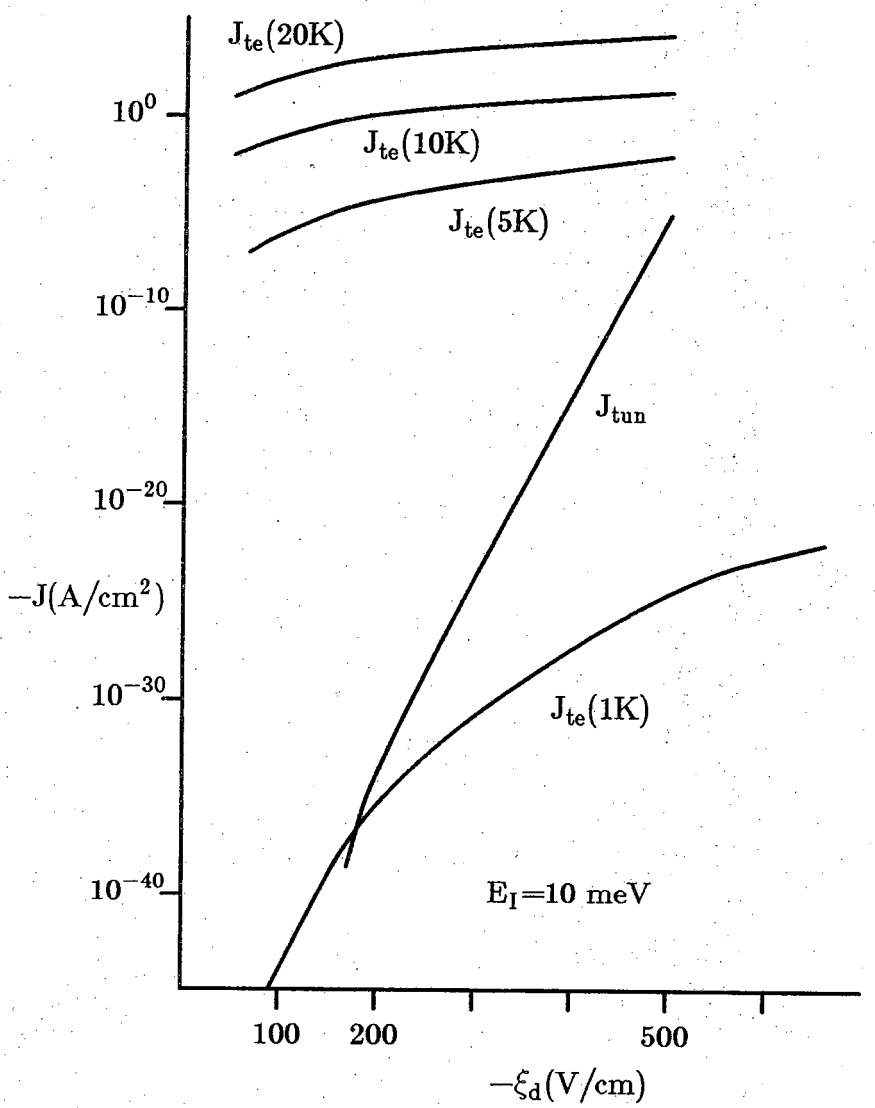

Figure F.2 Theoretical J_{te} and J_{tun} from the impurity band of a BIB detector. $E_I = 10$ meV.

Figures F.1 and F.2 show that even though it may be possible to lower the Poole-Frenkel effect by lowering the temperature, tunneling-field emission ionization is an unavoidable problem because tunneling is fairly independent of temperature. More importantly, the value of ξ_d in the impurity band layer must decrease as the ionization energy decreases.

F.5 Conclusions

Two results arise from this limitation on the value of ξ_d in the impurity band layer. First, as the wavelength which a BIB detector is designed to detect increases [Watson & Huffman 1988], the depletion region width and consequently, the quantum efficiency must necessarily decrease (for the same compensation dopant concentration). Second, since $(E_C - E_D)_{min}$ decreases as the impurity band dopant concentration is increased [Lee & McGill 1975], the depletion region width must also necessarily decrease as the impurity band dopant concentration is increased.

Appendix G.

Reflection and transmission for radiation propagating normal to a set of layers

G.1 Introduction

There are three methods of solving for reflection and transmission at a multiple layer sample. 1) Direct solution of Maxwell's equations at the boundaries. 2) Solving for the n+1 layer sample using the results of the n layer sample. 3) The matrix analysis described in Born and Wolf appears to be the most versatile and the simplest to solve. It appears that the way to solve for 2 is just a special case of 3. 1 and 2 are described in detail in this section, 3 was not found until after these two previous methods. The first two methods are strictly for normal incidence but can be expanded to oblique incidence. Before this is done, Born and Wolf should be considered since the matrix analysis therein should be conceptually easier to solve. At this time Born and Wolf has not been considered because normal incidence is adequate enough for the case in interest.

G.2 Direct solution of Maxwell's equations

This method was first attempted and determined to be too difficult for anything more than three layers (It will be considered that the number of layers includes the two semi-infinite layers.

Consider a three layer sample (See Fig G.1). The left layer is labeled the first layer, the middle layer is labeled the second layer and the right semi-infinite layer is labeled the third layer. Assuming normal incidence, select the x-axis such that the total component of the electric field is directed in the x-direction. The electric fields in the layers are then

$$E_{x1} = (E_{x1}^{+} e^{-jk_{z1}z} + E_{x1}^{-} e^{+jk_{z1}z}) e^{j\omega t} \quad ,$$

$$E_{x2} = (E_{x2}^{+} e^{-jk_{z2}z} + E_{x2}^{-} e^{+jk_{z2}z}) e^{j\omega t} \quad ,$$

and

$$E_{x3} = (E_{x3}^{+} e^{-jk_{z3}(z-l)}) e^{j\omega t}$$

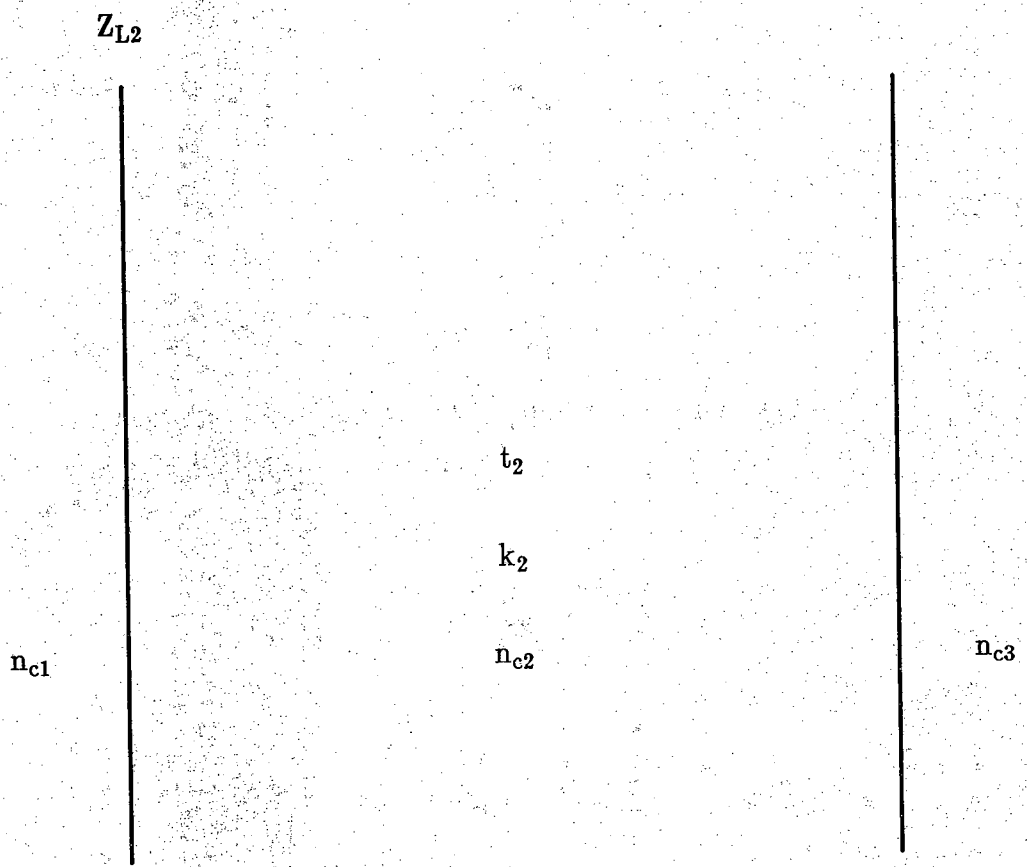

Figure G.1 Parameters needed to calculate the reflection coefficient

where l is the second layer's thickness.

The magnetic field necessarily points in the y-direction and using one of Maxwell's equation

$$\frac{\partial E_{xm}}{\partial z} = -\mu \frac{\partial H_{yi}}{\partial t} = -j\mu\omega H_{yi} \ ,$$

$$H_{y1} = \frac{1}{-j\mu\omega}(-jk_{z1}\ E_{x1}^{+}e^{-jk_{z1}z} + jk_{z1}\ E_{x1}^{-}e^{+jk_{z1}z})e^{j\omega t} \ ,$$

$$H_{y2} = \frac{1}{-j\mu\omega}(-jk_{z2}\ E_{x2}^{+}e^{-jk_{z2}z} + jk_{z2}\ E_{x2}^{-}e^{+jk_{z2}z})e^{j\omega t} \ ,$$

and

$$H_{y3} = \frac{1}{-j\mu\omega}(-jk_{z3}\ E_{x3}^{+}e^{-jk_{z3}z})e^{j\omega t} \ .$$

These tangential electric and magnetic fields must be continuous across the boundaries. Using this result on the previous equations, @ $z = 0$, $E_{x1} = E_{x2}$ and

$$E_{x1}^{+} + E_{x1}^{-} = E_{x2}^{+} + E_{x2}^{-} \ .$$

@ $z = l$, $E_{x2} = E_{x3}$ and

$$E_{x2}^{+}e^{-jk_{z2}l} + E_{x2}^{-}e^{+jk_{z2}l} = E_{x3}^{+} \ .$$

@ $z = 0$, $H_{y1} = H_{y2}$ and

$$jk_{z1}(-E_{x1}^{+} + E_{x1}^{-}) = jk_{z2}(-E_{x2}^{+} + E_{x2}^{-}) \ .$$

@ $z = l$, $H_{y2} = H_{y3}$ and

$$jk_{z2}(-E_{x2}^{+}e^{-jk_{z2}l} + E_{x2}^{-}e^{+jk_{z2}l} = jk_{z3}(-E_{x3}^{+}) \ .$$

The wave number k_{z1} is related to the complex index of refraction by the equation

$$k_{z1} = \frac{\omega}{v_1} = \omega\sqrt{\mu_o\epsilon_1} = \omega\sqrt{\mu_o\epsilon_0}\sqrt{\epsilon_{r1}}$$

$$= \frac{\omega}{c}\sqrt{\epsilon_{r1}} = \frac{\omega}{c}(n_{r1}-j\kappa_1) = \frac{\omega}{c}(n_{c1})$$

where n_{c1} is the complex index of refraction, n_{r1} is the real part of the index of refraction and κ_1 is the imaginary part of the index of refraction, also known as the extinction coefficient.

For the second and third layers,

$$k_{z2} = \frac{\omega}{c}(n_{r2}-j\kappa_2) = \frac{\omega}{c}(n_{c2})$$

and

$$k_{z3} = \frac{\omega}{c}(n_{r3}-j\kappa_3) = \frac{\omega}{c}(n_{c3}) \ .$$

Reinserting this relationship into Maxwell's equations at the boundaries,

$$E_{x1}^{+} + E_{x1}^{-} = E_{x2}^{+} + E_{x2}^{-} \ , \tag{A1}$$

$$E_{x2}^{+}e^{-jk_{z2}l} + E_{x2}^{-}e^{+jk_{z2}l} = E_{x3}^{+} \ , \tag{A2}$$

$$n_{c1}(-E_{x1}^{+} + E_{x1}^{-}) = n_{c2}(-E_{x2}^{+} + E_{x2}^{-}) \ , \tag{A3}$$

and

$$n_{c2}(-E_{x2}^{+}e^{-jk_{z2}l} + E_{x2}^{-}e^{+jk_{z2}l}) = n_{c3}(-E_{x3}^{+}) \quad . \tag{A4}$$

There are two ways to eliminate the constants (ie. E_{x1}^{+} , E_{x2}^{-} , ...) of the electric and magnetic fields. First, the electric fields are compared at all adjacent the boundaries and the magnetic fields are compared at all adjacent the boundaries. For a three layer sample, multiply (A1) by n_{c2} and add to (A3),

$$(n_{c2}-n_{c1})\,E_{x1}^{+} + (n_{c2}+n_{c1})\,E_{x1}^{-} = (2n_{c2})\,E_{x2}^{-} \tag{A5}$$

and multiply (A2) by n_{c2} and add to (A4),

$$(2n_{c2})\,E_{x2}^{-}e^{+jk_{z2}l} = (n_{c2}-n_{c3})\,E_{x3}^{+} \quad . \tag{A6}$$

Second, the electric and magnetic fields are compared at the boundary of the semi-infinite layers. For a three layer sample, multiply (A1) by $-e^{-jk_{z2}l}$ and add to (A2),

$$(E_{x1}^{+} + E_{x1}^{-})-e^{-jk_{z2}l} + E_{x3}^{+} = E_{x2}^{-}2j\sin k_{z2}l \tag{A7}$$

and multiply (A3) by $-e^{-jk_{z2}l}$ and add to (A4),

$$n_{c1}(-E_{x1}^{+} + E_{x1}^{-})-e^{-jk_{z2}l} - n_{c3}E_{x3}^{+} = n_{c2}E_{x2}^{-}2j\sin k_{z2}l \quad . \tag{A8}$$

Comparing equations (A5) and (A6),

$$[(n_{c2}-n_{c1})\,E_{x1}^{+} + (n_{c2}+n_{c1})\,E_{x1}^{-}]e^{+jk_{z2}l} = (n_{c2}-n_{c3})\,E_{x3}^{+} \quad . \tag{A9}$$

Comparing equations (A7) and (A8),

$$[(n_{c2}+n_{c1})\,E_{x1}^{+} + (n_{c2}-n_{c1})\,E_{x1}^{-}]e^{-jk_{z2}l} = (n_{c2}+n_{c3})\,E_{x3}^{+} \quad . \tag{A10}$$

Eliminating E_{x3}^{+} from eqns. (A9) and (A10),

$$\frac{E_{x1}^{-}}{E_{x1}^{+}} = \frac{(n_{c2}+n_{c1})(n_{c2}-n_{c3})e^{-jk_{z2}l} - (n_{c2}-n_{c1})(n_{c2}+n_{c3})e^{jk_{z2}l}}{(n_{c2}+n_{c1})(n_{c2}+n_{c3})e^{jk_{z2}l} - (n_{c2}-n_{c1})(n_{c2}-n_{c3})e^{-jk_{z2}l}}$$

$$= -\left(\frac{(n_{c2}-n_{c1})(n_{c2}+n_{c3})e^{jk_{z2}l} - (n_{c2}+n_{c1})(n_{c2}-n_{c3})e^{-jk_{z2}l}}{(n_{c2}+n_{c1})(n_{c2}+n_{c3})e^{jk_{z2}l} - (n_{c2}-n_{c1})(n_{c2}-n_{c3})e^{-jk_{z2}l}}\right)$$

$$= -\left(\frac{(n_{c2}n_{c3}-n_{c2}n_{c1})\cos k_{z2}l + j(n_{c2}^2-n_{c1}n_{c3})\sin k_{z2}l}{(n_{c2}n_{c3}+n_{c2}n_{c1})\cos k_{z2}l + j(n_{c2}^2+n_{c1}n_{c3})\sin k_{z2}l}\right)$$

$$= -\left(\frac{-n_{c1}(n_{c2}\cos k_{z2}l+jn_{c3}\sin k_{z2}l) + n_{c2}(n_{c3}\cos k_{z2}l+jn_{c2}\sin k_{z2}l)}{n_{c1}(n_{c2}\cos k_{z2}l+jn_{c3}\sin k_{z2}l) + n_{c2}(n_{c3}\cos k_{z2}l+jn_{c2}\sin k_{z2}l)}\right) . \quad \text{(A11)}$$

$\frac{E_{x3}^+}{E_{x1}^+}$ is calculated by comparing (A9) and (A10),

$$\frac{E_{x3}^+}{E_{x1}^+} = \frac{(n_{c2}+n_{c1})^2-(n_{c2}-n_{c1})^2}{n_{c2}(n_{c3}+n_{c1})2\cos k_{z2}l + j(n_{c2}^2+n_{c1}n_{c3})2\sin k_{z2}l} . \quad \text{(A12)}$$

To compare this transmission coefficient with the transmission coefficient in Pankove [Pankove 1971], the equation needed to be considered is

$$\frac{E_{x3}^+}{E_{x1}^+} = \frac{(n_{c2}+n_{c1})^2-(n_{c2}-n_{c1})^2}{(n_{c2}+n_{c1})(n_{c2}+n_{c3})e^{jk_{z2}l} - (n_{c2}-n_{c1})(n_{c2}-n_{c3})e^{-jk_{z2}l}} .$$

In Pankove's book, $n_{c1} = n_{c3} = 1.$, so

$$\frac{E_{x3}^+}{E_{x1}^+} = \frac{(n_{c2}+1.)^2-(n_{c2}-1.)^2}{(n_{c2}+1.)^2e^{jk_{z2}l} - (n_{c2}-1.)^2e^{-jk_{z2}l}} .$$

In Pankove's book, R_{em} is defined as

$$R_{em} = \frac{(n_{c2}-1)^2}{(n_{c2}+1)^2}$$

so

$$\frac{E_{x3}^{+}}{E_{x1}^{+}} = \frac{(1-R_{em})e^{-jk_{z2}l}}{1-R_{em}e^{-j2k_{z2}l}} .$$

The transmission coefficient, T_{em}, is defined as

$$T_{em} = \left| \frac{E_{x3}^{+}}{E_{x1}^{+}} \right|^2 = \frac{(1.-R_{em})^2 e^{-2\alpha_E l}}{(1.-R_{em}e^{-2\alpha_E l}(\cos\beta l - j\sin\beta l))^2}$$

where $k_{z2}=\beta-j\alpha_E$ and α_E is the absorption coefficient of the electric field (not the intensity). Rearranging the denominator,

$$T_{em} = \frac{(1-R_{em})^2 e^{-2\alpha_E l}}{1+R_{em}^2 e^{-4\alpha_E l} - 2R_{em}e^{-2\alpha_E l}\cos\beta l} .$$

The intensity absorption coefficient, α, is related to α_E by

$$\alpha = 2\alpha_E .$$

Subsequently,

$$T_{em} = \frac{(1-R_{em})^2 e^{-\alpha l}}{1+R_{em}^2 e^{-2\alpha l} - 2R_{em}e^{-\alpha l}\cos\beta l} . \qquad \text{(A13)}$$

while in Pankove's book

$$T_{em} = \frac{(1.-R_{em})^2 e^{-\alpha l}}{1.-R_{em}^2 e^{-2\alpha l}} . \qquad \text{(A14)}$$

The difference between Pankove's equation (A14) and equation (A13) is that Pankove uses Fresnel's equations for intensities. Pankove's procedure is an incorrect procedure, the correct procedure is to use Fresnel's equations for electric fields and multiply the transmission coefficient of the electric field by its complex conjugate to get the transmission coefficient for the intensity. This is clearly shown in sec. 7.6 in Born and Wolf.

In conclusion, the correct form of T_{em} is

$$T_{em} = \frac{(1.-R_{em})^2 e^{-\alpha l}}{1.+R_{em}^2 e^{-2\alpha l} - 2R_{em} e^{-\alpha l}\cos\beta l} \quad . \tag{A13}$$

G.3 Solving for the n+1 layer sample using the results of the n layer sample.

Although the procedure in the previous section is straightforward, the mathematics become very tedious. To avoid this problem, another approach can be used.

Unlike the last section, the layer labeled 1 will be on the transmission side (the right side in Fig. G.2). The electric field equations in the layers are in the first layer

$$E_{x1} = E_{x1}^{+} e^{-jk_{z1}(z)} \quad ,$$

the second layer

$$E_{x2} = (E_{x2}^{+} e^{-jk_{z2}(z)} + E_{x2}^{-} e^{+jk_{z2}(z)}) \quad ,$$

and the third layer

$$E_{x3} = (E_{x3}^{+} e^{-jk_{z3}(z+z_2)} + E_{x3}^{-} e^{+jk_{z3}(z+z_2)}) \quad .$$

In general, for the m^{th} layer,

$$E_{xm} = (E_{xm}^{+} e^{-jk_{zm}(z+z_{m-1})} + E_{xm}^{-} e^{+jk_{zm}(z+z_{m-1})}) \quad .$$

The magnetic fields in the layers are

$$H_{y1} = \frac{-1}{j\mu\omega}(-k_{z1} E_{x1}^{+} e^{-jk_{z1}(z)}$$

for the first layer,

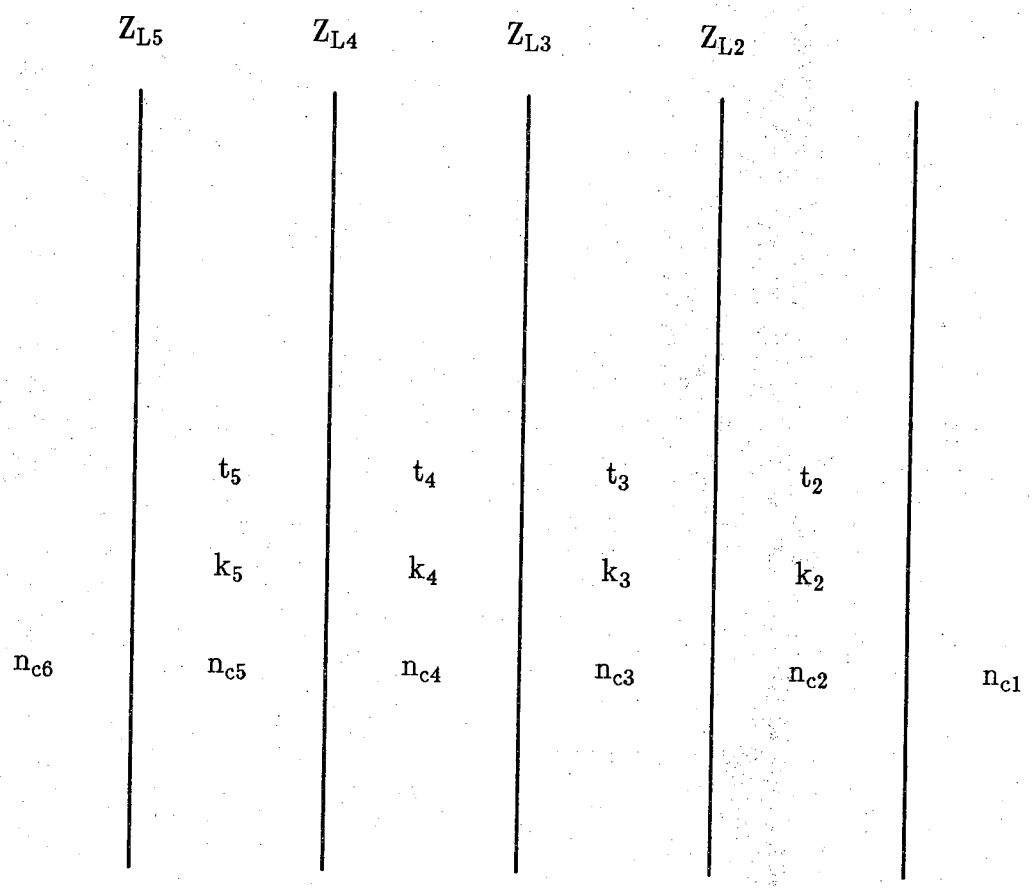

Figure G.2 Parameters needed to calculate the reflection coefficient (six layer sample)

$$H_{y2} = \frac{-1}{j\mu\omega}(-k_{z2}E_{x2}^{+}e^{-jk_{z2}(z)} + k_{z2}E_{x2}^{-}e^{+jk_{z2}(z)})$$

for the second layer,

$$H_{y3} = \frac{-1}{j\mu\omega}(-k_{z3}E_{x3}^{+}e^{-jk_{z3}(z+z_2)} + k_{z3}E_{x3}^{-}e^{+jk_{z3}(z+z_2)})$$

for the third layer, and in general,

$$H_{ym} = \frac{-1}{j\mu\omega}(-k_{zm}E_{xm}^{+}e^{-jk_{zm}(z+z_{m-1})} + k_{zm}E_{xm}^{-}e^{+jk_{zm}(z+z_{m-1})})$$

for the m^{th} layer.

Due to Maxwell's equations, the boundary conditions are that the tangential magnetic and electric fields at an interface must be continuous. Assuming that there are no magnetic effects, $k = \omega/c\ n_c$ where n_c is the complex index of refraction. Keeping this relationship in mind, the boundary conditions are for the first layer-second layer interface

$$E_{x1}^{+} = E_{x2}^{+} + E_{x2}^{-} \tag{B1}$$

and

$$-n_{c1}E_{x1}^{+} = n_{c2}(-E_{x2}^{+} + E_{x2}^{-}) \ , \tag{B2}$$

for the second layer-third layer interface

$$E_{x2}^{+}e^{+jk_{z2}t_2} + E_{x2}^{-}e^{-jk_{z2}t_2} = E_{x3}^{+} + E_{x3}^{-} \tag{B3}$$

and

$$n_{c2}(-E_{x2}^{+}e^{+jk_{z2}t_2} + E_{x2}^{-}e^{-jk_{z2}t_2}) = n_{c3}(-E_{x3}^{+} + E_{x3}^{-}) \ , \tag{B4}$$

for the third layer-fourth layer interface

$$E^+_{x3}e^{+jk_{z3}t_3} + E^-_{x3}e^{-jk_{z3}t_3} = E^+_{x4} + E^-_{x4} \tag{B5}$$

and

$$n_{c3}(-E^+_{x3}e^{+jk_{z3}t_3} + E^-_{x3}e^{-jk_{z3}t_3}) = n_{c4}(-E^+_{x4} + E^-_{x4}) \ . \tag{B6}$$

In general for the m^{th} layer-$(m+1)^{th}$ layer interface

$$E^+_{xm}e^{+jk_{zm}t_m} + E^-_{xm}e^{-jk_{zm}t_m} = E^+_{x(m+1)} + E^-_{x(m+1)} \tag{B7}$$

and

$$n_{cm}(-E^+_{xm}e^{+jk_{zm}t_m} + E^-_{xm}e^{-jk_{zm}t_m}) = n_{c(m+1)}(-E^+_{x(m+1)} + E^-_{x(m+1)}) \ . \tag{B8}$$

Comparing $\dfrac{E^-_{xm}}{E^+_{xm}}$ to $\dfrac{E^-_{x(m+1)}}{E^+_{x(m+1)}}$,

$$E^+_{xm}(e^{+jk_{zm}t_m} + \frac{E^-_{xm}}{E^+_{xm}}e^{-jk_{zm}t_m}) = E^+_{x(m+1)} + E^-_{x(m+1)} \tag{B9}$$

and

$$n_{cm}E^+_{xm}(-e^{+jk_{zm}t_m} + \frac{E^-_{xm}}{E^+_{xm}}e^{-jk_{zm}t_m}) = n_{c(m+1)}(-E^+_{x(m+1)} + E^-_{x(m+1)}) \ . \tag{B10}$$

Changing the exponentials to sines and cosines,

$$E^+_{xm}((1 + \frac{E^-_{xm}}{E^+_{xm}})\cos k_m t_m + j(1 - \frac{E^-_{xm}}{E^+_{xm}})\sin k_{zm} t_m) = E^+_{x(m+1)} + E^-_{x(m+1)} \tag{B11}$$

and

$$E^{+}_{xm}(-n_{cm})((1-\frac{E^{-}_{xm}}{E^{+}_{xm}})\cos k_{zm}t_m + j(1+\frac{E^{-}_{xm}}{E^{+}_{xm}})\sin k_{zm}t_m) =$$

$$n_{c(m+1)}(-E^{+}_{x(m+1)} + E^{-}_{x(m+1)}) \quad . \tag{B12}$$

Eliminating $E^{+}_{x(m+1)}$(except in the ratio $\frac{E^{-}_{x(m+1)}}{E^{+}_{x(m+1)}}$),

$$(-n_{cm})((1-\frac{E^{-}_{xm}}{E^{+}_{xm}})\cos k_{zm}t_m + j(1+\frac{E^{-}_{xm}}{E^{+}_{xm}})\sin k_{zm}t_m)(E^{+}_{x(m+1)} + E^{-}_{x(m+1)}) =$$

$$n_{c(m+1)}((1+\frac{E^{-}_{xm}}{E^{+}_{xm}})\cos k_{zm}t_m + j(1-\frac{E^{-}_{xm}}{E^{+}_{xm}})\sin k_{zm}t_m)(-E^{+}_{x(m+1)} + E^{-}_{x(m+1)}) \tag{B13}$$

Rearranging the equation, the ratio $\frac{E^{-}_{x(m+1)}}{E^{+}_{x(m+1)}}$ is found as

$$\frac{E^{-}_{x(m+1)}}{E^{+}_{x(m+1)}} = \frac{n_{c(m+1)}\left(\dfrac{(1+\frac{E^{-}_{xm}}{E^{+}_{xm}})\cos k_{zm}t_m + j(1-\frac{E^{-}_{xm}}{E^{+}_{xm}})\sin k_{zm}t_m}{(1-\frac{E^{-}_{xm}}{E^{+}_{xm}})\cos k_{zm}t_m + j(1+\frac{E^{-}_{xm}}{E^{+}_{xm}})\sin k_{zm}t_m}\right) - n_{cm}}{n_{c(m+1)}\left(\dfrac{(1+\frac{E^{-}_{xm}}{E^{+}_{xm}})\cos k_{zm}t_m + j(1-\frac{E^{-}_{xm}}{E^{+}_{xm}})\sin k_{zm}t_m}{(1-\frac{E^{-}_{xm}}{E^{+}_{xm}})\cos k_{zm}t_m + j(1+\frac{E^{-}_{xm}}{E^{+}_{xm}})\sin k_{zm}t_m}\right) + n_{cm}} \quad . \tag{B14}$$

$\hat{Z}_{Im}$, which is defined as the normalized input impedance, is

$$\hat{Z}_{Im} = \frac{(1+\frac{E^{-}_{xm}}{E^{+}_{xm}})\cos k_{zm}t_m + j(1-\frac{E^{-}_{xm}}{E^{+}_{xm}})\sin k_{zm}t_m}{(1-\frac{E^{-}_{xm}}{E^{+}_{xm}})\cos k_{zm}t_m + j(1+\frac{E^{-}_{xm}}{E^{+}_{xm}})\sin k_{zm}t_m} \tag{B15}$$

then (B14) becomes

$$\rho_{em} = \frac{E^-_{xm}}{E^+_{xm}} = \frac{n_{cm}\hat{Z}_{I(m-1)} - n_{c(m-1)}}{n_{cm}\hat{Z}_{I(m-1)} + n_{c(m-1)}} \tag{B16}$$

where ρ_{em} is defined as the reflection coefficient. To relate $\hat{Z}_{Im}$ to $\hat{Z}_{I(m-1)}$, place the results from (B16) into (B15),

$$\hat{Z}_{Im} = \frac{n_{cm}\hat{Z}_{I(m-1)}\cosh_{zm}t_m + jn_{c(m-1)}\sinh_{zm}t_m}{n_{c(m-1)}\cosh_{zm}t_m + jn_{cm}\hat{Z}_{I(m-1)}\sinh_{zm}t_m} \quad . \tag{B17}$$

This is related to the input impedance Z_{im} in Ramo, Whinnery, and van Duzer [Ramo, Whinnery, & van Duzer 1965] by

$$\hat{Z}_{Im} = \frac{Z_{im}}{\eta_i}$$

where η_i is known as the intrinsic impedance.

Now that one knows the reflection coefficient, the transmission coefficient is rather straightforward. One has to consider the boundary conditions equations of the electric field. For the first layer-second layer interface

$$E^+_{x1} = E^+_{x2} + E^-_{x2} \quad . \tag{B1}$$

For the second layer-third layer interface

$$E^+_{x2}e^{+jk_{z2}t_2} + E^-_{x2}e^{-jk_{z2}t_2} = E^+_{x3} + E^-_{x3} \quad . \tag{B3}$$

For the third layer-fourth layer interface

$$E^+_{x3}e^{+jk_{z3}t_3} + E^-_{x3}e^{-jk_{z3}t_3} = E^+_{x4} + E^-_{x4} \quad . \tag{B5}$$

In general for the i^{th} layer-$(i+1)^{th}$ layer interface

$$E^{+}_{xm} e^{+jk_{zm}t_m} + E^{-}_{xm} e^{-jk_{zm}t_m} = E^{+}_{x(m+1)} + E^{-}_{x(m+1)} \quad . \tag{B7}$$

Placing equation (B16) into these equations and using the fact that $\hat{Z}_{I1} = 1$,

$$E^{+}_{x1} = (1 + \frac{n_{c2} - n_{c1}}{n_{c2} + n_{c1}})E^{+}_{x2} \quad . \tag{B18}$$

For the second layer-third layer interface

$$(e^{+jk_{z2}t_2} + \frac{n_{c2} - n_{c1}}{n_{c2} + n_{c1}} e^{-jk_{z2}t_2})E^{+}_{x2} = (1 + \frac{n_{c3}\hat{Z}_{I2} - n_{c2}}{n_{c3}\hat{Z}_{I2} + n_{c2}})E^{+}_{x3} \quad . \tag{B19}$$

For the third layer-fourth layer interface

$$(e^{+jk_{z3}t_3} + \frac{n_{c3}\hat{Z}_{I2} - n_{c2}}{n_{c3}\hat{Z}_{I2} + n_{c2}} e^{-jk_{z3}t_3})E^{+}_{x3} = (1 + \frac{n_{c4}\hat{Z}_{I3} - n_{c3}}{n_{c4}\hat{Z}_{I3} + n_{c3}})E^{+}_{x4} \quad . \tag{B20}$$

In general for the i^{th} layer-$(i+1)^{th}$ layer interface

$$(e^{+jk_{zm}t_m} + \frac{n_{cm}\hat{Z}_{I(m-1)} - n_{c(m-1)}}{n_{cm}\hat{Z}_{I(m-1)} + n_{c(m-1)}} e^{-jk_{zm}t_m})E^{+}_{xm} =$$

$$(1 + \frac{n_{c(m+1)}\hat{Z}_{Im} - n_{cm}}{n_{c(m+1)}\hat{Z}_{Im} + n_{cm}})E^{+}_{x(m+1)} \quad . \tag{B21}$$

Using (B21), one can find the ratio,

$$\frac{E^{+}_{xm}}{E^{+}_{x(m+1)}} = \frac{(1 + \frac{n_{c(m+1)}\hat{Z}_{Im} - n_{cm}}{n_{c(m+1)}\hat{Z}_{Im} + n_{cm}})}{(e^{+jk_{zm}t_m} + \frac{n_{cm}\hat{Z}_{I(m-1)} - n_{c(m-1)}}{n_{cm}\hat{Z}_{I(m-1)} + n_{c(m-1)}} e^{-jk_{zm}t_m})}$$

$$= \frac{(n_{c(m+1)}\hat{Z}_{Im})(n_{cm}\hat{Z}_{I(m-1)} + n_{c(m-1)})}{(n_{c(m+1)}\hat{Z}_{Im} + n_{cm})(n_{cm}\hat{Z}_{I(m-1)}\cosh_{zm}t_m + jn_{c(m-1)}\sinh_{zm}t_m)} \quad \text{(B22)}$$

From (B18),

$$\frac{E^+_{x1}}{E^+_{x2}} = \frac{2n_{c2}}{n_{c2} + n_{c1}} \quad . \quad \text{(B23a)}$$

Using (B22),

$$\frac{E^+_{x2}}{E^+_{x3}} = \frac{(n_{c3}\hat{Z}_{I2})(n_{c2} + n_{c1})}{(n_{c3}\hat{Z}_{I2} + n_{c2})(n_{c2}\cosh_{z2}t_2 + jn_{c1}\sinh_{z2}t_2)} \quad , \quad \text{(B23b)}$$

$$\frac{E^+_{x3}}{E^+_{x4}} = \frac{(n_{c4}\hat{Z}_{I3})(n_{c3}\hat{Z}_{I2} + n_{c2})}{(n_{c4}\hat{Z}_{I3} + n_{c3})(n_{c3}\hat{Z}_{I2}\cosh_{z3}t_3 + jn_{c2}\sinh_{z3}t_3)} \quad , \quad \text{(B23c)}$$

and

$$\frac{E^+_{x4}}{E^+_{x5}} = \frac{(n_{c5}\hat{Z}_{I4})(n_{c4}\hat{Z}_{I3} + n_{c3})}{(n_{c5}\hat{Z}_{I4} + n_{c4})(n_{c4}\hat{Z}_{I3}\cosh_{z4}t_4 + jn_{c3}\sinh_{z4}t_4)} \quad . \quad \text{(B23d)}$$

Using equations (B22) and (B23), one can solve for $\frac{E^+_{x1}}{E^+_{xm}}$. For 4 layers (2 semi-infinite layers),

$$\frac{E^+_{x1}}{E^+_{x4}} = \frac{E^+_{x1}}{E^+_{x2}}\frac{E^+_{x2}}{E^+_{x3}}\frac{E^+_{x3}}{E^+_{x4}} = \left(\frac{2n_{c2}n_{c3}n_{c4}}{n_{c4}\hat{Z}_{I3} + n_{c3}}\right)$$

$$\frac{\hat{Z}_{I2}}{[n_{c2}\cosh_{z2}t_2 + jn_{c1}\sinh_{z2}t_2]}\frac{\hat{Z}_{I3}}{[n_{c3}\hat{Z}_{I2}\cosh_{z3}t_3 + jn_{c2}\sinh_{z3}t_3]} \quad . \quad \text{(B24)}$$

In general,

$$\tau_{em} = \frac{E^+_{x1}}{E^+_{x(m+1)}}$$

$$= \frac{2}{n_{c(m+1)}\hat{Z}_{Im}+n_{cm}}\left(\prod_{i=2}^{m+1} n_{ci}\right)\left(\prod_{i=2}^{m}\frac{\hat{Z}_{Ii}}{[n_{ci}\hat{Z}_{I(i-1)}\cos k_{zi}t_i + jn_{c(i-1)}\sin k_{zi}t_i]}\right) \quad \text{(B25a)}$$

or

$$\tau_{em} = \frac{E^+_{x1}}{E^+_{xm}}$$

$$= \frac{2}{n_{cm}\hat{Z}_{I(m-1)}+n_{c(m-1)}}\left(\prod_{i=2}^{m} n_{ci}\right)\left(\prod_{i=2}^{m-1}\frac{\hat{Z}_{Ii}}{[n_{ci}\hat{Z}_{I(i-1)}\cos k_{zi}t_i + jn_{c(i-1)}\sin k_{zi}t_i]}\right) \quad \text{(B25b)}$$

where τ_{em} is known as the transmission coefficient.

Using equation (B17),

$$\tau_{em} = \frac{E^+_{x1}}{E^+_{xm}}$$

$$= \frac{2}{n_{cm}\hat{Z}_{I(m-1)}+n_{c(m-1)}}\left(\prod_{i=2}^{m} n_{ci}\right)\left(\prod_{i=2}^{m-1}\frac{1}{[n_{c(i-1)}\cos k_{zi}t_i + jn_{ci}\hat{Z}_{I(i-1)}\sin k_{zi}t_i]}\right) \quad \text{(B26)}$$

So in conclusion,

$$\hat{Z}_{Im} = \frac{n_{cm}\hat{Z}_{I(m-1)}\cos k_{zm}t_m + jn_{c(m-1)}\sin k_{zm}t_m}{n_{c(m-1)}\cos k_{zm}t_m + jn_{cm}\hat{Z}_{I(m-1)}\sin k_{zm}t_m} \quad \text{(B17)}$$

where $\hat{Z}_{Im}$ is defined as the normalized input impedance. Combining (B14) and (B15),

$$\rho_{em} = \frac{E^{-}_{xm}}{E^{+}_{xm}} = \frac{n_{cm}\hat{Z}_{I(m-1)} - n_{c(m-1)}}{n_{cm}\hat{Z}_{I(m-1)} + n_{c(m-1)}} \tag{B16}$$

where ρ_{em} is defined as the reflection coefficient.

$$\tau_{em} = \frac{E^{+}_{x1}}{E^{+}_{xm}}$$

$$= \frac{2}{n_{cm}\hat{Z}_{I(m-1)} + n_{c(m-1)}} \left(\prod_{i=2}^{m} n_{ci}\right)\left(\prod_{i=2}^{m-1} \frac{1}{[n_{c(i-1)}\cos k_{zi} t_i + j n_{ci}\hat{Z}_{I(i-1)}\sin k_{zi} t_i]}\right) \tag{B26}$$

where τ_{em} is defined as the transmission coefficient.

Z_{im} and ρ_{em} are discussed in depth in Ramo, Whinnery and van Duzer [Ramo, Whinnery, & van Duzer 1965].

For these equations, it can be noticed that there are four variables - the wavelength, the index of refraction, the layer thicknesses and the number of layers.

SUBJECT INDEX